Neutron Stratigraphy in the Lunar Regolith

Thesis by

Guston Price Russ III

In Partial Fulfillment of the Requirements

for the Degree of

Doctor of Philosophy

California Institute of Technology

Pasadena, California

1974

(Submitted 27 November 1973)

B.,

ℓ.

P.

"Pardon, O beautiful Diana of the Ephesians! Pardon, O Phoebe, thou pearl-faced goddess of night beloved of Greece! O Isis, thou sympathetic queen of Nile-washed cities! O Astarte, thou favorite deity of the Syrian hills! O Artemis, thou symbolical daughter of Jupiter and Latona, that is of light and darkness! O brilliant sister of the radiant Apollo!"

Ardan in Jules Verne's
All Around the Moon
(translated by Edward Roth)

Acknowledgment

I am gratefully indebted to T. Felder Dorn who suggested that I apply to Caltech. I have profited greatly from countless discussions with my fellow inmates of the Lunatic Asylum who have freely shared their achievements, secrets, hopes, prejudices, and occasional frustrations. In particular, I would like to acknowledge the help of Fouad Tera who developed the procedures used to separate the rare earth elements, Ottokar J. Eugster who taught me how to analyze gadolinium on the mass spectrometer, and John C. Huneke, who helped me understand rare gas mass spectra and who participated in the development of lunar regolith mixing models.

It has been an extraordinary privilege to participate in the analysis of the first lunar samples and to work with Donald S. Burnett, my thesis advisor, and Gerald J. Wasserburg, the director of the Lunatic Asylum. I would particularly like to thank Don Burnett for the patience he has shown and Jerry Wasserburg for the persistent comment, "I don't understand!"

This work was supported by the National Science Foundation under grants GP-9114 and GP-28027 and by the National Aeronautics and Space Administration under contracts NAS-9-8074 and NGL-05-002-188. In addition, I was supported for three years by the Department of Health, Education, and Welfare under a Title IV Fellowship, and more recently by my wife. These sources of support are gratefully acknowledged.

Chapters 6-9 are reproduced with the permission of North-Holland Publishing Company.

Abstract

Differences in the isotopic composition of Gd and Sm among lunar samples collected during the Apollo 11, 12, 14, 15, and 16 and Luna 16 missions have been measured by high precision mass spectrometry. These differences (up to 1.9% in $^{158}Gd/^{157}Gd$ and 2.0% in $^{150}Sm/^{149}Sm$) can be attributed unambiguously to low energy neutron capture reactions and correspond to neutron fluences as high as 10^{17} n/cm^2 ($E < 0.18$ eV). For the Apollo 16 samples, enrichments are reported for the $^{152}Gd/^{160}Gd$ ratio which appear to be due to neutron capture by ^{151}Eu. The measured ratio of the number of neutrons captured per atom by ^{149}Sm to the number captured per atom by ^{157}Gd indicates that the low energy lunar neutron spectrum is in reasonable agreement with that calculated by Lingenfelter, Canfield, and Hampel but that the lunar spectrum is somewhat harder. A synthesis of all the available lunar neutron capture data for ^{157}Gd, ^{155}Gd, ^{149}Sm, ^{151}Eu, ^{59}Co, ^{79}Br, ^{81}Br, ^{130}Ba, ^{186}W, ^{235}U, ^{238}U, and ^{40}Ca indicates that only the ^{186}W and ^{235}U data are incompatible with the LCH neutron spectrum and flux.

Based on the LCH neutron flux, the neutron fluences, ψ, determined for the lunar soils are all lower than would be expected for materials mixed in the upper few meters of the regolith for $> 3 \times 10^9$ yr. In terms of a uniform mixing model the measured neutron fluences imply that the depth of the regolith is between 10 and 14 m at all of the Apollo sites studied. These are greater than the depths implied from cratering theory. The $^{126}Xe/\psi$ ratios for the soils indicate that they have been well mixed to a depth of > 200 g/cm^2. Detailed fluence

studies in the Apollo 12 double core show that these materials could not have been undisturbed for > 10^8 yr. The upper layers of the Apollo 15 and 16 drill stems also imply mixing on this time scale. However, the Apollo 15 drill stem has a smooth peak in the fluence at a depth of ~ 190 g/cm^2. From the magnitude of this peak, it can be concluded that below a depth of ~ 75 g/cm^2 these materials have been undisturbed for at least 400 my. The fluence profile in the Apollo 16 drill stem is more complicated but indicates an area where material has been accumulating for several hundred million years.

A model is presented for the depth dependence of the ratio of ^{131}Xe produced by neutron capture on ^{130}Ba to ^{126}Xe produced by spallation reactions on Ba. Effective exposure depths are calculated for 24 rocks from Apollo 11 and 12. Detailed irradiation histories are presented for rocks 10017, 14310, and 15595. An erosion rate for Hadley Rille of ~1 cm/my is calculated from the neutron fluence of rock 15595.

From Gd and Sm isotopic measurements it is shown that the Norton County meteorite has been exposed to a neutron flux with a spectrum compatible with that predicted by the LCH calculations. The neutron fluence to which our sample of Norton County has been exposed is 1.2 x 10^{16} n/cm^2. No neutron produced effects were observed in the isotopic composition of Gd from a bulk sample of the Allende meteorite.

Table of Contents

List of Figures

List of Tables

1. General Introduction

The material in the upper few meters of the lunar regolith, *i.e.*, the layer of fine-grained debris covering the lunar surface, is irradiated by cosmic ray produced neutrons. If one knows the capture rate of these neutrons as a function of depth and their energy spectrum, then measurements of time integrated fluxes, fluences, can be used to determine the depositional history of the lunar surface. The fluence of neutrons to which a sample has been exposed can be determined by mass spectrometrically measuring depletions in the abundance of isotopes which have large neutron capture cross sections or enrichments in isotopes which are produced by neutron capture.

In this work, low energy neutron fluences have been determined for samples from six lunar sites — Apollo 11, 12, 14, 15, and 16, and Luna 16 — by high precision measurements of the isotopic composition of gadolinium and samarium, which have large neutron capture cross sections near and below 0.1 eV. These fluences, especially those for core samples, have been used to determine the time scale for the deposition of the regolith and to model its depositional history at the various lunar sites. In addition, neutron capture rates have been calculated for eleven nuclides for which capture products have been reported in the literature. These capture rates, which are based on the theoretical calculations of the lunar neutron flux made by Lingenfelter, Canfield and Hampel [1] (hereafter referred to as LCH), are compared to the measured effects attributed to neutron capture.

In Chapter 2, the experimental procedures will be explained and the measured gadolinium and samarium isotopic compositions will be presented. It was realized at least as early as 1953 [2] that the large neutron absorption cross section of ^{157}Gd ($\sigma_{thermal} = 2.6 \times 10^5$ barns) made gadolinium a logical choice for measuring neutron fluences in geological samples. However, until the advent of high precision mass spectrometers like the *Lunatics* [3] used in this work with which it is possible to measure gadolinium or samarium isotopic ratios to $\pm$ 1-2 $\times 10^{-2}$% ($2\sigma_{mean}$), no deviations from the normal terrestrial composition were discovered [4,5,6] in extraterrestrial samples. The first neutron produced anomaly in gadolinium was measured by Eugster, Tera, Burnett and Wasserburg [7] in the meteorite Norton County. These workers were also the first to report neutron effects in lunar gadolinium [8]. The differences which they observed in the Gd isotopic compositions of the lunar samples can be unambiguously attributed to neutron capture by ^{157}Gd and ^{155}Gd because the capture products ^{158}Gd and ^{156}Gd are stable isotopes, and one can show that the depletions of ^{157}Gd and ^{155}Gd are accompanied by corresponding increases in ^{158}Gd and ^{156}Gd. The relative amounts of capture by ^{157}Gd and ^{155}Gd are also in agreement with the expected ratio. In addition to the work of Eugster *et al.* [8] and that reported here, Lugmair and Marti [9,10,11] have measured the composition of Gd in samples from three lunar missions. Their data will be interpreted in terms of the LCH energy spectrum for the first time.

Murthy, Schmitt and Rey [6] measured $^{149}Sm/^{148}Sm$ ratios for several Apollo 11 samples but saw no definite effect at their level of

precision ($\sim 0.2\%$). The first measured anomalies in Sm were reported by Russ, Burnett, Lingenfelter, and Wasserburg in the paper which comprises Chapter 6. Because Sm and Gd capture neutrons in slightly different energy ranges, the ratio of the number of neutrons captured per atom by ^{149}Sm to the number captured per atom by ^{157}Gd is an indicator of the energy dependence of the neutron spectrum and will be used as a check on the LCH predictions.

The possibility of neutron capture by ^{151}Eu was recognized by previous workers [4,5,6], but the precision of their data was too low to resolve any depletions of ^{151}Eu or enrichments in ^{152}Gd or ^{152}Sm produced by the β decay of ^{152}Eu. In the Apollo 16 samples, enrichments are observed in the ^{152}Gd abundance which appear to be due to neutron capture by ^{151}Eu.

In order to interpret the measured neutron capture effects in terms of neutron fluences and/or the depositional history of the regolith, it is necessary as stated above to use the LCH calculation of the lunar neutron flux, energy spectrum, and depth dependence. Historically it is interesting to note that these calculations were preceded by those of Lingenfelter, Canfield, and Hess [12] which were carried out to predict the effects of chemical composition especially the water content on the lunar neutron albedo. The basis for the LCH calculations will be discussed in Chapter 3. In this chapter, the origin, moderation, and absorption of neutrons in the regolith will be discussed, and the LCH predictions which are based on multi-group transport theory will be compared with those which can be made by simple considerations of neutron physics.

One may assume that the LCH calculations are valid for the moon and use the LCH spectrum and the fluence as measured by $^{158}Gd/^{157}Gd$ to predict the magnitude of the effects which should be measured in other nuclides. The agreement or disagreement of these predictions with the measured effects can be used as a check on the validity of the calculations. This will be done in Chapter 4 for all the nuclides for which lunar neutron capture effects have been reported in the literature.

In Chapter 5, the fluence data will be used to model the depositional history of the regolith at the six sites studied. It will be shown that the surface soils all have similar histories of neutron exposure, that the core samples collected from depths of two meters were deposited at least one-half billion years ago, and that the near surface soils have been mixed much more recently. The implications of these observations for the rate and depth of regolith mixing will be discussed. In order to obtain more information on the depositional history of the regolith samples, a model will be developed for the depth dependence of the production rate of ^{126}Xe by spallation reactions. Because this nuclide is expected to have a different depth dependence for its production rate than ^{158}Gd, the ratio of the ^{126}Xe concentration to the neutron fluence can be used to estimate exposure depths. In addition a model based on the ratio of neutron capture produced ^{131}Xe to spallogenic ^{126}Xe will be developed for indicating depths of irradiation. This model will be useful because it does not rely on measurements of absolute concentrations of xenon. These models will be used to discuss the exposure histories of selected rocks. Neutron fluence data for the meteorites Allende and Norton County will also be discussed in Chapter 5.

Chapters 6-9 are reprints of papers describing the first measurement in lunar samples of neutron capture by ^{149}Sm (Chapter 6), the neutron exposure of the Luna 16 soil (Chapter 7), and the neutron stratigraphy measured in the Apollo 15 and 16 drill stems (Chapters 8 and 9, respectively), which sampled the lunar regolith to depths of more than two meters. Chapters 8 and 9 also present models for the depth dependence expected for the fluence under the conditions of rapid mixing, accretion, erosion, and no disturbance. Minor typographical errors have been corrected in the reprints.

Throughout the thesis, the notation, "Section a.b.c." means Chapter "a", section "b", and subsection "c." Figures and tables will be labeled "a-b" indicating table or figure "b" in chapter "a." The word "Table" or "Figure" will accompany such references.

For the benefit of the reader who is not familiar with the various lunar landing sites, Figure 1-1 indicates their locations. A chart of the naturally occurring nuclides in the mass region around Sm and Gd is given in Figure 1-2, and the neutron capture reactions affecting the isotopic composition of Gd and Sm are indicated.

Figure 1-1

Map of the moon by Karel Anděl (Prague, 1926). Apollo 11 landed on the western edge of Mare Tranquillitatis. Apollo 12 landed in the southeastern part of Mare Procellarum. Apollo 14 was the first mission to visit a non-mare area. It landed on the Fra Mauro formation which is believed to be associated with the formation of the Imbrium basin. Apollo 15 went to the eastern edge of Palus Putredinis and sampled material from the base of the Apennine Mountains and from Hadley Rille. Apollo 16 sampled the lunar highlands near the crater Descartes. The last Apollo mission, Apollo 17, visited the Taurus-Littrow area, which is an embayment at the southeastern edge of Mare Serenitatis. The unmanned probes, Luna 16 and 20, returned samples from the eastern part of Mare Fecunditatis and the highland area adjacent to this mare.

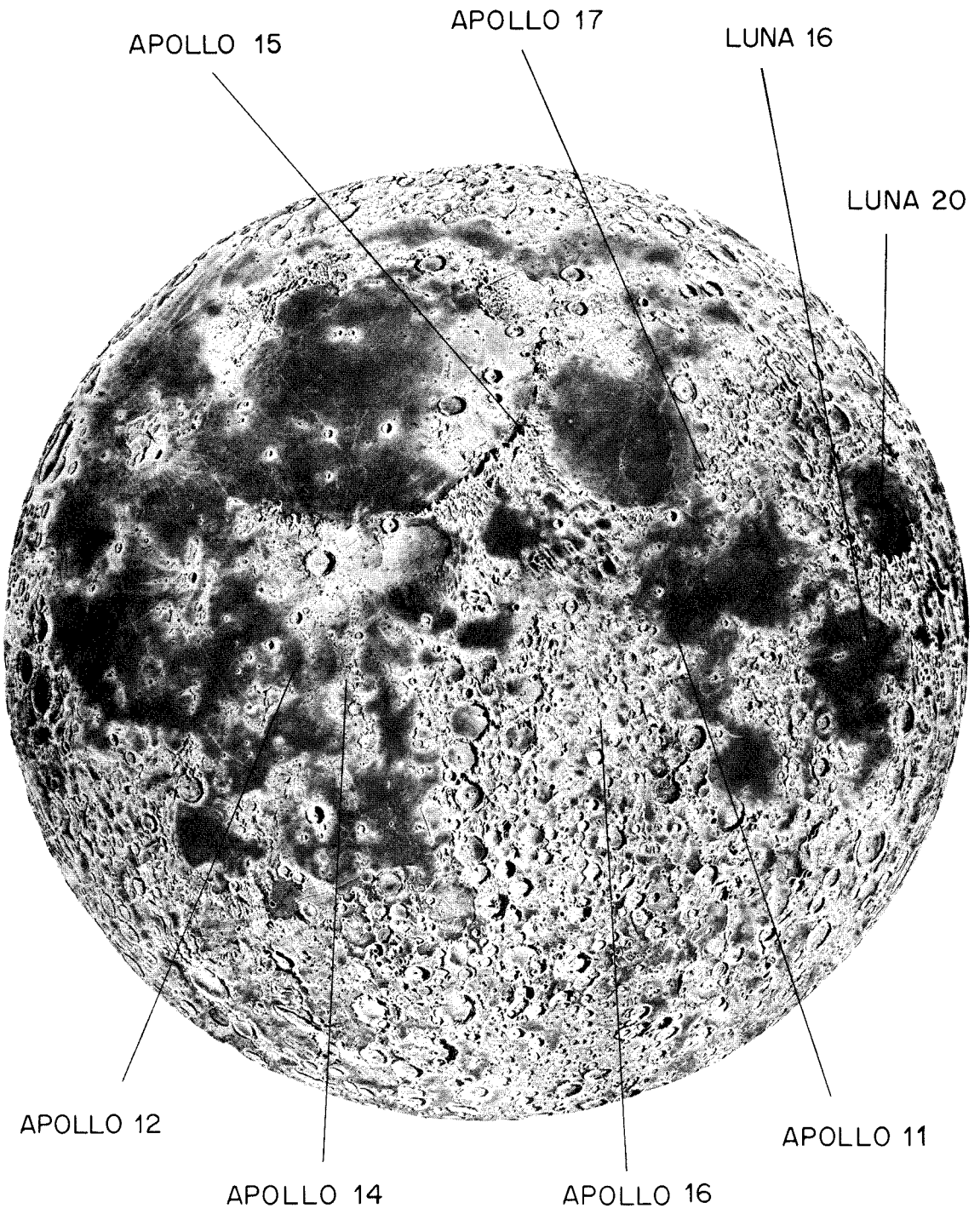
APOLLO 15
APOLLO 17
LUNA 16
LUNA 20
APOLLO 12
APOLLO 14
APOLLO 16
APOLLO 11

Figure 1-1

Figure 1-2

Chart of the naturally occurring nuclides from Ba(Z=56) through Dy(Z=66). The neutron capture reactions which affect the isotopic composition of Gd and Sm are emphasized by arrows linking the targets to their products. The Sm and Gd percent abundances are those measured in this work (Sec. 2.5 and 6.3.1). The other data shown were taken from reference [13].

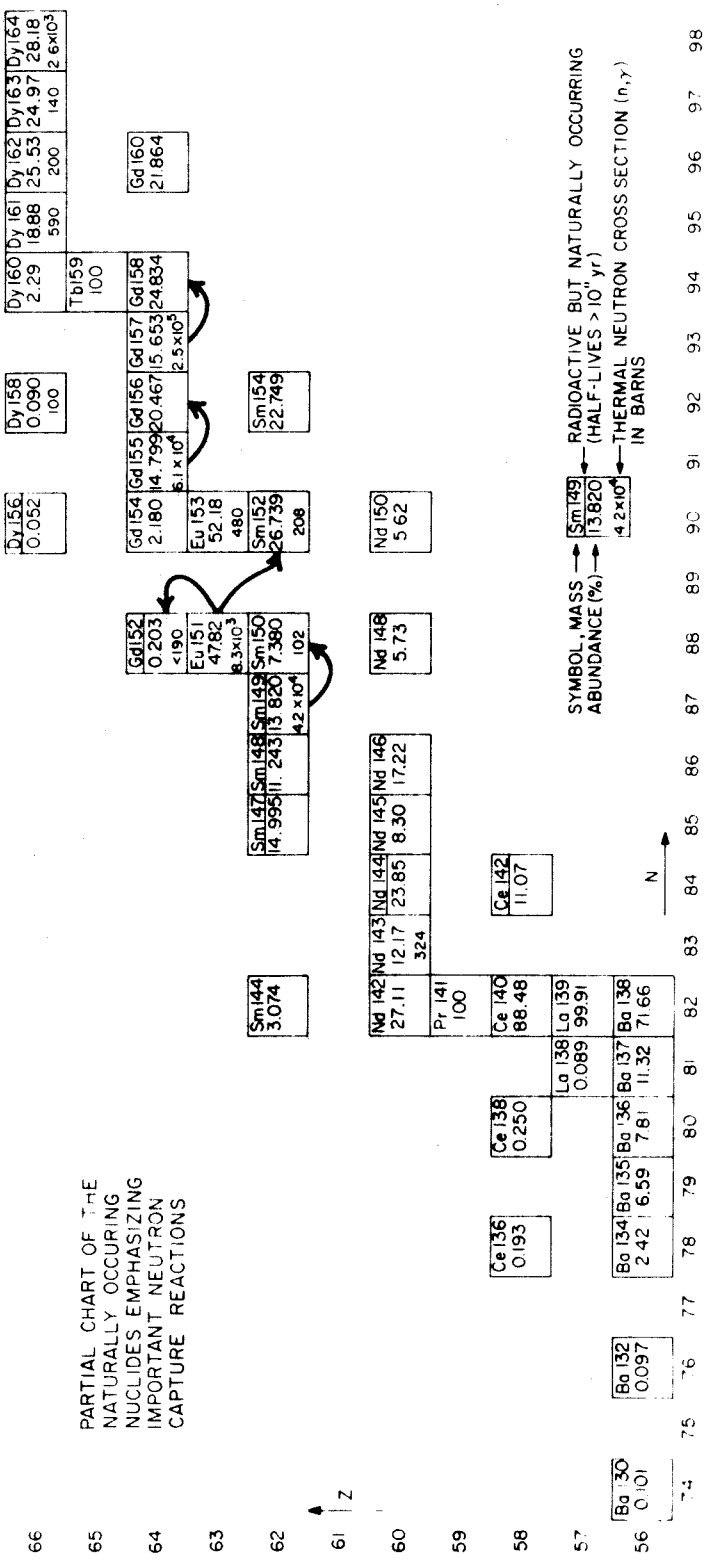
PARTIAL CHART OF THE
NATURALLY OCCURING
NUCLIDES EMPHASIZING
IMPORTANT NEUTRON
CAPTURE REACTIONS
SYMBOL, MASS
ABUNDANCE (%)
RADIOACTIVE BUT NATURALLY OCCURRING
(HALF-LIVES > 10⁸ yr)
THERMAL NEUTRON CROSS SECTION (n,γ)
IN BARNS
Z
N

Figure 1-2

References

[1] R. E. Lingenfelter, E. H. Canfield, and V. E. Hampel, The lunar neutron flux revisited, Earth Planet. Sci. Letters 16 (1972) 355.

[2] Farrington Daniels, Comment, Proceedings of the Conference on Nuclear Processes in Geologic Settings (Nat. Res. Council, 1953) 35.

[3] G. J. Wasserburg, D. A. Papanastassiou, E. V. Nenow, and C. A. Bauman, A programmable magnetic field mass spectrometer with on-line data processing, Rev. Sci. Instr. 40 (1969) 288.

[4] V. Rama Murthy and R. A. Schmitt, Isotope abundances of the rare-earth elements in meteorites, J. Geophys. Res. 68 (1963) 911.

[5] A. J. Loveless, S. Yanagita, H. Mabuchi, M. Ozima, and R. D. Russell, Isotopic ratios of Gd, Sm and Eu in "Abee" enstatite chondrite, Geochim. Cosmochim. Acta 36 (1972) 685.

[6] V. Rama Murthy, R. A. Schmitt, and P. Rey, Rubidium-strontium age and elemental and isotopic abundances of some trace elements in lunar samples, Science 167 (1970) 476.

[7] O. Eugster, F. Tera, D. S. Burnett, and G. J. Wasserburg, Isotopic composition of gadolinium and neutron-capture effects in some meteorites, J. Geophys. Res. 75 (1970) 2753.

[8] O. Eugster, F. Tera, D. S. Burnett, and G. J. Wasserburg, The isotopic composition of Gd and the neutron capture effects in samples from Apollo 11, Earth Planet. Sci. Letters 8 (1970) 20.

[9] K. Marti and G. W. Lugmair, Kr^{81}-Kr and K-Ar^{40} ages, cosmic-ray spallation products, and neutron effects in lunar samples from Oceanus Procellarum, Proc. Second Lunar Sci. Conf. 2 (MIT Press, 1971) 1591.

[10] G. W. Lugmair and K. Marti, Neutron capture effects in lunar gadolinium and the irradiation histories of some lunar rocks, Earth Planet. Sci. Letters 13 (1971) 32.

[11] G. W. Lugmair and K. Marti, Exposure ages and neutron capture record in lunar samples from Fra Mauro, Proc. Third Lunar Sci. Conf. 2 (MIT Press, 1972) 1891.

[12] R. E. Lingenfelter, E. H. Canfield, and W. N. Hess, The lunar neutron flux, J. Geophys. Res. 66 (1961) 2665.

[13] _____, Chart of the Nuclides (U.S. Government Printing Office, 0-389-841, 1970).

2. Experimental Procedures and Results

2.1 Chemical Separations

Gd and Sm were isolated from the samples by the procedure of Eugster, Tera, Burnett, and Wasserburg [1]. This procedure will be only briefly summarized here. (A detailed discussion of the procedures is given in Appendix I). The samples, which were about 50 mg, were first dissolved in a mixture of HF and $HClO_4$ (typically 1 ml each); then the resulting solution was evaporated to dryness. This solid was dissolved in 1.5*N* HCl and loaded on a Dowex 50-X8, 100-200 mesh, cation exchange column, which was 1 cm in diameter and ~ 20 cm long. The elutant was 4*N* HCl. The rare earth elements and part of the barium were simultaneously eluted from this column. A second column with an inside diameter of 2 mm and a length of 32 cm filled with sized beads (50-90 μm diameter) of Dowex 50W-X4 resin in the NH_4^+ form was used to separate these elements. The resin in this column was changed for each sample, and the old resin was discarded. Before loading the sample, the column was conditioned with 0.2 M 2-hydroxy-2-methyl-propanoic acid which had previously been adjusted to pH 4.10 with concentrated NH_3 solution. This solution was allowed to drip through the column overnight, then a slight positive pressure was applied to the column to achieve a drop rate of 1 per minute for one hour. In the meantime, the rare earth fraction from the first column was evaporated to dryness and redissolved in four drops of 0.75*N* HCl. This solution was loaded on the second column, which using the 2-hydroxy-2methyl-propanoic acid solution described above, separated the Gd and Sm from the Ba, the remaining rare earths, and each

other. Again a slight positive pressure, achieved by a column of water, was applied to maintain a flow rate of 1 drop per minute.

By this procedure, one is able to get a good separation of the rare earth elements. Gd is completely separated from Tb. A few percent of the Gd *tails* into the Eu, but this is no problem because the collection of the Gd fraction can be stopped before the Eu comes through, and because there is no mass interference, *i.e.*, nuclides with the same atomic weight, between Gd and Eu. This is important for the mass spectrometry. Sm is cleanly separated from both Eu and Nd. The only deviations from this procedure were to use unsized beads of > 400 mesh (< 40 μm diameter) resin in the second column when the original supply of 50-90 μm resin was exhausted and to use a slower elution rate of ~ 2 min/drop with this new resin. These changes had no noticeable effect on the separations.

The columns were calibrated from time to time with radioactive tracers to be certain that the proper fractions were being collected. It was found that the individual rare earth elements were not eluted from the second column in a reproducible number of drops, but that the ratio of the number of drops required to elute one element, *e.g.*, Tb, to the number of drops required to elute another rare earth element, *e.g.*, Gd, was constant. For this reason, ^{160}Tb of high specific activity was added to each sample before it was passed through the second column. The γ-ray activity of each drop was measured until the ^{160}Tb was detected; then the drop number corresponding to the ^{160}Tb peak was multiplied by the appropriate factor to determine in which

drops Gd and Sm would be eluted. Because the laboratory contained HCl fumes, the collected Gd and Sm fractions were evaporated to dryness within one day to prevent a buildup of NH_4Cl in the NH_3-rich solutions.

2.2 Blanks

Whenever new reagents or resin were prepared, the quantity of contamination of *blank* Gd introduced was determined by isotope dilution. A ^{155}Gd spike, *i.e.*, a solution enriched in ^{155}Gd relative to the other isotopes, was passed through the chemical separation procedure and analyzed on the mass spectrometer. By knowing the isotopic composition of the spike and the quantity used, the concentration of the blank in the resin and reagents could be calculated. The Gd blank for the complete analytical procedure was $< 3 \times 10^{-11}$ g. This is negligible in comparison with the $\sim 4 \times 10^{-7}$ g of Gd analyzed in a typical sample. Furthermore, the isotopic composition of the blank has been determined to be the same within the errors as normal terrestrial Gd [1].

The Sm blank was not determined directly, but it can be inferred as follows. When the Gd blank of the ^{160}Tb tracer was determined, the Sm fraction was also collected. This Sm was analyzed on the mass spectrometer to be certain that the ^{160}Tb solution did not contain Sm of abnormal isotopic composition. The composition of this blank Sm could not be determined with high precision and there was an unexplained peak at mass 151 (not Eu), which was larger than the Sm peaks by about a factor of 2, but the Sm isotopic ratios appeared normal to within about 10%. The amplitude of the Sm signal in the mass spectrometer was

$\sim 3 \times 10^{-2}$% of the signal during a typical sample analysis. Therefore, one concludes that the Sm blank is too small to significantly affect our results.

Reagent Gd and Sm, which had not been processed through the chemical separation procedure, were found to have the same isotopic composition as samples of the terrestrial Knippa Basalt and certain lunar rocks which were unexposed to neutrons. Because these samples were processed through the chemical separation procedure, this is further evidence that the procedure does not introduce Gd or Sm of abnormal composition or other nuclides or compounds, *e.g.*, hydrocarbons, which affect the mass spectra.

2.3 Mass Spectrometry and Data Reduction

The *Lunatic* mass spectrometers used in this work have been described by Wasserburg, Papanastassiou, Nenow and Bauman [2]. The magnetic field is programmable so that one can cyclically step through the fields corresponding to the various masses. The collector entrance slit is adjusted to be wider than the ion beam at a given mass and the magnetic field and acceleration voltage are controlled so that the beam remains in the slit. One is therefore able to measure the ion current at one mass setting, then magnetically step to the next mass and measure its intensity. This process can be continued throughout the mass range of interest; then the field can be stepped back to the starting mass, and the whole process can be repeated for as many scans as desired. In addition to reading the peak intensities, the background on each side

of each peak is measured. There are two systems available for measuring the ion current. One is a Faraday cage hooked to a vibrating-reed electrometer (Cary model 36) with a 10^{11} ohm feedback resistor. The other is an electron multiplier with a nominal gain of 10^4 which is hooked to second vibrating-reed electrometer (Cary model 401) using a 10^9 ohm resistor. In this work, only the Faraday cage system was used except for measurements of the less abundant isotopes of Gd, ^{154}Gd and ^{152}Gd. The output from the electrometer is read by a digital voltmeter, and its output is recorded on paper tape and/or processed directly by an on-line computer. During a given scan of the peaks all the isotopes except ^{154}Gd and ^{152}Gd were measured on the same voltmeter range to avoid any scale factors which might affect the data. Throughout the runs except in rare cases where the beam intensity was too low, the 1 volt range was used for the major peaks, and the $^{160}Gd^{16}O$ signal was kept between 100 mv and 350 mv.

Isotopic ratios are formed for each scan of the mass region as follows. One first measures the intensity of the *reference mass*, with respect to which the ratios are to be formed, by integrating its beam current for a given period of time — usually one second. The magnet is then stepped to the next mass and the beam current is measured. This procedure is continued throughout the mass region of interest until the reference peak has been measured a second time. After correcting the intensities for any background signal, the intensity of the reference peak is interpolated to the time at which each of the other peaks was measured. The ratio of the intensity of each of the *other* masses to the reference mass is then formed. The total time elapsed between two

readings of the reference peak is about one minute for an element with seven isotopes, *e.g.*, Gd and Sm.

The Gd isotopic composition was determined by the method of Eugster *et al.* [1] except for the data-filtering procedure described below. In this procedure, the isolated Gd is dissolved in a drop of dilute HCl and evaporated onto a zone-refined Re ribbon, which has previously been outgassed at $\sim 2000°$ for 2 hours. The filament becomes the mass spectrometer's thermal ionization source. Before the filament is put into the mass spectrometer, it is heated red hot for about one minute by passing a current of 2 amps through it. This serves to oxidize the sample and increases the ratio of GdO^+/Gd^+ ions in the mass spectrometer to more than a thousand. As explained by Eugster *et al.* [1], it is possible by this technique to obtain a larger stable beam of GdO^+ ions than the Gd^+ beam obtained by the other methods tried. For this reason, an oxide beam is used to measure the Gd isotopic composition. The ion current obtainable for ~ 400 ng of Gd is typically $\sim 2 \times 10^{-12}$ amps of $^{160}Gd^{16}O$, and this current can be maintained for a period of 6-8 hours; therefore, $\sim 5 \times 10^{-2}$% of the Gd atoms are ionized and reach the collector.

In the Gd case, $^{160}Gd^{16}O$ is taken as the reference peak for calculating isotopic ratios. These ratios are grouped in *sets* of ten, *i.e.*, ten complete scans through the masses, and average ratios are calculated for each set. These set averages are then converted from oxide to atom ratios by starting at the lightest isotope and calculating its ^{17}O and ^{18}O contributions to the next two heavier isotopes. These

corrections are subtracted, and corrections are sequentially applied to the heavier isotopes. Because the ratios are relative to ^{160}Gd, all the ratios must then be corrected for the $^{158}Gd^{18}O$ contribution to the measured intensity at mass 176. The variations due to neutron-induced isotopic anomalies are small so constant correction factors could have been used [1] rather than the procedure described here.

At this stage, the data are also *screened* for ion beam stability. In order for the set averages to be included in the final average ratios for the analysis, the standard deviations of the $^{158}Gd/^{160}Gd$ and $^{157}Gd/^{160}Gd$ ratios in the set were required to be less than 0.125%; simultaneously the standard deviations of the $^{156}Gd/^{160}Gd$ and $^{155}Gd/^{160}Gd$ ratios were required to be less than 0.25%. No uniform screening procedure was established for $^{154}Gd/^{160}Gd$ and $^{152}Gd/^{160}Gd$, but these data were normally acquired in sets for which the $^{156}Gd/^{160}Gd$ ratios satisfied the above criterion. Data on these less abundant isotopes were often collected with the multiplier system in sets in which ^{158}Gd, ^{157}Gd, and ^{155}Gd data were not taken. For this reason, only the $^{156}Gd/^{160}Gd$ criterion applies to these isotopes.

Isotopic ratios measured with a mass spectrometer are subject to variations caused by a mass-dependent fractionation in the evaporation and ionization processes. This mass fractionation changes as the sample is depleted from the filament and as the spot on the filament which is emitting changes during the analysis. It is therefore necessary to *normalize* the data to some constant value for the ratio of two given isotopes. In the case of Gd, this ratio is defined as $^{156}Gd/^{160}Gd \equiv 0.9361$ [1]. For this work it is not critical for this ratio to be

highly accurate because one is concerned with ratios relative to a standard rather than with absolute abundances. When the data are normalized to a constant $^{156}Gd/^{160}Gd$ value, the other ratios are corrected by assuming that the fractionation varies linearly with the mass difference from ^{156}Gd, *e.g.*, $^{158}Gd/^{160}Gd$ is corrected by $\frac{1}{2}$ the correction necessary for $^{156}Gd/^{160}Gd$. In the case of Gd, all of the major isotopes except ^{160}Gd may be affected by neutron capture. This makes the normalization more complicated. In those samples with neutron capture effects, the normalization procedure will overcompensate for the mass fractionation because of the neutron-produced ^{156}Gd. This effect can, however, be taken into account, as is shown in Appendix O and does not cause any loss of information.

The normalized average ratios for the sets satisfying the screening criteria are averaged to obtain the mean value for the analysis. These means for the whole analysis are the ratios tabulated in this work, *e.g.*, Table 2-1. The errors are calculated as two standard deviations of the mean, $2\sigma_{mean}$, of the distribution of the screened normalized set averages.

The isotopic composition of Sm was measured and the data analyzed as described in Section 6.2.3.

2.4 Calculation of Neutron Fluences from Gadolinium Isotopic Ratios

In Appendix O the equations relating the normalized ratios obtained as described above to the *correct* ratios, *i.e.*, those corrected for the overcompensation of the normalization procedure in

samples with neutron capture effects, and the equations for calculating neutron fluences, ψ, from $^{158}Gd/^{157}Gd$ ratios - correct or normalized - will be derived. For the correct ratios, the fluence is related to the $^{158}Gd/^{157}Gd$ ratio by

$$\psi = \frac{(158/157)_C - (158/157)_T}{\sigma_7[1+(158/157)_C]} \qquad (2.4\text{-}1)$$

where the symbol Gd has been omitted from the ratios, the subscripts C and T refer to the correct sample ratio and the terrestrial ratio respectively, and σ_7 is the ^{157}Gd neutron capture cross section.

For normalized ratios, ψ can be calculated from the expression

$$\psi = \frac{(158/157)_N - (158/157)_T}{\sigma_7[1+(158/157)_T] + \frac{1}{4}\sigma_5(158/157)_T(155/156)_T} \qquad (2.4\text{-}2)$$

where the subscript N refers to the normalized ratio and σ_5 is the ^{155}Gd neutron capture cross section. For the range of fluences observed in this work Equation 2.4-2 is accurate to >99% of the actual fluence. The details of the numerical values of the cross sections will be discussed in Sections 4.2 and 4.3.

2.5 Standards

Throughout this work, Gd and Sm from terrestrial samples were routinely analyzed to check the long-term reproducibility of the isotopic ratios. Reagent standards, which were not processed through the chemical separation procedure, were prepared from spectroscopic standard Gd_2O_3 and Sm_2O_3 and analyzed. In addition samples of Knippa Basalt, a high Ti continental alkali-olivine basalt which approximates lunar samples, and Knippa Basalt doped with reagent Gd were passed through

the separation process and analyzed. In the case of Sm, the ratios $^{152}Sm/^{154}Sm$, $^{148}Sm/^{154}Sm$, and $^{144}Sm/^{154}Sm$ are unaffected by neutron capture reactions and can be used in all analyses as checks on reproducibility and interfering peaks in the mass spectrum. The $^{154}Gd/^{160}Gd$ data can also be useful in this context, but these data are usually of lower precision because of the low ^{154}Gd abundance.

The average ratios for the Gd samples with *normal* terrestrial isotopic composition are displayed in Table 2.1. Only those data which satisfied the screening criteria described in Section 2.3 have been included. The averages of the sets of the first six analyses (underlined in the table) have been used as the terrestrial values throughout this work. These values which were published previously in the paper which constitutes Chapter 8, are in good agreement with those calculated from the screened data sets of all the runs prior to DK 177 or those calculated excluding the unstable run DK 129. Analyses DK 177 and DK 178, though not appreciably different, were not included in the averages because they were made after a major change in the electronics of the mass spectrometer. These data are presented graphically in Figure 2.1. No trend outside the errors is observable in the data, and only rarely does the error bar of a run average fail to cross the average of all runs. This is even more true if run 129 is excluded. If the individual averages are plotted for each analysis, no trend in the data is seen during the course of an individual analysis.

These data indicate that the data acquisition system of the mass spectrometer has been free of changes in its response characteristics over the time span represented by these analyses ($\sim$ 4 years). Furthermore, the agreement of the various analyses gives one confidence that

Table 2-1

Gadolinium Isotopic Composition - Normals[a]

Run[b]	No. of sets[c] $\frac{155-156Gd}{160Gd}$	$\frac{158Gd}{160Gd}$	$\frac{157Gd}{160Gd}$	$\frac{155Gd}{160Gd}$	No. of sets[c] $\frac{152,154Gd}{160Gd}$	$\frac{154Gd}{160Gd}$	$\frac{152Gd}{160Gd}$	$\frac{158Gd}{157Gd}$[d]
E	10[e]	1.135 90	0.715 89	0.676 92	12	0.099 75	0.0092 8	1.586 70
		± 9	± 4	± 9		± 2	± 2	± 15
R 45	8	1.135 85	0.715 94	0.676 76	7	0.099 63	0.0092 74	1.586 52
		± 15	± 10	± 15		± 8	± 8	31
R 102	27	1.135 90	0.715 86	0.676 87	11	0.099 82	0.0092 82	1.586 76
		± 10	± 8	± 12		± 6	± 15	± 23
R 105	23	1.135 76	0.715 93	0.676 85	12	0.099 72	0.0092 79	1.586 41
		± 7	± 5	± 8		± 3	± 19	± 15
DK 112	8	1.135 77	0.715 80	0.676 83	-	-	-	1.586 71
		± 28	± 27	± 37				± 71
DK 120	17	1.135 77	0.715 85	0.676 91	10	0.099 75	0.0093 03	1.586 52
		± 8	± 4	± 8		± 4	± 23	± 14
"Terrestrial Ratio" (Average of Above)	92[f]	1.135 82	0.715 88	0.676 87	52	0.099 74	0.0092 85	1.586 60
		± 5	± 4	± 5		± 3	± 8	± 11
DK 124	14	1.135 81	0.715 89	0.676 89	3	0.099 82	0.0092 43	1.586 57
		± 15	± 12	± 15		± 13	± 1 21	± 34
DK 129	6	1.136 13	0.716 66	0.674 71	3	0.099 51	0.0093 18	1.585 31
		± 46	± 54	± 1 22		± 10	± 63	± 1 36
DK 130	24	1.135 76	0.715 93	0.676 83	0	-	-	1.586 41
		± 9	± 6	± 8				± 24
DK 136	23	1.135 80	0.715 92	0.676 89	9	0.099 79	0.0093 08	1.586 49
		± 14	± 9	± 9		± 8	± 54	± 28

Table 2-1 (Continued)

Run[b]	No. of sets[a] $\frac{155-158Gd}{160Gd}$	$^{158}Gd/^{160}Gd$	$^{157}Gd/^{160}Gd$	$^{155}Gd/^{160}Gd$	No. of sets[a] $\frac{152,154Gd}{160Gd}$	$^{154}Gd/^{160}Gd$	$^{152}Gd/^{160}Gd$	$^{158}Gd/^{157}Gd$[d]
K 148	13	1.135 88 ± 8	0.715 90 ± 9	0.676 97 ± 12	3	0.099 72 ± 3	0.0092 76 ± 47	1.586 64 ± 24
DK 155	18	1.135 88 ± 9	0.715 87 ± 7	0.676 83 ± 8	4	0.099 72 ± 7	0.0092 57 ± 86	1.586 70 ± 20
DK 161	22	1.135 82 ± 7	0.715 94 ± 5	0.676 91 ± 7	0	-	-	1.586 47 ± 15
DK 163	12	1.136 00 ± 17	0.716 00 ± 9	0.676 86 ± 15	0	-	-	1.586 61 ± 31
DK 169	22	1.135 82 ± 10	0.715 95 ± 6	0.676 99 ± 9	15	0.099 70 ± 7	0.0092 74 ± 10	1.586 44 ± 20
DK 174	22	1.135 87 ± 8	0.715 96 ± 5	0.676 95 ± 6	10	0.099 67 ± 9	0.0092 65 ± 25	1.586 50 ± 16
Average of all runs (above)	269[c]	1.135 84 ± 3	0.715 93 ± 3	0.676 84 ± 5	87	0.099 73 ± 3	0.0092 82 ± 10	1.586 52 ± 7[g]
Average of all runs (above) except DK 129	263[c]	1.135 83 ± 3	0.715 91 ± 2	0.676 89 ± 3	84	0.099 73 ± 3	0.0092 81 ± 10	1.586 55 ± 6[g]
DK 177	19	1.135 88 ± 11	0.715 98 ± 10	0.676 89 ± 7	8	0.099 62 ± 12	0.0093 01 ± 43	1.586 47 ± 27
DK 178	27	1.135 84 ± 7	0.715 92 ± 5	0.676 83 ± 8	19	0.099 73 ± 7	0.0092 92 ± 39	1.586 54 ± 15

[a] Normalized to $^{156}Gd/^{160}Gd = 0.9361$. Errors are $2\sigma_{mean}$. Data screened as described in Section 2.3.

[b] E=Eugster *et al.*[1], R=Reagent, DK=Doped Knippa Basalt, K=Knippa Basalt. Numbers refer to mass spectrometer analysis number. The larger the number, the more recent the analysis.

[c] A set consists of ten ratios for a given pair of isotopes.

[d] Calculated from the average $^{158}Gd/^{160}Gd$ and $^{157}Gd/^{160}Gd$ for the run rather than for each data set.

[e] Includes one set which does not satisfy the data screening criteria (Section 2.3).

[f] Excludes the poorer quality set in run E (see footnote a).

[g] Calculated from errors in average $^{158}Gd/^{160}Gd$ and $^{157}Gd/^{160}Gd$. If this ratio is calculated on a set by set basis and then all the sets are averaged, this error would be reduced by one unit, i.e., from 7 to 6 or 6 to 5.

Figure 2-1

Distribution of the average normalized isotopic ratios for the individual Gd normal runs (analyses). The runs are plotted in chronological order with the most recent at the top. The error bar associated with each point is the $2\sigma_{mean}$ uncertainty for the run. The solid vertical lines are the averages of the individual sets for all analyses prior to DK 177 and the shaded areas are the $2\sigma_{mean}$ uncertainties of these averages. The dashed vertical lines are the averages excluding run DK 129. The run numbers and the number of sets of data in each run are indicated. The symbol → or ← indicates that the value and its error are out of the range of the diagram. The symbol ⊣ or ⊢ indicates the end of an error bar for a point which is outside the range depicted.

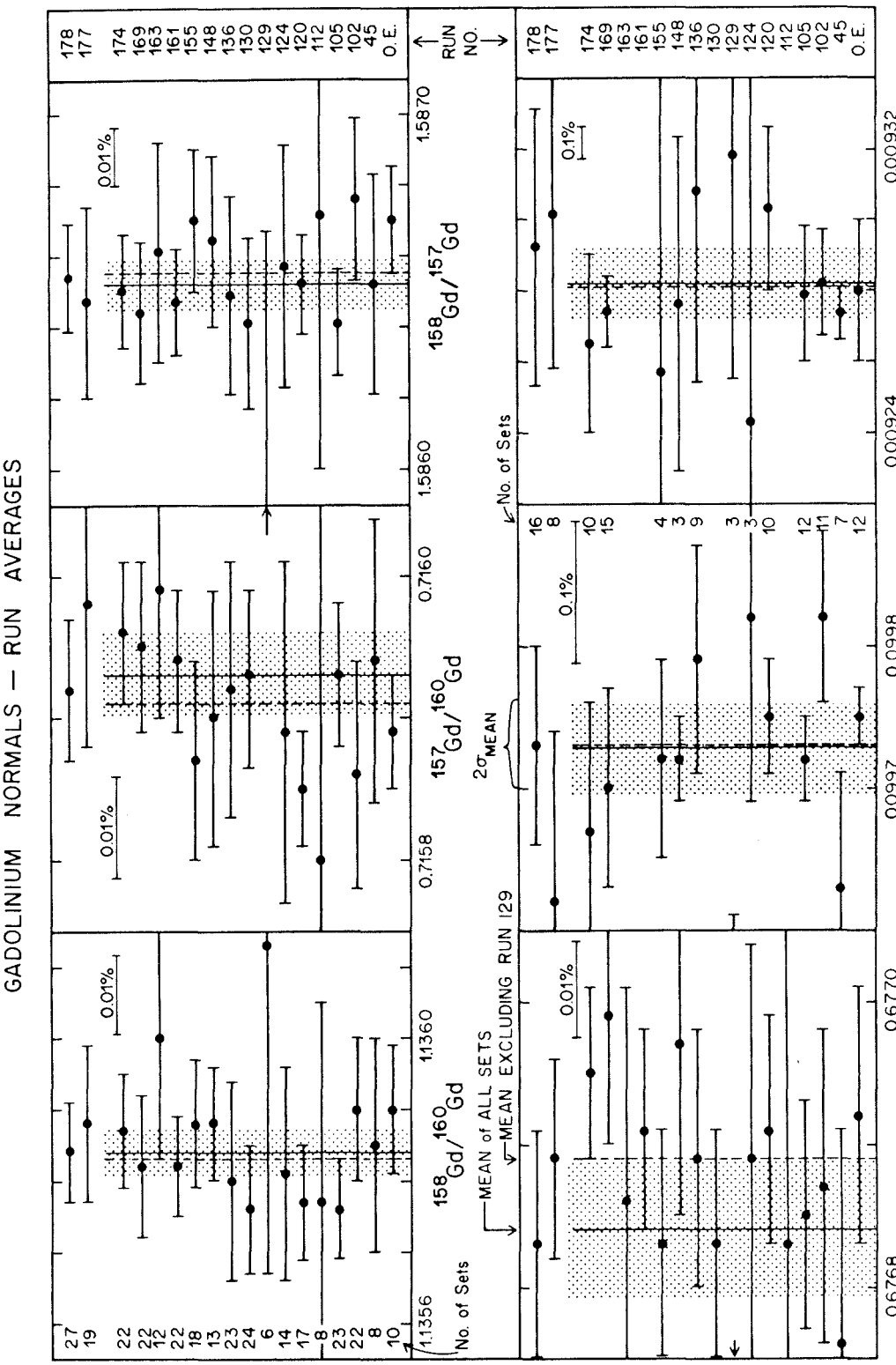
GADOLINIUM NORMALS — RUN AVERAGES
RUN NO.
No. of Sets
MEAN of ALL SETS
MEAN EXCLUDING RUN 129
$2\sigma_{MEAN}$
0.01%
0.1%
$^{158}Gd/^{160}Gd$
$^{157}Gd/^{160}Gd$
$^{158}Gd/^{157}Gd$
$^{155}Gd/^{160}Gd$
$^{154}Gd/^{160}Gd$
$^{152}Gd/^{160}Gd$
1.1356
1.1360
0.7158
0.7160
1.5860
1.5870
0.6768
0.6770
0.0997
0.0998
0.00924
0.00932
178 177 174 169 163 161 155 148 136 130 129 124 120 112 105 102 45 O.E.
27 19 22 22 12 22 18 13 23 24 6 14 17 8 23 22 8 10
16 8 10 15 4 3 9 3 3 10 12 11 7 12

Figure 2-1

the assigned error bars ($2\sigma_{mean}$) reasonably represent the uncertainty of an individual analysis. This is particularly important for the $^{158}Gd/^{157}Gd$ ratio which is most sensitive to neutron capture effects and which is used to compare relative neutron exposures of the extra-terrestrial samples.

The data in Table 2-1 can be used to calculate the terrestrial percentage abundances for the Gd isotopes. Using any one of the three averages for multiple determinations presented in Table 2-1, one calculates that 160:158:157:156:155:154:152 = 21.864:24.834:15.653:20.467:14.799:2.180:0.203 percent where the 156 data are normalized to $^{156}Gd/^{160}Gd = 0.9361$ [1]. Considering only the statistical uncertainties given in Table 2-1, one calculates $2\sigma_{mean}$ uncertainties for the percentage abundances of $\pm$ 0.001 for each isotope. In that these abundances have been determined to a higher precision than was formerly possible, they should be used in preference to previously determined values for the terrestrial Gd isotopic abundances; however, it should be remembered that the abundances reported here are normalized to $^{156}Gd/^{160}Gd = 0.9361$.

Because the abundances are normalized to a constant $^{156}Gd/^{160}Gd$ value, the uncertainty in the accuracy of the abundances is much greater than the uncertainty in their precision. To the extent that the total spread observed in the unnormalized $^{156}Gd/^{160}Gd$ set averages during a typical run ($0.934 \leq {}^{156}Gd/^{160}Gd \leq 0.938$) defines the range of possible $^{156}Gd/^{160}Gd$ values, one can estimate the uncertainties in the absolute percentage abundances of the Gd isotopes as $\pm$ 0.03. The percentage abundances measured in this work are in good agreement with those of Bainbridge and Nier [5].

Because $^{158}Gd/^{157}Gd$ is very important in this work, the distribution of the individual sets, which were averaged to obtain the average of all runs prior to DK 177, has been plotted in the lower part of Figure 2-2. The distribution is seen to be approximately gaussian as would be expected for normally distributed data. For comparison the distribution of the averages for each run is plotted in the upper part of Figure 2-2.

The average ratios for the Sm normals are displayed in Table 2-2. For comparison the ratios measured in samples for isotopes which are unaffected by neutron capture are presented in Table 2-3. (The complete data for these samples are tabulated in Chapters 6, 7, 8, and 9 where the neutron capture effects are discussed.) The data from Tables 2-2 and 2-3 are also presented graphically in Figures 2-3 and 2-4. These data have been screened as described in Section 6.2.3. The average values calculated from the individually measured ratios of the first four normal analyses have been used as the terrestrial ratios throughout this work. These values are underlined in Table 2-2. The average values for all the terrestrial data are in agreement with the adopted values within the calculated errors.

In Figure 2-3, there appears to be a slight trend with time toward decreasing ^{152,150}, and $^{148}Sm/^{154}Sm$ ratios in the normals; however, when the sample data are also considered (Fig. 2-4), this trend is not observable in ^{152} or $^{148}Sm/^{154}Sm$. The $^{150}/^{154}Sm$ ratios cannot be compared in this way because of the neutron capture effects. Several samples show low $^{152}Sm/^{154}Sm$ ratios. This is discussed in Sections 6.2.3, 8.3, and 9.3.1 and is apparently due to a slight interference at mass 154.

Figure 2-2

The lower histogram is the distribution of the $^{158}Gd/^{157}Gd$ set averages for the normal runs. The sets from each analysis have been indicated by various shading patterns. One and two standard deviations for the distribution and two deviations of the mean for all of these runs combined are indicated above the histogram for the cases including and excluding run 129. The distribution is seen to be approximately gaussian, as would be expected for normally distributed data.

The upper histogram is the distribution of the run averages. The width of this distribution is somewhat wider than the $2\sigma_{mean}$ uncertainty calculated for the distribution of the data sets, but as was shown in Figure 2-1, the $2\sigma_{mean}$ uncertainty for each run average crosses the mean ratio calculated from the composite distribution of the sets shown in the lower part of this figure. Therefore the $2\sigma_{mean}$ uncertainties calculated for the individual runs (see Fig. 2-1) appear to adequately describe the uncertainty of a single analysis.

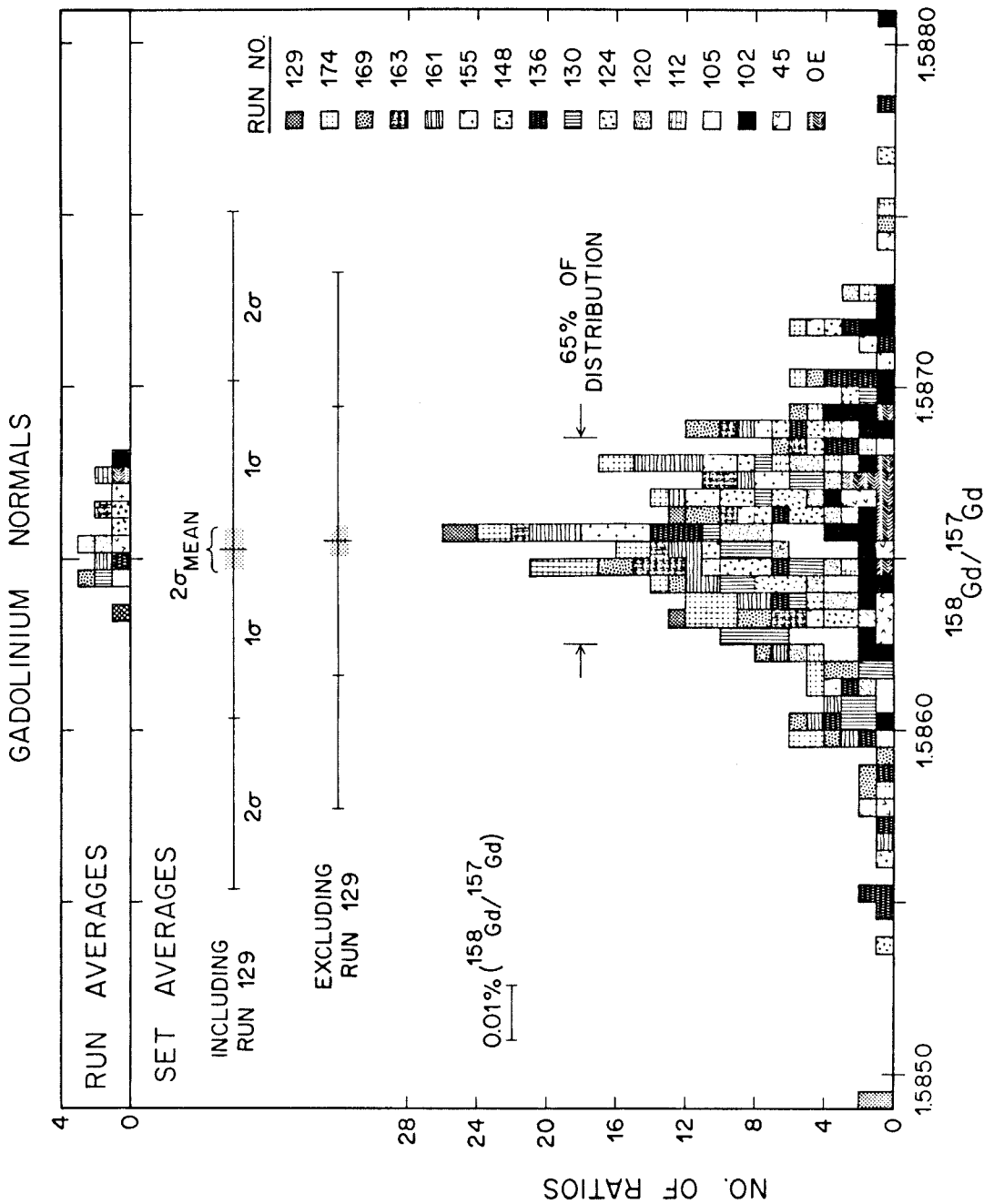
GADOLINIUM NORMALS
RUN AVERAGES
SET AVERAGES
INCLUDING RUN 129
EXCLUDING RUN 129
$2\sigma_{MEAN}$
1σ
2σ
RUN NO.
129
174
169
163
161
155
148
136
130
124
120
112
105
102
45
OE
65% OF DISTRIBUTION
0.01% ($^{158}Gd/^{157}Gd$)
NO. OF RATIOS
$^{158}Gd/^{157}Gd$
1.5850
1.5860
1.5870
1.5880

Figure 2-2

Table 2-2

Samarium Isotopic Composition - Normals[a]

Run	No. of ratios $^{150}Sm/^{154}Sm$	$^{152}Sm/^{154}Sm$	$^{150}Sm/^{154}Sm$	$^{149}Sm/^{154}Sm$	$^{148}Sm/^{154}Sm$	$^{144}Sm/^{154}Sm$	$^{150}Sm/^{149}Sm$
R 318	102	1.175 49	0.324 47	0.607 51	0.494 21	0.135 21	0.534 10
		± 8	± 4	± 5	± 5	± 3	± 7
R 319	87	1.175 39	0.324 42	0.607 51	0.494 22	0.135 12	0.534 03
		± 10	± 5	± 10	± 6	± 5	± 10
K 324	100	1.175 45	0.324 41	0.607 51	0.494 28	0.135 18	0.534 00
		± 19	± 10	± 13	± 11	± 10	± 15
R 325	194	1.175 33	0.324 41	0.607 49	0.494 22	0.135 10	0.534 02
		± 9	± 5	± 7	± 6	± 5	± 9
"Terrestrial Ratio" (Average of Above)	483	1.175 40	0.324 42	0.607 50	0.494 23	0.135 14	0.534 03[d]
		± 6	± 3	± 4	± 4	± 3	± 5
R 330	190	1.175 47	0.324 49	0.607 55	0.494 23	0.135 15	0.534 09
		± 20	± 7	± 10	± 9	± 5	± 12
R 332	254	1.175 40	0.324 40	0.607 51	0.494 19	0.135 16	0.533 99
		± 7	± 3	± 5	± 4	± 2	± 6
R 335	231	1.175 34	0.324 37	0.607 50	0.494 16	0.135 19	0.533 94
		± 5	± 3	± 3	± 3	± 2	± 5
R 337	223	1.175 27	0.324 37	0.607 42	0.494 11	0.135 19	0.534 01
		± 8	± 3	± 4	± 4	± 2	± 5
R 340	225	1.175 32	0.324 36	0.607 51	0.494 17	0.135 18	0.533 91
		± 7	± 4	± 5	± 5	± 3	± 7
Average of All Data	1605	1.175 37	0.324 40	0.607 50	0.494 19	0.135 16	0.534 00[d][e]
		± 4	± 2	± 2	± 2	± 1	± 3

[a] Normalized to $^{147}Sm/^{154}Sm = 0.65918$. Errors are $2\sigma_{mean}$. Data screened as described in Section 6.2.3.

[b] R=Reagent, K=Knippa Basalt, Numbers refer to mass spectrometer analysis number. The larger the number, the more recent the analysis.

[c] Calculated from each $^{150}Sm/^{154}Sm$ ratio and the immediately following $^{149}Sm/^{154}Sm$ ratio.

[d] Calculated from the individual ratios rather than the average value for each analysis.

[e] Includes 1592 ratios not 1605 because in some cases $^{149}Sm/^{154}Sm$ data were lost due to errors in data acquisition.

Table 2-3

Partial Samarium Isotopic Composition - Samples [a]

Sample	Run Number	No. of ratios $^{152}Sm/^{154}Sm$	$^{152}Sm/^{154}Sm$	$^{148}Sm/^{154}Sm$	$^{144}Sm/^{154}Sm$
14163,110	307	70	-	0.494 ± 21 10	-
12042,44 Ace. Fl.	320	114	1.175 ± 33 13	0.494 ± 32 9	0.135 ± 17 5
10084,12	321	218	1.175 ± 11 8	0.494 ± 23 5	0.135 ± 16 4
14321,161	322	116	1.175 ± 23 12	0.494 ± 11 7	0.135 ± 17 5
14310,100	323	220	1.175 ± 15 6	0.494 ± 24 4	0.135 ± 20 3
10017,32	326	121	1.175 ± 22 16	0.494 ± 25 7	0.135 ± 23 11
14310,88	327	116	1.175 ± 12 14	0.494 ± 20 8	0.135 ± 16 6
Luna 16, G-2	328	186	1.175 ± 31 8	0.494 ± 18 5	0.135 ± 18 4
15601,65	329	220	1.175 ± 27 5	0.494 ± 18 3	0.135 ± 18 2
15041,54	333	87	1.175 ± 05 18	0.494 ± 13 13	0.135 ± 14 4
15004,27	336	99	1.175 ± 28 25	0.494 ± 21 20	0.135 ± 21 10
15595,20	338	173	1.175 ± 38 12	0.494 ± 30 8	0.135 ± 18 7
60007,108	339	187	1.175 ± 50 14	0.494 ± 25 8	0.135 ± 21 5
60004,23	341	85	1.175 ± 55 27	0.494 ± 33 17	0.135 ± 14 11
60001,8	342	112	1.175 ± 38 30	0.494 ± 28 14	0.135 ± 14 9
60003,10	343	84	1.175 ± 43 18	0.494 ± 14 10	0.135 ± 17 7
60004,14	344	84	1.175 ± 24 30	0.494 ± 20 15	0.135 ± 13 7
Norton County	345	276	1.175 ± 41 7	0.494 ± 15 5	0.135 ± 15 4

[a] Normalized to $^{147}Sm/^{154}Sm = 0.65918$. Errors are $2\sigma_{mean}$. Data screened as described in Section 6.2.3.

Figure 2-3

Distribution of the average isotopic ratios for the individual Sm normal runs. The runs are arranged chronologically with the most recent at the top. The error bars associated with the points are the $2\sigma_{mean}$ uncertainties for the run. The vertical lines are the averages of the individual ratios of all of the normal analyses. The shaded areas are $2\sigma_{mean}$ uncertainties for the averages of all the ratios.

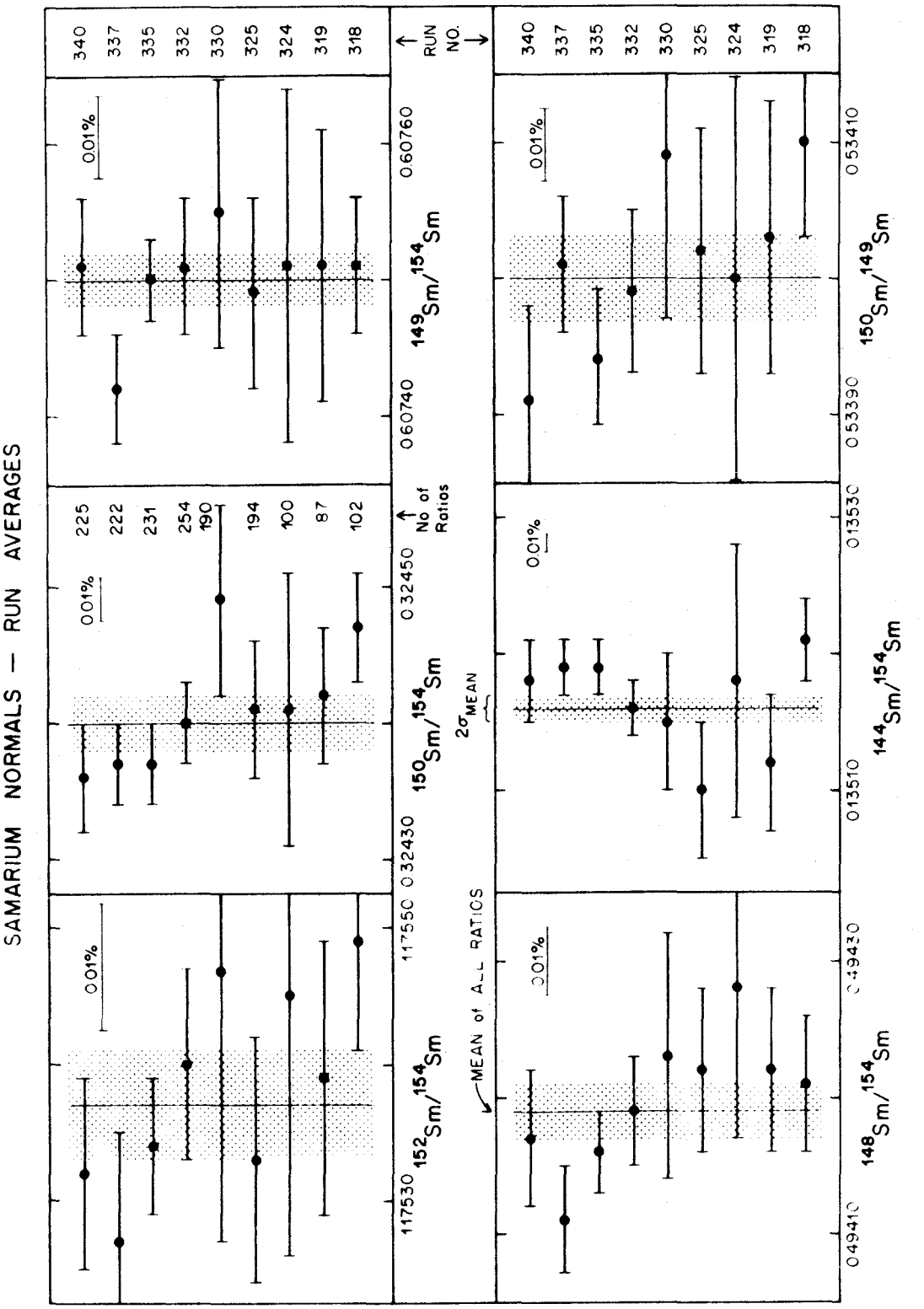
SAMARIUM NORMALS — RUN AVERAGES
0.01%
$^{152}Sm/^{154}Sm$
$^{150}Sm/^{154}Sm$
$^{149}Sm/^{154}Sm$
$^{148}Sm/^{154}Sm$
$^{144}Sm/^{154}Sm$
$^{150}Sm/^{149}Sm$
MEAN of ALL RATIOS
$2\sigma_{MEAN}$
No of Ratios
RUN NO.
225 222 231 254 190 194 100 87 102
340 337 335 332 330 325 324 319 318
117530 032430 060740 060760
049410 049430 013510 013530 053390 053410

Figure 2-3

Figure 2-4

Distribution of the average $^{152}Sm/^{154}Sm$, $^{148}Sm/^{154}Sm$, and $^{144}Sm/^{154}Sm$ ratios for all of the Sm analyses and their $2\sigma_{mean}$ uncertainties. The runs are arranged chronologically with the most recent at the top. The vertical lines and shaded areas are the averages of all the ratios for the normals and their $2\sigma_{mean}$'s.

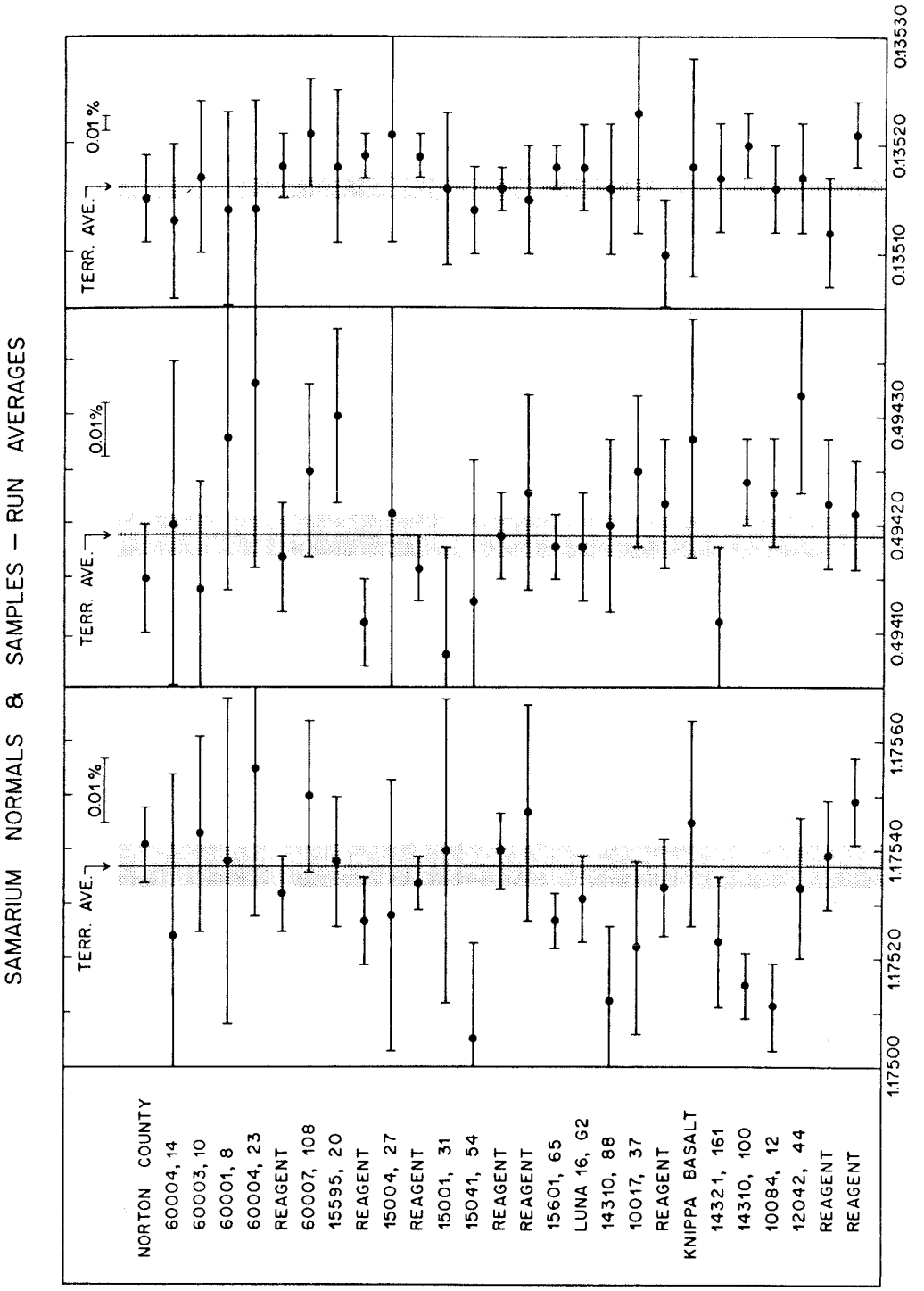
SAMARIUM NORMALS & SAMPLES – RUN AVERAGES
NORTON COUNTY
60004, 14
60003, 10
60001, 8
60004, 23
REAGENT
60007, 108
15595, 20
REAGENT
15004, 27
REAGENT
15001, 31
15041, 54
REAGENT
REAGENT
15601, 65
LUNA 16, 62
14310, 88
10017, 37
REAGENT
KNIPPA BASALT
14321, 161
14310, 100
10084, 12
12042, 44
REAGENT
REAGENT
TERR. AVE.
0.01%
1.17500
1.17520
1.17540
1.17560
$^{152}Sm/^{154}Sm$
0.49410
0.49420
0.49430
$^{148}Sm/^{154}Sm$
0.13510
0.13520
0.13530
$^{144}Sm/^{154}Sm$

Figure 2-4

The distribution of the individual $^{150}Sm/^{149}Sm$ ratios (1592 points) which were included in the average $^{150}Sm/^{149}Sm$ for all the normal data (Table 2-2) is shown in Figure 2-5. This distribution indicates that the ratios are approximately normally distributed both throughout the total time span of this work and within each analysis.

2.6 Results

The normalized isotopic composition data for Gd are presented in Tables 2-4, 7-1 (Luna 16), 8-1 (Apollo 15), and 9-1 (Apollo 16). The $^{158}Gd/^{160}Gd$ ratios of the samples are generally higher than the terrestrial ratio, while the $^{157}Gd/^{160}Gd$ ratios are correspondingly lower than the terrestrial ratio. As is shown in Figure 2-6, the variations in $^{158}Gd/^{160}Gd$ (up to 0.6%) and $^{157}Gd/^{160}Gd$ (up to 1.2%) are negatively correlated as expected for neutron capture by ^{157}Gd. Within the errors, all of the samples fall on the line *predicted* for the variation in isotopic composition caused by neutron capture on Gd of terrestrial composition. It should be emphasized that the correlation line in Figure 2-6 (also Figs. 8-1 and 9-2) is not a fit of the data but the theoretically calculated correlation line (see Appendix O). It can also be shown (Fig. 2-7) that the variations in $^{157}Gd/^{160}Gd$ and $^{155}Gd/^{160}Gd$ are positively correlated as expected for neutron capture by ^{157}Gd and ^{155}Gd, and that within the errors all the data points lie along the predicted correlation line. These correlations are unambiguous evidence that the effects observed in these isotopes are due to neutron capture by ^{157}Gd and ^{155}Gd.

Figure 2-5

The lower histogram is the distribution of the $^{150}Sm/^{149}Sm$ ratios for the normal runs. The ratios from each analysis have been indicated by different shading patterns. One and two standard deviations for the distribution and two standard deviations of the mean are indicated. The distribution is approximately gaussian as would be expected for normally distributed data. This figure differs from Figure 2-2 because in the Sm data reduction individual ratios rather than set averages are used.

The upper histogram is the distribution of the run averages for the Sm normals. The width of this distribution is wider than the overall $2\sigma_{mean}$ uncertainty of the individual ratios, but as shown in Figure 2-3, with a few exceptions, the run averages agree within their $2\sigma_{mean}$ uncertainties with the average of all the data points. The fact that there are some exceptions implies that the quoted uncertainty for each run may slightly underestimate the actual uncertainty.

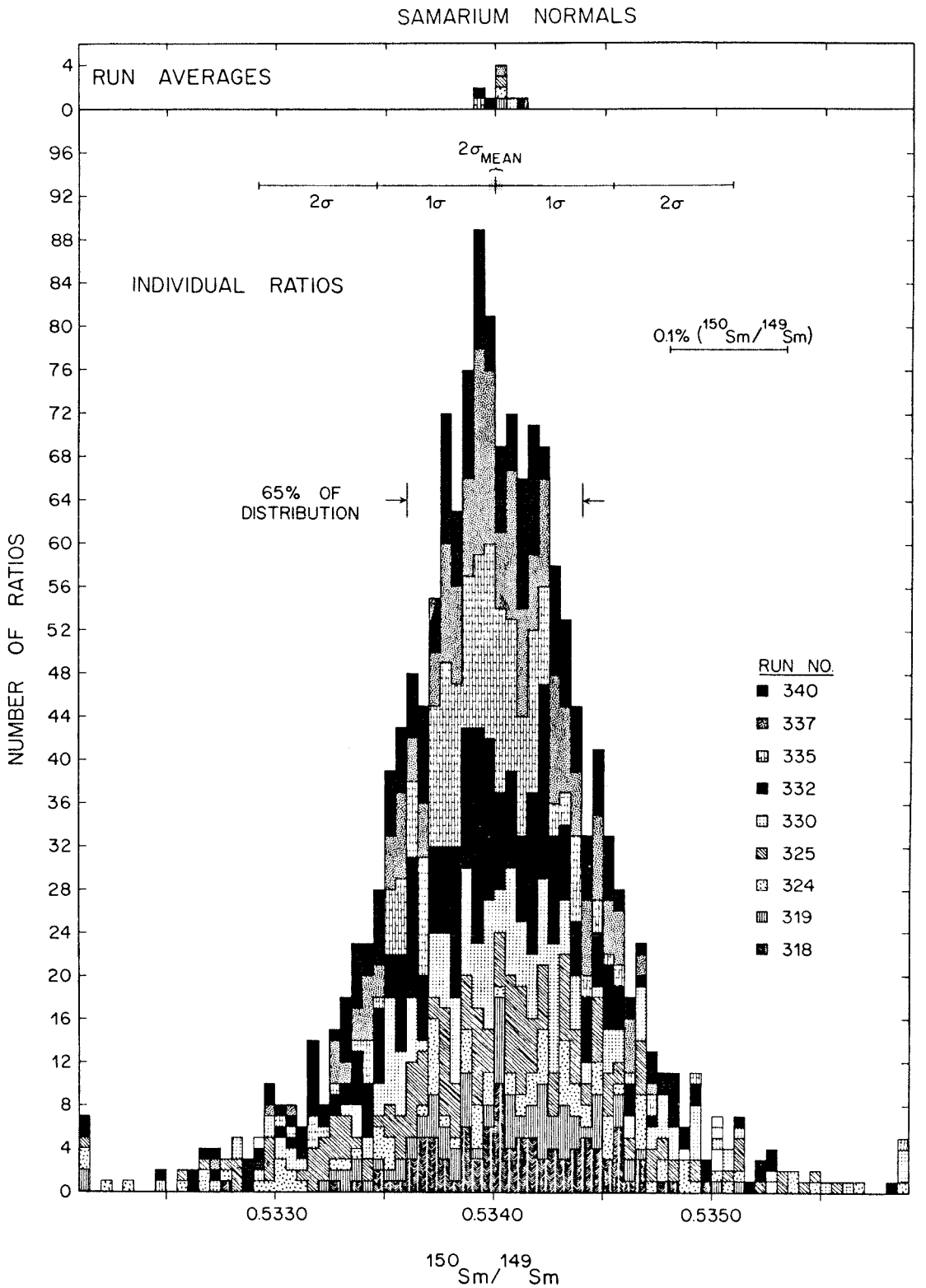
SAMARIUM NORMALS
RUN AVERAGES
$2\sigma_{MEAN}$
2σ 1σ 1σ 2σ
INDIVIDUAL RATIOS
0.1% ($^{150}Sm/^{149}Sm$)
65% OF DISTRIBUTION
RUN NO.
340
337
335
332
330
325
324
319
318
NUMBER OF RATIOS
0.5330
0.5340
0.5350
$^{150}Sm/^{149}Sm$

Figure 2-5

Table 2-4

Normalized Gadolinium Isotopic Composition - Samples[a]

Sample	No. of sets[b] $\frac{155\text{-}158Gd}{160Gd}$	$^{158}Gd/^{160}Gd$	$^{157}Gd/^{160}Gd$	$^{155}Gd/^{160}Gd$	No. of sets[b] $\frac{154,152Gd}{160Gd}$	$^{154}Gd/^{160}Gd$	$^{152}Gd/^{160}Gd$
Lunar Soils							
12070,5	16	1.13 715 ± 17	0.71 422 ± 17	0.67 627 ± 15	9	0.10 003 ± 12	0.009 646 ± 18
12042,34	24	1.13 721 ± 14	0.71 403 ± 9	0.67 613 ± 14	10	0.09 965 ± 8	0.009 337 ± 13
12033,102	27	1.13 704 ± 7	0.71 418 ± 6	0.67 623 ± 9	12	0.09 960 ± 8	0.009 327 ± 33
14259,97	34	1.13 757 ± 5	0.71 361 ± 4	0.67 601 ± 5	16	0.09 968 ± 5	0.009 333 ± 15
14163,110	25	1.13 763 ± 6	0.71 346 ± 5	0.67 590 ± 5	15	0.09 964 ± 3	0.009 311 ± 25
Sized Lunar Soils							
10084,12 <37μm	13	1.13 752 ± 14	0.71 351[c] ± 8	0.67 603 ± 8	5	0.09 967 ± 5	0.009 307 ± 36
12042,44 100-300μm	28	1.13 707 ± 6	0.71 424 ± 4	0.67 620 ± 6	16	0.09 969 ± 5	0.009 288 ± 17
12042,44 <44μm	19	1.13 731 ± 12	0.71 400 ± 7	0.67 616 ± 10	3	0.09 998 ± 4	0.009 724 ± 27
12042,44 Acetone Floats	15	1.13 722 ± 12	0.71 400 ± 10	0.67 608 ± 14	7	0.09 963 ± 14	0.009 342 ± 70
14141,22 <150μm	8	1.13 603 ± 23	0.71 565 ± 16	0.67 675 ± 14	0	-	-
Apollo 12							
Double Core							
12025,22 (0.4-1.2)[e]	25[d]	1.13 721 ± 15	0.71 408 ± 12	0.67 617 ± 14	9	0.09 977 ± 7	0.009 405 ± 25
12025,56 (8.0-9.0)	22	1.13 719 ± 6	0.71 405 ± 5	0.67 614 ± 6	20	0.09 973 ± 4	0.009 344 ± 14

Table 2-4 (Continued)

Sample	No. of sets[b] $\frac{155\text{-}158Gd}{160Gd}$	$158Gd/160Gd$	$157Gd/160Gd$	$155Gd/160Gd$	No. of sets[b] $\frac{154,152Gd}{160Gd}$	$154Gd/160Gd$	$152Gd/160Gd$
Apollo 12							
Double Core							
12028,59 (12.0-12.8)	20	1.13 728 ± 11	0.71 415 ± 14	0.67 626 ± 13	11	0.09 985 ± 13	0.009 401 ± 13
12028,77 (16.4-17.4)	27	1.13 713 ± 10	0.71 400 ± 7	0.67 609 ± 10	9	0.09 968 ± 10	0.009 392 ± 48
12028,110A (28.8-30.0) Coarse	25	1.13 710 ± 6	0.71 408 ± 5	0.67 612 ± 6	15	0.09 970 ± 4	0.009 343 ± 18
12028,110B (28.8-30.0) Fine	24	1.13 746 ± 7	0.71 387 ± 6	0.67 610 ± 7	19	0.09 971 ± 5	0.009 354 ± 16
12028,110 (28.8-30.0) Total	-	1.13 740	0.71 390	0.67 610	-		
12028,161 (39.8-40.0)	29	1.13 734 ± 10	0.71 387 ± 8	0.67 616 ± 12	10	0.09 978 ± 7	0.009 388 ± 21
Lunar Rocks							
Luny Rock 1 10085	16	1.13 671 ± 21	0.71 453 ± 14	0.67 639 ± 14	11	0.09 972 ± 10	0.009 344 ± 24
10058,20	14	1.13 634 ± 5	0.71 516 ± 3	0.67 654 ± 7	12	0.09 979 ± 6	0.009 312 ± 13
10017,32	24	1.13 860 ± 6	0.71 216 ± 5	0.67 546 ± 8	12	0.09 963 ± 7	0.009 382 ± 21
12002,29-E	18	1.13 655 ± 8	0.71 498 ± 9	0.67 643 ± 12	14	0.10 011 ± 7	0.009 806 ± 61
12002,29-D2	15	1.13 658 ± 12	0.71 506 ± 14	0.67 650 ± 12	10	0.09 980 ± 8	0.009 337 ± 19
12002,29-2A	8	1.13 648 ± 18	0.71 497 ± 15	0.67 671 ± 20	7	0.09 968 ± 8	0.009 299 ± 26
12002,147	22	1.13 654 ± 11	0.71 498 ± 7	0.67 659 ± 10	9	0.09 976 ± 6	0.009 325 ± 11

Table 2-4 (Continued)

Sample	No. of sets[b] $\frac{155-158Gd}{160Gd}$	$^{158}Gd/^{160}Gd$	$^{157}Gd/^{160}Gd$	$^{155}Gd/^{160}Gd$	$\frac{154,152Gd}{160Gd}$[b]	$^{154}Gd/^{160}Gd$	$^{152}Gd/^{160}Gd$
Lunar Rocks							
12013,10-38 (Light)	21	1.13 611 ± 10	0.71 566 ± 5	0.67 673 ± 9	9	0.09 975 ± 10	0.009 310 ± 21
12013,10-01 (Dark)	23	1.13 595 ± 11	0.71 570 ± 7	0.67 674 ± 10	8	0.09 974 ± 5	0.009 338 ± 29
14310,100	16[d]	1.13 763 ± 33	0.71 355 ± 22	0.67 595 ± 14	0	-	-
14310,88	30	1.13 743 ± 8	0.71 369 ± 4	0.67 602 ± 6	13	0.09 965 ± 5	0.009 347 ± 34
14321,161	22	1.13 578 ± 7	0.71 589 ± 5	0.67 693 ± 9	13	0.09 985 ± 6	0.009 409 ± 27
15595,19 (Exterior)	24	1.13 642 ± 9	0.71 509 ± 10	0.67 663 ± 8	15	0.09 973 ± 5	0.009 324 ± 13
15595,20 (Interior)	23	1.13 641 ± 10	0.71 519 ± 9	0.67 665 ± 11	7	0.09 968 ± 11	0.009 352 ± 32
Meteorites							
Norton County	24	1.13 693 ± 8	0.71 443 ± 7	0.67 638 ± 9	10	0.09 964 ± 10	0.009 308 ± 29
Allende	17	1.13 581 ± 9	0.71 580 ± 7	0.67 677 ± 12	0	-	-
Terrestrial[f]	92	1.13 582 ± 5	0.71 588 ± 4	0.67 687 ± 5	52	0.09 974 ± 3	0.009 285 ± 8

[a] Normalized to $^{156}Gd/^{160}Gd = 0.9361$. Errors are $2\sigma_{mean}$. Data screened as described in Section 2.3.

[b] A set consists of ten measurements of the ratio of a given pair of isotopes.

[c] Corrected 2×10^{-2}% for barium interference in mass spectrum.

[d] Includes sets which do not satisfy the data screening procedure of Section 2.3.

[e] Depth in core tube in cm.

[f] From Table 2-1.

Figure 2-6

Correlation diagram for the variation of the normalized $^{158}Gd/^{160}Gd$ and $^{157}Gd/^{160}Gd$ ratios. The "theoretical correlation line" is calculated for neutron capture on Gd of terrestrial isotopic composition. The slope of this line (see Appendix O) depends only on the ratios of the ^{157}Gd and ^{155}Gd neutron capture cross sections and the isotopic composition of terrestrial Gd. The experimental data points all fall on this line within the limits of the rectangle defined by the $2\sigma_{mean}$ uncertainties in $^{157}Gd/^{160}Gd$ and $^{158}Gd/^{160}Gd$. For a list of those samples which only barely meet this criterion see Table 2-5.

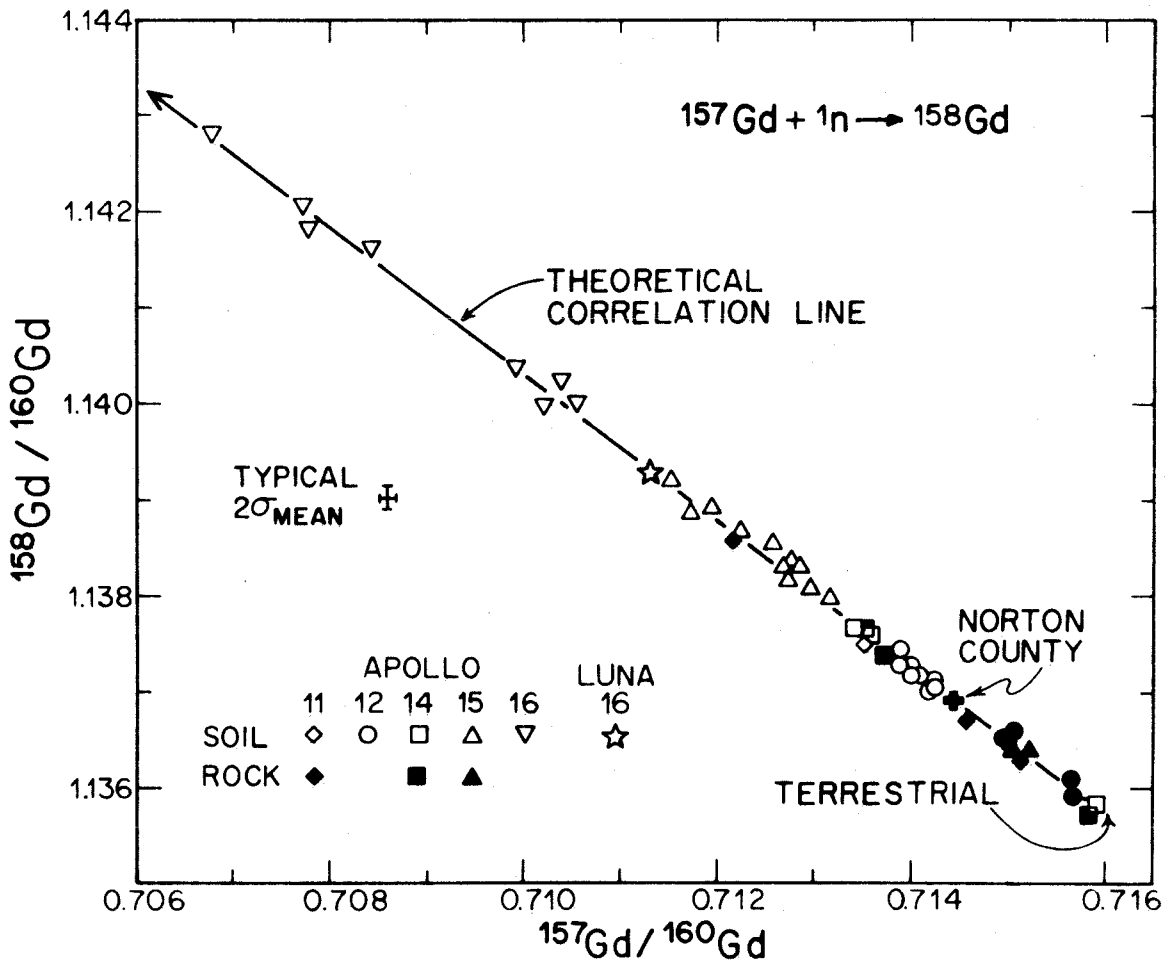
1.144
1.142
1.140
1.138
1.136
158Gd / 160Gd
0.706
0.708
0.710
0.712
0.714
0.716
157Gd / 160Gd
157Gd + 1n → 158Gd
THEORETICAL
CORRELATION LINE
TYPICAL
2σMEAN
APOLLO
11 12 14 15 16
LUNA
16
SOIL
ROCK
NORTON
COUNTY
TERRESTRIAL

Figure 2-6

Figure 2-7

Correlation diagram for the variations in the normalized $^{155}Gd/^{160}Gd$ and $^{157}Gd/^{160}Gd$ ratios due to neutron capture by ^{155}Gd and ^{157}Gd. Within the limits of the rectangle defined by the $2\sigma_{mean}$ uncertainties of the $^{157}Gd/^{160}Gd$ and $^{155}Gd/^{160}Gd$ ratios, the experimental data points all fall on the line predicted for neutron capture by Gd of terrestrial isotopic composition.

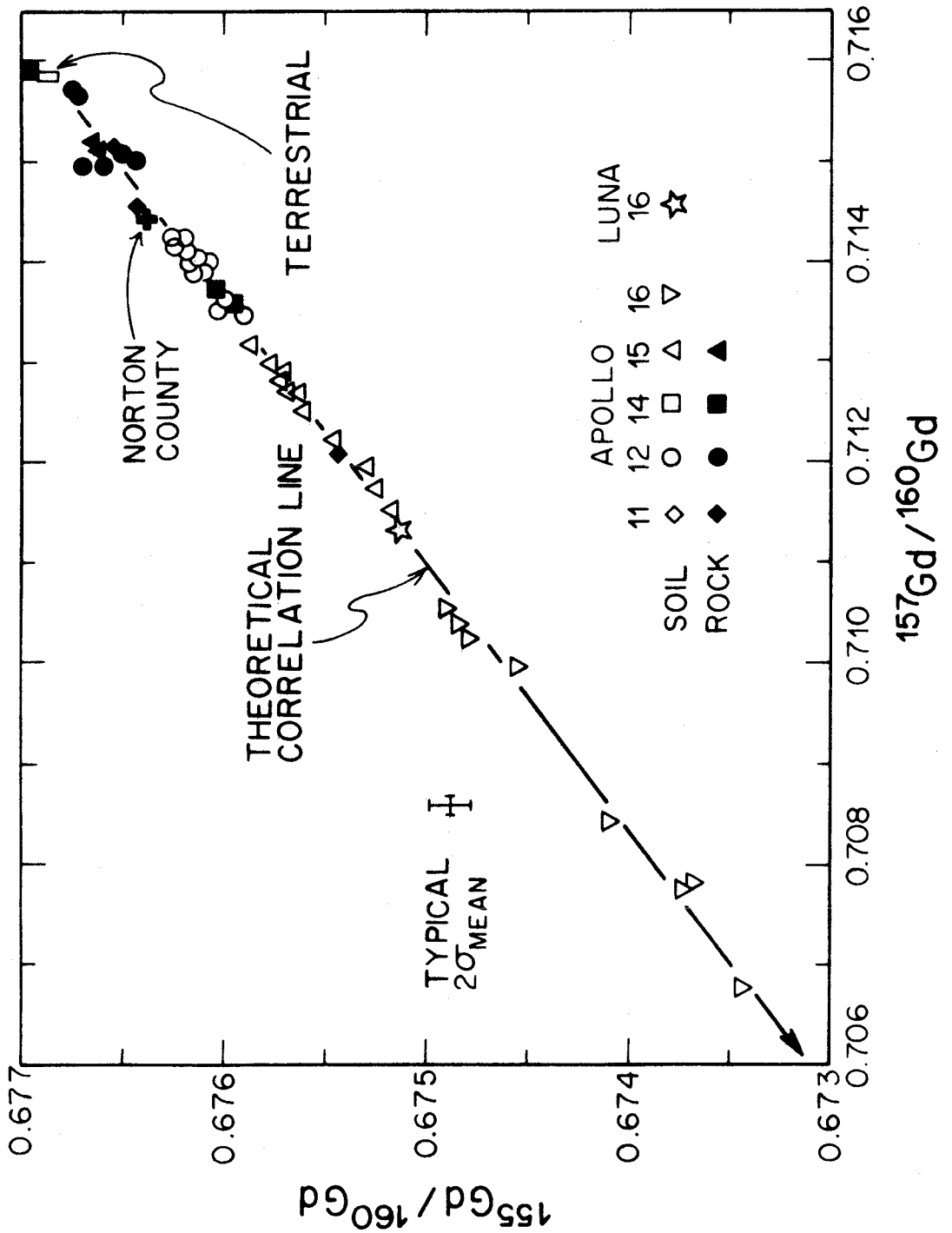
TERRESTRIAL
NORTON COUNTY
THEORETICAL CORRELATION LINE
TYPICAL $2\sigma_{MEAN}$
APOLLO 11 12 14 15 16
LUNA 16
SOIL
ROCK
$^{155}Gd/^{160}Gd$
$^{157}Gd/^{160}Gd$
0.677
0.676
0.675
0.674
0.673
0.706
0.708
0.710
0.712
0.714
0.716

Figure 2-7

The normalized $^{154}Gd/^{160}Gd$ and $^{152}Gd/^{160}Gd$ ratios also show variations from the terrestrial values. This is at least partly due to the normalization procedure (see Appendix O). The effect of the false discrimination correction introduced by the normalization procedure can be removed by equation 6 of Appendix O. The fluence corrected $^{154}Gd/^{160}Gd$ and $^{152}Gd/^{160}Gd$ ratios (Table 2-5) for all the samples can then be compared to the terrestrial ones. This is most easily done graphically. In Figure 2-8, the $^{159}Gd/^{157}Gd$ ratio, which is sensitive to neutron exposure, is plotted against the $^{154}Gd/^{160}Gd$ and $^{152}Gd/^{160}Gd$ ratios. This method of presentation was chosen because the $^{152}Gd/^{160}Gd$ ratio may be increased by neutron capture on ^{151}Eu and the subsequent β decay of ^{152}Eu. If this effect is significant, the $^{152}Gd/^{160}Gd$ and $^{158}Gd/^{157}Gd$ ratios should be positively correlated while the $^{154}Gd/^{160}Gd$ ratios should be the same as the terrestrial ratio.

The fluence corrected $^{154}Gd/^{160}Gd$ ratios for the samples generally agree with the terrestrial value within errors, but there are several samples with ratios distinctly higher than terrestrial. This may be due to Sm interference in the mass spectrum. If this is the case, then Sm must also interfere at mass 152, and its effect there will be about ten times as significant as at mass 154 because of the $^{152}Gd/^{154}Gd$ ratio. Ignoring this problem for a moment, consider the $^{152}Gd/^{160}Gd$ data. These ratios are generally higher than the terrestrial value and the samples with the highest $^{158}Gd/^{157}Gd$ ratios also have high $^{152}Gd/^{160}Gd$ ratios. The possibility of a correlation between $^{158}Gd/^{157}Gd$ and $^{152}Gd/^{160}Gd$ is complicated by the fact that some of the Apollo 12

Table 2-5

Fluence Corrected Gadolinium Isotopic Composition - All Samples*

Sample	$^{158}Gd/^{160}Gd$	$^{157}Gd/^{160}Gd$	$^{156}Gd/^{160}Gd$	$^{155}Gd/^{160}Gd$	$^{154}Gd/^{160}Gd$	$^{152}Gd/^{160}Gd$	$^{158}Gd/^{157}Gd$
Apollo 11 Soil							
10084,12 <37μm	1.13 780 ± 14	0.71 378 ± 8	0.93 656 ± 2	0.67 645 ± 8	0.099 74 ± 5	0.009 316 ± 36	1.59 406 ± 27
Rock							
10017,32	1.13 905 ± 6	0.71 258 ± 5	0.93 684 ± 1	0.67 613 ± 8	0.099 75 ± 7	0.009 397 ± 21	1.59 848 ± 14
10058,20	1.13 642 ± 5	0.71 524 ± 3	0.93 624 ± 1	0.67 667 ± 7	0.099 81 ± 6	0.009 315 ± 13	1.58 887 ± 10
10085 Luny Rock 1	1.13 686 ± 21	0.71 468 ± 14	0.93 636 ± 3	0.67 662 ± 14	0.099 76 ± 10	0.009 349 ± 24	1.59 074 ± 43
Apollo 12 Soils							
12042,34	1.13 743 ± 14	0.71 424 ± 9	0.93 647 ± 2	0.67 646 ± 14	0.099 71 ± 8	0.009 344 ± 13	1.59 251 ± 28
12042,44 100-300μm	1.13 727 ± 6	0.71 443 ± 4	0.93 643 ± 1	0.67 650 ± 6	0.099 74 ± 5	0.009 294 ± 17	1.59 186 ± 12
12042,44 <44μm	1.13 754 ± 12	0.71 422 ± 7	0.93 648 ± 1	0.67 650 ± 10	0.100 04 ± 4	0.009 732 ± 27	1.59 271 ± 23
12042,44 Ace. Fl.	1.13 744 ± 12	0.71 421 ± 10	0.93 647 ± 2	0.67 642 ± 14	0.099 69 ± 14	0.009 349 ± 70	1.59 258 ± 28
12070,5	1.13 735 ± 17	0.71 441 ± 17	0.93 644 ± 3	0.67 657 ± 15	0.100 08 ± 12	0.009 653 ± 18	1.59 201 ± 45
12033,102	1.13 724 ± 7	0.71 437 ± 6	0.93 643 ± 1	0.67 653 ± 9	0.099 65 ± 8	0.009 334 ± 33	1.59 195 ± 17

Table 2-5 (Continued)

Sample	$^{158}Gd/^{160}Gd$	$^{157}Gd/^{160}Gd$	$^{156}Gd/^{160}Gd$	$^{155}Gd/^{160}Gd$	$^{154}Gd/^{160}Gd$	$^{152}Gd/^{160}Gd$	$^{158}Gd/^{157}Gd$
Core							
12025,22	1.13 743	0.71 429	0.93 647	0.67 650	0.099 83	0.009 412	1.59 246
	± 15	± 12	± 2	± 14	± 7	± 25	± 34
12025,56	1.13 741	0.71 426	0.93 646	0.67 647	0.099 79	0.009 351	1.59 243
	± 6	± 5	± 1	± 6	± 4	± 14	± 14
12028,59	1.13 750	0.71 435	0.93 646	0.67 658	0.099 91	0.009 408	1.59 234†
	± 11	± 14	± 2	± 13	± 13	± 13	± 35
12028,77	1.13 735	0.71 421	0.93 647	0.67 642	0.099 74	0.009 399	1.59 246†
	± 10	± 7	± 1	± 10	± 10	± 48	± 21
12028,110A	1.13 731	0.71 428	0.93 645	0.67 644	0.099 76	0.009 350	1.59 225†
	± 6	± 5	± 1	± 6	± 4	± 18	± 14
12028,110B	1.13 771	0.71 410	0.93 651	0.67 647	0.099 78	0.009 362	1.59 319†
	± 7	± 6	± 1	± 7	± 5	± 16	± 17
12028,110 Total	1.13 764	0.71 413	0.93 650	0.67 646	-	-	1.59 305
12028,161	1.13 758	0.71 410	0.93 650	0.67 652	0.099 84	0.009 396	1.59 303
	± 10	± 8	± 1	± 12	± 7	± 21	± 23
Rocks							
12013,10-38	1.13 614	0.71 569	0.93 615	0.67 678	0.099 76	0.009 311	1.58 748†
	± 10	± 5	± 1	± 9	± 10	± 27	± 18
12013,10-01	1.13 597	0.71 572	0.93 613	0.67 677	0.099 75	0.009 339	1.58 717
	± 11	± 7	± 1	± 10	± 5	± 29	± 22
12002,147	1.13 665	0.71 508	0.93 628	0.67 676	0.099 79	0.009 329	1.58 953
	± 11	± 7	± 1	± 10	± 6	± 11	± 22
12002,29-2A	1.13 659	0.71 507	0.93 628	0.67 687	0.099 71	0.009 303	1.58 947
	± 18	± 15	± 3	± 20	± 8	± 26	± 42
12002,29-D2	1.13 669	0.71 516	0.93 627	0.67 666	0.099 83	0.009 340	1.58 941
	± 12	± 14	± 2	± 12	± 8	± 19	± 36
12002,29-E	1.13 666	0.71 508	0.93 628	0.67 660	0.100 14	0.009 810	1.58 954
	± 8	± 9	± 1	± 12	± 7	± 61	± 23

Table 2-5 (Continued)

Sample	$^{158}Gd/^{160}Gd$	$^{157}Gd/^{160}Gd$	$^{156}Gd/^{160}Gd$	$^{155}Gd/^{160}Gd$	$^{154}Gd/^{160}Gd$	$^{152}Gd/^{160}Gd$	$^{158}Gd/^{157}Gd$
Apollo 14							
Soils							
14163,110	1.13 792	0.71 373	0.93 658	0.67 633	0.099 72	0.009 321	1.59 432
	± 6	± 5	± 1	± 5	± 3	± 25	± 14
14259,97	1.13 784	0.71 387	0.93 655	0.67 642	0.099 75	0.009 342	1.59 391
	± 5	± 4	± 1	± 5	± 5	± 15	± 11
14141,22 <150μm	1.13 606	0.71 568	0.93 615	0.67 679	-	-	1.58 739
	± 23	± 16	± 3	± 14			± 48
Rocks							
14310,88	1.13 769	0.71 394	0.93 653	0.67 641	0.099 72	0.009 356	1.59 355
	± 8	± 4	± 1	± 6	± 5	± 34	± 14
14310,100	1.13 791	0.71 382	0.93 657	0.67 637	-	-	1.59 412
	± 33	± 22	± 4	± 14			± 68
14321,161	1.13 578	0.71 589	0.93 610	0.67 693	0.099 85	0.009 409	1.58 653
	± 7	± 5	± 1	± 9	± 6	± 27	± 15
Luna 16							
G-2	1.13 981	0.71 185	0.93 701	0.67 596	0.099 74	0.009 453	1.60 120
	± 16	± 14	± 2	± 16	± 5	± 28	± 39
Apollo 15							
Soils							
15221,46	1.13 871	0.71 312	0.93 673	0.67 629	0.099 77	0.009 335	1.59 680+
	± 8	± 6	± 1	± 7	± 4	± 22	± 18
15231,47	1.13 869	0.71 307	0.93 674	0.67 627	0.099 74	0.009 336	1.59 687
	± 8	± 6	± 1	± 8	± 6	± 17	± 18
15601,65	1.13 856	0.71 308	0.93 673	0.67 623	0.099 78	0.009 351	1.59 668
	± 10	± 8	± 1	± 9	± 5	± 32	± 23
15041,54	1.13 832	0.71 347	0.93 665	0.67 637	0.099 70	0.009 325	1.59 546
	± 9	± 8	± 1	± 8	± 8	± 39	± 22

Table 2-5 (Continued)

Sample	$^{158}Gd/^{160}Gd$	$^{157}Gd/^{160}Gd$	$^{156}Gd/^{160}Gd$	$^{155}Gd/^{160}Gd$	$^{154}Gd/^{160}Gd$	$^{152}Gd/^{160}Gd$	$^{158}Gd/^{157}Gd$
Drill Stem							
15006,27	1.13 865	0.71 317	0.93 672	0.67 627	0.099 73	0.009 353	1.59 659
	± 11	± 11	± 2	± 11	± 14	± 35	± 29
15005,222	1.13 911	0.71 261	0.93 684	0.67 613	0.099 79	0.009 368	1.59 850
	± 8	± 4	± 1	± 6	± 5	± 25	± 14
15005,26	1.13 941	0.71 220	0.93 692	0.67 599	0.099 80	0.009 380	1.59 984
	± 14	± 11	± 2	± 9	± 18	± 31	± 32
15004,27	1.13 973	0.71 203	0.93 697	0.67 597	0.099 73	0.009 342	1.60 068
	± 9	± 8	± 1	± 14	± 12	± 27	± 22
15003,29	1.13 941	0.71 238	0.93 690	0.67 602	0.099 69	0.009 352	1.59 944
	± 11	± 8	± 1	± 7	± 7	± 29	± 24
15002,27	1.13 893	0.71 296	0.93 678	0.67 623	0.099 81	0.009 371	1.59 748†
	± 12	± 13	± 2	± 15	± 2	± 48	± 34
15001,31	1.13 842	0.71 328	0.93 669	0.67 629	0.099 76	0.009 356	1.59 604
	± 7	± 5	± 1	± 5	± 5	± 19	± 15
Rocks							
15595,20	1.13 650	0.71 527	0.93 624	0.67 678	0.099 70	0.009 355	1.58 890
	± 10	± 9	± 1	± 11	± 11	± 32	± 24
15595,19	1.13 651	0.71 518	0.93 626	0.67 677	0.099 76	0.009 327	1.58 913
	± 9	± 10	± 2	± 8	± 5	± 13	± 26
Apollo 16							
Soil							
60501,31	1.14 068	0.71 087	0.93 722	0.67 580	0.099 85	0.009 403	1.60 461†
	± 8	± 6	± 1	± 8	± 4	± 13	± 18
Drill Stem							
60007,115	1.14 091	0.71 103	0.93 721	0.67 585	-	-	1.60 457
	± 36	± 10	± 3	± 17			± 56
60007,108	1.14 068	0.71 114	0.93 718	0.67 587	0.099 66	0.009 405	1.60 400
	± 10	± 10	± 2	± 11	± 7	± 25	± 27
60006,8	1.14 114	0.71 060	0.93 729	0.67 565	0.099 76	0.009 407	1.60 588
	± 19	± 14	± 3	± 25	± 16	± 21	± 42

Table 2-5 (Continued)

Sample	$^{156}Gd/^{160}Gd$	$^{157}Gd/^{160}Gd$	$^{156}Gd/^{160}Gd$	$^{155}Gd/^{160}Gd$	$^{154}Gd/^{160}Gd$	$^{152}Gd/^{160}Gd$	$^{158}Gd/^{157}Gd$
Drill Stem							
60004,23	1.14 256 ± 9	0.70 925 ± 8	0.93 760 ± 1	0.67 544 ± 8	0.099 90 ± 7	0.009 437 ± 19	1.61 093 ± 22
60004,14	1.14 310 ± 12	0.70 865 ± 13	0.93 773 ± 2	0.67 520 ± 13	0.099 82 ± 9	0.009 455 ± 29	1.61 307 ± 34
60003,10	1.14 284 ± 19	0.70 870 ± 18	0.93 771 ± 3	0.67 513 ± 21	-	-	1.61 258 ± 49
60001,8	1.14 393 ± 10	0.70 778 ± 7	0.93 793 ± 1	0.67 508 ± 10	0.099 82 ± 7	0.009 451 ± 28	1.61 622 ± 21
Meteorites							
Norton County	1.13 710 ± 8	0.71 460 ± 7	0.93 639 ± 1	0.67 664 ± 9	0.099 69 ± 10	0.009 314 ± 29	1.59 126 ± 19
Allende	1.13 581 ± 9	0.71 581 ± 7	0.93 611 ± 1	0.67 678 ± 12	-	-	1.58 676 ± 20

*Uncertainties are calculated by quadratically adding the uncertainty of the normalized ratio and the uncertainty from the fluence except for $^{156}Gd/^{160}Gd$ for which there is by definition no uncertainty in the normalized ratio. The calculations for this table were performed by Stephen P. Smith.

±Denotes samples for which the rectangle defined by the error bars but not the error bars themselves intersect the predicted correlation line in Figure 2-6 for variations in $^{157}Gd/^{160}Gd$ and $^{158}Gd/^{160}Gd$ due to neutron capture by ^{157}Gd.

Figure 2-8

Variation of $^{154}Gd/^{160}Gd$ and $^{152}Gd/^{160}Gd$ with $^{158}Gd/^{157}Gd$. The error limits for terrestrial values are indicated by open rectangles. The vertical lines and shaded areas indicate the terrestrial $^{154,152}Gd/^{160}Gd$ ratios and their error bars. If $^{152}Gd/^{160}Gd$ is enriched by ^{151}Eu neutron capture, the $^{152}Gd/^{160}Gd$ and $^{158}Gd/^{157}Gd$ ratios should be positively correlated. The correlation will not be unique for all samples because of variations in the Eu/Gd ratio and in the neutron energy spectrum. The variations in $^{154}Gd/^{160}Gd$ may, however, indicate Sm contamination. If the differences in the measured and terrestrial $^{154}Gd/^{160}Gd$ ratios are assumed to be due to ^{154}Sm, the $^{152}Gd/^{160}Gd$ ratios can be corrected for the appropriate amount of ^{152}Sm interference. The corrected values are indicated by X's. Symbols near the edges of the fields with arrows attached to them indicate values which fall outside the range of the illustration. The Apollo 16 and Luna 16 samples have enrichments in $^{152}Gd/^{160}Gd$ which can not be explained by ^{152}Sm interference and which, therefore, appear to result from neutron capture by ^{151}Eu (see Sec. 9.4.2).

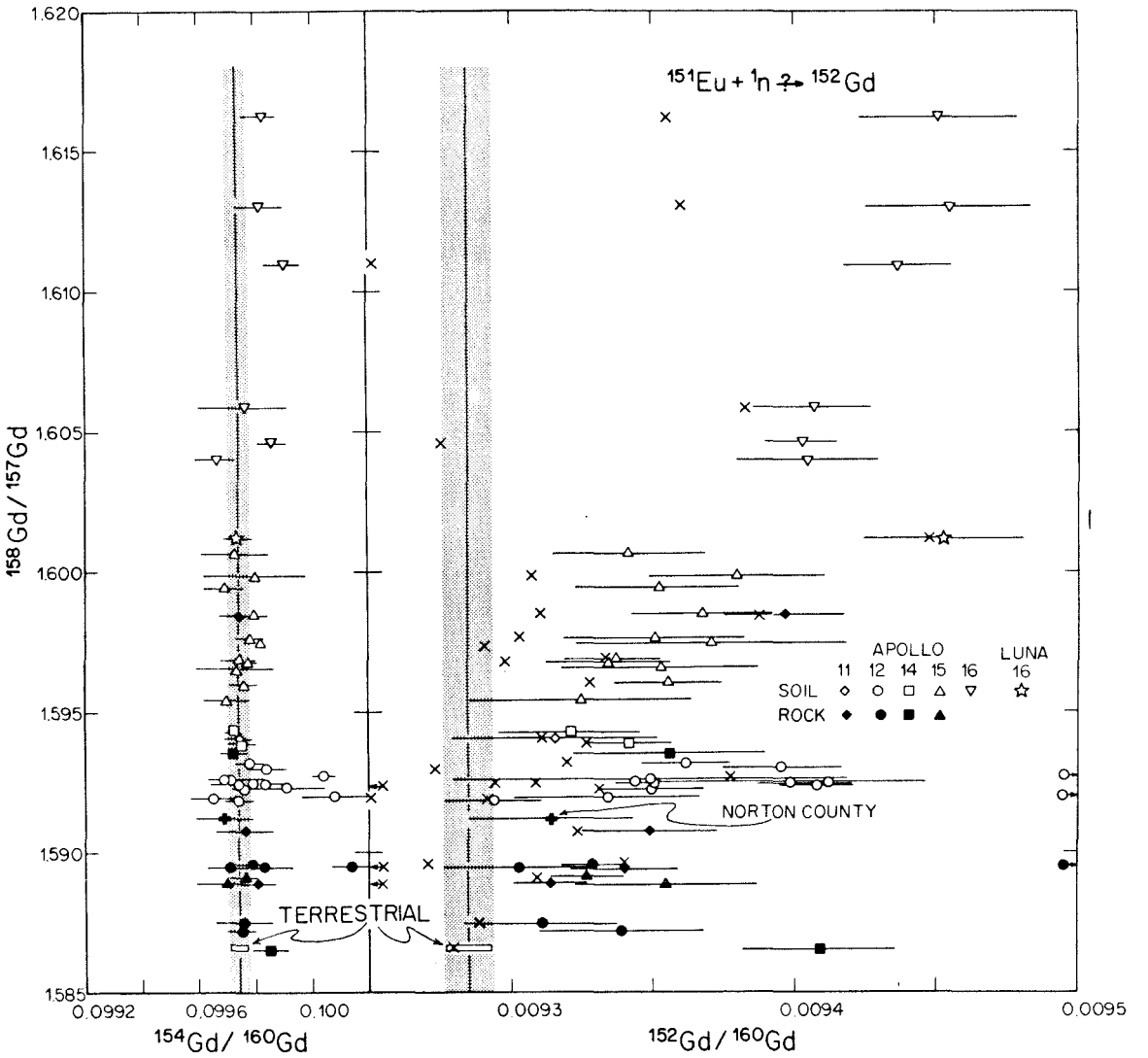
$^{151}Eu + {}^{1}n \not\rightarrow {}^{152}Gd$
APOLLO
11 12 14 15 16
LUNA
16
SOIL
ROCK
NORTON COUNTY
TERRESTRIAL
$^{158}Gd/{}^{157}Gd$
$^{154}Gd/{}^{160}Gd$
$^{152}Gd/{}^{160}Gd$
1.620
1.615
1.610
1.605
1.600
1.595
1.590
1.585
0.0992
0.0996
0.100
0.0093
0.0094
0.0095

Figure 2-8

samples have high $^{152}Gd/^{160}Gd$ ratios although they have relatively low $^{158}Gd/^{157}Gd$ values. However, these samples also have high $^{154}Gd/^{160}Gd$ ratios, indicating that they probably have a significant Sm contamination. If the difference between the measured and the terrestrial $^{154}Gd/^{160}Gd$ ratios is attributed to Sm for each sample where the ratio is higher than the terrestrial one, the $^{152}Gd/^{160}Gd$ ratios can be corrected accordingly. These corrected values are indicated by the X's in the figure. The Sm correction is sufficient to explain the high $^{152}Gd/^{160}Gd$ values for the Apollo 12 samples which appear to have too high ratios. It cannot, however, account for the excess ^{152}Gd of the Luna 16 sample or four of the Apollo 16 samples; therefore, these samples appear to have ^{152}Gd excesses which are most probably due to ^{151}Eu capture. Because the Sm corrections may overestimate the actual Sm contamination, as is the case for the X's which lie to the left of the terrestrial value, and because the errors are large, it is impossible to accurately define the correlation between $^{158}Gd/^{157}Gd$ and $^{152}Gd/^{160}Gd$. The situation is also complicated by the fact that the Eu/Gd ratio is not a constant, *e.g.*, Luna 16 has a higher ratio than the other samples, and the relative capture cross sections for ^{157}Gd and ^{151}Eu will vary depending on the neutron energy spectrum at the site (see Sec. 4.5). For the Apollo 16 samples, where the neutron effects are the largest, the quantitative aspects of the correlation will be considered further in Section 9.4.2.

The isotopic composition data for Sm are displayed in Tables 2-6, 6-1, 7-2 (Luna 16), 8-2 (Apollo 15), and 9-2 (Apollo 16). The $^{150}Sm/^{154}Sm$ and $^{149}Sm/^{154}Sm$ ratios are negatively correlated as expected

Table 2-6

Samarium Isotopic Composition - Samples[a]

Sample	No. of ratios $^{150}Sm/^{154}Sm$	$^{152}Sm/^{154}Sm$	$^{150}Sm/^{154}Sm$	$^{149}Sm/^{154}Sm$	$^{148}Sm/^{154}Sm$	$^{144}Sm/^{154}Sm$	$^{150}Sm/^{149}Sm$
Lunar Rock							
15595,20	173	1.175 38 ± 12	0.32 481 ± 6	0.60 716 ± 9	0.494 30 ± 8	0.135 18 ± 7	0.53 497 ± 10
Meteorite							
Norton County	276	1.175 41 ± 7	0.32 481 ± 4	0.60 702 ± 5	0.494 15 ± 5	0.135 15 ± 4	0.53 510 ± 8
Terrestrial[b]	484	1.175 40 ± 6	0.32 442 ± 3	0.60 750 ± 4	0.494 23 ± 4	0.135 14 ± 3	0.53 403 ± 3

[a] Normalized to $^{147}Sm/^{154}Sm = 0.65918$. Errors are $2\sigma_{mean}$. Data screened as described in Section 6.2.3.

[b] From Table 2-2.

for neutron capture by ^{149}Sm (Fig. 2-9). The variations in $^{150}Sm/^{154}Sm$ and $^{149}Sm/^{154}Sm$ are as great as 1.3 and 0.7%, respectively, and within the errors most of the sample points fall on the predicted correlation line. The slight deviations of the others -14321, 15601, and Luna 16 - from the line can be explained by interference at mass 154 and/or the tendence noted with the normals for the quoted uncertainty to slightly underestimate the true uncertainty. As in the case of Gd, the observed correlation is unambiguous evidence for neutron capture by ^{149}Sm. The other Sm isotopic ratios with respect to ^{154}Sm are in good agreement with the terrestrial values (see Sec. 2.5), except for some slight variations in $^{152}Sm/^{154}Sm$, which apparently arise from an interference at mass 154 (see Secs. 6.2.3, 8.3, and 9.3.1). As discussed in Section 6.2.4 such an interference will not affect the $^{150}Sm/^{149}Sm$ ratios used to calculate neutron capture effects.

Because the experimentally measured Gd and Sm isotopic compositions agree with the terrestrial compositions except for the neutron-induced effects, it is reasonable to assume that unirradiated lunar Gd and Sm have the same isotopic composition as our terrestrial standards. This is supported by the fact that samples with low cosmic ray exposure ages, *e.g.*, 14321 [2], have the same isotopic composition as the terrestrial standards within the limits of the uncertainties of the sample and terrestrial ratios. No sample shows a *less irradiated* composition than the terrestrial standards.

The fluence measured in a soil sample is actually an average fluence of the individual grains. For this reason, the dependence of the fluence on grain size was investigated for several samples from

Figure 2-9

Correlation diagram for the variation of $^{150}Sm/^{154}Sm$ and $^{149}Sm/^{154}Sm$ due to neutron capture by ^{149}Sm. The "theoretical correlation line" is calculated for neutron capture by ^{149}Sm in Sm with the terrestrial isotopic composition. The position of the calculated line depends only on the terrestrial Sm isotopic composition.

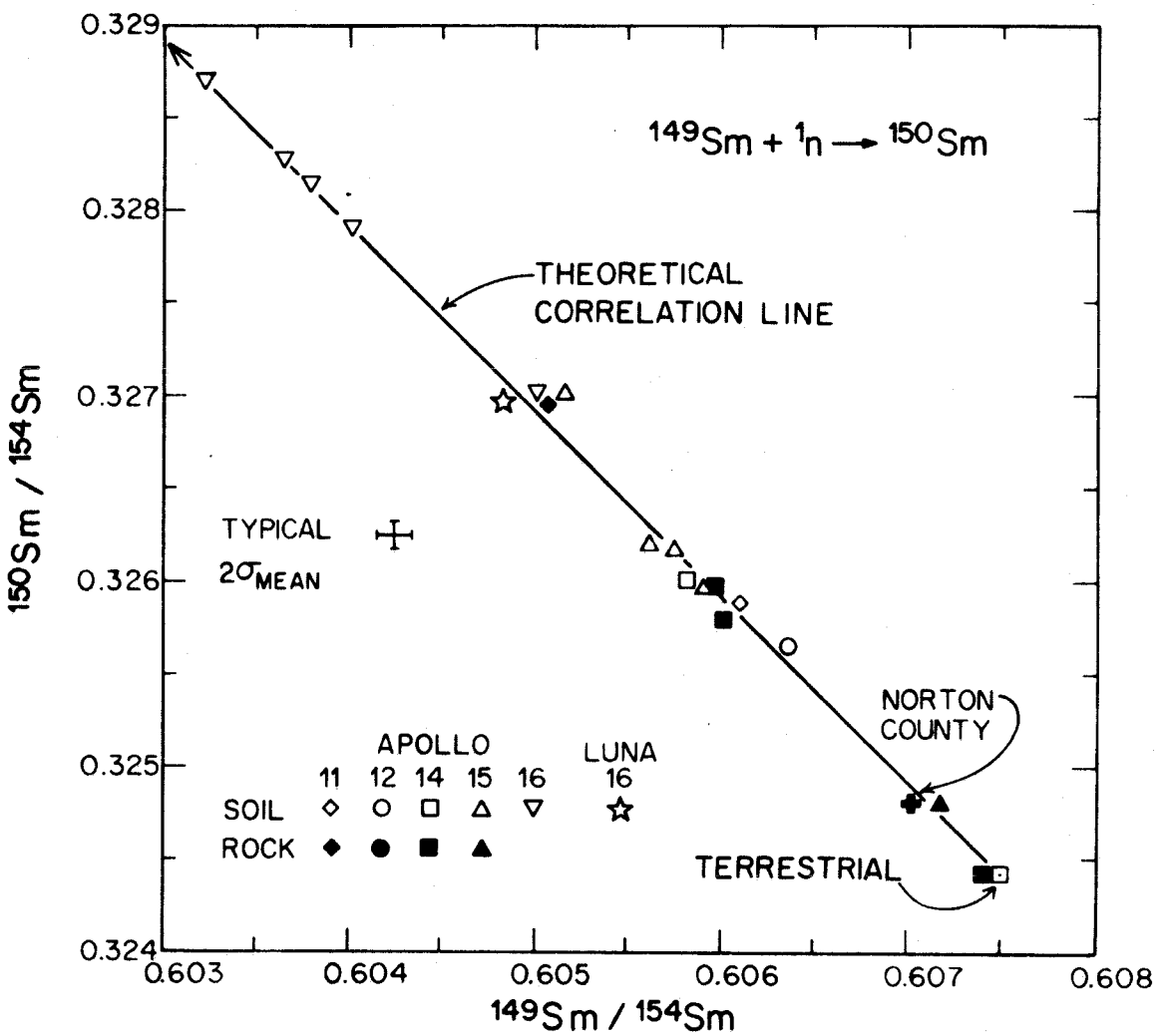
0.329
0.328
0.327
0.326
0.325
0.324
0.603
0.604
0.605
0.606
0.607
0.608
$^{150}Sm / ^{154}Sm$
$^{149}Sm / ^{154}Sm$
$^{149}Sm + {}^{1}n \rightarrow {}^{150}Sm$
THEORETICAL
CORRELATION LINE
TYPICAL
$2\sigma_{MEAN}$
APOLLO
11 12 14 15 16
LUNA
16
SOIL
ROCK
NORTON
COUNTY
TERRESTRIAL

Figure 2-9

Apollos 11 and 12 (Figs. 2-10). Four surface soils were analyzed from Apollo 11. Two of these, 10084 and 10004, were not sieved except at the Lunar Receiving Laboratory where the particles larger than 1 mm were removed. An additional part of the 10084 soil was sieved such that only particles < 37 μm in diameter were analyzed. This sample had a higher $^{158}Gd/^{157}Gd$ ratio than the unsieved samples. *Luny Rock 1*, an 83-mg fragment from the larger than 1 mm soil had a lower $^{158}Gd/^{157}Gd$ ratio than the unsieved samples. This behavior is consistent with the concept of the soil being created from rock by repeated impacts. The finer material has presumably undergone more impacts and been exposed to more cosmic radiation than the larger grains. The situation is qualitatively the same for the Apollo 12 samples. A sample of 100-300 μm grains from 12042 had been less irradiated than the total soil, while a sample of < 44 μm grains and a sample of very fine *acetone floats* had been slightly more irradiated than the bulk soil. The coarsest 25 mg of material was handpicked from a 153 mg sample of 12028,110 from the Double Core. These coarser grains, including glass particles, were less irradiated than the remaining finer material. Although the exact effect of grain size on the measured neutron fluence is not clear from these data, the variations are less than ~ 20% for variations in grain size from ≅ 200 to ⩽ 50 μm. For this work, where all grains less than 1 mm in diameter, or in the cases of Apollos 15 and 16 less than 300 μm, are used, the effect of grain size differences among the samples should be small. (It should be noted, however, that for a given site, all the samples were sieved to the same size.) For individual coarse grains like Luny Rock 1, the

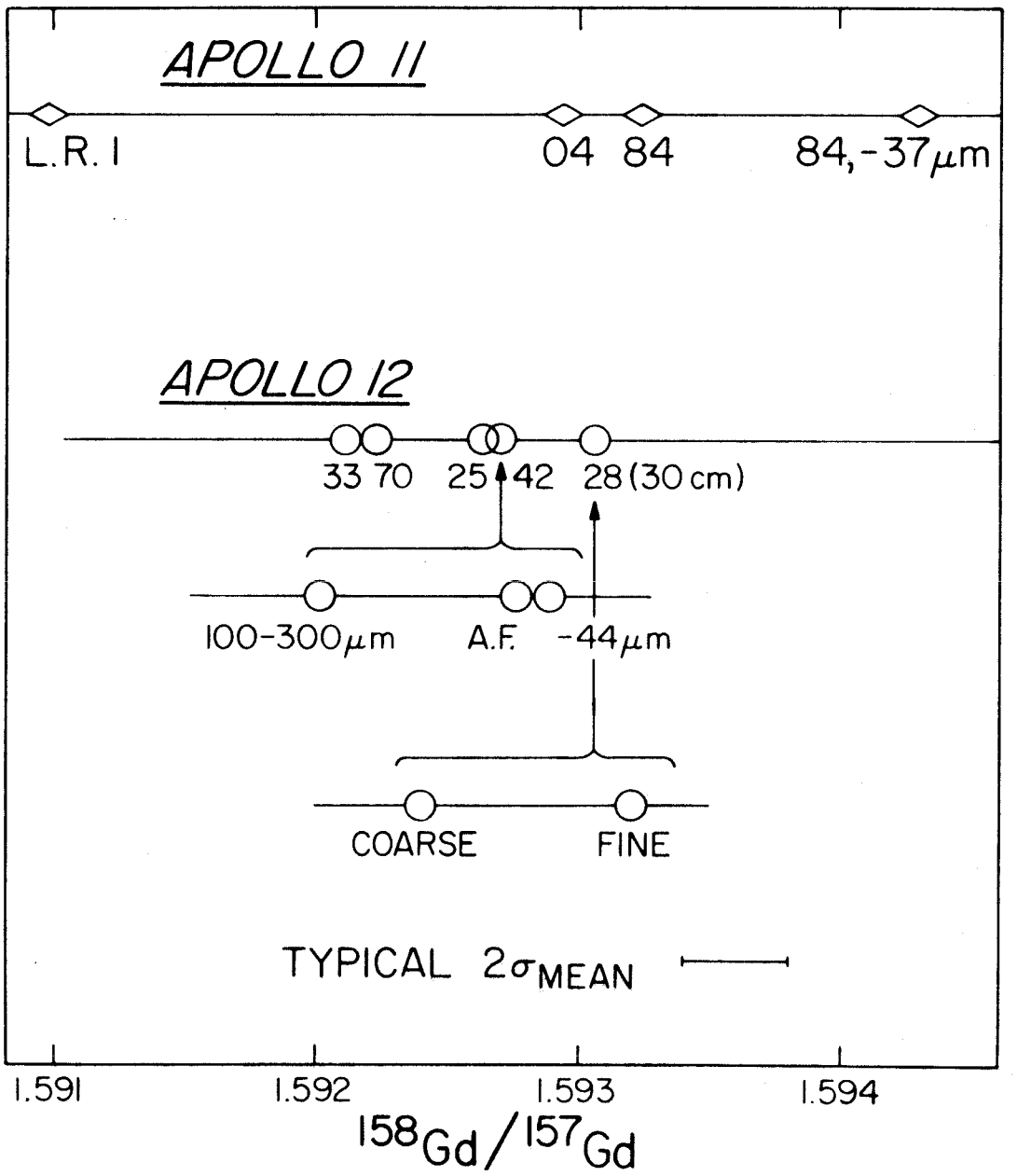

Figure 2-10

Effect of grain size on $^{158}Gd/^{157}Gd$ in Apollo 11 and 12 soils. Recall that $^{158}Gd/^{157}Gd = 1.5866$ for unirradiated samples. Samples are labeled by the last two digits of their official designations, *e.g.*, "33" refers to soil 12033. L.R. 1 is Luny Rock 1. The sample from 12028 came from a depth of 30 cm. A.F. means acetone floats.

fluence may vary significantly from grain to grain. Lugmair and Marti [4] have shown that "peanuts" from the soil 14160 have a wide range of neutron fluences and distinct irradiation histories.

Before the isotopic composition data can be interpreted in terms of neutron fluences, and before they can be used to establish the mixing history of the regolith at the various sites, the processes of formation, moderation, and capture of neutrons must be considered. This will be done in the next two chapters.

2.7 References

[1] O. Eugster, F. Tera, D. S. Burnett and G. J. Wasserburg, Isotopic composition of gadolinium and neutron-capture effects in some meteorites: J. Geophys. Res. 75 (1970) 2753.

[2] G. J. Wasserburg, D. A. Papanastassiou, E. V. Nenow, and C. A. Bauman, A programmable magnetic field mass spectrometer with on-line data processing, Rev. Sci. Instr. 40 (1969) 288.

[3] D. S. Burnett, J. C. Huneke, F. A. Podosek, G. P Russ III, G. Turner, and G. J. Wasserburg, The irradiation history of lunar samples, Lunar Science III (Lunar Sci. Inst. Cont. No. 88, 1972) 105.

[4] G. W. Lugmair and K. Marti, Exposure ages and neutron capture record in lunar samples from Fra Mauro, Proc. Third Lunar Sci. Conf. 2 (MIT Press, 1972) 1891.

[5] K. T. Bainbridge and O. A. Nier, National Research Council Nuclear Energy Series, Preliminary Report No. 9 (Dec. 1950).

3. Lunar Neutrons

In this chapter the origin, moderation, and spatial distribution of lunar neutrons will be discussed. Certain basic equations of neutron physics will be presented, and it will be shown that the energy spectrum and spatial distribution of lunar neutrons predicted by detailed neutron transport calculations can be qualitatively understood in terms of the basic physical principles. The reactions which produce the neutrons and the depth dependence of these reactions will be discussed in Section 3.1. Then the energy spectrum of the neutrons during moderation (Sec. 3.2) and the distance neutrons travel from their source will be considered (Sec. 3.3). Finally because the interpretation of the neutron capture effects studied in this work depends heavily on the neutron transport equations performed by others, the basic equations used in these calculations will be presented (Sec. 3.4).

3.1 Origin

3.1.1 Major Sources

Essentially all lunar neutrons are created by interaction of galactic cosmic ray protons with the lunar material. Three processes contribute to the production of these neutrons. 1) Neutrons are *evaporated* from nuclei which have been excited to more than ~ 8 MeV above their ground states by inelastic collisions with cosmic ray protons. This energy is greater than typical neutron binding energies

(6-7 MeV). If a nucleus is sufficiently excited, two or more neutrons may be evaporated. The energy spectrum of such neutrons can be described by

$$N(E) \propto E \cdot \exp(-E/\theta)$$

where N(E) is the number of neutrons emitted per unit energy at energy E, and θ is the *evaporation temperature*, $\sim$ 1 MeV [1,2] (Fig. 3-1). 2) Neutrons may be produced directly in collisions of cosmic ray protons with lunar material. These *knock-on* or *cascade* neutrons are more energetic than those produced by evaporation and are predominantly forward scattered. Hess, Canfield, and Lingenfelter [3] have described the energy spectrum of the knock-on neutrons by the semi-empirical formula

$$N(E) \propto E^{-2} \cdot \exp(-160\ E^{-2})$$

where E is in MeV (Fig. 3-1). 3) In solid materials, the density is high enough that negative pions ($t_{\frac{1}{2}} \sim 2 \times 10^{-8}$ sec) produced in knock-on reactions can be slowed down and captured before they decay. When these pions are captured by nuclei, part of their rest-mass energy is given off by evaporating an average of 4 neutrons per pion [4]. These neutrons should have an energy spectrum similar to that for case (1).

In addition to the neutrons produced by galactic cosmic ray protons, multiply-charged heavy cosmic ray nuclei, in particular He nuclei, can interact to produce neutrons. The importance of such reactions has not been calculated explicitly for the lunar case; however,

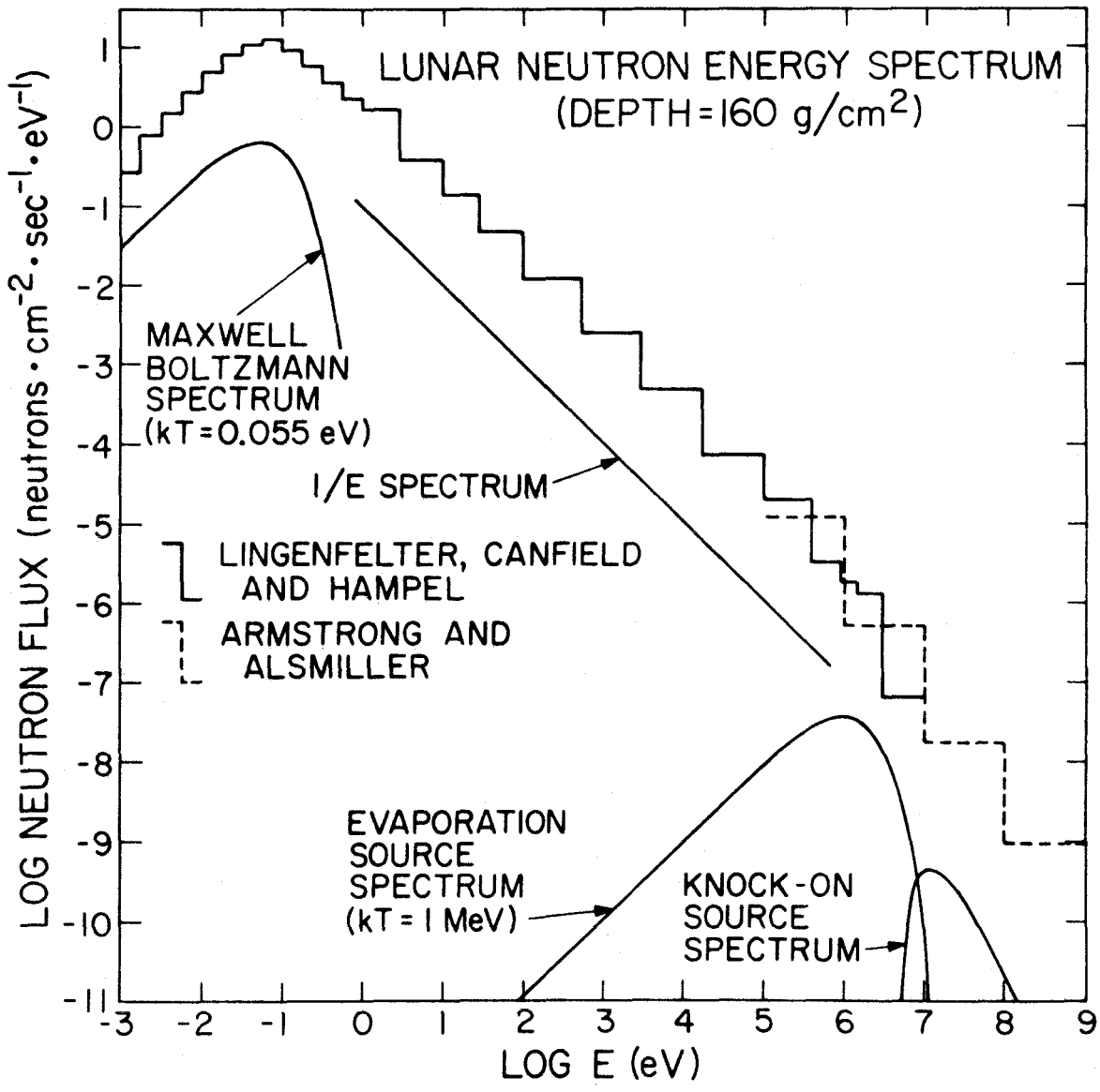

Figure 3-1

Lunar neutron flux spectrum at a depth of 160 g/cm^2 as calculated by LCH [6] and Armstrong and Alsmiller [7] for material with the chemical composition of the Apollo 11 soil. The LCH calculations assume a neutron source spectrum which has an evaporation and a knock-on component. In the absence of absorption neutrons can be accurately described by a 1/E spectrum in the slowing down region (~10^5 to ~1 eV) and a Maxwell-Boltzmann distribution at lower energies.

Armstrong, Chandler and Barish [5] have calculated that in the terrestrial atmosphere at a latitude of 42°, about 20% of the neutron flux between 1 and 10 MeV is produced by α particle interactions. At higher terrestrial latitudes and on the moon, the fractional contribution from α's will be smaller because the earth's magnetic field discriminates against protons more strongly than α particles. (Although the attenuation length for cosmic ray α particles is somewhat less than that for protons, the fact that the α contribution to the neutron flux is small implies that no serious error is introduced by not calculating the α contribution to the neutron flux explicitly.)

Two methods have been used to calculate the magnitudes of the various contributions to the lunar neutron flux. A) Lingenfelter, Canfield, and Hess [4] and more recently Lingenfelter, Canfield, and Hampel [6] (LCH) have estimated the lunar neutron production rate from galactic cosmic rays (p and α) by scaling the contributions of processes (1) and (2) from the neutron production rate observed at the terrestrial poles where the geomagnetic field is negligible and adding a component for pion production. Using the data from the more recent paper [6], their argument is as follows.

Over the last solar cycle the polar atmospheric neutron production rate above a unit surface area varied from 8.4 to 5.6 $n \cdot cm^{-2} \cdot sec^{-1}$ with an average flux of 7.1 $n \cdot cm^{-2} \cdot sec^{-1}$. The cross section for neutron production varies roughly as the square root of the average atomic weight of the medium; therefore, the neutron production rate on the moon (A=23) estimated from the measured value for the terrestrial atmosphere (A=14.5) at polar latitudes is 8.9 $n \cdot cm^{-2} \cdot sec^{-1}$.

About 20% of these neutrons are produced by knock-on reactions and have energies above 10 MeV. LCH estimate that half of the neutrons produced above 10 MeV are captured or escape (escape/capture ≈ 0.12 [3]) before being scattered below that energy. The lunar production rate by processes (1) and (2) for neutrons with E < 10 MeV is therefore estimated to be 8.1 $n \cdot cm^{-2} \cdot sec^{-1}$. The pion production rate is estimated to be $\sim 1\pi^-$ per proton with a proton flux of ~ 2 $p \cdot cm^{-2} \cdot sec^{-1}$. Using the neutron production rate from pions of 4, one has 8 $n \cdot cm^{-2} \cdot sec^{-1}$ produced by π^- mesons. The total production rate of neutrons with E < 10 MeV is therefore estimated to be 16 $n \cdot cm^{-2}$(column)$\cdot sec^{-1}$ to which an uncertainty of $\pm$ 5 is attached by LCH. Approximately 90% of these neutrons with E < 10 MeV are considered to have an evaporation spectrum and 10% to have a knock-on spectrum; however, because the neutrons will undergo many collisions in the process of slowing down, the exact shape of the source spectrum is only important for nuclei produced by MeV neutron capture, *e.g.*, ^{37}Ar from $^{40}Ca(n, \alpha)$.

B) Armstrong and Alsmiller [7], using the Monte Carlo technique in a detailed calculation of the neutron production rate from galactic cosmic ray protons, predicted the rate to be 17.5 $n \cdot cm^{-2} \cdot sec^{-1}$ (E < 15 MeV).

3.1.2 Other Possible Sources

In addition to the production of neutrons by galactic cosmic rays, there are five other possible sources of neutrons which should be considered. (1) Energetic solar protons can produce neutrons in the lunar

surface layers, but Mendell, Verschell, Merker, Light and Korff [8] have calculated for the terrestrial atmosphere that over the last solar cycle (#20), solar protons contributed 2-3 orders of magnitude less neutrons at high latitudes than galactic cosmic rays. On the other hand, the "major event" of February 23, 1956 is calculated to have contributed ~10% of the ^{14}C produced in the atmosphere during the more active cycle 19. Such large events are, however, accompanied by increased solar magnetic fields which result in less neutron production by galactic cosmic rays; so that the average neutron production rate over these two cycles was essentially the same. The LCH method of scaling the lunar flux to that measured in the atmosphere takes any solar proton contribution into account. (2) Neutrons produced in the sun with $E \geq 100$ MeV have a reasonable probability (40% at 100 MeV) of reaching the orbit of the earth before they decay ($t_{\frac{1}{2}} = 11$ m) [9], but no positive evidence has been obtained for such a flux. Cortellessa, Di Benedetto, and Paigis [10] have set an upper limit of $< 5.5 \times 10^{-3}$ n·cm^{-2}·sec^{-1} for the continuous flux of solar neutrons in the energy range from 10 MeV to 200 MeV. This range corresponds to that in which Lingenfelter, Flamm, Canfield and Kellman [9] have calculated the maximum solar neutron flux should occur. This limit is $< 4 \times 10^{-2}$% of the galactic cosmic ray produced flux of ~ 16 n·cm^{-2}·sec^{-1}. This source would, however, be concentrated near the lunar surface rather than distributed over depth like the cosmic ray neutron production. Assuming the source function for cosmic ray produced neutrons drops from the surface as $e^{-X/165}$ where X is the depth in g/cm^2 (see below), the solar neutron flux would still be <5% of the cosmic ray produced flux in the upper 1 g/cm^2. (3) The spontaneous fission of

^{238}U produces ~2 neutrons per fission. The flux of such neutrons to which a sample is exposed is a function for the U concentration but not depth of irradiation; therefore, even samples with no exposure to cosmic rays could in principle have measurable neutron effects. For a sample with 3 ppm U, ~5 x 10^{10} neutrons per cm^3 will be produced by this mechanism in 4.5 x 10^9 yr. For the LCH neutron energy spectrum, one calculates that the fluence of spontaneous fission produced neutrons detectable by ^{157}Gd would be $< 10^{13}$ n/cm^2 (see Sec. 5.6 for such a calculation), which is below the detection limit (~10^{14} n/cm^2) for isotopic changes in Gd. (4) The natural decay of U and Th will release α particles in lunar samples which can in turn interact with other nuclei, *e.g.*, ^{18}O, ^{23}Na, ^{25}Mg, ^{26}Mg, ^{27}Al, ^{29}Si and ^{30}Si, to emit neutrons. For a sample with 3 ppm U and 12 ppm Th, ~4 x 10^{17} α particles will be emitted per cm^3 in 4.5 x 10^9 yr. Using the neutron production rate from alpha particles of about one neutron per 10^8 alphas calculated by Morrison and Pine [26], one estimates that ~4 x 10^9 n/cm^3 have been produced by this mechanism. The neutron production rate for (α,n) reactions is less than for spontaneous fission of ^{238}U and is therefore insignificant. (5) Induced fission of ^{235}U could lead to an enhancement of the cosmic ray neutron flux because ~2.5 neutrons are released for every one causing a fission event. However, at the depth corresponding to the peak of the cosmic ray neutron flux, the induced fission rate is calculated (see Sec. 4.13) to be ~2 x 10^{-7} $fission \cdot cm^{-3} \cdot sec^{-1}$ (3 ppm U) which is also insignificant.

3.1.3 Depth Dependence of Neutron Sources and Its Effect on the Depth Dependence of the Low Energy Neutron Flux

Not only the number, but also the spatial distribution of the source neutrons, must be known in order to calculate the low energy neutron flux in the lunar regolith. The lunar surface can be represented by a semi-infinite homogeneous slab which is isotropically irradiated at the surface of the slab. In that most GeV protons are stopped by nuclear interactions rather than ionization, one would expect the intensity of a beam of cosmic rays to be attenuated exponentially with depth along a given path in the moon. However, integrating over space for the isotropic irradiation of a semi-infinite slab, one finds that the intensity I of the cosmic ray particles should decrease with increasing depth, X, more rapidly than exponentially. In particular the cosmic ray intensity as a function of depth should vary as

$$I(X) \propto 2\pi \int_0^{\pi/2} \exp\left(-\frac{X}{\Lambda \cos\theta}\right) \sin\theta d\theta = 2\pi E_2(X/\Lambda)$$

where Λ is the attenuation length, θ is the angle between the trajectory of a particle and the zenith, and $E_2(X/\Lambda)$ is an exponential integral [27]. This discussion, however, has omitted the effect of secondary particles produced by cosmic ray nuclear interactions, which themselves have sufficient energy to induce additional nuclear interactions. Near the surface, these secondary particles will cause the number of nuclear interactions per unit depth (and the neutron production rate) to increase rather than decrease with increasing depth. Below a depth of

about one attenuation length, empirical data for the earth's atmosphere indicates that the flux (primary and secondary) has an approximately exponential decrease. In the terrestrial atmosphere below 200 g/cm^2, the neutron production rate at polar latitudes has been shown by Soberman [11] to decrease exponentially with an effective attenuation length of 165 g/cm^2. (At lower latitudes where the geomagnetic field excludes low energy cosmic rays, the attenuation length is somewhat longer.) This effective attenuation length has been shown by Greenhill, Fenton, and Fenton [12] to vary during the solar cycle from ~165 g/cm^2 at solar maximum to ~150 g/cm^2 at solar minimum.

For the moon, experimental estimate of the depth distribution of the MeV neutron flux can be obtained from the ^{37}Ar data of Stoenner, Davis, and Bauer [13] and Fireman, D'Amico, and DeFelice [14] for the Apollo 16 drill stem. These data show that the MeV neutron flux increases by a factor of two from the surface to a peak at a depth of ~60 g/cm^2 then decreases smoothly with increasing depth. Below a depth of ~100 g/cm^2, the ^{37}Ar data are compatible with an exponential decrease where the attenuation length is ~160 $\pm$ 35 g/cm^2 if one assumes no material was spilled from this core (see Sec. 9.3.2).

The Monte Carlo intranuclear-cascade-evaporation model calculations of Armstrong and Alsmiller [7] predict that the 1-10 MeV neutron flux should rise by a factor of $\sim$ 2.5 from the surface to a depth of $\sim$ 80 g/cm^2. Below this depth, the flux is predicted to decrease approximately exponentially with an attenuation length of $\sim$ 200 g/cm^2. As discussed by LCH, this is a longer attenuation length than would be

expected from an analogy to the terrestrial atmosphere; however, the difference may result from a different depth dependence for the pion contribution which is only important for the moon.

The LCH multi-group transport calculations, which are used in this work to interpret isotopic data, are based on the simple exponential source function

$$N(E,X) = N_o E \exp(-E/\theta) \exp(-X/\Lambda)$$

where N(E,X) is the number of neutrons per unit energy and depth produced at energy, E, and depth, X. The evaporation temperature, θ, is taken as 1 MeV and the attenuation length, Λ, is taken as 165 g/cm^2. N_o is normalized to give 16 $n \cdot cm^{-2}(column) \cdot sec^{-1}$ ($E < 10$ MeV). Using this source, the lunar neutrons are calculated to have the energy spectrum shown in Figure 3-1. The flux of neutrons with $E < 0.18$ eV (to which ^{157}Gd capture is sensitive) is calculated to rise by a factor of ~10 from the surface to a peak at a depth of 155 g/cm^2, then to drop with an attenuation length of ~165 g/cm^2 (see Fig. 5-3). For the equivalent energy region the Armstrong and Alsmiller [7] calculations predict the peak to occur at $\sim$ 180 g/cm^2. As a check on the sensitivity of the depth distribution of the low energy flux to the depth distribution of the neutron sources, a second calculation was performed by LCH in which the source strength was kept constant to a depth of 175 g/cm^2. It was then decreased exponentially with Λ = 165 g/cm^2. The total neutron production per cm^2 of lunar surface was kept at 16. This calculation predicted low energy capture rates which were 10% higher than for the previous case and which were

peaked at a depth of 180 g/cm^2. The differences in the low energy neutron capture rates as a function of depth calculated for the simple exponential source and the "constant-then-exponential" source are not large and would not significantly alter any conclusions reached in this work which were based on the simple exponential source model. The Lunar Neutron Probe Experiment (Sec. 4.15) indicates that the LCH depth dependence for low energy neutrons based on the simple exponential source is essentially correct and that the low energy flux has a broad maximum between 120 and 170 g/cm^2. Throughout this work, the LCH calculations for this simple exponential source function will be used, and it will be assumed that the neutron production rate has been constant since the formation of the moon.

3.2 Energy Spectrum of Moderated Neutrons

A basic understanding of why moderated lunar neutrons should have an energy spectrum like that shown in Figure 3-1 can be obtained from a consideration of basic neutron physics. In Subsection 3.2.1 the basic neutron physics equations will be presented without being specifically applied to the lunar case. These equations will then be used (Sec. 3.2.2) to calculate the average number of collisions a lunar neutron undergoes during moderation and the probability that it will be slowed to given energies without being captured.

3.2.1 General Form of Neutron Flux Spectra

In the preceding section, references were made to the neutron

flux, but flux was not defined. The neutron *flux* is the number of neutrons crossing a square centimeter normal to the neutron velocity per second; therefore, at a given energy the flux per unit energy is equal to the number of neutrons at that energy per unit energy and volume, *i.e.*, the neutron density, multiplied by the velocity of the neutrons. For an isotropic irradiation, the flux can be thought of geometrically as the number of neutrons passing through a sphere of unit cross-sectional area per second. This is twice the number of particles crossing a plane of unit area [15].

The general form of the neutron flux spectrum can be understood by first considering the special case of no thermal scattering, *i.e.*, 0°K, and no absorption. As neutrons are slowed down, the number of collisions which they undergo per unit energy increases; however, it can be shown [16] that the average change in $ln\ E$ per collision, ξ, is independent of energy

$$\left(\xi = 1 + \frac{(A-1)^2}{2A}\ ln\left(\frac{A-1}{A+1}\right) \approx \frac{2}{A + \frac{2}{3}} \right) .$$

For this reason, it is convenient to perform certain calculations in terms of the dimensionless variable, u, called *lethargy* which is defined as

$$u \equiv ln\,(E_o/E)$$

where E_o is an arbitrary energy - usually 10 MeV - selected so that the lethargy is positive for almost all the neutrons in the system.

From the steady state requirement that the number of neutrons entering a lethargy interval equal the number leaving the interval, it can be shown [17] that the number of collisions per unit lethargy, time, and volume as a function of lethargy, F(u), must be a constant if absorption and leakage are zero and if the neutrons have already undergone several collisions. Because of the requirement of no absorption or leakage,F(u) must equal the neutron production rate divided by the average lethargy change per collision. Rearranging terms one can therefore write

$$F(u)\xi = \Phi(u)N\sigma(u)\xi = Q$$

where $\Phi(u)$ is the flux per unit lethargy, N is the number of atoms per cm^3, $\sigma(u)$ is the microscopic, *i.e.*, single nucleus, neutron scattering cross section, and Q is the neutron production rate in the source. The flux per unit energy, $\phi(E)$, can be related to $\Phi(u)$ by $\Phi(u) = E\phi(E)$. In general $\sigma(u)$ is a constant; therefore, one can write

$$\phi(E) = \frac{Q}{N\sigma\xi E}$$

From this expression one sees that for the case of no absorption or leakage and at energies significantly below the source energy the flux varies as 1/E. As shown in Figure 3-1, the LCH spectrum varies approximately as 1/E in the energy range 1 eV - 1 MeV because absorption is fairly weak in this energy range.

From the above discussion it also follows that the number of neutrons crossing a given energy per unit time and volume, q(E),

the *slowing down density*, must also equal Q; therefore one can write

$$q(E) = \xi\phi(E)N\sigma(E)E$$

If the restriction of no absorption is removed, q(E) is no longer a constant and $\phi(E)$ becomes the flux with no absorption multiplied by the probability that a neutron is not captured before reaching energy E. This probability is called the *resonance escape probability*. For a medium in which capture varies slowly with energy, which is an adequate description of the moon for these considerations, the resonance escape probability, p(E), can be written [16] as

$$p(E) = \frac{q(E)}{Q} = \exp\left(-\int_E^{E_o} \frac{\Sigma_a}{\xi\Sigma_s+\gamma\Sigma_a}\,\frac{dE'}{E'}\right)$$

where Σ_s is the macroscopic scattering cross section, *i.e.*, $N\sigma_s$, Σ_a is the macroscopic absorption cross section, and γ is a function of the atomic weight of the medium. Σ_a and Σ_s are in general functions of energy, but in most cases, Σ_s may be considered to be constant. In the absence of strong resonances, Σ_a varies as $E^{-\frac{1}{2}}$. For such a case, and assuming weak capture, *i.e.*, $\xi\Sigma_s >> \gamma\Sigma_a$, the neutron spectrum can then be described at energies well below the source energy, E_o, by

$$\phi(E) = \frac{Q}{\xi\Sigma_s E} \cdot \exp\left[-\frac{2\Sigma_a{}^o}{\xi\Sigma_s}\left(\frac{E^o}{E}\right)^{\frac{1}{2}}\right]$$

$$\propto \frac{1}{E}\exp(-c/E^{\frac{1}{2}})$$

where Σ_a^o and E^o refer to some reference energy, usually 0.025 eV, and c is a constant. Such a spectrum will vary with decreasing energy as 1/E until absorption becomes important. At some energy determined by $\Sigma_a/\xi\Sigma_s$, the flux will peak, and below that energy it will decrease. As can be seen in Figure 3-1, these basic considerations lead to an energy spectrum with essentially the form predicted by the detailed LCH calculations.

For neutrons at 0°K, the above equation should adequately describe the flux over all energies; however, at higher temperatures, the thermal energy of the system will result in the low energy neutrons having a spectrum which is a mixture of the slowing down spectrum given above and a Maxwell-Boltzmann distribution (Fig. 3-1), *i.e.*,

$$\phi(E) \propto \frac{E}{kT^2} \exp(-E/kT)$$

The exact shape of the spectrum will depend on $\Sigma_a/\xi\Sigma_s$.

An adequate description of neutron spectra can often be obtained by considering them to have a 1/E component and a thermal component where the neutron temperature, T_n, is defined by

$$T_n = T_o(1 + CA\Sigma_a/\Sigma_s)$$

where T_o is the temperature of the moderator, C is a constant in the range 0.6-1.1, A is the atomic mass of the moderator, and Σ_a is the absorption cross section at the energy corresponding to T_o. This expression is calculated to be valid for $A\Sigma_a/\Sigma_s < 0.5$ [18]. Outside of

this range, detailed calculations are required to describe neutron spectra.

The above treatment of neutron spectra has considered the scattering medium to be an ideal gas and has ignored any effects which might be introduced by the crystal lattice. These effects may be important at low energies but have been ignored in all lunar calculations. The discussion given here has only treated the case of a single element target. For a mixture of elements, average values must be calculated for A, ξ, Σ_a and Σ_s.

3.2.2 Lunar Neutron Spectrum

The above equations can now be used to calculate the characteristics of lunar neutron energy spectra. On the moon, the elements which control the scattering of neutrons in order of decreasing importance are O, Si, Fe, Mg, and Ca. Because the abundance of O and Si is nearly constant in the lunar samples, the scattering properties of all the lunar materials studied in this work are essentially the same. The Σ_s applicable to the lunar samples can be calculated by simply adding the Σ_s values for the various elements and has been calculated by LCH to be 0.092 cm^2/g. For a mixture of elements, the effective value of ξ is calculated by evaluating $\xi\Sigma_s$ and Σ_s for each element, summing the individual contributions, and dividing the total $\xi\Sigma_s$ for the mixture by the total Σ_s. For the lunar case, the effective ξ has been cal-

culated by LCH to be 0.0954. This value implies an effective scattering atomic weight for the lunar material of 20.3. Calculating an effective Σ_a is more complicated because the elements which make the largest contribution, Fe, Ti, Gd, and Sm, vary from site to site, and because the cross sections for the rare earth elements are dominated by resonances rather than varying simply as $E^{-\frac{1}{2}}$. In the LCH calculations, Σ_a is replaced by Σ_{eff}, which is defined to vary as $E^{-\frac{1}{2}}$ and to give the same total amount of absorption when integrated over the energy spectrum, as the sum of the individual elemental Σ_a's. For materials with the composition of the Apollo 11 soil, Σ_{eff} is calculated to be 0.0092 $cm^2 \cdot g^{-1}$.

From these values, it follows that for the Apollo 11 materials $A\Sigma_a/\Sigma_s = 2$ which is significantly outside the range of $A\Sigma_a/\Sigma_s < 0.5$, in which one could expect to describe the low energy spectrum by the neutron temperature T_n. Nevertheless, using the upper limit of 1.1 for the constant C, one calculates that for $T_o = 200°K$, the moderator temperature used by LCH which is closest to the lunar temperature,

$$T_n = 200° \times [1+(1.1)(20)(0.1)] = 640°K$$

The maximum flux for a thermal distribution occurs at E = kT; therefore, a temperature of 640°K implies a maximum in the flux at 0.055 eV. The LCH calculations indicate that the maximum should occur at $\sim$ 0.063 eV (Fig. 4-4). The experimental data also indicate that the spectrum is peaked at a higher energy than 0.055 eV (Sec. 4.4). Although the simple theory only approximately describes the neutron spectrum, it can be

used to calculate several quantities which lend insight into the moderation process.

The number of collisions, n, necessary to increase the average lethargy to the value corresponding to the energy E is

$$n = (1/\xi)\ell n\,(E_o/E)$$

This number is also approximately the average number of collisions necessary to reduce the energy of a neutron from E_o to E [16,19]. In lunar material to reduce the energy of a 1 MeV neutron to 100 keV, 1 keV, 1 eV, 0.1 eV, and 0.025 eV therefore requires on the average 24, 72, 144, 169, and 184 collisions respectively. From the resonance escape probability, the fraction of the 1 MeV neutrons reaching given energies can also be calculated. Approximately 100, 99, 71, 35, and 12%, respectively, of the 1 MeV neutrons will reach the energies specified above without being captured.

3.3 Spatial Distribution of Neutrons about a Source

The average number of collisions undergone by a neutron in slowing down and its probability of not being captured were calculated above. If one also knows how far neutrons travel while slowing down, one can qualitatively understand how low energy neutrons are distributed with depth in the moon. The probability of a neutron having a collision in a distance dr is $(\Sigma_a + \Sigma_s)dr$. Because $\Sigma_a/\Sigma_s = 0.1$ at 0.025 eV and Σ_a varies as $E^{-\frac{1}{2}}$ while Σ_s is essentially constant, one can approximate $\Sigma_a + \Sigma_s$ by Σ_s and consider the collision

probability as energy-independent. The root mean square *crow-flight* distance, R_{rms}, which neutrons travel in slowing down from energy E_1 to E_2 can be shown [20] to be

$$R_{rms} = \left[\frac{2(\ell n\, E_1/E_2)}{(1-\frac{2}{3A})\xi\Sigma_s^2}\right]^{\frac{1}{2}}$$

The root mean square distances traveled by a neutron with an initial energy of 1 MeV in slowing down to 100 KeV, 1 KeV, 1 eV, 0.1 eV, and 0.025 eV in Apollo 11 material are 77, 133, 189, 204, and 212 g/cm^2 or assuming a density of 1.8 g/cm^3 - 0.43, 0.74, 1.05, and 1.13 meters, respectively.

If a large number of collisions are necessary to slow down neutrons in a medium, *i.e.*, $A \gg 1$, if $\Sigma_s(E)$ is slowly varying, and if absorption can be neglected, the spatial distribution of neutrons can be described by the neutron diffusion equation *(Fermi Age equation)* [20]

$$\nabla^2 q(r,\tau) = \frac{\partial q(r,\tau)}{\partial \tau}$$

where $q(r,\tau)$ is the slowing down density as a function of distance from the source, r, and neutron *age*, τ. The neutron age is defined as

$$\tau(u) \equiv \int_o^u \frac{du}{3\xi\Sigma_s^2(1-\frac{2}{3A})} = \frac{\ell n\, E_o/E}{3\xi\Sigma_s^2(1-\frac{2}{3A})}$$

and has dimensions of length squared. From the equation given above for the root mean square distance traveled by neutrons in slowing down from E_1 to E_2, one sees that the neutron age is 1/6 of the mean square distance.

Consider the problem of the equilibrium spatial distribution of the neutrons produced at a given depth in the lunar regolith. Ignoring absorption and considering the moon as an infinite medium, the problem is just that of the distribution of neutrons from a planar source in an infinite medium. The solution to this problem can be shown [15,17] to be

$$q(r,\tau) = S(4\pi\tau)^{-\frac{1}{2}} \exp(-r^2/4\tau)$$

where S is the number of neutrons emitted per cm^2 and sec at energy E_o. The distributions calculated at 100 KeV, 1 KeV, 1 eV, and 0.1 eV for neutrons with an initial energy of 1 MeV in material of the Apollo 11 composition is shown in the left half of Figure 3-2.

If the medium absorbs weakly and if the cross section does not vary rapidly with energy, it is possible to modify the Fermi age theory to take this absorption into account. It can be shown [16,19] that the slowing down density with absorption, $q_a(r,u)$, can be expressed as

$$q_a(r,u) = q(r,u)p(u)$$

where $q(r,u)$ is the slowing down density without absorption and $p(u)$ is the resonance escape probability. From this relation, one sees that the shape of the spatial distribution curves is the same with and without absorption and that only the magnitude of the slowing down density is affected by absorption. The slowing down densities calculated for

Figure 3-2

Fermi age theory calculation of the neutron density in lunar material as a function of energy and distance from a planar source emitting 1 MeV neutrons. Absorption lowers the density at a given energy and distance but does not affect the shape of the spatial distribution for a given energy. The source plane is assumed to be parallel to the lunar surface and located at a depth where leakage to the surface is negligible.

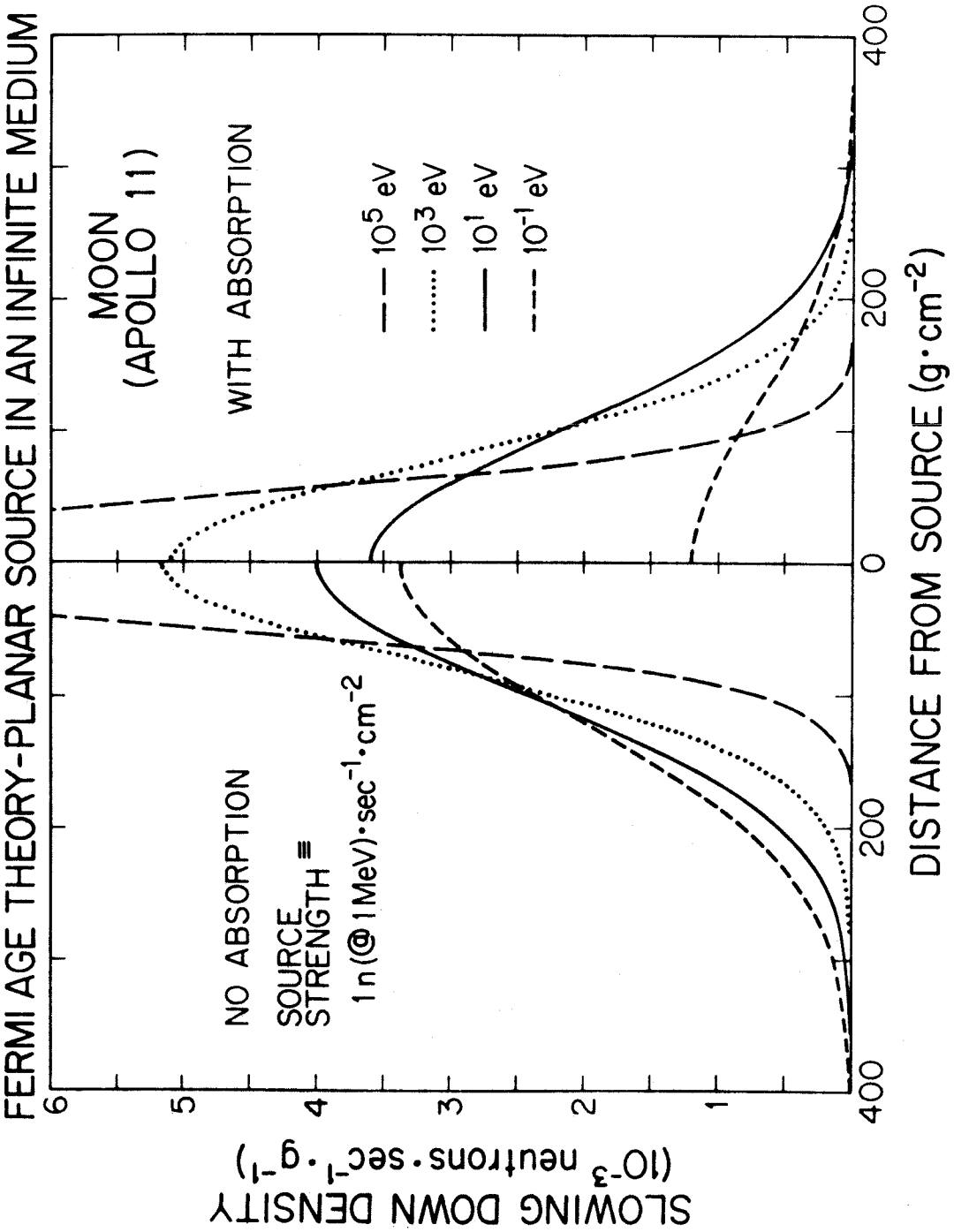
FERMI AGE THEORY-PLANAR SOURCE IN AN INFINITE MEDIUM
MOON
(APOLLO 11)
WITH ABSORPTION
NO ABSORPTION
SOURCE STRENGTH ≡ 1n(@1MeV)·sec⁻¹·cm⁻²
10⁵ eV
10³ eV
10¹ eV
10⁻¹ eV
SLOWING DOWN DENSITY
(10⁻³ neutrons·sec⁻¹·g⁻¹)
DISTANCE FROM SOURCE (g·cm⁻²)
0
200
400
1
2
3
4
5
6

Figure 3-2

the lunar case with absorption are shown in the right half of Figure 3-2.

The Fermi Age calculations presented in Figure 3-2, can be used as a basis for qualitatively understanding the depth dependence of the low energy neutron flux calculated by LCH (see Sec. 3.1.3 and Fig. 5-3) which rises rapidly from the surface to a peak at a depth of ~155 g/cm^2 then decreases exponentially with an attenuation length of ~165 g/cm^2. At depths from which surface leakage is negligible, one can see from Figure 3-2 that at all energies the density of neutrons which were produced at a given depth is highest at that depth. Furthermore the distribution of such neutrons will be symmetric above and below the source depth. For a distributed source, the depth dependence of the low energy flux will be the same as the depth dependence of the source. The LCH calculations assume an attenuation length of 165 g/cm^2 for the neutron source function which is directly reproduced by the depth dependence calculated for the low energy flux at large depths. Near the surface the depth dependence of the flux will depend on the leakage of neutrons from the surface. Because the flux must drop to zero slightly above the surface, it follows that the flux must have a maximum at some depth and then decrease at decreasing depths. The leakage affects the depth distribution of the low energy flux in two ways. 1) The contribution from the near surface sources is smaller than would be the case for deeply buried sources of the same strength. 2) The distribution of low energy neutrons from a single source is not symmetric about that source. Because every neutron which reaches the surface at any time during

moderation is lost, the distribution of low energy neutrons produced at a given depth will be peaked at a deeper depth. It is the combination of these effects, which are dependent on how far neutrons travel during moderation, which determines the depth of the low energy flux peak. From the distribution of 0.1 eV neutrons shown in Figure 3-2, one sees that ~20% of the total number of neutrons are located at a distance of more than 160 g/cm^2 from their source when they are slowed down past 0.1 eV. A much higher fraction must have been at least this far from their source at sometime before they were slowed to 0.1 eV. Therefore even for a source located at a depth of 160 g/cm^2 a significant number of neutrons will be lost by leakage; for this reason the depth of the peak of the low energy neutron flux calculated by LCH (~155 g/cm^2) seems qualitatively reasonable.

As a comparison to the lunar case Fermi age calculations have also been made for the terrestrial atmosphere (ξ = 0.134, A = 14.3, Σ_a = 0.0315 (E = 0.025 eV) $cm^2 \cdot g^{-1}$, and Σ_s = 0.202 $cm^2 \cdot g^{-1}$). As seen in Figure 3-3, atmospheric neutrons are slowed down in less distance than lunar neutrons. This reflects the larger $\xi\Sigma_s$ for the atmosphere and qualitatively explains why the low energy neutron flux at the terrestrial poles is peaked at a depth of $\sim$ 75 g/cm^2 [11] whereas the peak occurs at $\sim$ 155 g/cm^2 on the moon. The ratio $\Sigma_a/\xi\Sigma_s$ is, however, similar for the two cases so they would be expected to have similar energy spectra. A comparison of the detailed calculations of LCH for the moon and Armstrong *et al.* [5] for the atmosphere indicates that in the atmosphere, which has the higher $\Sigma_a/\xi\Sigma_s$ ratio, the energy spectrum is peaked at

Figure 3-3

Fermi age theory calculation of the neutron density in the terrestrial atmosphere as a function of energy and distance from a planar source emitting 1 MeV neutrons. The source plane is assumed to be parallel to the surface of the earth and located at a depth where leakage is negligible. Note that in the atmosphere neutrons diffuse only about half as far as in the lunar material.

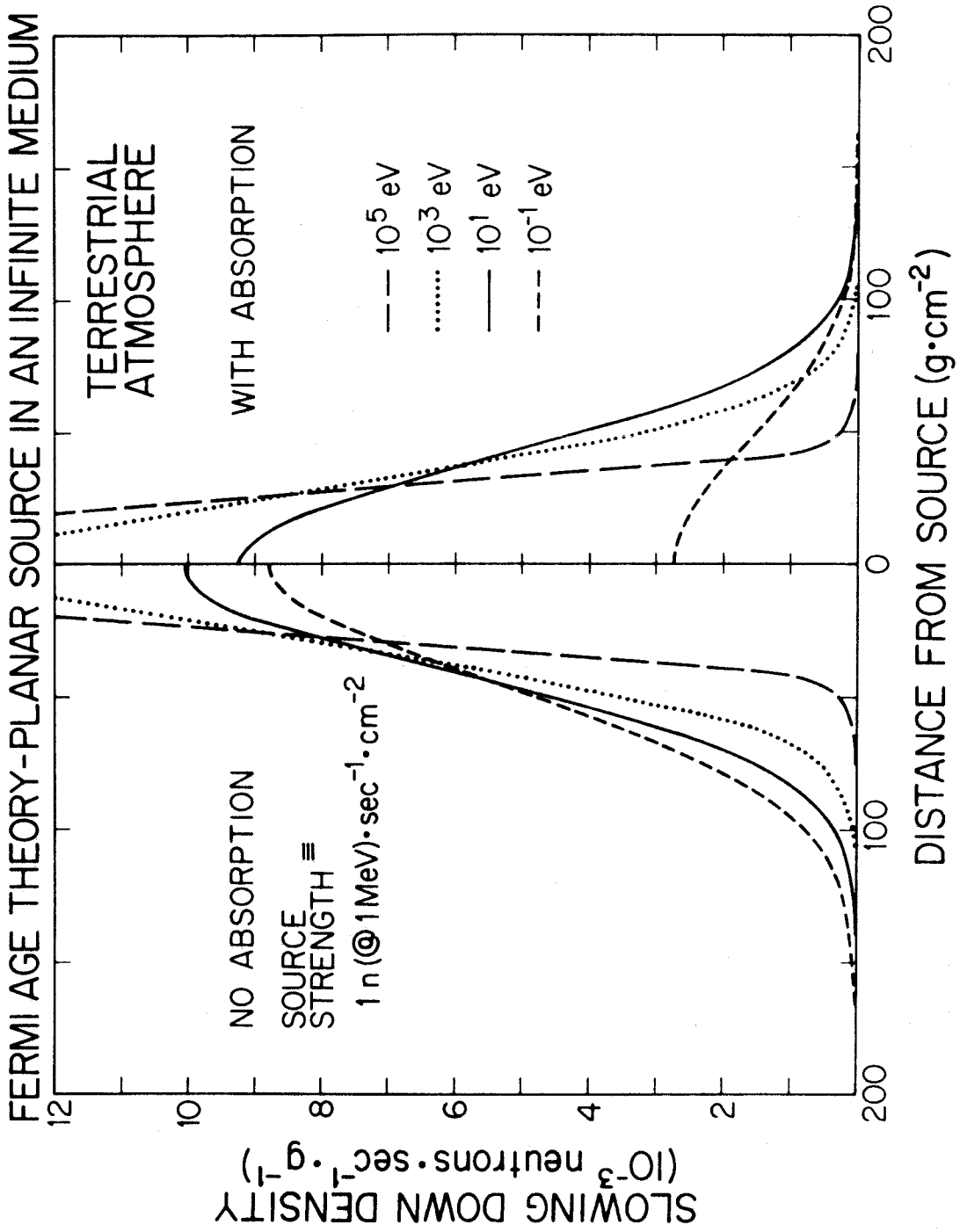
FERMI AGE THEORY-PLANAR SOURCE IN AN INFINITE MEDIUM
TERRESTRIAL ATMOSPHERE
WITH ABSORPTION
NO ABSORPTION
SOURCE STRENGTH ≡ 1 n(@1MeV)·sec⁻¹·cm⁻²
10^5 eV
10^3 eV
10^1 eV
10^{-1} eV
SLOWING DOWN DENSITY (10^{-3} neutrons·sec⁻¹·g⁻¹)
DISTANCE FROM SOURCE (g·cm⁻²)
12
10
8
6
4
2
200
100
0
100
200

Figure 3 3

a slightly higher energy than in the lunar surface.

A question which has been frequently raised [21,22, and references therein] is whether or not the moon has a permafrost layer beneath the surface. In such a layer unlike in the observed lunar samples, neutrons would be well thermalized. One might ask how far such neutrons would diffuse into material of the type sampled by the lunar missions. Neutrons in thermal equilibrium can be considered to diffuse with no change in energy. The diffusion length, L, *i.e.*, the distance necessary for the flux from a plane source to drop by a factor of e, can be defined for weakly absorbing media as [16]

$$L \equiv \left[3\Sigma_s\Sigma_a\left(1 - \frac{2}{3A}\right)\right]^{-\frac{1}{2}}$$

which like the age is equal to the square root of $1/6^{th}$ of the mean square distance. For material of the composition of the Apollo 11 soil, this diffusion length is 22 g/cm^2 or ~12 cm (ρ = 1.8 g/cm^3). If there were a permafrost layer on the moon with a well defined boundary, one would not expect to detect the effect of this layer in samples collected more than ~ 50 g/cm^2 above the boundary.

One might also ask how long a neutron takes to slow down. In the region above ~ 1 eV, the time, t, necessary for a neutron to slow down from velocity, V_1 to V_2 can be shown by age theory [19] to be

$$t = -2\int_{V_1}^{V_2} \frac{dV}{\xi\Sigma_s V^2} = \frac{2}{\xi\Sigma_s}\left(\frac{1}{V_2} - \frac{1}{V_1}\right)$$

A lunar neutron will be slowed down from 1 MeV to 1 eV in ~ 30 μsec.

3.4 LCH Multi-Group Transport Calculations

The interpretations of measured isotopic effects which will be presented in subsequent chapters will depend heavily on the LCH calculations of the lunar neutron flux; therefore, the basis of these calculations will be described in this section. In LCH, the equilibrium neutron flux spectrum in lunar material was calculated as a function of energy and depth using the neutron transport equation. The derivation of this equation can be found in a number of reactor theory texts [16,23,24]. Diffusion theory which is used for the Fermi age equation is based on the assumption that the angular distribution of the neutron velocity vectors is isotropic. In transport theory, the instantaneous neutron velocity vectors are taken into account and the neutron distribution can be more completely characterized.

In a given element of volume, solid angle, and energy, the equilibrium neutron density must be the sum of the net number of neutrons entering the volume element per second by diffusion, the number of neutrons scattered into the element per second from different angles and energies within the same volume and the number of neutrons created in the volume per second minus the number removed from the element per second by scattering and absorption. Let $n(\vec{r},\vec{\Omega},E)dVd\vec{\Omega}dE$ be the number of neutrons in the volume element dV at $\vec{r}$ whose directions of motion are contained in the element of solid angle $d\vec{\Omega}$ about the unit direction vector $\vec{\Omega}$ and whose energies lie in the element dE about E. The vector flux can then be defined by

$$\vec{F}(\vec{r},\vec{\Omega},E) \equiv n(\vec{r},\vec{\Omega},E)v\vec{\Omega}$$

where v is the neutron scalar velocity. It can be shown that the net number of neutrons entering dV in the element of solid angle $d\vec{\Omega}$ and the energy interval dE is $-\text{div}\ \vec{F}(\vec{r},\vec{\Omega},E)dVd\vec{\Omega}dE$. The number scattered within the element dV is

$$dVd\vec{\Omega}dE\int_{E'}\int_{\Omega'}\Sigma_s(\vec{\Omega}',E' \rightarrow \vec{\Omega},E)\ F(\vec{r},\vec{\Omega}',E')d\vec{\Omega}'dE'$$

where $\Sigma_s(\vec{\Omega}',E' \rightarrow \vec{\Omega},E)$ is the macroscopic cross section for scattering neutrons with directions in $d\vec{\Omega}'$ about $\vec{\Omega}'$ and with energies in dE' about E' into $d\vec{\Omega}$ and dE about $\vec{\Omega}$ and E. Let the number of neutrons created in dV per second be $S(\vec{r},\vec{\Omega},E)dVd\vec{\Omega}dE$. The number of neutrons removed by scattering and absorption is $\Sigma_t(E)F(\vec{r},\vec{\Omega},E)dVd\vec{\Omega}dE$ where $\Sigma_t(E)$ is the total macroscopic cross section. The neutron transport equation can therefore be written as

$$\text{div}\ \vec{F}(\vec{r},\vec{\Omega},E) + \Sigma_t(E)F(\vec{r},\vec{\Omega},E) = \int_{E'}\int_{\Omega'}\Sigma_s(\vec{\Omega}',E'\rightarrow\vec{\Omega},E)F(\vec{r},\vec{\Omega}',E')d\Omega'dE' + S(\vec{r},\vec{\Omega},E)$$

In that the lunar surface can be considered as a semi-infinite slab, where depth is the only significant dimension, the transport equation can be simplified to the one-dimensional form. Expressing the angular dependence of the scattering cross section in spherical harmonics, the one-dimensional equation can be written

$$\left[\mu\frac{d}{dx} + \Sigma_t(E)\right]F(x,\mu,E) = \sum_{\ell=0}^{\infty}\frac{2\ell+1}{2}P_\ell(\mu)\int_{E'}\Sigma_{s\ell}(E'\rightarrow E)\int_{-1}^{1}P_\ell(\mu')F(x,\mu',E')d\mu'dE' + S(x,\mu,E)$$

where μ is the cosine of angle between the neutron direction and the X axis and $P_\ell(\mu)$ is a Legendre polynomial.

In the multi-group approach used by LCH to solve the transport equation, the energy scale is divided into discrete segments for which average cross sections are calculated. Each segment of the energy scale is called a "group". For neutrons in group i, the transport equation becomes

$$\left[\mu \frac{d}{dx} + \Sigma_{ti}\right] F_i(x,\mu) = S_i(x,\mu) + \sum_{\ell=o}^{\infty} \frac{2\ell+1}{2} P_\ell(\mu) \sum_j \Sigma_{s\ell,j\to i} \int_{-1}^{1} P_\ell(\mu') F_j(x,\mu') d\mu'$$

$\Sigma_{ti} = \Sigma_{ai} + \Sigma_{si}$; where Σ_{ai} is the average of the macroscopic absorption cross section ($cm^2 \cdot g^{-1}$) for the group and

$$\Sigma_{si} = \frac{1}{F_{oi}} \int_i dE\, F_o(E) \int_o^\infty dE' \int_{-1}^{1} d\mu' \Sigma_s(E\to E',\mu')$$

where F_{oi} is the group scalar flux.

The cross section for neutrons being scattered into group i can be written

$$\Sigma_{s\ell,j\to i} = \frac{1}{F_{\ell j}} \int_i dE \int_j dE' F_\ell(E') \int_{-1}^{1} d\mu\, P_\ell(\mu) \Sigma_s(E'\to E,\mu)$$

The above equations were solved by LCH using the ANISN code [25] which is based on discrete meshes in x and μ. In these calculations, the

flux was calculated for 31 depth intervals between the lunar surface and a depth of 1155 g/cm^2. The energy spectrum from 10 MeV to 0 eV was divided into 25 groups. In the energy range from 1 eV to 0.00178 eV where neutron captures by Gd and Sm occur, eleven groups of equal logarithmic width were used. Calculations were also carried out for three temperatures - 0°, 200°, and 400°K - and four chemical compositions which span the range of lunar samples. Tabulations of the lunar neutron flux as a function of energy, depth, temperature, and Σ_a {or more precisely Σ_{eff} (Sec. 3.2.2)} can be obtained from Professor Lingenfelter. In the next chapter, these calculated fluxes will be compared to those measured in the lunar samples.

3.5 References

[1] E. Gross, The absolute yield of low energy neutrons from 190 MeV proton bombardment of gold, silver, nickel, aluminum, and carbon, Lawrence Radiation Lab. Report (UCRL-3330, 1956).

[2] H. E. Mitler, Particle evaporation from excited nuclei, Smithsonian Inst. Astrophys. Obs. (Special Rpt. No. 204, 1966).

[3] W. N. Hess, E. H. Canfield, and R. E. Lingenfelter, Cosmic-ray neutron demography, J. Geophys. Res. 66 (1961) 665.

[4] R. E. Lingenfelter, E. H. Canfield, and W. N. Hess, The lunar neutron flux, J. Geophys. Res. 66 (1961) 2665.

[5] T. W. Armstrong, K. C. Chandler, and J. Barish, Calculations of neutron flux spectra induced in the earth's atmosphere by galactic cosmic rays, J. Geophys. Res. 78 (1973) 2715.

[6] R. E. Lingenfelter, E. H. Canfield, and V. E. Hampel, The lunar neutron flux revisited, Earth Planet. Sci. Letters 16 (1972) 355.

[7] T. W. Armstrong and R. G. Alsmiller, Jr., Calculation of cosmogenic radionuclides in the Moon and comparison with Apollo measurements, Proc. Second Lunar Sci. Conf. 2 (MIT Press, 1971) 1729.

[8] R. B. Mendell, H. J. Verschell, M. Merker, E. S. Light, and S. A. Korff, Time dependent worldwide distribution of atmospheric neutrons and of their products, 3, neutrons from solar protons, J. Geophys. Res. 78 (1973) 2763.

[9] R. E. Lingenfelter, E. J. Flamm, E. H. Canfield, and S. Kellman, High-energy solar neutrons, 2, flux at the earth, J. Geophys. Res. 70 (1965) 4087.

[10] Paolo Cortellessa, Paolo Di Benedetto, and Constantinos Paigis, A search for solar neutrons near solar maximum, II, Solar Physics 20 (1971) 474.

[11] Robert K. Soberman, High-altitude cosmic-ray neutron intensity variations, Phys. Rev. 102 (1956) 1399.

[12] J. G. Greenhill, A. G. Fenton, and K. B. Fenton, Solar cycle variations in the polar atmospheric neutron flux at balloon altitudes, Conf. Papers 12th Internat. Conf. Cosmic Rays 2 (1971) 758.

[13] R. W. Stoenner, Raymond Davis, Jr., and Michael Bauer, Radioactive rare gases and tritium in the sample return container, and the ^{37}Ar depth profile in the Apollo 16 drill stem, to be published in Proc. Fourth Lunar Sci. Conf. (1973)

[14] E. L. Fireman, J. D'Amico, and J. De Felice, Depth variation of Ar^{37}, Ar^{39}, and H^3 in Apollo 16 material, Lunar Science IV (Lunar Sci. Inst., 1973) 248.

[15] D. J. Hughes, Pile Neutron Research (Addison-Wesley Publishing Co., 1953) 84-86.

[16] Samuel Glasstone and Milton C. Edlund, The Elements of Nuclear Reactor Theory (D. Van Nostrand Co., 1952).

[17] Alvin M. Weinberg and Eugene P. Wigner, The Physical Theory of Neutron Chain Reactors (The University of Chicago Press, 1958) 287.

[18] S. B. Wright, Neutron spectra, Neutron Fluence Measurements (International Atomic Energy Agency Technical Report Series No. 107, 1970) 23-24.

[19] John R. Lamarsh, Introduction to Nuclear Reactor Theory (Addison-Wesley Publishing Co., 1966).

[20] Jay Orear, A. H. Rosenfeld, and R. A. Schluter, Nuclear Physics: A Course Given by Enrico Fermi (The University of Chicago Press, 1950) Chapter IX.

[21] J. W. Freeman, Jr., H. K. Hills, and R. R. Vondrak, Water Vapor, whence comest thou?, Proc. Third Lunar Sci. Conf. 3 (MIT Press, 1972) 2217.

[22] G. Schubert, R. E. Lingenfelter, and S. Peale, The morphology, distribution and origin of lunar sinuous rilles, Rev. Geophys. Space Sci. 8 (1970) 199.

[23] George I. Bell and Samuel Glasstone, Nuclear Reactor Theory (Van Nostrand Reinhold Co., 1970).

[24] J. H. Tait, An Introduction to Neutron Transport Theory (American Elsevier Publishing Co., Inc., 1964).

[25] W. Engle, ANISN (Oak Ridge National Lab. Report K-1693, 1967).

[26] P. Morrison and J. Pine, Radiogenic origin of the helium isotopes in rocks, Annals New York Acad. Sci. 62 (1955) 69.

[27] Walter Gautschi and William F. Cahill, Exponential integral and related functions, Handbook of Mathematical Functions - M. Abramowitz and J. A. Stegun (ed.) (Dover, 1965) 227.

4. Neutron Capture Rates

4.1 Introduction

In addition to neutron capture by ^{157}Gd, ^{155}Gd, ^{149}Sm, and ^{151}Eu for which experimental data are presented in this work, other lunar sample investigators have reported isotopic anomalies or limits for anomalies which have been attributed to neutron capture by ^{79}Br, ^{81}Br, ^{130}Ba, ^{186}W, ^{235}U, ^{238}U, ^{59}Co, and ^{40}Ca. Lingenfelter, Canfield, and Hampel [1] (LCH) have predicted that anomalies caused by neutron capture on ^{113}Cd should also be measurable in Cd.

In this chapter, the measured effects will be compared with those predicted from the LCH calculations of the neutron flux and energy spectrum. It will be convenient to compare the measured and predicted effects in several different ways depending on the particular nuclide involved, but this should present no difficulty in that the different modes of presentation are all consistent and, in essence, equivalent. For example, the predicted equilibrium activities of radioactive neutron capture products will be expressed in terms of calculated production rates which can be directly compared with the measured activities. On the other hand, the concentrations of stable products cannot be directly compared with their calculated production rates, without a knowledge of the time for which they were exposed to the neutron flux. In such cases, the ratio of the measured concentrations of two stable products, typically ^{158}Gd and some other nuclide, will be compared to the predicted ratio of their production rates. The ratio of two neutron capture products may alternatively be expressed as the ratio of the

neutron fluences measured by the two nuclides, or the fluence measured by one nuclide, again typically ^{158}Gd, may be used to predict the concentration of the other capture product nuclide. To the extent that the target nuclides capture neutrons in different energy regions, the agreement or disagreement of the measured and predicted fluence or production rate ratios provides a check on the validity of the LCH energy spectrum.

In order to evaluate the neutron capture rate for the nuclides mentioned above, one in principle evaluates the integral of the product of the energy-dependent flux and cross section. In practice, however, LCH tabulate the average neutron flux for each of their energy groups (see Sec. 3.4). For a given nuclide, the neutron capture rate in each group can therefore be obtained by multiplying this average flux by the average capture cross section for the group and the total capture rate can be obtained by summing the product of the average flux and cross section over the various groups. For this reason, the average cross section for each group $\langle\sigma\rangle_g$, has been calculated for the various nuclides. If the energy dependence of the flux, $\phi(E)$, and cross section, $\sigma(E)$, are known, the *group cross section* $\langle\sigma\rangle_g$ can be calculated from the equation:

$$\langle\sigma\rangle_g = \frac{\int\sigma(E)\phi(E)dE}{\int\phi(E)dE} \qquad (4.1\text{-}1)$$

where the integral is carried out over the energy range of the group.

The energy-dependent cross sections, $\sigma(E)$, were evaluated by summing the contributions from the individual neutron capture resonances as evaluated from the Breit-Wigner single level formula

$$\sigma(E) = \frac{g\lambda^2}{4\pi} \cdot \frac{\Gamma_n(E)\Gamma_\gamma}{[(E-E_o)^2 + (\Gamma/2)^2]} \qquad (4.1\text{-}2)$$

where E_o is the energy of the resonance, E is the energy of the incoming neutron, λ is the deBroglie wavelength of the neutron, Γ_γ is the "level width" for γ-ray emission, *i.e.*, the probability of the γ-ray being ejected (for fission Γ_F would replace Γ_γ), $\Gamma_n(E)$ is a measure of the probability of re-emission of the neutron, g is a statistical factor giving the probability of the neutron and target combining their angular momenta to give the necessary spin, J, of the excited state, and $\Gamma = \Gamma_\gamma + \Gamma_n(E) + \Gamma_F + \ldots$. If I is the spin of the target nucleus, then $g = \frac{1}{2}(2J+1/2I+1)$ [2,3,4]. There are several other forms of the Breit-Wigner equation which commonly appear in the literature and which can lead to confusion because of notational ambiguity. These are distinguished in Appendix II.

No attempt has been made to compensate for interferences among the resonances. Interference which can be constructive or destructive may arise from the interaction of resonances with the same g [5]. This should only be important in the ^{235}U fission case where the resonances at 0.290 and 1.142 eV are known to interact [5]. In the region between $\sim$ 0.290 and $\sim$ 1.0 eV, where the interference is most pronounced, the calculated group cross section is about 25% lower than the experimental data, but this region only contributes about 5% of the total neutron absorptions. Neglecting interference terms, therefore, will not appreciably affect our conclusions. In all cases, the resonance parameters used to calculate the average cross sections were taken from BNL 325 [6]

or LCH. In some cases, cross sections were evaluated separately from each set of parameters and compared.

In order to calculate group cross sections, one must find an expression which will describe the energy dependence of the flux within each group. Because the groups are rather narrow, especially at low energy where the flux would be expected to vary rapidly with energy, the flux will not change a great deal within any one group. For this reason, the function which is used to describe the flux within a group will not greatly affect the calculated group cross section. This would not be true if one were evaluating the cross section for an energy range which was wide in comparison with the energy range over which appreciable capture occurred for the nuclide in question. In calculating their energy spectrum, LCH assumed that below 0.18 eV the flux could be described by a hardened Maxwellian distribution for which the flux is proportional to $Ee^{-E/kT}$ where kT = 0.0835 eV. Above this energy, they assumed that the flux was proportional to 1/E as would be expected for a non-absorbing medium (see Sec. 3.2). In this work, $Ee^{-E/0.0835}$ has been retained below 0.18 eV, but above this energy the flux has been taken as proportional to $E^{-0.91}$, which gives a better fit to the energy spectrum defined by the LCH group fluxes. These functions, joined at 0.18 eV, reasonably describe the energy dependence of the flux calculated by LCH for materials of the composition of the Apollo 11 soils at a temperature of 200°K (Fig. 4-1). For materials with lower concentrations of absorbers, *e.g.*, those found at the other lunar sites, the peak of the spectrum would be expected to shift to a slightly lower

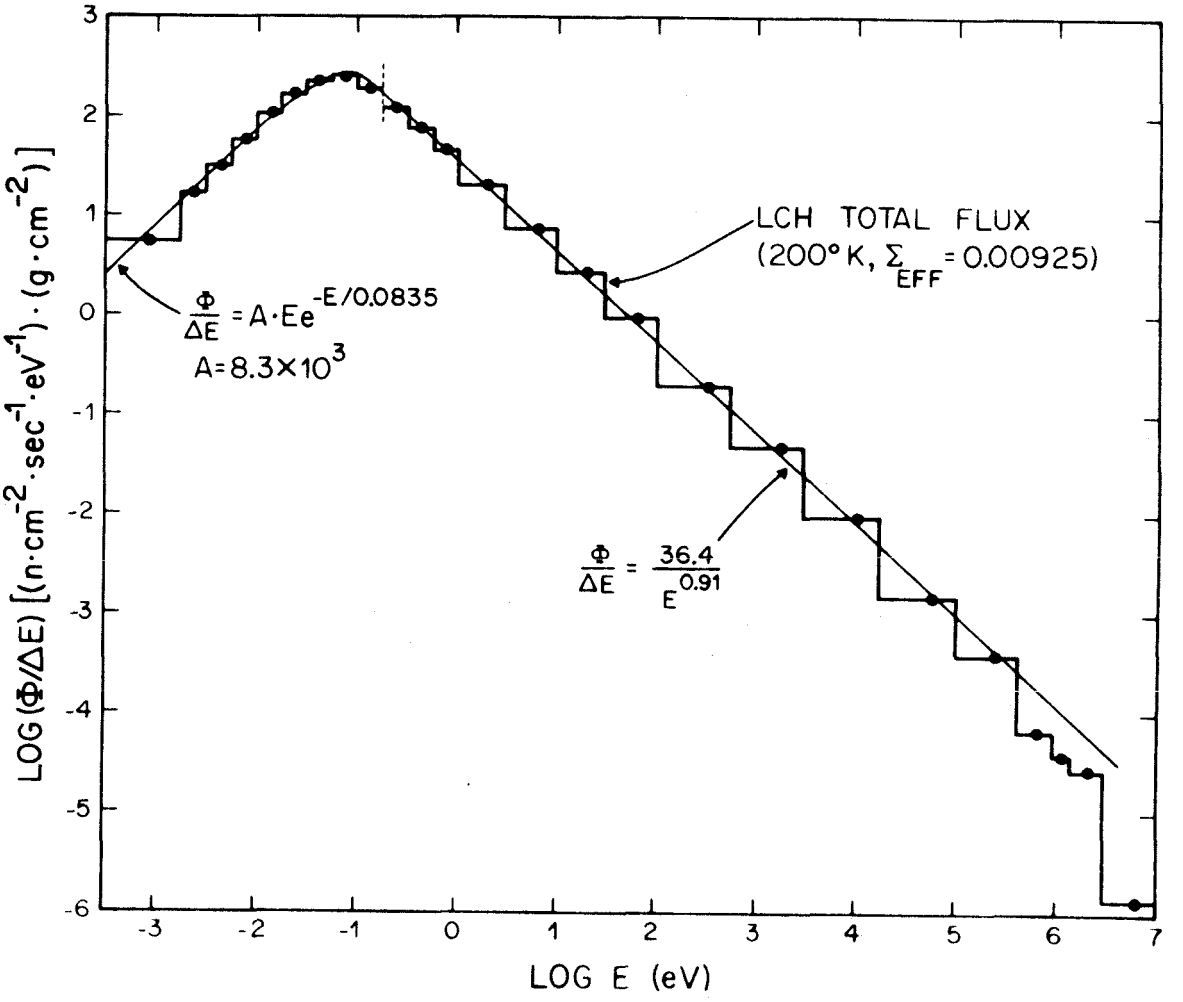

Figure 4-1

Fit of $Ee^{-E/kT}$ and $E^{-0.91}$ analytical functions to be LCH group fluxes. The circles mark the midpoints of the energy groups. The "LCH Total Flux" is the depth integrated flux under a cm^2 of the lunar surface calculated for a total production rate of 1 $n \cdot cm^{-2}$(column)$\cdot sec^{-1}$. The actual production rate is estimated to be 16 $n \cdot cm^{-2}$(column)$\cdot sec^{-1}$. The dashed vertical line at 0.18 eV indicates the point at which the two functional forms are joined.

energy than that of this Apollo 11 model; however, because the cross section for each group is evaluated separately and the production rate is calculated for the appropriate LCH flux in each group, such slight inadequacies in the description of the energy dependence of the flux within the groups is not important, and the group cross sections calculated for the assumed spectrum can be used for all of the samples studied.

The actual integration of the terms of equation 4.1-1 to obtain the group cross sections was accomplished by using a Simpson integration routine in the C.I.T. Fortran Library [7].

For those capture products for which it will be desirable to calculate fluences or production rates over an energy range encompassing several groups, an average cross section, $\langle\sigma\rangle_{a-b}$, can be defined where a-b indicates the energy region over which the cross section is to be averaged. This average cross section is simply

$$\langle\sigma\rangle_{a-b} = \sum_{g=i}^{j} \langle\sigma\rangle_g \phi_g \Big/ \sum_{g=i}^{j} \phi_g \qquad (4.1\text{-}3)$$

where the i^{th} group has a as its minimum energy and the j^{th} group has b as its maximum energy. Normally, this average cross section would be evaluated over the energy range in which the nuclide of interest had an appreciable capture rate. Because of the variation of the energy spectrum with chemical composition, which is important at energies below a few eV, it is important that the group fluxes appropriate to the composition of the sample be used to calculate average cross sections. These fluxes are provided by the LCH calculations.

4.2 $^{157}Gd(n,\gamma)^{158}Gd$

During the course of this work, several sets of group cross sections for this reaction have been evaluated. These values are displayed in Table 4-1. The sets labeled "BNL Res. Param." and "LCH Res. Param." were calculated from the resonance parameter data of BNL 325 [6] and LCH, respectively (except that it was necessary to correct the LCH values of I and J for a mistake in their table), according to the methods described in the previous section. These sets are in good agreement indicating that the slight differences in the parameters are not important. The set labeled "Canfield" was calculated by Canfield [8] from the LCH parameters (using the correct I and J values). These "Canfield" values are about 2% higher than those calculated in this work. However, they are probably more reliable because they include the contributions from higher energy resonances which were omitted in the calculations done in this work. The Canfield set of group cross sections will be adopted as the *true* set and used in the following discussions. A fourth set of group cross sections, labeled "Previously Used" in Table 4-1 was calculated earlier in this work from data which were less reliable. They are included here because they were used to calculate the fluences in Chapters 6-9. These fluences should be slightly revised as discussed below.

From the group cross sections and the LCH flux, one can show that most of the ^{157}Gd neutron absorption will occur between 0.02 and 0.10 eV and that $\geq$ 95% occurs below 0.178 eV (the upper boundary of LCH group 17).

Table 4-1

^{157}Gd Neutron Capture Group Cross Sections

LCH Group	E_{max} (eV)	σ_g (10^3 barns)			
		Previously Used	BNL[a] Res Param	LCH[a] Res Param	Canfield[b]
25	0.00178	931.	953.	958.	989.
24	0.00316	605.	624.	628.	641.
23	0.00562	466.	483.	486.	495.
22	0.0100	366.	381.	379.	390.
21	0.0178	296.	309.	311.	315.
20	0.0316	240.	251.	252.	255.
19	0.0562	171.	181.	181.	182.
18	0.100	81.2	85.3	85.7	86.4
17	0.178	23.7	24.9	45.0	25.4
16	0.316	5.49	5.68	5.70	5.84
15	0.562	1.20	1.24	1.24	1.28
14	1.00	0.268	0.279	0.280	0.287
13	3.00	0.126	0.138	0.137	0.136

[a] Includes contributions from the resonances at 0.0314 and 2.85 eV

[b] Includes contributions from 8 resonances with E_o < 26 eV.

The exact fraction captured below this energy is a function of the neutron energy spectrum which, in turn, depends on the macroscopic absorption cross section of the medium, Σ_{eff} (Sec. 3.2.2), and the temperature. The dependence of this fraction, f, on Σ_{eff} and temperature is shown in the top portion of Figure 4-2.

Using equation 4.1-3, the average cross section for ^{157}Gd neutron capture at E < 0.18 eV has been calculated for the Canfield group cross sections and the LCH energy spectrum. This average cross section is also a function of Σ_{eff} and temperature. At lower temperatures and lower absorber concentrations, the average cross section rises due to the higher fraction of neutrons near the low energy resonance (E_o = 0.0314 eV). This variation is shown in the lower part of Figure 4-2.

These values can then be used to calculate the fluence of neutrons with energies below 0.18 eV to which lunar samples have been exposed. Modifying equation 2.4-8, one has

$$\psi_{E<0.18eV} = \frac{f[(^{158}Gd/^{157}Gd)_C - (^{158}Gd/^{157}Gd)_T]}{\langle^{157}\sigma\rangle_{<0.18}\,[1 + (^{158}Gd/^{157}Gd)_C]} \qquad (4.2\text{-}1)$$

An internally-consistent set of fluences calculated from this formula or the analogous formula for normalized ratios, using the f and $\langle^{157}\sigma\rangle_{<0.18}$ values in Figure 4.2 at a temperature of 200°K will differ slightly from those calculated previously because of the change in group cross sections and because the value of the fraction of captures occurring below 0.18 eV was taken as unity in much of the earlier work. For these reasons, the fluences for all the

Figure 4-2

Fraction of the neutron captures by ^{157}Gd which occur below 0.18 eV and the average ^{157}Gd neutron capture cross section for energies below 0.18 as a function of Σ_{eff} and temperature. The +'s mark the points calculated from the LCH neutron spectra. The range of Σ_{eff} observed in lunar samples is $0.0045 < \Sigma_{eff} < 0.0135$.

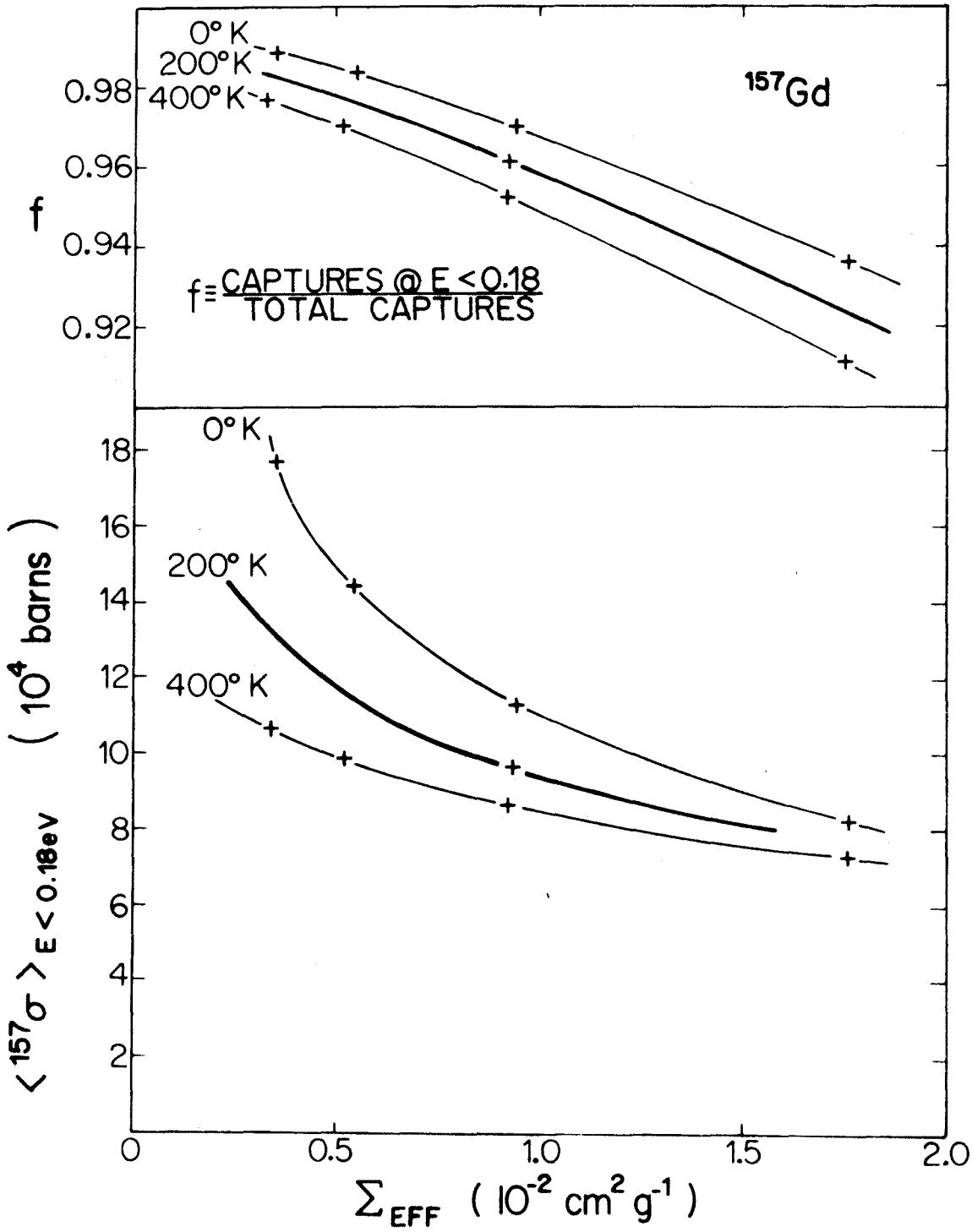
0° K
200° K
400° K
^{157}Gd
f
0.98
0.96
0.94
0.92
f ≡ CAPTURES @ E < 0.18 / TOTAL CAPTURES
0° K
200° K
400° K
$\langle ^{157}\sigma \rangle_{E<0.18eV}$ (10^4 barns)
18
16
14
12
10
8
6
4
2
0
0.5
1.0
1.5
2.0
Σ_{EFF} (10^{-2} cm^2 g^{-1})

Figure 4-2

samples analyzed in this laboratory and by Lugmair and Marti [9,10,11] have been re-evaluated. The revised fluences and the macroscopic cross section applicable to each sample are presented in Table 4-2. This re-evaluation lowers the fluences presented in Chapters 6-9 by $<10\%$. One should note that this is the first time the fluences reported by Eugster, Tera, Burnett, and Wasserburg [12] for Apollo 11 samples and those of Lugmair and Marti [9,10,11] have been interpreted in terms of the LCH calculations. These data will be discussed more fully in Chapter 5.

In that this is the first time the Lugmair and Marti data has been compared with the Lunatic Asylum data, it is worth noting that for the Apollo 11 and Apollo 12 samples, the fluences are in good agreement. For the Apollo 14 samples, however, the Lugmair and Marti data indicate slightly higher ($\sim 2 \times 10^{15}$ n/cm^2) fluences than the Asylum data. This systematic difference does not seem to arise from a shift in the Asylum data because samples of 10017 and the Norton County meteorite analyzed concurrently with the Apollo 14 samples and more recently, respectively, indicate the same fluences as calculated from the Eugster *et al.* [12,13] data collected 2-3 years earlier.

The rate of neutron capture by ^{157}Gd is a function of both the average cross section and the flux. Because both of these quantities increase with decreasing Σ_{eff}, the capture rate will vary more rapidly than the average cross section. This is illustrated by Figure 4-3.

In the papers presented in Chapters 7-9, comparisons of measured neutron fluences and calculated capture rates for ^{157}Gd have been used

Table 4-2

Neutron Fluence Revisited

Sample	$^{158}Gd/^{157}Gd$ [a]	Σ_{eff} ($10^{-2}cm^2g^{-1}$)	$\psi_{E<0.18eV}$ ($10^{16}n\cdot cm^{-2}$)
Apollo 11			
Soils			
10084,12 <37μm	1.59 ± 406 27	1.03	2.95 ± .11 [b]
10084*	1.59 ± 305 31	1.03†	2.55 ± .13
10004* top	1.59 ± 275 36	1.03	2.44 ± .13
10004* bottom	1.59 ± 286 40	1.03	2.47 ± .16
Rocks			
10017,32*	1.59 ± 847 41	1.03 (soil) [c] 1.34† (rock) [c]	4.66 ± .16 5.03 ± .17
10017,32	1.59 ± 848 14	1.03 (soil) 1.34† (rock)	4.66 ± .05 5.03 ± .06
10017,56#	-	1.03	4.71 ± .16
10017,T4,2#	-	1.03	4.55 ± .13
10040,30*	1.58 ± 681 31	1.03	<0.20
10050,24*	1.59 ± 257 26	1.03	2.36 ± .10
10057,39*	1.58 ± 733 17	1.03	0.29 ± .07
10057#	-	1.03	0.20 ± .03

Table 4-2 (Continued)

Sample	$^{158}Gd/^{157}Gd$ [a]	Σ_{eff} ($10^{-2}cm^2g^{-1}$)	$\psi_{E<0.18eV}$ ($10^{16}n\cdot cm^{-2}$)
10057,58#	-	1.03	0.18 ± .08
10058,20	1.58 887 ± 10	1.03	0.47 ± .04
10059,29*	1.59 190 ± 18	1.03	2.09 ± .07
10069,26*	1.58 674 ± 39	1.03	<0.21
10071,118*	1.58 962 ± 28	1.03	1.19 ± .11
10071,32#	-	1.03	1.28 ± .13
10085 Luny Rock I	1.59 074 ± 43	1.03	1.63 ± .17
Apollo 12			
Soils			
12042,34	1.59 251 ± 28	0.87	2.21 ± .11
12042,44 100-300μm	1.59 186 ± 12	0.87	1.97 ± .05
12042,44 <44μm	1.59 271 ± 23	0.87	2.28 ± .09
12042,44 Ace. Fl.	1.59 258 ± 28	0.87	2.24 ± .10
12070,5	1.59 201 ± 45	0.87†	2.02 ± .17
12033,102	1.59 195 ± 17	0.94†	2.06 ± .07
Double Core			
12025,22 (0.4-1.2) [d]	1.59 246 ± 34	0.87	2.19 ± .13
12025,34# (2.5-3.3)	-	0.87	2.05 ± .12

Table 4-2 (Continued)

Sample	$^{158}Gd/^{157}Gd$ [a]	Σ_{eff} ($10^{-2}cm^2g^{-1}$)	$\psi_{E<0.18eV}$ ($10^{16}n\cdot cm^{-2}$)
12025,56 (8.0-9.0)	1.59 243 ± 14	0.87	2.18 ± .05
12028,59 (12.0-12.8)	1.59 234 ± 35	0.87	2.15 ± .13
12028,77 (16.4-17.4)	1.59 246 ± 21	0.87	2.19 ± .08
12028,200# (25.4-26.1)	-	0.87	2.42 ± .12
12028,110A (28.8-30.0) (coarse)	1.59 225 ± 14	0.87	2.11 ± .05
12028,110B (28.8-30.0) (fine)	1.59 319 ± 17	0.87	2.47 ± .06
12028,110 (28.8-30.0) (total)	1.59 305	0.87	2.41
12028,161 (39.8-40.0)	1.59 303 ± 23	0.87	2.41 ± .09
12028,162# (39.8-40.0)	-	0.87	2.58 ± .10
Rocks			
12013,10-38 (light)	1.58 748 ± 18	0.87	0.33 ± .07
12013,10-01 (dark)	1.58 717 ± 22	0.87	0.21 ± .08
12002,147	1.58 953 ± 22	0.87	1.10 ± .08
12002,29-2A	1.58 947 ± 42	0.87	1.07 ± .16
12002,29-D2	1.58 941 ± 36	0.87	1.05 ± .13
12002,29-E	1.58 954 ± 23	0.87	1.10 ± .09
12002# bottom	-	0.87	1.12 ± .07

Table 4-2 (Continued)

Sample	$^{158}Gd/^{157}Gd$	Σ_{eff} ($10^{-2}cm^2g^{-1}$)	$\psi_{E<0.18eV}$ ($10^{16}n\cdot cm^{-2}$)
12009,34#	-	0.87	1.49 ± .07
12018,39#	-	0.87	1.68 ± .15
12021,61#	-	0.87	1.55 ± .05
12052,85#	-	0.87	1.54 ± .08
12053,37#	-	0.87	1.86 ± .06
12063,64#	-	0.87	1.15 ± .08
Apollo 14			
Soils			
14163,110	1.59 432 ± 14	0.86†	2.90 ± .05
14259,97	1.59 391 ± 11	0.86	2.74 ± .05
14163,95#	-	0.86	3.09 ± .09
14259,58#	-	0.86	3.00 ± .09
14141,22 <150μm	1.58 739 ± 48	0.86	0.30 ± .18
Rocks			
14310,88	1.59 355 ± 14	0.86 (soil) 0.74† (rock)	2.59 ± .05 2.49 ± .05
14310,100	1.59 412 ± 68	0.86 (soil) 0.74† (rock)	2.82 ± .25 2.71 ± .24

Table 4-2 (Continued)

Sample	$^{158}Gd/^{157}Gd$	Σ_{eff} ($10^{-2}cm^2g^{-1}$)	$\psi_{E<0.18eV}$ ($10^{16}n\cdot cm^{-2}$)
14321,161	1.58 653 ± 15	0.86	<0.03
14310,47#	-	0.86	2.93 ± .08
14321,FM3#	-	0.86	<0.14
14160,3#	-	0.86	2.26 ± .07
14160,4#	-	0.86	4.18 ± .07
14160,6#	-	0.86	1.88 ± .08
14160,8#	-	0.86	0.64 ± .09
14160,10#	-	0.86	1.86 ± .06
Luna 16			
Luna 16 G-2	1.60 120 ± 39	0.83†	5.39 ± .15
Apollo 15 Soils			
15221,46	1.59 680 ± 18	0.66§	3.54 ± .07
15231,47	1.59 687 ± 18	0.66§	3.56 ± .07
15601,65	1.59 668 ± 23	0.80†	3.71 ± .08
15041,54	1.59 546 ± 22	0.76§	3.20 ± .07
Drill Stem			
15006,27	1.59 659 ± 29	0.76	3.62 ± .10
15005,222	1.59 850 ± 14	0.76	4.31 ± .05

Table 4-2 (Continued)

Sample	$^{158}Gd/^{157}Gd$	Σ_{eff} ($10^{-2}cm^2g^{-1}$)	$\psi_{E<0.18eV}$ ($10^{16}n\cdot cm^{-2}$)
15005,26	1.59 984 ± 32	0.77	4.79 ± .12
15004,27	1.60 068 ± 22	0.77†	5.11 ± .07
15003,29	1.59 944 ± 24	0.78	4.68 ± .07
15002,27	1.59 748 ± 34	0.79	3.98 ± .12
15001,31	1.59 604 ± 15	0.80†	3.49 ± .05
Rocks			
15595,20	1.58 890 ± 24	0.80	0.85 ± .09
15595,19	1.58 913 ± 26	0.80	0.94 ± .10
Apollo 16			
Soils			
60501,31	1.60 461 ± 18	0.46§	5.62 ± .06
Drill Stem			
60007,115	1.60 457 ± 56	0.46	5.60 ± .17
60007,108	1.60 400 ± 27	0.46	5.43 ± .09
60006,8	1.60 588 ± 42	0.46†	6.01 ± .13
60004,23	1.61 093 ± 22	0.46	7.58 ± .06
60004,14	1.61 307 ± 34	0.46	8.24 ± .11
60003,10	1.61 258 ± 49	0.46	8.09 ± .15

Table 4-2 (Continued)

Sample	$^{158}Gd/^{157}Gd$	Σ_{eff} ($10^{-2}cm^2g^{-1}$)	$\psi_{E<0.18eV}$ ($10^{16}n\cdot cm^{-2}$)
60001,8	1.61 622 ± 21	0.46†	9.20 ± .06
Meteorites			
Norton County*	1.59 093 ± 60	0.24†	1.14 ± .16
Norton County	1.59 126 ± 19	0.24†	1.23 ± .05
Allende	1.58 676 ± 20	0.81†	<0.14

*Data from Eugster *et al.* [12,13].

#Data from Lugmair and Marti [9,10,11]. The Lugmair and Marti $^{158}Gd/^{157}Gd$ ratios are not directly comparable to our data because of mass interferences (see [10]).

†Samples for which Σ_{eff}'s were calculated directly. Unmarked samples were assigned Σ_{eff} values. The following major elements, arranged in approximate order of decreasing importance, were included in the calculation of Σ_{eff}: Fe, Ti, Si, Ca, Al, Mn, Mg, Cr, Na, K, and O. The trace elements included were Gd, Sm, and Eu. The contributions of these trace elements to Σ_{eff} can be calculated from the data given in Table 6 of LCH. The procedure used to calculate Σ_{eff} is to sum the 2200 m/sec Σ_a's for the individual major elements; then to add the appropriate contributions for the rare earths as determined from the values of Table 6 of LCH. Because the contribution for the rare earths varies with Σ_{eff}, the appropriate values must be obtained by successive approximations of Σ_{eff}.

§Samples for which Σ_{eff}'s were calculated from compositions of soils collected nearby.

(a) Corrected for false discrimination. Uncertainties are $2\sigma_{mean}$.

(b) Uncertainty calculated from the uncertainty in ($^{158}Gd/^{157}Gd$) of the sample only. The uncertainties in the cross section (~10%) and the terrestrial ratio are not included.

(c) "Soil" indicates Σ_{eff} and ψ values expected for a small rock irradiated in the soil found at this site; whereas "rock" indicates the Σ_{eff} and ψ applicable if the rock was irradiated in material of its own chemical composition.

(d) Depth in core tube in cm.

Addendum to Table 4-2

Sources of Chemical Composition Data Used for Calculating Σ_{eff}

Sample	Major Elements	Rare Earths
10017 and 10084	Wiik and Ojanpera [20]	Gast and Hubbard [48]
12033	Goles *et al.* [49]	Hubbard and Gast [36]
12070	Cuttitta *et al.* [50]	Schnetzler and Philpotts [37]
14163 and 14310	Hubbard and Gast [51]	Hubbard and Gast [51]
Luna 16	Gillum *et al.* [52]	N. J. Hubbard *et al.* [53]
15221 and 15231 (15101)*	Apollo 15 Preliminary Investigation Team [54]	N. J. Hubbard (pers. comm.)
15601	Apollo 15 Preliminary Investigation Team [54]	Helmke and Haskin [55]
15041 (15021)*	Apollo 15 Preliminary Investigation Team [54]	N. J. Hubbard (pers. comm.)
15004 and 15001	M. Rhodes (pers. comm.)	J. Philpotts (pers. comm.)
60501 (60600)*	Apollo 16 Preliminary Investigation Team [56]	same as 60001
60001	Nava and Philpotts [57]	Philpotts *et al.* [58]
60006	Nava and Philpotts [57]	estimated
Norton County	Beck and La Paz [59]	Schmitt *et al.* [60]
Allende	Clarke *et al.* [61]	Clark *et al.* [61]

*Sample numbers in parentheses refer to the samples whose chemical compositions were used to calculate Σ_{eff}, *e.g.*, Σ_{eff} for 15221 and 15231 was calculated by assuming these samples had the same chemical composition as 15101.

Figure 4-3

Average ^{157}Gd neutron capture rate in the upper 1155 g/cm^2 of the lunar surface as a function of Σ_{eff} and temperature. The total number of neutrons produced under a cm^2 of lunar surface is assumed to be 1 $n \cdot sec^{-1} \cdot cm^{-2}$. The X's mark the points calculated from the LCH depth integrated fluxes and the group cross sections of Canfield (Table 4-1). The depth integrated capture rate was divided by the total depth considered in the LCH calculations, *i.e.*, 1155 g/cm^2, to obtain the average capture rate over that depth.

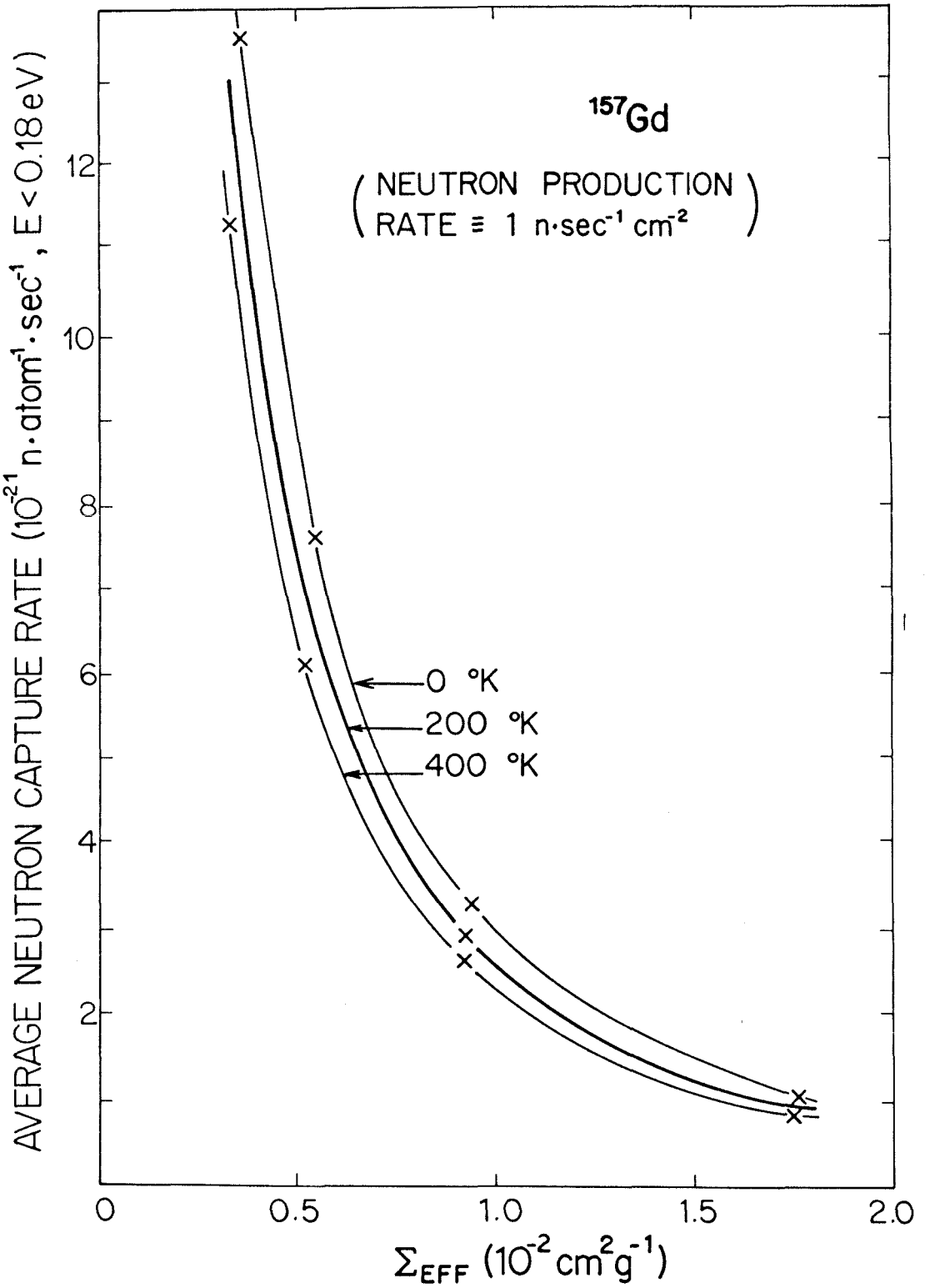
157Gd
(NEUTRON PRODUCTION
RATE ≡ 1 n·sec⁻¹ cm⁻²)
0 °K
200 °K
400 °K
AVERAGE NEUTRON CAPTURE RATE (10⁻²¹ n·atom⁻¹·sec⁻¹, E<0.18 eV)
ΣEFF (10⁻² cm² g⁻¹)
0
0.5
1.0
1.5
2.0
2
4
6
8
10
12

Figure 4-3

to model the depositional history of the regolith. Because these calculations were made using the "Previously Used" group cross sections, one would expect that the conclusions would be altered by this re-evaluation of the cross section. This is not the case, however, because the model calculations were carried out in such a way that the effect of the change in cross section cancels to within ~ 2%. The discussions of regolith history are therefore essentially unaffected by the revision of the fluences.

4.3 $^{155}Gd(n,\gamma)^{156}Gd$

The cross section for ^{155}Gd is dominated by a resonance near 0.03 eV (E_o = 0.0268) as was the case for ^{157}Gd. Therefore, the ratio of $^{155}\sigma(E)$ to $^{157}\sigma(E)$ is roughly constant. Throughout this work $\langle^{155}\sigma\rangle$ has been taken as 0.24 × $\langle^{157}\sigma\rangle$ [13].

4.4 $^{149}Sm(n,\gamma)^{150}Sm$

Group cross sections for this reaction have been calculated by Canfield [8] and in this work (Table 4-3), and the values derived from the two calculations are in good agreement. For subsequent calculations, the Canfield values will be adopted.

The capture cross section of ^{149}Sm is dominated by a resonance near 0.1 eV. This is appreciably above the energy of the major ^{157}Gd resonance (Fig. 4-4); therefore, because these nuclides capture in different energy ranges, the ratio of the number of neutrons captured per atom by Sm to the number captured per atom by Gd is an indicator of

Table 4-3

^{149}Sm Neutron Capture Group Cross Sections

LCH Group	E_{max} (eV)	σ_g (10^3 barns)	
		Canfield	LCH Res. Param
25	0.00178	116.	113.
24	0.00316	75.8	74.1
23	0.00562	59.0	57.7
22	0.0100	47.4	46.3
21	0.0178	40.4	39.4
20	0.0316	38.7	37.7
19	0.0562	48.4	46.7
18	0.100	94.2	93.2
17	0.178	50.9	50.8
16	0.316	4.80	4.63
15	0.562	0.780	0.759
14	1.00	3.66	3.65
13	3.00	0.108	0.100
12	10.0	0.360	0.379
11	30.0	0.001	0.001

Figure 4-4

^{157}Gd and ^{149}Sm neutron capture cross sections as a function of energy. The ^{157}Gd cross section has a large resonance at 0.03 eV. The ^{149}Sm cross section is dominated by a resonance at 0.096 eV. The shape of the LCH spectrum for lunar neutrons at the Apollo 11 site indicates that the spectrum peaks between the ^{157}Gd and ^{149}Sm resonances; therefore, the ratio of the amount of ^{157}Gd neutron capture to that for ^{149}Sm should be a sensitive indicator of variations in the spectral shape.

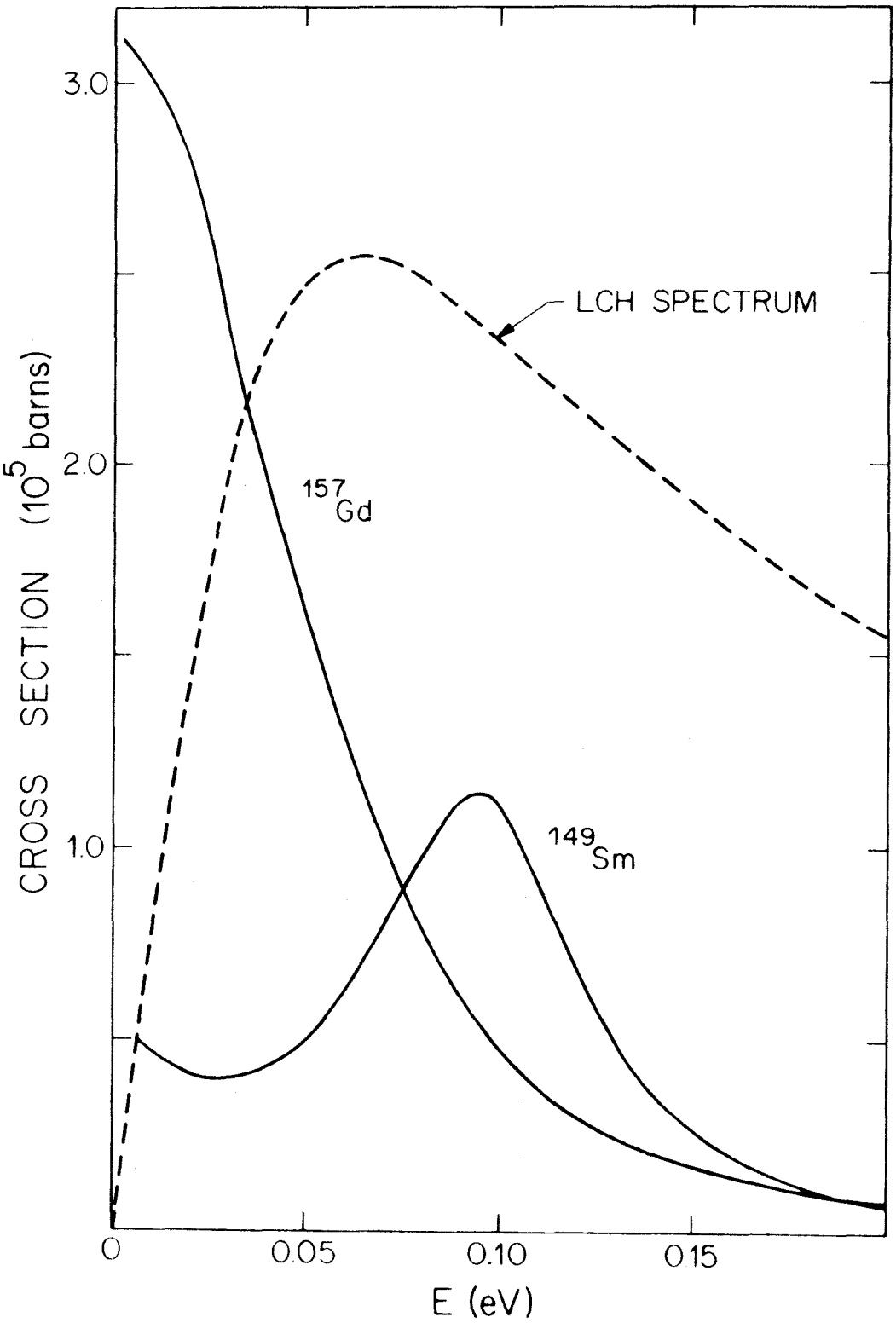
3.0
2.0
1.0
CROSS SECTION (10^5 barns)
LCH SPECTRUM
^{157}Gd
^{149}Sm
0
0.05
0.10
0.15
E (eV)

Figure 4-4

the energy spectrum of the low energy neutron flux. This ratio, which can be determined experimentally as described in Chapter 6, is just the ratio $\langle {}^{149}\sigma \rangle_\infty / \langle {}^{157}\sigma \rangle_\infty$ where the subscript ∞ indicates that the average is carried over all energies. From equation 4.1-3, it can be seen that this ratio is equivalent to the ratio of the production rates,

$$\langle {}^{149}\sigma \rangle_\infty \Big/ \langle {}^{157}\sigma \rangle_\infty = \sum_{g=1}^{\infty} \langle {}^{149}\sigma \rangle_g \phi_g \Big/ \sum_{g=1}^{\infty} \langle {}^{157}\sigma \rangle_g \phi_g$$

For the LCH spectrum, most of the capture by ^{149}Sm ($\sim$ 75%) occurs in the energy range 0.056-0.18 eV (groups 17 and 18), and greater than 99% occurs below 1 eV except at high values of Σ_{eff}. For this reason, it is sufficient to average the cross sections only below 1 eV. The average ^{157}Gd and ^{149}Sm cross sections below this energy as a function of Σ_{eff} are displayed in Figure 4-5.

The Σ_{eff} dependence of the ratio of these calculated cross sections, $\varepsilon_{Sm}/\varepsilon_{Gd}$, is shown by the curves in Figure 4-6. As the concentration of absorbers is increased, *i.e.*, larger Σ_{eff}, the $\varepsilon_{Sm}/\varepsilon_{Gd}$ rises due to the higher energy of the spectrum. This version of the $\varepsilon_{Sm}/\varepsilon_{Gd}$ plot differs from that in Chapter 9 because the Canfield group cross sections for Gd were used in this version. The effect of this change is to lower the predicted $\varepsilon_{Sm}/\varepsilon_{Gd}$ values ~ 9%.

For the experimental lunar points, which are discussed in Section 9.4.1, $\varepsilon_{Sm}/\varepsilon_{Gd}$ increases with increasing Σ_{eff} as expected, but the values are all higher than predicted by LCH. Assuming the resonance parameters for the cross sections are correct, this implies that the

Figure 4-5

^{149}Sm and ^{157}Gd capture cross sections averaged over the range $0 \leq E \leq 1.0$ eV as a function of Σ_{eff} and temperature. The +'s indicate the calculated points to which the curves were fitted.

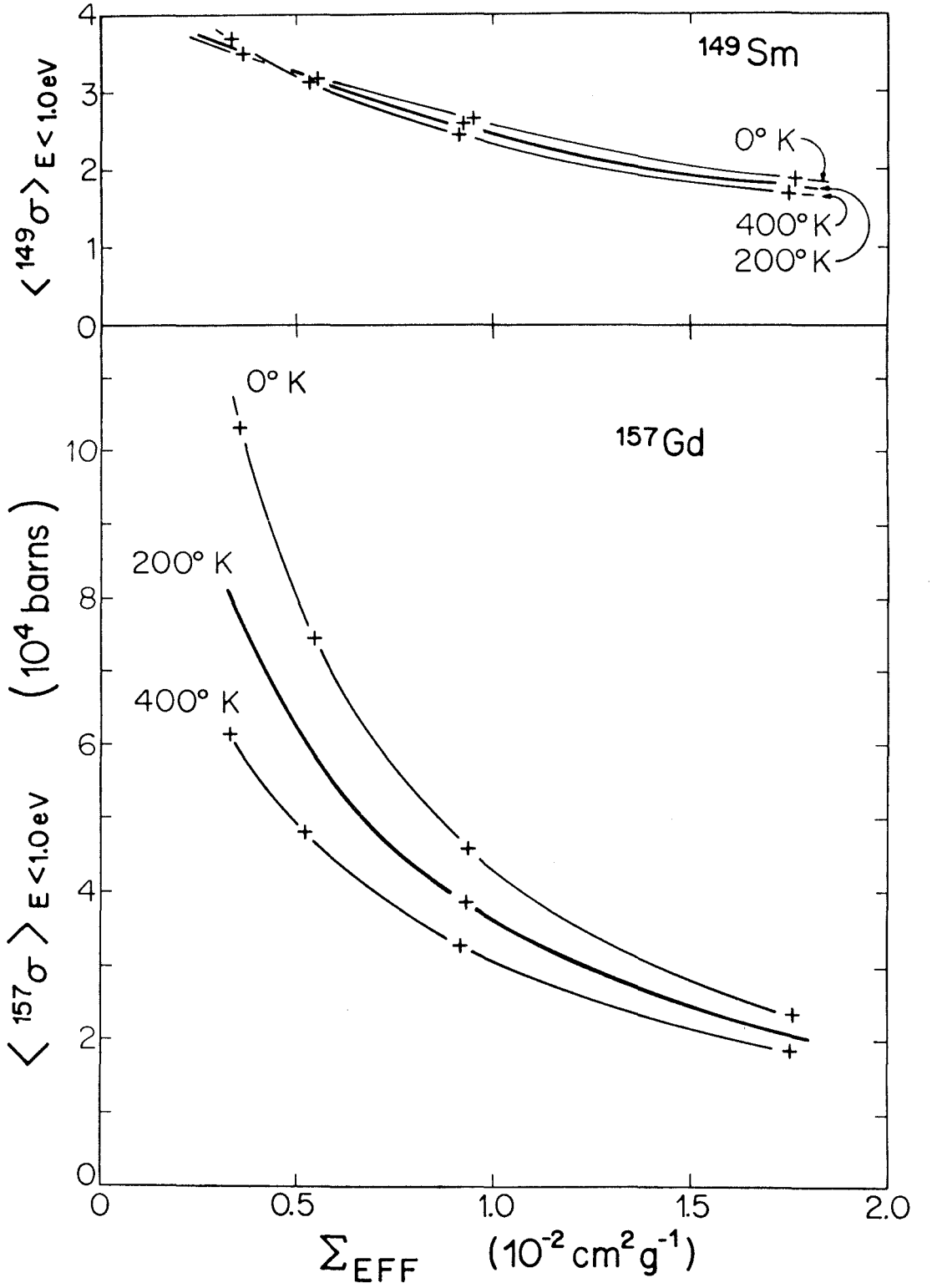
149Sm
0° K
400° K
200° K
157Gd
0° K
200° K
400° K
⟨149σ⟩ E<1.0eV
⟨157σ⟩ E<1.0eV (10⁴ barns)
ΣEFF (10⁻² cm² g⁻¹)
0
0.5
1.0
1.5
2.0
1
2
3
4
6
8
10

Figure 4-5

Figure 4-6

Predicted and measured variation of $\varepsilon_{Sm}/\varepsilon_{Gd}$ as a function of Σ_{eff} and temperature. The data imply a somewhat higher energy spectrum than that calculated by LCH for lunar materials at a temperature of 200°K, but variation of $\varepsilon_{Sm}/\varepsilon_{Gd}$ with Σ_{eff} is similar to that predicted. The Norton County meteorite appears to have been irradiated at a lower temperature than the lunar samples.

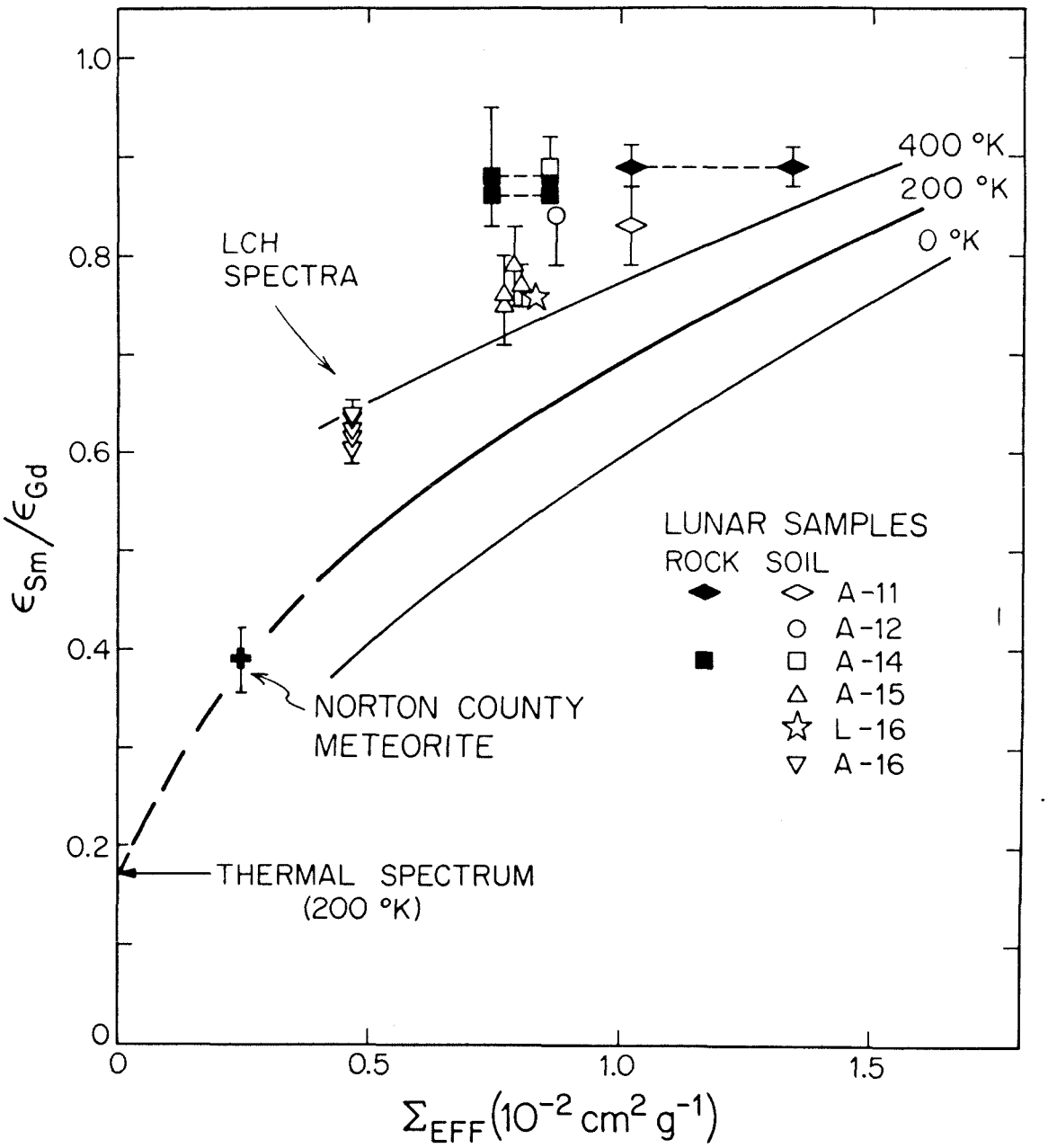
1.0
0.8
0.6
0.4
0.2
0
0
0.5
1.0
1.5
$\epsilon_{Sm}/\epsilon_{Gd}$
$\Sigma_{EFF}(10^{-2}\,cm^2\,g^{-1})$
400 °K
200 °K
0 °K
LCH
SPECTRA
NORTON COUNTY
METEORITE
THERMAL SPECTRUM
(200 °K)
LUNAR SAMPLES
ROCK SOIL
A-11
A-12
A-14
A-15
L-16
A-16

Figure 4-6

lunar neutron spectrum is somewhat more energetic than predicted and that the fluences calculated from the Gd data are somewhat low. This point will be discussed further in Section 4.16.

The resonance parameters used by Canfield [8] and those preferred by BNL 325 for ^{149}Sm are based on the work of Marshak and Sailor [14]. The measurements of Pattenden [15] indicate a cross section which is $\sim$ 6% higher than the Marshak and Sailor value. If the Pattenden value is more nearly correct than that of Marshak and Sailor, $\sim \frac{1}{2}$ of the discrepancy between the measured and predicted $\varepsilon_{Sm}/\varepsilon_{Gd}$ ratios could be explained.

4.5 $^{151}Eu(n,\gamma)^{152}Eu \nearrow (\beta^-)^{152}Gd$ $\searrow (\beta^+)^{152}Sm$

The cross section for ^{151}Eu capture is dominated by resonances at 0.321 and 0.460 eV and a bound state. Because an appreciable fraction of the captures by this isotope occur around 0.4 eV, measurements of excess ^{152}Gd or ^{152}Sm provide an additional test of the LCH spectrum.

The contribution of the bound state to the cross section cannot be determined from the BNL 325 or LCH resonance parameters; therefore the group cross sections for groups 17-25 (Table 4-4) were simply estimated from the plot of $\sigma(E)$ in BNL 325. For groups 11-16, the cross sections (Table 4-4) were calculated from the BNL 325 resonance parameters in the usual way. In the region where the resonances control the cross section, the group cross sections calculated from the BNL parameters, the LCH parameters, and by Canfield, are in good agreement.

Table 4-4

^{151}Eu Neutron Capture Group Cross Sections

LCH Group	E_{max} (eV)	σ_g (10^3 barns)
25	0.00178	50.
24	0.00316	38.5
23	0.00562	29.4
22	0.0100	21.3
21	0.0178	14.9
20	0.0316	9.01
19	0.0562	5.14
18	0.100	2.80
17	0.178	1.88
16	0.316	2.53
15	0.562	11.2
14	1.00	0.953
13	3.00	0.419
12	10.0	0.520
11	30.0	0.001

As discussed in Section 2.6, there seems to be a correlation between increases in the $^{158}Gd/^{157}Gd$ ratio and the $^{152}Gd/^{160}Gd$ ratio. One would therefore like to calculate the correlation line predicted from the LCH energy spectrum for neutron capture by ^{151}Eu and ^{157}Gd. Because the $^{158}Gd/^{157}Gd$ neutron effect has been described in terms of a fluence of neutrons with $E < 0.18$ eV, it is convenient to use this fluence to calculate the predicted change in the $^{152}Gd/^{160}Gd$. This has been accomplished by evaluating the average cross section for ^{151}Eu over this energy region and by calculating what fraction of the ^{151}Eu captures occur at $E < 0.18$ eV. These quantities, which are a function of the macroscopic cross section of the medium, are displayed in Figure 4-7. One must also know the branching ratio for the decay of ^{152}Eu to ^{152}Gd and ^{152}Sm. This ratio was taken to be the same as the ratio of the thermal cross sections for the production of these two products by ^{151}Eu capture. ^{152}Gd is predicted by this treatment to result from $\sim 45\%$ of the ^{152}Eu decays [6]. The error in this assumption is difficult to estimate because there is a metastable isomer of ^{152}Eu which has a different branching ratio than the ground state [16].

The only samples which have shown a clear excess in the $^{152}Gd/^{160}Gd$ ratio are those from Apollo 16 and Luna 16. No evidence for excess ^{152}Sm was obtained, but the larger normal ^{152}Sm abundance makes the excess more difficult to detect. The possibility that the Apollo 16 ^{152}Gd excesses are due to ^{151}Eu capture is discussed in Section 9.4.2 (also see Fig. 9-4). If they are due to ^{151}Eu capture then, because the excess is larger than predicted from the $^{158}Gd/^{157}Gd$ ratios in the

Figure 4-7

Function of the neutron captures by ^{151}Eu which occur at energies below 0.18 eV and the average ^{151}Eu capture cross section in the region $0 \leq E \leq 0.18$ as a function of Σ_{eff} and temperature. The +'s indicate the calculated points.

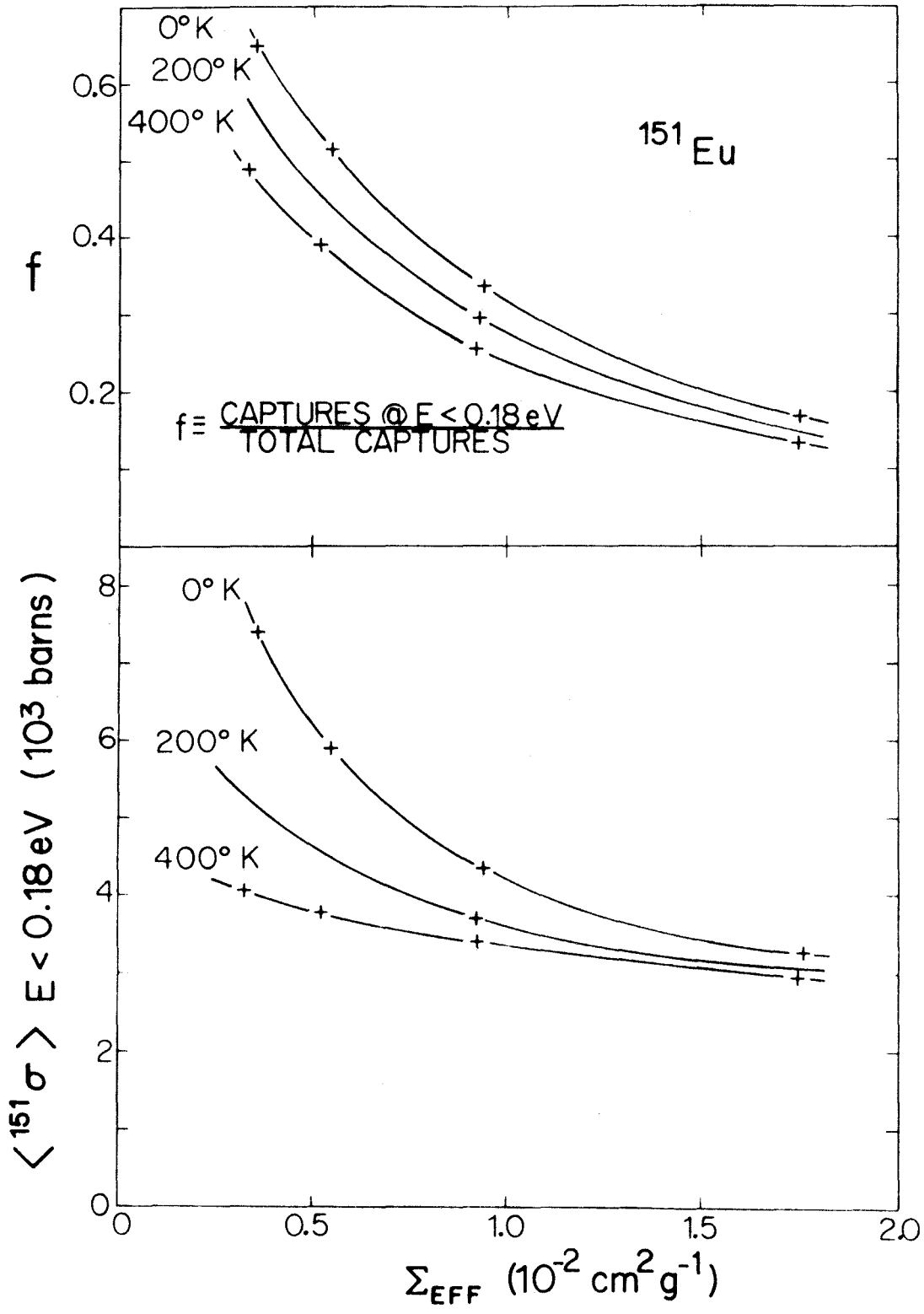
0° K
200° K
400° K
^{151}Eu
f
f ≡ CAPTURES @ E < 0.18 eV / TOTAL CAPTURES
$\langle^{151}\sigma\rangle$ E < 0.18 eV (10^3 barns)
Σ_{EFF} (10^{-2} cm^2 g^{-1})

Figure 4-7

same samples, the neutron energy spectrum must be more energetic than predicted by LCH. This is in agreement with the $\varepsilon_{Sm}/\varepsilon_{Gd}$ results presented in the previous section.

4.6 $^{59}Co(n,\gamma)^{60}Co$

This reaction provides one of the few checks on the magnitude of the neutron flux (as opposed to fluence) because of the relatively short half-life of ^{60}Co (5.2 yr). The cross section is dominated by a resonance at E_o = 132 eV and the reaction rate is essentially independent of the chemical composition of the sample. This is true because above ~10 eV absorption is relatively unimportant, and the energy spectrum and flux are determined by the scattering cross section which remains essentially constant over the range of lunar compositions.

Group cross sections (Table 4-5) were calculated from the BNL 325 parameters. According to these calculations, ~ 70% of the ^{59}Co capture occurs between 100 and 550 eV (group 9). Wahlen, Finkel, Imamura, Kohl, and Arnold [17] reached a different conclusion but have since revised their calculations and are now in approximate agreement with this work [18]. The low energy group cross sections calculated here are slightly low compared with the accepted value of 37 barns [6] at 0.025 eV, but this is not significant because only a small fraction of the capture occurs at low energy. Using the group cross sections from Table 4-5 and the LCH fluxes, a ^{60}Co production rate of 2.34×10^{-23}(captures)·(atom·sec)$^{-1}$ is calculated for the upper 2 g/cm^2 of the lunar regolith. In the depth interval of 20-33 g/cm^2, the production rate is calculated

Table 4-5

^{59}Co Neutron Capture Group Cross Sections

LCH Group	E_{max} (eV)	σ_g (barns)
25	1.78×10^{-3}	132.
24	3.16×10^{-3}	84.4
23	5.62×10^{-3}	63.4
22	1.00×10^{-2}	47.5
21	1.78×10^{-2}	35.7
20	3.16×10^{-2}	26.8
19	5.62×10^{-2}	20.2
18	1.00×10^{-1}	15.2
17	1.78×10^{-1}	11.5
16	3.16×10^{-1}	8.69
15	5.62×10^{-1}	6.54
14	1.00	4.93
13	3.00	3.31
12	1.00×10^{1}	1.98
11	3.00×10^{1}	1.36
10	1.00×10^{2}	2.25
9	5.50×10^{2}	29.3
8	3.00×10^{3}	0.003

to be 1.10×10^{-22}. Because of the short ^{60}Co half-life, one would expect the activity of ^{60}Co in a lunar sample to be in equilibrium with the production rate. The activities for the two depth intervals given above should therefore be 14 and 70 dpm/g(Co) respectively.

O'Kelly, Eldridge, Schonfeld, and Bell [19] reported a ^{60}Co activity of 1.1 ± 0.8 dpm/kg (rock) in rock 10017 which has a cobalt concentration of 30 ppm [20]. Taking the cobalt concentration into account, this gives an activity of 37 ± 27 dpm/g(Co) for this rock which is ~ 5 cm thick. Taking the density of the rock as 3, one would expect the ^{60}Co activity for the whole rock to be between the calculated surface value and the value calculated at 15 g/cm^2 if the LCH flux is correct. Although the errors are large, the measured activity is in good agreement with that predicted. Recent measurements by Wahlen *et al.* [17] show surface soil 10084 to have an activity of 17 ± 8 dpm/g(Co) and rock 14321 to have 26 ± 18 dpm/g(Co). They have also measured ^{60}Co activities in samples from the Apollo 15 drill stem. These activities roughly follow the depth dependence predicted by LCH and are consistent with a surface activity of ~ 15 dpm/g(Co).

Although the errors associated with these measurements are large, the activities seem to be in agreement with those predicted by LCH. This agreement implies that if the spectrum is somewhat harder than predicted as was indicated by the $\varepsilon_{Sm}/\varepsilon_{Gd}$ data and by the ^{152}Gd data, this deviation from the predicted spectrum is restricted to the low energy region, or at least that the deviation does not become significantly more pronounced at higher energies.

4.7 $^{113}Cd(n,\gamma)^{114}Cd$

It has been predicted by LCH that because of the large resonance at E_o = 0.178 eV, it should be possible to measure neutron capture effects in lunar cadmium. Although there are no experimental data on the isotopic composition of cadmium in lunar samples, ^{113}Cd group sections were evaluated (Table 4-6). These group cross sections were used to calculate the ^{113}Cd capture rate which would be predicted at the peak of the neutron flux in material of the composition of the Apollo 11 soil at a temperature of 200°K. This rate is calculated to be 2.5×10^{-3} (neutrons)·(atoms)$^{-1}$·(10^9yr)$^{-1}$ which is in agreement with the value of $\sim 2.5 \times 10^{-3}$ given by LCH.

4.8 $^{79}Br(n,\gamma)^{80}Kr$ $^{81}Br(n,\gamma)^{82}Kr$

Lugmair and Marti [10,11,21] have reported excess ^{80}Kr and ^{82}Kr in Apollo 14 rocks which they attribute to the capture of resonance energy neutrons ($\sim$ 10-1000 eV) by ^{79}Br and ^{81}Br. From the group cross sections of Canfield [8] and the LCH fluxes, one can estimate that for both of these reactions >95% of the captures occur between 30 and 550 eV (groups 9 and 10). Because the capture is essentially restricted to two of the LCH energy groups in the resonance region where changes in Σ_{eff} are not important, group cross sections for Br capture were not evaluated explicitly in this work. However, following the procedure described for Sm (Sec. 4.4), the cross section ratio $\langle^{79}\sigma\rangle_\infty / \langle^{81}\sigma\rangle_\infty$ was calculated for the $E^{-0.91}$ spectrum (Sec. 4.1). The average cross

Table 4-6

^{113}Cd Neutron Capture Group Cross Sections

LCH Group	E_{max} (eV)	σ_g(10^3 barns)
25	0.00178	77.0
24	0.00316	50.1
23	0.00562	38.3
22	0.0100	29.8
21	0.0178	23.9
20	0.0316	20.3
19	0.0562	19.3
18	0.100	23.5
17	0.178	46.4
16	0.316	29.9
15	0.562	2.59
14	1.00	0.340
13	3.00	0.0377

section $\langle^{79}\sigma\rangle_{30-550}$ was also evaluated for this spectrum for both the LCH and BNL 325 resonance parameters. The ratio $\langle^{79}\sigma\rangle_\infty/\langle^{81}\sigma\rangle_\infty$ is calculated to be 2.28 for the LCH parameters or 2.46 for those of BNL 325. An independent check on this ratio can be obtained from the ratio of experimentally determined resonance integrals for ^{79}Br and ^{81}Br. Ryves [22] has measured both of these resonance integrals. From his values, the ratio of the resonance integrals is calculated to be 2.5. Because he has measured both integrals relative to the same standard, this ratio should be more reliable than comparing values from different workers even if his absolute values are not correct.

Lugmair and Marti [11] report on excess ^{80}Kr/^{82}Kr ratio of 2.69 ± 0.28 as the best fit to their data for several Apollo 14 rocks. This implies $\langle^{79}\sigma\rangle_\infty/\langle^{81}\sigma\rangle_\infty = 2.84 \pm 0.30$ when the differences in isotopic abundances and the branching ratio of ^{80}Br decay are taken into account.

The BNL 325 resonance parameters yield the ratio in best agreement with the experimental value; therefore, they have been used to calculate a $\langle^{79}\sigma\rangle_{30-550}$ value of 32.2 barns. (The LCH parameters give $\langle^{79}\sigma\rangle_{30-550}$ = 31.1 barns). This cross section can be used to calculate the ^{80}Kr production rate. In the depth interval from 139-165 g/cm^2 in which the neutron flux is at its maximum, one calculates that in the energy range 30-550 eV, 9.0×10^{-6} ^{80}Kr atoms are produced per ^{79}Br atom per 10^9 years or that about 9.5×10^{-6} ^{80}Kr atoms/(^{79}Br atoms$\cdot 10^9$ yr) are produced over all energies. This is in agreement with the LCH value of 9.5×10^{-6} in the same units. This cross section can also be used to calculate 30-550 eV fluences, and these values can be compared to the fluences predicted for this energy region from

the LCH energy spectrum and the fluences measured by ^{158}Gd. In principle this provides a check of the LCH energy spectrum over a wider energy range than was possible with the rare earth elements discussed above.

To compare the Gd and Kr effects, the ratio of the flux in the $30 \leq E \leq 550$ eV range to the flux in the range $0 \leq E \leq 0.18$ eV must be known as a function of the absorbing properties of the sample, the temperature, and the depth. As shown in the upper portion of Figure 4-8, this ratio can vary by a factor of two with depth for material with a Σ_{eff} value and temperature typical of the lunar samples. In order to illustrate the variation of the ratio of the resonance energy to low energy flux as a function of Σ_{eff}, it is most convenient to average out the depth variation by using the total flux under a square centimeter of surface. This has been done in the lower portion of Figure 4-8 where $\Phi_{30-550}/\Phi_{<0.18}$ has been plotted as a function of Σ_{eff} for the 400° and 0°K calculations of LCH. These curves are seen to intersect near $\Sigma_{eff} = 0.09$.

The reason for this intersection is not completely clear. One might expect that at any given Σ_{eff} the ratio $\Phi_{30-550}/\Phi_{<0.18}$ should be larger for a high temperature than for a low one. This is because at higher temperatures more neutrons would have energies greater than 0.18 eV while the flux between 30 and 550 eV would remain constant. Above $\Sigma_{eff} = 0.01$ this is the relationship predicted by LCH, and it must be true at $\Sigma_{eff} = 0$ where there is no absorption. The reversal predicted by LCH may indicate that in this region the effect of absorption is stronger on the low temperature spectrum than on the higher temperature

Figure 4-8

Top: Ratio of the neutron flux in the range $30 \leq E \leq 550$ eV to the flux with $E < 0.18$ eV as a function of depth.

Bottom: Depth averaged ratio of the 30-550 eV flux to the $E < 0.18$ eV flux as a function of Σ_{eff} and temperature. The +'s indicate the calculated points. The 200°K curve is dotted because its extrapolation from the calculated point is uncertain.

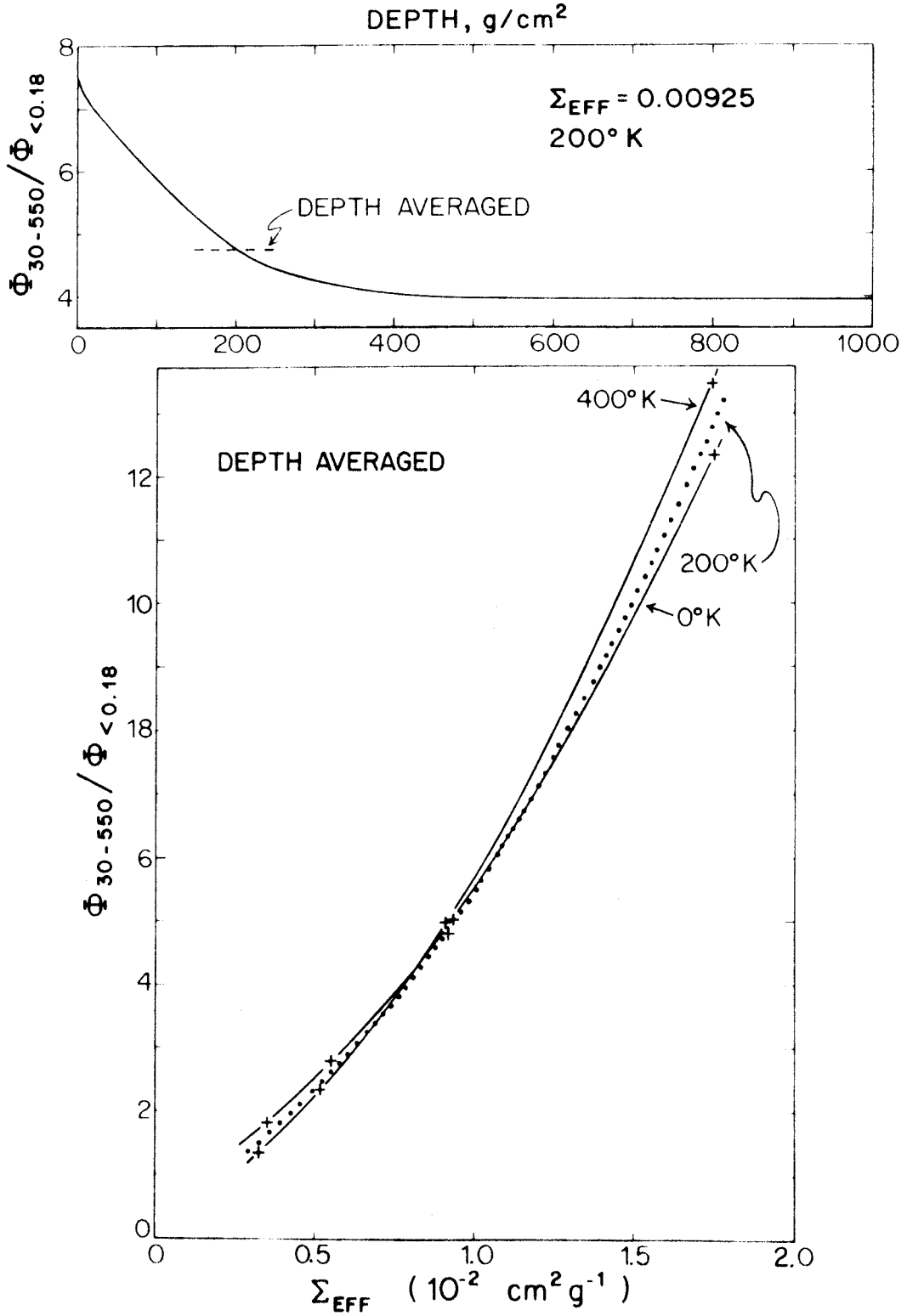
DEPTH, g/cm²
$\Phi_{30-550}/\Phi_{<0.18}$
Σ_{EFF} = 0.00925
200° K
DEPTH AVERAGED
400° K
200° K
0° K
Σ_{EFF} (10^{-2} $cm^2 g^{-1}$)

Figure 4-8

one in which the neutrons are less affected by 1/V absorption.

In general, the 200°K flux ratio, which is applicable to the lunar case might be expected to fall between those for 0° and 400°, but for the single 200° case for which fluxes were evaluated by LCH, it falls outside the others. Because this point is near the intersection of the 0° and 400° curves, this may be an artifact of the calculations. In any case, it makes it difficult to extrapolate the ratio to other values of Σ_{eff} with confidence. The dotted line in the lower part of Figure 4-8 has been constructed by assuming that the ratio at 200° should lie between those for 0° and 400° except near the intersection.

The only sample for which measured Gd and Kr effects can be compared quantitatively is rock 14310. Assume that this rock was irradiated at a depth of ~ 200 g/cm^2 so that the depth averaged ratio $\Phi_{30-550}/\Phi_{<0.18}$ is applicable. This assumption is not necessary but it is convenient for comparing the measured effects. Rock 14310 has a Σ_{eff} of 0.0074 cm$^2 \cdot$g^{-1} while the soil in which it was founded has Σ_{eff} = 0.0086. Because it is not known in what type material this sample received most of its irradiation, the comparison will be made for each of the above Σ_{eff} values. If it was irradiated in material with Σ_{eff} = 0.0074, the ratio $\Phi_{30-550}/\Phi_{<0.18}$ should be 3.65. The fluence measured by Gd is $\sim 2.5 \times 10^{16}$n/cm^2(E < 0.18 eV). The fluence predicted for the 30-550 eV region would therefore be 9.1×10^{16}n/cm^2. For an irradiation in material with Σ_{eff} = 0.0086, the predicted fluence (30-550 eV) would be 1.2×10^{17}n/cm^2.

The concentration of neutron-produced ^{80}Kr reported by Marti and

Lugmair [21] for 14310 was 1.05 x 10^{-10} ccSTP/g. If the Br concentration is 0.235 ppm, as given by Morgan *et al.* [23] (a higher value of 0.85 ppm was reported by Reed *et al.* [24]), is applicable to this sample, one calculates that the fluence necessary to produce this amount of ^{80}Kr would be 9.8 × 10^{16} n/cm^2 in the energy range 30-550 eV. This is in good agreement with either of the estimates made from the fluence below 0.18 eV, but because of the uncertainty in the depth of irradiation and the other assumptions, one cannot make a strong conclusion concerning the energy dependence of the neutron flux.

4.9 $^{130}Ba(n,\gamma)^{131}Ba(\varepsilon)^{131}Cs(\varepsilon)^{131}Xe$

Excesses in the concentration of ^{131}Xe, first observed in the Apollo 11 samples [25,26,27,28], have been attributed to neutron capture reactions on Ba [29]. This could be a very useful reaction because high energy spallation products, *e.g.*, ^{126}Xe and a relatively low energy product, ^{131}Xe, from neutrons, could be observed in a single element. The ratio of these two products could then be used to indicate the depth at which the sample had been irradiated (see Sec. 5.5.2) because the production functions for the two processes have a different depth dependence. However, at the time of Apollo 11, the differential cross section of ^{130}Ba had not been measured, and the assignment of the excess ^{131}Xe to Ba neutron capture was only tentative. Berman and Browne [30] have recently measured this cross section and assigned 18 resonances at energies between 40 and 1000 eV to ^{130}Ba capture. Their data for all these resonances have been used to evaluate an average cross section

in the range 30 to 550 eV, where 94% of the captures should occur for an $E^{-0.91}$ spectrum. This average cross section is 58 barns. Because the captures occur in the same energy region as for Br, one can employ the same procedure to compare measured and predicted effects. Unfortunately, as was the case with Br, there are only a few samples on which both Gd and Xe data are available, and the absolute quantities of rare gases are not as well determined as the isotopic ratios.

The data for the rocks, which can be used to compare measured and predicted 30-550 eV neutron fluences, are summarized in Table 4-7. Only rocks have been used because soil samples have much larger concentrations of trapped Xe which makes it difficult to obtain reliable spectra for the cosmogenic components. The fluences of 30-550 eV neutrons as measured by Xe, ψ^{Xe}_{30-550}, have been estimated from the reported spallation ($^{131}Xe/^{126}Xe$) ratios and ^{126}Xe concentrations by assuming that the actual spallation ratio of 131 to 126 was 3.5 and that the remainder of the ^{131}Xe was due to neutron capture by ^{130}Ba. This estimate of the true spallation ratio is based on the measured ratio in rock 10049, which appears to have had only a surface irradiation [31] and which should have the smallest contribution from neutron capture.

As discussed in the preceding section, interpretation of the capture effects in the 30-550 eV region relative to those at low energies is complicated by the fact that one needs to know at what depth and in what type material the sample was irradiated. Without this knowledge, one can only say whether or not the effects are compatible with the range permitted by the theoretical calculations. For the Apollo 11

Table 4-7

Comparison of ^{131}Xe and ^{158}Gd Neutron Capture Effects in Rocks

Sample	Σ_{eff} ($10^{-2}cm^2/g$)	$\psi^{Gd}_{<0.18}$ ($10^{16}n/cm^2$)	$\left(\frac{\Phi_{30-550}}{\Phi_{<0.18}}\right)_{LCH}$	ψ^{Gd}_{30-550} ($10^{16}n/cm^2$)	ψ^{Xe}_{30-550} ($10^{16}n/cm^2$)	$\frac{\psi^{Gd}_{30-550}}{\psi^{Xe}_{30-550}}$
10017	1.03[s]	4.66	4.90[a]	22.8		0.88
	1.34[r]	5.03	8.45[a]	42.5	26[b,c]	1.6
	1.03[s]	4.66	7.50[t]	35.0		1.3
10057	1.03[s]	0.29	7.50[t]	2.2	3.4[d,e]	0.65
	1.34[r]	0.31	12.9 [t]	4.0		1.2
10069	1.03[s]	<0.21	7.50[t]	<1.6	0.93[b,c]	<1.7
12002	0.87[s]	1.10	4.50[a]	5.0	1.8 [f,g]	2.8
	0.81[r]	1.10	4.10[a]	4.4	1.8 [f,g]	2.4
	0.87[s]	1.10	4.50[a]	5.0	1.4 [h,g]	3.6
12009	0.87[s]	1.49	4.50[a]	6.71	4.2 [i,e]	1.6
					0.46[h,e]	14.6
12018	0.87[s]	1.68	4.50[a]	7.56	5.5 [i,e]	1.4
					1.9 [h,e]	4.0
12052	0.87[s]	1.54	4.50[a]	6.93	8.5 [i,j]	0.82
					1.4 [h,j]	5.0
12063	0.87[s]	1.15	4.50[a]	5.18	3.9 [i,e]	1.3
					2.9 [h,e]	1.8
14310	0.86[s]	2.7	4.40[a]	11.9	10.6 [k]	1.1

Footnotes for Table 4-7

s ≡ irradiated in the soil from which it was collected.

r ≡ irradiated in the material with the same chemical composition as the rock.

a ≡ depth averaged exposure

t ≡ exposure only at the surface (top)

Xe data from the following references. The uncertainty on ψ^{Xe}_{30-550} is ~ 20%, excluding systematic inter-laboratory differences.

b Huneke *et al.* [31]

d Hohenberg *et al.* [32]

f Alexander [33]

h Marti and Lugmair [9]

i Bogard *et al.* [34]

k Lugmair and Marti [11]

Ba concentrations from the following references

e Tera *et al.* [35]

c estimated

g Hubbard and Gast [36]

j Schnetzler and Philpotts [37]

rocks and 14310 the fluence in the 30-550 eV range predicted from the fluence below 0.18 eV as measured by Gd can be brought into agreement with that measured by the ^{131}Xe concentration $\left(\psi^{Gd}_{30-550} \Big/ \psi^{Xe}_{30-550} = 1\right)$ by varying the depths at which the samples were irradiated and/or the composition of the material in which the rock was exposed (Table 4-7). The situation with the Apollo 12 rocks is more difficult to evaluate because there are Xe concentration data for given rocks but from different laboratories which differ by as much as a factor of ten. Assuming the higher concentrations and therefore fluences are more nearly correct, these samples also appear to be in approximate agreement with the energy spectrum of LCH (Table 4-7). (This assumption may be justified because the lower values imply ^{126}Xe to $\psi_{<0.18}$ ratios which are incompatible with the $^{131}Xe/^{126}Xe$ to $\psi_{<0.18}$ ratios according to the irradiation depth models which will be presented in Chapter 5.)

Rock 14310 is especially important because it is the only sample on which the effects of both Br and Ba neutron capture have been reported. Because these captures occur in the same energy region, their ratio does not provide a strong test of the energy spectrum, but it does provide a check on the relative values of the rare gas concentrations, target element concentrations, and cross sections which were used in the calculations. The fluence of neutrons in the 30-550 eV region calculated from the ^{80}Kr concentration ($9.8 \times 10^{16} n/cm^2$) is in good agreement with the value of $1.06 \times 10^{17} n/cm^2$ calculated from ^{131}Xe. In that the rare gas concentrations due to neutron capture introduce the most significant uncertainty into this calculation, the agreement of the fluences calculated for ^{131}Xe and ^{80}Kr suggests that at least the relative

concentrations of neutron produced ^{80}Kr and ^{131}Xe inferred from the rare gas data are correct. Because these fluences agree with those predicted from Gd, one would also like to believe that the absolute concentrations of the rare gases in 14310 were also correct.

The large uncertainty in the concentration of the spallogenic Xe in the samples especially those from Apollo 12 makes it impossible to conclude at this time whether or not the ^{131}Xe and ^{158}Gd data are in quantitative agreement with the LCH spectrum but there is no strong evidence that they are not.

4.10 $^{186}W(n,\gamma)^{187}W(\beta^-)^{187}Re$

Michel, Herpers, Kulus, and Herr [38] have reported excess ^{187}Re in samples from the Apollo 12 and 14 missions, which they attribute to neutron capture by ^{186}W. The group cross sections of Canfield [8] indicate that for the LCH flux, $\sim$ 93% of the captures by ^{186}W should occur in the energy range 10-30 eV (group 11) because of the resonance at E_o = 18.8 eV. Furthermore, the capture rate should be essentially independent of chemical composition. In this thesis, no group cross sections were evaluated for this reaction, but capture rates were calculated from the LCH and BNL 325 resonance parameters for a $E^{-0.91}$ spectrum. These rates were 95% and 111%, respectively, of the value given by LCH. Adopting the LCH value, one calculates that for material of the Apollo 11 soil composition at 200°K, the capture rate per atom of ^{186}W is 3.7×10^{-6} neutrons per 10^9 yr at the lunar surface or 3.8×10^{-5} at the depth corresponding to the peak of the

neutron flux. While discussing capture rates it should be noted that the plot of $\sigma(E)$ in BNL 325 and in Michel, Herpers, Kulus, and Herr [38] appears to underestimate the cross section around the 18.8 eV resonance, as calculated from the resonance parameters, by about a factor of ten. The value calculated from the resonance parameters is supported by the resonance integral reported by Rahn *et al.* [39] and the references therein.

The measured effect in ^{187}Re relative to that in ^{158}Gd can be compared to the calculated effect most conveniently in terms of the measured ε values (see Sec. 6.4) and calculated capture rates. A similar treatment was used in discussing ^{149}Sm capture (Sec. 4.4). The ratio $\varepsilon_W/\varepsilon_{Gd}$ is a measurement of the ratio of the ^{186}W and ^{157}Gd capture rates. The capture rate for ^{186}W, but not for ^{157}Gd will be independent of the composition of the material.

For materials of the composition of soil 14163, the depth averaged ratio $\varepsilon_W/\varepsilon_{Gd}$ is calculated to be 0.0060. For a surface irradiated sample, the ratio would have its maximum value of 0.0085.

As can be seen in Table 4-8, only one of the five samples, where the effects can be compared, has an $\varepsilon_W/\varepsilon_{Gd}$ ratio near the range predicted by LCH. The others are more than a factor of ten higher than predicted. Although there is no Gd data on 14305 (breccia), one can calculate the time necessary to develop the reported effect at the peak of the LCH flux. Taking an average ε_W for the four pieces of 14305, one has $\varepsilon_W = 8.4 \times 10^{-5}$. This implies an unreasonably long exposure time of 2.2×10^9 yr at the peak of the flux (~ 150 g/cm^2). If these effects in

Table 4-8

Comparison of Measured ^{187}Re and ^{158}Gd Neutron Capture Effects

Sample	ε_W (10^{-3})	ε_{Gd} (10^{-3})	$\varepsilon_W/\varepsilon_{Gd}$
14163†	0.14 ±.01	3.05	0.046
14163†	0.027 ±.01	3.05	0.0088
14259†	0.12 ±.06	2.90	0.041
14321†	0.071 ±.007	<0.03	>2.37
14321†	0.081 ±.006	<0.03	>2.7
14305† BD1	0.18 ±.01	-	
14305†	0.081 ±.005	-	
14305* DD1	0.043	-	
14305* CA1	0.032	-	

†Michel *et al.* [38a]

*Herpers *et al.* [38b]

^{187}Re are correctly measured and due to neutron capture, then the LCH spectrum must be highly inaccurate. This will be discussed further in Section 4.16.

4.11 $^{238}U(n,\gamma)^{239}U(\beta^-)^{239}Np(\beta^-)^{239}Pu$

The possibility of finding neutron-produced ^{239}Pu ($t_{\frac{1}{2}}=2.44\times10^4$yr) in lunar samples has been explored experimentally by Fields, Diamond, Metta, and Rokop [40] and Fields, Diamond, Metta, Rokop, and Stevens [41] who have been able to set upper limits as low as $<2\ 10^{-16}$g ^{239}Pu per gram of sample. In order to calculate what ^{239}Pu concentration might be expected for lunar samples, group cross sections (Table 4-9) were calculated using the BNL 325 resonance parameters for resonances with $E_o < 1$ keV. About 98% of the captures are calculated to occur in the energy range 3.0<E<550 eV. Because the spectrum becomes sensitive to the composition of the medium only below ~ 3 eV, the capture rate of ^{238}U should be essentially independent of the macroscopic absorption cross section of the sample.

If a sample has been on the lunar surface long enough for the ^{239}Pu activity to reach equilibrium, the production rate $[^{238}U]^{238}\sigma\phi$, will equal the disintegration rate $^{239}\lambda[^{239}Pu]$ or $^{239}Pu/^{238}U = \phi^{238}\sigma/^{239}\lambda$. In terms of group fluxes and cross sections one has

$$^{239}Pu/^{238}U = \sum_g \langle^{238}\sigma\rangle_g\phi_g/^{239}\lambda$$

which gives $^{239}Pu/^{238}U = 7.2 \times 10^{-11}$ at the lunar surface or more

Table 4-9

^{238}U Neutron Capture Group Cross Sections

LCH Group	E_{max} (eV)	σ_g (barns)
25	1.78×10^{-3}	12.3
24	3.16×10^{-3}	7.86
23	5.62×10^{-3}	5.90
22	1.00×10^{-2}	4.42
21	1.78×10^{-2}	3.32
20	3.16×10^{-2}	2.49
19	5.62×10^{-2}	1.89
18	1.00×10^{-1}	1.43
17	1.78×10^{-1}	1.09
16	3.16×10^{-1}	0.845
15	5.62×10^{-1}	0.659
14	1.00	0.533
13	3.00	0.473
12	1.00×10^{1}	111.5
11	3.00×10^{1}	55.1
10	1.00×10^{2}	45.0
9	5.50×10^{2}	10.5
8	3.00×10^{3}	1.05

precisely in the upper LCH depth interval (< 1.65 g/cm^2). A high U soil, *e.g.*, one from Apollo 14, might have ~ 3 ppm U [42]; therefore, the equilibrium ^{239}Pu concentration should be ~ 2×10^{-16} g/g(sample). For samples irradiated near the peak of the neutron flux, the ^{239}Pu concentration would be a factor of ten higher.

Because the time required to reach equilibrium (~ 10^5 yr) is relatively short by lunar standards, the ^{239}Pu should be in equilibrium in most samples. If the experimental sensitivity could be slightly improved, it should be possible to detect ^{239}Pu in high U samples from Apollo 14. If trench or core samples could be analyzed, which is not unreasonable in terms of the one gram samples needed, it should be possible to detect ^{239}Pu with the present capability.

4.12 $^{235}U(n,\gamma)^{236}U$

Fields *et al.* [40,41] have also measured the $^{236}U/^{238}U$ ratio in lunar samples. Using the resonance parameters of BNL 325, group cross sections for this reaction have been evaluated which take into account the resonances with E_o <50 eV including the bound state capture. Above 50 eV, the group cross sections were estimated from the curves in BNL 325. These group cross sections are displayed in Table 4-10. Captures occur over a wide energy range with enough occurring below 3 eV for the capture rate to vary with the macroscopic absorption cross section as shown in the top part of Figure 4-9. For this isotope the capture rate is essentially independent of temperature in the range 0° to 400°K.

The half-life of ^{236}U is 2.4×10^7 yr; therefore, $\gtrsim 5 \times 10^7$ yr

Table 4-10

^{235}U Neutron Capture Group Cross Sections

LCH Group	E_{max} (eV)	σ_g (barns)
25	1.78×10^{-3}	598.
24	3.16×10^{-3}	381.
23	5.62×10^{-3}	284.
22	1.00×10^{-2}	210.
21	1.78×10^{-2}	153.
20	3.16×10^{-2}	110.
19	5.62×10^{-2}	76.8
18	1.00×10^{-1}	52.9
17	1.78×10^{-1}	38.2
16	3.16×10^{-1}	38.5
15	5.62×10^{-1}	19.6
14	$1.00 \times$	9.32
13	$3.00 \times$	10.4
12	1.00×10^{1}	35.0
11	3.00×10^{1}	39.7
10	1.00×10^{2}	26.
9	5.50×10^{2}	5.
8	3.00×10^{3}	4.
7	1.70×10^{4}	2.

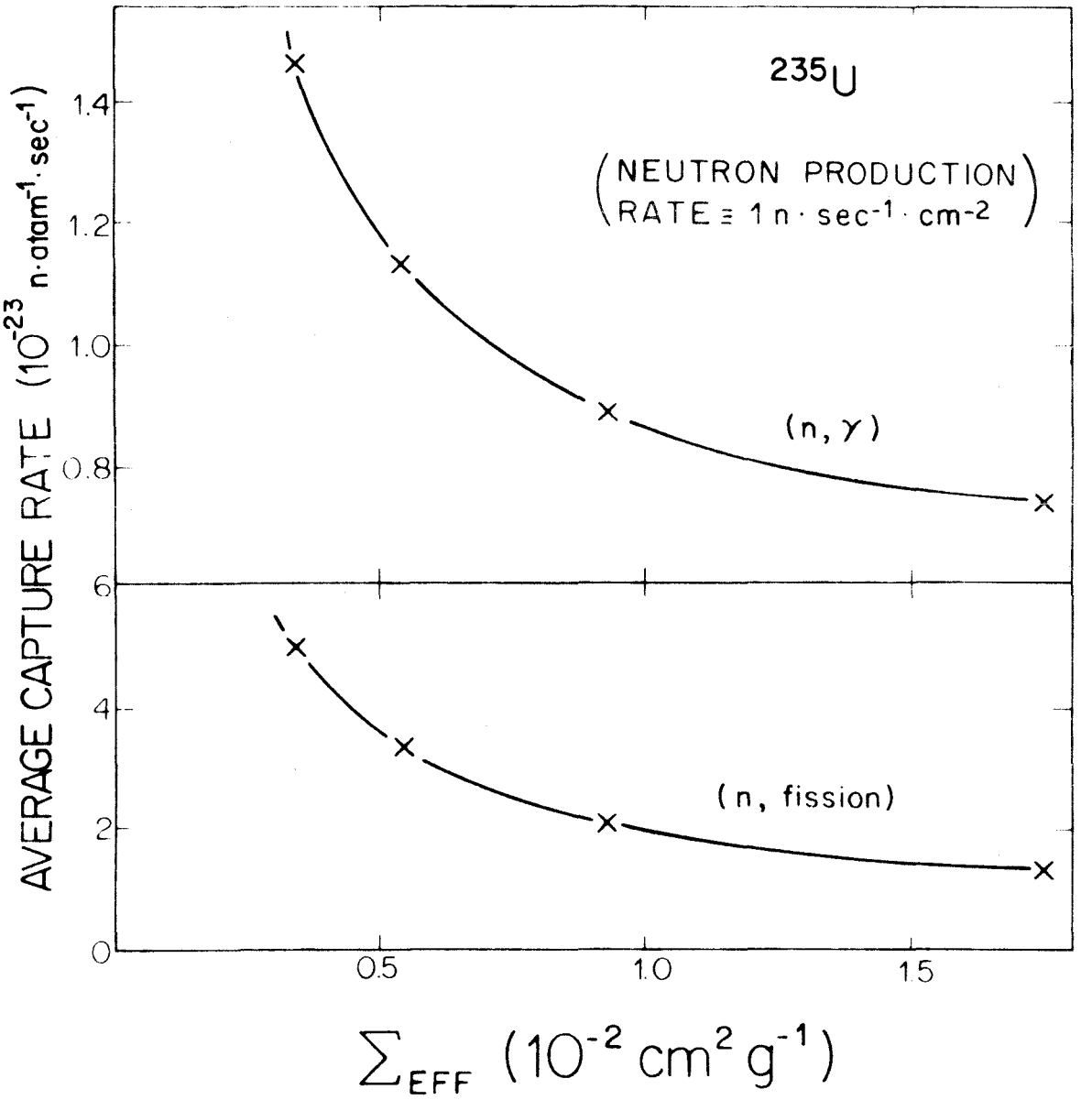

Figure 4-9

Depth averaged neutron capture rates for ^{235}U for captures leading to (n,γ) and (n,fission) reactions as a function of Σ_{eff}. The average is carried out over the upper 1155 g/cm^2 of lunar material and assumes a neutron production rate of 1 n·sec^{-1}·cm^{-2} of lunar surface. The actual lunar neutron production rate is estimate to be 16 n·sec^{-1}·cm^{-2}. The curves are calculated to apply throughout the temperature range $0 \leq T \leq 400°K$. The x's indicate the calculated points.

are required for its activity to reach equilibrium with the flux at the depth at which the sample is being irradiated. The upper limit for the $^{236}U/^{238}U$ ratio, is the equilibrium ratio at the peak of the neutron flux. For an Apollo 15 sample, this ratio is calculated to be 4×10^{-9}. Apollo 11, 12, and 14 samples should have lower ratios. Samples 10084 and 14163 have $^{236}U/^{238}U < 3 \times 10^{-9}$ [41] which is compatible with neutron production of ^{236}U; however, several other soils have $^{236}U/^{238}U$ ratios between 4×10^{-9} and 5×10^{-8} and one sample, 12070, has a ratio of 2.3×10^{-7} [41]. Even if 12070 is excluded, most of the samples studied have $^{236}U/^{238}U$ ratios which are too high to explain by neutron capture if the LCH calculations are correct. The 12070 sample with the high $^{236}U/^{238}U$ ratio also had a high ^{237}Np content, which might imply that at least part of the ^{236}U was due to spallation reactions on ^{238}U; however, the magnitude of the excess is too large to be explained in this way.

4.13 $^{235}U(n,f)$ Fission Products

Group cross sections for neutron induced fission of ^{235}U were calculated using the BNL 325 resonance parameters for resonances with $E_o < 50$ eV. Above this energy group cross sections were simply estimated from the BNL 325 cross section curves. These group cross sections are displayed in Table 4-11. The variation of the fission rate with the macroscopic cross section of the material is illustrated in the lower portion of Figure 4-9. For materials of the Apollo 11 composition, $\Sigma = 0.010$, a surface induced fission rate of 1.1×10^{-22} fissions per

Table 4-11

^{235}U Neutron Induced Fission Group Cross Sections

LCH Group	E_{max} (eV)	σ_g (barns)
25	1.78×10^{-3}	2999.
24	3.16×10^{-3}	1913.
23	5.62×10^{-3}	1428.
22	1.00×10^{-2}	1062.
21	1.78×10^{-2}	783.
20	3.16×10^{-2}	571.
19	5.62×10^{-2}	409
18	1.00×10^{-1}	289.
17	1.78×10^{-1}	207.
16	3.16×10^{-1}	174.
15	5.62×10^{-1}	94.7
14	1.00	47.1
13	3.00	28.3
12	1.00×10^{1}	31.5
11	3.00×10^{1}	23.3
10	1.00×10^{2}	30.
9	5.50×10^{2}	15.
8	3.00×10^{3}	7.0
7	1.70×10^{4}	5.0
6	1.00×10^{5}	2.5
5	4.00×10^{5}	1.5
4	9.00×10^{5}	1.2
3	1.40×10^{6}	1.2
2	3.00×10^{6}	1.3
1	1.00×10^{7}	1.5

atom per second is predicted. At the peak of the flux (interval 16: 139-165 g/cm^2), the rate is calculated to be 1.25×10^{-21}.

It is interesting to compare the calculated rate for induced fission to the spontaneous fission rate of ^{238}U. The fission decay constant of ^{238}U is 7×10^{-17} yr^{-1} or 2×10^{-24} sec^{-1}. This is, of course, the fission rate per atom. Adjusting for the abundance ratio, $^{238}U/^{235}U = 137.8$, the ratio of the number of ^{238}U fissions to ^{235}U fissions at the lunar surface today is calculated to be ~ 3. At the peak of the flux, this ratio is ~ 0.3. Consider a rock which is 3.3×10^9 yr old which has been irradiated for the last 500 my at the peak of the neutron flux. In the 3.3×10^9 yr, 40% of the original ^{238}U ($t_{\frac{1}{2}} = 4.5 \times 10^9$yr) will decay and of these atoms $\sim 4.7 \times 10^{-5}$% will spontaneously fission. Taking the modern abundance of ^{238}U as 138, the initial abundance must have been 230. This means that 4.3×10^{-5} "atoms" have fissioned. Now consider ^{235}U, which has a modern abundance of 1 and $t_{\frac{1}{2}} = 7.1 \times 10^8$yr. The average ^{235}U abundance over the last 500 my was 1.3; therefore, at the peak of the flux 2.5×10^{-5} "atoms" would have undergone fission in the last 500 my. The ratio of 2.5×10^{-5} to 4.3×10^{-5} is ~ 0.6, which means that in such a sample the concentration of fission products from the induced fission of ^{235}U would be 2/3 of the concentration from the spontaneous fission of ^{238}U.

If instead of being irradiated for 500 my at the peak of the low energy neutron flux, the mixing of the regolith caused the sample to be exposed for essentially equal times at all depths in the upper ~3000 g/cm^2 of the moon as may be the case for soils (Sec. 5.2);

then the average ^{235}U induced fission rate for the sample would be ~0.1 of that for a sample at the peak of the flux. However, if the sample has been exposed to this average fission rate throughout its 3.3×10^9 yr existence, one calculates that the average ^{235}U abundance over this period was 7.4 as opposed to 1 today and the length of the irradiation was 6.6 times longer than the 500 my case considered above; therefore, the ratio of induced ^{235}U fission to ^{238}U spontaneous fission would be ~2.5. In addition induced fission of ^{238}U and ^{232}Th by high energy neutrons could also contribute to the induced fission component. Although a sample may not be in the upper 3000 g/cm^2 of the moon for its complete "life" these calculations show that induced fission may be an important source of fission products, *e.g.*, fissiogenic Xe.

4.14 $^{40}Ca(n,\alpha)^{37}Ar$

Kornblum, Levine, Aronson, and Fireman [43] have argued that this reaction, which occurs primarily in the MeV region, provides the most direct determination of the production rate of MeV neutrons on the moon and have calculated this production rate to be between 57 and 48 $n \cdot cm^{-2} \cdot sec^{-1}$. They have recently lowered their estimate to 26.4 ± 4.5 $n \cdot cm^{-2} \cdot sec^{-1}$ ($E < 15$ MeV) on the basis of improved cross section measurements [44]. This new value is a factor of approximately 1.7 higher than estimated by LCH by analogy to the terrestrial atmosphere or by the Armstrong and Alsmiller [45] Monte Carlo calculations of cosmic ray neutron production.

Kornblum *et al.* [44] calculated the lunar neutron production rate from the ^{37}Ar data by assuming that the neutron flux had the same energy dependence in the MeV region as the LCH production function (Sec. 3.1.1). The ^{40}Ca (n,α) cross section is essentially zero below 2.5 MeV, rises rapidly between 2.5 and 5 MeV, and is essentially constant from 5 to 15 MeV [44]; therefore, the magnitude of the ^{40}Ca (n,α) reaction is sensitive only to the neutron flux above ~2 MeV. Armstrong, Chandler, and Barish [46] have shown that for the earth's atmosphere in the MeV region, neutron spectra of the type used by LCH decrease more rapidly with increasing energy than the actual neutron flux and that in the range $2 \leq E \leq 5$ MeV where most of the ^{40}Ca capture occurs, the flux calculated for an LCH spectrum is about one-half the measured flux if the curves are normalized at 1 MeV. It is reasonable that this should also be the case for the moon; therefore, one would expect Kornblum *et al.* [44] to calculate a higher apparent neutron production rate from the ^{37}Ar data than that estimated by LCH. For this reason, the ^{37}Ar data do not seem to be in conflict with the LCH estimate of the lunar neutron source strength. One should note, however, that because the LCH calculations are primarily concerned with lower energy neutrons which have undergone many collisions and have forgotten the details of their initial energy distribution, only the total number of neutrons produced by cosmic rays, not their energy distribution, is important to the LCH calculations.

4.15 LNPE

The Lunar Neutron Probe Experiment (LNPE), flown on Apollo 17,

was designed to measure the magnitude, depth dependence, and energy spectrum of the lunar neutron flux [47]. The probe consisted of a two-meter rod which was inserted in a drill hole on the lunar surface. Three systems were used to detect neutrons. ^{10}B, ^{235}U, and $^{79,81}Br$ (KBr) targets were located along the length of the rod. The ^{10}B undergoes an (n,α) reaction producing ^{7}Li. The α particles are detected by means of the radiation damage *tracks* which they leave in plastic detectors placed near the B targets. Neutron induced fission of the ^{235}U produces fission fragments which leave tracks when they are absorbed in mica placed near the U. As discussed in Section 4.8, neutron capture on Br produces ^{80}Kr and ^{82}Kr. In addition, part of the plastic detector was shielded with Cd foil which strongly absorbs neutrons with $E < 0.5$ eV. The number of events recorded by each system as a function of depth will indicate the depth dependence and magnitude of the neutron flux. Because the various targets absorb at different energies, the ratio of the number of captures by the various detectors is an indicator of the energy spectrum.

Only the ^{235}U-mica data have been analyzed at this time. These data indicate that the LCH depth dependence of the flux is very nearly correct and that the measured capture rate of ^{235}U is within $\sim 10\%$ of the value predicted from the LCH flux and the cross sections given in Section 4.13.

4.16 Conclusions

Of the reactions considered above, only ^{236}U and ^{187}Re show abundances more than a factor of two higher than predicted. As dis-

cussed above, the excesses in the ^{236}U of certain samples appear to be correlated with ^{237}Np but the excesses are too large to be explained in terms of spallation reactions on ^{238}U. No other source of ^{236}U is immediately apparent. The ^{187}Re is also difficult to explain. There are no elements heavier than Re with sufficient abundance to explain the excess ^{187}Re by spallation reactions. Because the other reactions discussed give activities in rough agreement with LCH, it is unlikely that the flux in the 10-30 eV region, where W captures, is sufficiently different from the calculated value to explain the reported ^{187}Re effects. ^{187}Re is also produced in the laboratory irradiation necessary for the Re measurement, and this laboratory-produced ^{187}Re is as much as 80% of the total measured excess. This means that a 25% uncertainty in the Re/W ratio or in the Re correction would explain the reported effect. Without independent analyses by other workers, it is impossible to assess whether the reported ^{236}U and ^{187}Re effects are real.

Of the effects showing smaller deviations from the LCH calculations, the largest disagreement is in ^{40}Ca. As discussed above, this may be due to differences in the high energy spectrum assumed by Kornblum *et al.* [44] and the actual lunar neutron spectrum. Differences in the high energy spectrum are not critical for the lower energy LCH predictions. The ^{131}Xe data scatter about the predicted values so that no firm conclusion is possible concerning this nuclide. The Kr and Co data are compatible with the calculated effects but the data are limited and the errors are large.

In the sub-eV region, the ratios of the Sm and Eu induced effects to those induced by Gd capture indicate that the low energy spectrum is

somewhat *harder* than predicted. The preliminary LNPE results, however, imply that the capture rate for nuclei which capture mainly in this region is not very different from that predicted by LCH and that the LCH depth dependence is essentially correct. If the spectrum is harder than predicted, the fluences necessary to produce the observed Gd effects would have to be larger than calculated for the LCH spectrum (Table 4-2). Because the average cross section varies rather slowly with Σ_{eff} (Fig. 4-2), this effect should be on the order of 10%. The effect on the Gd capture rate is more difficult to evaluate because the calculated low energy neutron flux would also be incorrect. However, the approximate agreement of the LNPE ^{235}U fission data with the calculated fission rate, implies that the Gd capture rate predicted by the LCH calculations must be approximately correct. This point should be clarified when the final LNPE results are available.

Throughout the rest of this work, the LCH flux, which was calculated for 200°K as a function of the macroscopic absorption cross section of the material, will be used to interpret measured Gd and Sm isotopic effects.

4.17 References

[1] R. E. Lingenfelter, E. H. Canfield, and V. E. Hampel, The lunar neutron flux revisited, Earth Planet. Sci. Letters 16 (1972) 355.

[2] Alvin M. Weinberg and Eugene P. Wigner, The Physical Theory of Neutron Chain Reactors (The University of Chicago Press, 1958) Chapter 3.

[3] Donald J. Hughes, Neutron Cross Sections (Pergamon Press, 1957) 95-98.

[4] Ernest R. Rae and Robert C. Block, Neutron scattering and capture cross-section measurements, Experimental Neutron Resonance Spectroscopy, J. A. Harvey (ed.) (Academic Press, 1970) 157.

[5] V. L. Sailor, The low energy cross sections of U^{235}, Proc. Int. Conf. Peaceful Uses Atomic Energy 4 (United Nations, 1956) 199.

[6] John R. Stehn, Murrey D. Goldberg, Benjamin A. Magurno, and Renati-Wiener-Chasman, Neutron Cross Sections (U.S.A.E.C., BNL 325 - Supp. No. 2, 1964).
D. J. Hughes, B. A. Magurno, and M. K. Brussel, Neutron Cross Sections (U.S.A.E.C., BNL 325 - Supp. No. 1, 1960).
Donald J. Hughes and Robert B. Schwartz, Neutron Cross Sections (U.S.A.E.C., BNL 325, 1958).

[7] James Lo, SIMSON/Simple Integration Subroutine (Booth Computing Center, Cal. Inst. Tech., C456-94-360-10, 1970).

[8] E. H. Canfield, personal communication.

[9] K. Marti and G. W. Lugmair, Kr^{81}-Kr and K-Ar^{40} ages, cosmic-ray spallation products, and neutron effects in lunar samples from Oceanus Procellarum, Proc. Second Lunar Sci. Conf. 2 (M.I.T. Press, 1971) 1591.

[10] G. W. Lugmair and K. Marti, Neutron capture effects in lunar gadolinium and the irradiation histories of some lunar rocks, Earth Planet. Sci. Letters 13 (1971) 32.

[11] G. W. Lugmair and K. Marti, Exposure ages and neutron capture record in lunar samples from Fra Mauro, Proc. Third Lunar Sci. Conf. 2 (M.I.T. Press, 1972) 1891.

[12] O. Eugster, F. Tera, D. S. Burnett, and G. J. Wasserburg, The isotopic composition of Gd and the neutron capture effects in samples from Apollo 11, Earth Planet. Sci. Letters 8 (1970) 20.

[13] O. Eugster, F. Tera, D. S. Burnett, and G. J. Wasserburg, Isotopic composition of gadolinium and neutron-capture effects in some meteorites, J. Geophys. Res. 75 (1970) 2753.

[14] H. Marshak and V. L. Sailor, Low-energy neutron resonances in Sm^{149}, Phys. Rev. 109 (1958) 1219.

[15] N. J. Pattenden, Some neutron cross sections of importance to reactors Tc^{99}, Nd^{143}, Nd^{145}, Sm^{149}, Sm^{152}, Eu^{151}, Eu^{153}, Gd^{155}, Gd^{157}, Pu^{240}, Proc. Second U.N. Int. Conf. Peaceful Uses Atomic Energy 16 (United Nations, 1958) 44.

[16] C. M. Lederer, J. M. Hollander, and I. Perlman, Table of Isotopes, John Wiley and Sons, Inc. (1967) 305-307.

[17] M. Wahlen, R. C. Finkel, M. Imamura, C. P. Kohl, and J. R. Arnold, ^{60}Co in lunar samples, preprint (1973).

[18] R. C. Finkel, personal communication.

[19] G. Davis O'Kelley, James S. Eldridge, Ernest Schonfeld, and P. R. Bell, Primordial radionuclide abundances, solar proton and cosmic-ray effects and ages of Apollo 11 lunar samples by non-destructive gamma ray spectrometry, Proc. Apollo 11 Lunar Sci. Conf. 2 (Pergamon Press, 1970) 1407.

[20] H. B. Wiik and P. Ojanpera, Chemical analyses of lunar samples 10017, 10072, and 10084, Science 167 (1970) 531.

[21] G. W. Lugmair and K. Marti, Neutron and spallation effects in Fra Mauro regolith, Lunar Science III (Lunar Sci. Inst. Cont. No. 88, 1972) 495.

[22] T. B. Ryves, Activation measurements of thermal neutron capture cross-sections and resonance integrals, J. Nuc. Energy 24 (1970) 35.

[23] J. W. Morgan, J. C. Laul, U. Krähenbühl, R. Ganapathy, and E. Anders, Major impacts on the moon: Chemical characterization of projectiles, Lunar Science III (Lunar Sci. Inst. Cont. No. 88, 1972) 552.

[24] G. W. Reed, Jr., S. Jovanovic, and L. H. Fuchs, Concentration and lability of the halogens, platinum metals and mercury in Apollo 14 and 15 samples, Lunar Science III (Lunar Sci. Inst. Cont. No. 88, 1972) 637.

[25] A. L. Albee, D. S. Burnett, A. A. Chodos, O. J. Eugster, J. C. Huneke, D. A. Papanastassiou, F. A. Podosek, G. Price Russ II, H. G. Sanz, F. Tera, and G. J. Wasserburg, Ages, irradiation history, and chemical composition of lunar rocks from the Sea of Tranquillity, Science 167 (1970) 463.

[26] J. H. Reynolds, C. M. Hohenberg, R. S. Lewis, P. K. Davis, and W. A. Kaiser, Isotopic analysis of rare gases from stepwise heating of lunar fines and rocks, Science 167 (1970) 545.

[27] K. Marti, G. W. Lugmair, and H. C. Urey, Solar wind gases, cosmic ray spallation products and the irradiation history, Science 167 (1970) 548.

[28] R. O. Pepin, L. E. Nyquist, Douglas Phinney, and David C. Black, Isotopic composition of rare gases in lunar samples, Science 167 (1970) 550.

[29] P. Eberhardt, J. Geiss, H. Graf, N. Grögler, U. Krähenbühl, H. Schwaller, J. Schwarzmüller, A. Stettler, Correlation between rock type and irradiation history of Apollo 11 igneous rocks, Earth and Planet. Sci. Letters 10 (1970) 67.

[30] B. L. Berman and J. C. Browne, Microscopic $^{130}Ba(n,\gamma)$ cross section and the origin of ^{131}Xe on the moon, Phys. Rev. C. 7 (1973) 2522.

[31] J. C. Huneke, F. A. Podosek, D. S. Burnett, and G. J. Wasserburg, Rare gas studies of the galactic cosmic ray irradiation history of lunar rocks, Geochim. Cosmochim. Acta 36 (1972) 269.

[32] C. M. Hohenberg, P. K. Davis, W. A. Kaiser, R. S. Lewis, and J. H. Reynolds, Trapped and cosmogenic rare gases from stepwise heating of Apollo 11 samples, Proc. Apollo 11 Lunar Sci. Conf. (2 Pergamon Press, 1970) 1283.

[33] E. C. Alexander, Jr., Spallogenic Ne, Kr, and Xe from a depth study of 12002, Proc. Second Lunar Sci. Conf. 2 (M.I.T. Press, 1971) 1643.

[34] D. D. Bogard, J. G. Funkhouser, O. A. Schaeffer, and J. Zähringer, Noble gas abundances in lunar material — cosmic ray spallation products and radiation ages from the Sea of Tranquility and the Ocean of Storms, J. Geophys. Res. 76 (1971) 2757.

[35] F. Tera, O, Eugster, D. S. Burnett, and G. J. Wasserburg, Comparative study of Li, Na, K, Rb, Cs, Ca, Sr, and Ba abundances in achondrites and in Apollo 11 lunar samples, Proc. Apollo 11 Lunar Sci. Conf. 2 (Pergamon Press, 1970) 1637.

[36] Norman J. Hubbard and Paul W. Gast, Chemical composition and origin of nonmare lunar basalts, Proc. Second Lunar Sci. Conf. 2 (M.I.T. Press, 1971) 999.

[37] C. C. Schnetzler and John A. Philpotts, Alkali, alkaline earth, and rare-earth element concentrations in some Apollo 12 soils, rocks, and separated phases, Proc. Second Lunar Sci. Conf. 2 (M.I.T. Press, 1972) 1917.

[38a] R. Michel, U. Herpers, H. Kulus, and W. Herr, Isotopic anomalies in lunar rhenium, Proc. Third Lunar Sci. Conf. 2 (M.I.T. Press, 1972) 1917.

[38b] U. Herpers, W. Herr, H. Kulus, R. Michel, K. Thiel, and R. Woelfle, Manganese-53, profile, particle track studies and the rehnium-187 isotopic anomaly of breccia 14305, Lunar Science IV (Lunar Sci. Inst., 1973) 360.

[39] F. Rahn, H. S. Camarda, G. Hacken, W. W. Havens, Jr., H. I. Liou, J. Rainwater, M. Stagowitz, and S. Wynchank, Values of the neutron resonance capture integral for some rare earth isotopes, Nuc. Sci. Eng. 48 (1972) 219.

[40] P. R. Fields, H. Diamond, D. N. Metta, and D. J. Rokop, The reaction products of lunar uranium and cosmic rays, Lunar Science IV (Lunar Sci. Inst., 1973) 239.

[41] P. R. Fields, H. Diamond, D. N. Metta, D. J. Rokop, and C. M. Stevens, ^{237}Np, ^{236}U, and other actinides on the moon, Proc. Third Lunar Sci. Conf. 2 (M.I.T. Press, 1972) 1637.

[42] Fouad Tera and G. J. Wasserburg, U-Th-Pb analyses of soil from the Sea of Fertility, Earth Planet. Sci. Letters 13 (1972) 457.

[43] J. J. Kornblum, M. Levine, A. Aronson, and E. L. Fireman, Neutrons in the moon, Lunar Science IV (Lunar Sci. Inst., 1973) 441.

[44] J. J. Kornblum, E. L. Fireman, M. Levine, and A. Aronson, Neutrons in the moon, Proc. Fourth Lunar Sci. Conf. 2 (Pergamon Press, 1973) in press.

[45] T. W. Armstrong and R. G. Alsmiller, Jr., Calculation of cosmogenic radionuclides in the Moon and comparison with Apollo measurements, Proc. Second Lunar Sci. Conf. 2 (M.I.T. Press, 1971) 1729.

[46] T. W. Armstrong, K. C. Chandler, and J. Barish, Calculations of neutron flux spectra induced in the earth's atmosphere by galactic cosmic rays, J. Geophys. Res. 78 (1973) 2715.

[47] Dorothy S. Woolum, D. S. Burnett, and C. A. Bauman, The Apollo 17 lunar neutron probe experiment, Lunar Science IV (Lunar Sci. Inst., 1973) 793.

[48] Paul W. Gast and Norman J. Hubbard, Abundance of alkali metals, alkaline and rare earths, and strontium-87/strontium-86 ratios in lunar samples, Science 167 (1970) 485.

[49] Gordon G. Goles, Andrew R. Duncan, David J. Lindstrom, Marilyn R. Martin, Robert L. Beyer, Masumi Osawa, Keith Randle, Linda T. Meek, Terry L. Steinborn, and Sheila M. McKay, Analyses of Apollo 12 specimens: compositional variations, differentiation processes, and lunar soil mixing models, Proc. Second Lunar Sci. Conf. 2 (MIT Press, 1971) 1063.

[50] F. Cuttitta, H. J. Rose, Jr., C. S. Annell, M. K. Carron, R. P. Christian, E. J. Dwornik, L. P. Greenland, A. W. Helz, and D. T. Ligon, Jr., Elemental composition of some Apollo 12 lunar rocks and soils, Proc. Second Lunar Sci. Conf. 2 (MIT Press, 1971) 1217.

[51] N. J. Hubbard and P. W. Gast, Chemical composition of Apollo 14 materials and evidence for alkali volatilization, Lunar Science III (Lunar Sci. Inst., 1972) 407.

[52] D. E. Gillum, W. D. Ehmann, H. Wakita, and R. A. Schmitt, Bulk and rare earth abundances in the Luna-16 soil levels A and D, Earth Planet. Sci. Letters 13 (1972) 444.

[53] N. J. Hubbard, L. E. Nyquist, J. M. Rhodes, B. M. Bansal, H. Wiesmann, and S. E. Church, Chemical features of the Luna 16 regolith sample, Earth Planet. Sci. Letters 13 (1972) 423.

[54] Apollo 15 Preliminary Examination Team, The Apollo 15 lunar samples: a preliminary description, Science 175 (1972) 363.

[55] Phillip A. Helmke and Larry A. Haskin, Rare earths and other trace elements in Apollo 15 samples, The Apollo 15 Lunar Samples (Lunar Sci. Inst., 1972) 217.

[56] Apollo 16 Preliminary Examination Team, the Apollo 16 lunar samples: a petrographic and chemical description, Science 179 (1973) 23.

[57] David F. Nava and John A. Philpotts, A lunar differentiation model in light of new chemical data on Luna 20 and Apollo 16 soils, Geochim. Cosmochim. Acta 37 (1973) 963.

[58] J. A. Philpotts, S. Schuhmann, A. L. Bickel, and R. K. L. Lum, Luna 20 and Apollo 16 core fines: large-ion lithophile trace-element abundances, Earth Planet. Sci. Letters 17 (1972) 13.

[59] Carl W. Beck and Lincoln La Paz, The Nortonite fall and its mineralogy, American Mineralogist 36 (1951) 45.

[60] R. A. Schmitt, R. H. Smith, J. E. Leach, A. W. Mosen, D. A. Olehy, and J. Vasilevskis, Abundances of fourteen rare-earth elements, scandium and yttrium in meteoritic and terrestrial matter, Geochim. Cosmochim. Acta 27 (1963) 577.

[61] Roy S. Clarke, Jr., Eugene Jarosewich, Brian Mason, Joseph Nelen, Manuel Gomez, and Jack R. Hyde, The Allende, Mexico, Meteorite Shower, Smithsonian Cont. Earth Sciences 5 (1970).

5. Exposure Histories of Samples

5.1 Introduction

As discussed in Chapters 3 and 4, the low energy neutron flux is a function of chemistry and depth; therefore, the fluence to which a sample has been exposed is a function of the chemical composition of the material and its depositional history, *i.e.*, at what depths the sample has been exposed and for how long. To the extent that the variations in chemistry and depth can be taken into account by the calculations of Lingenfelter, Canfield and Hampel [1] (LCH), the variation in fluence with depth in a core can be used to model the depositional history of the regolith at that site. The situation is somewhat more complicated for rocks and surface soil samples for which the depth(s) at which the material received most of its irradiation is unknown. One cannot calculate the time necessary to produce the observed fluence unless a depositional history is assumed. Alternatively, one can assume the total exposure time and calculate a model depositional history. The latter approach will be shown to be useful in comparing the relative development of the regolith at the various landing sites (Sec. 5.2).

A more detailed exposure history can be obtained by comparing the concentrations of irradiation products for which the depth dependences of the production rates are different. The ratio of two such products is an indicator in simple cases of the depth at which the sample was irradiated. For samples which have had a complicated history of irradiation at several depths, the ratio will indicate only an effective depth, but this may be sufficient to limit the number of

possible irradiation histories which could be proposed for the samples. In this chapter, two such depth models will be developed in addition to models based on the fluence alone. The first of these compares the concentration of ^{126}Xe produced by spallation reactions to the neutron fluence measured by $^{158}Gd/^{157}Gd$. This model suffers from the requirement that one must know the absolute concentration of ^{126}Xe. To avoid this requirement, a second model will be advanced which only employs isotopic ratios. In this model, the ratio of ^{131}Xe produced from Ba to the ^{126}Xe produced from Ba is used to indicate irradiation depths. This ratio is sensitive to depth because ^{131}Xe (excluding fission and trapped solar wind components) is produced by both ^{130}Ba neutron capture and spallation while ^{126}Xe is produced only by spallation. This model will be shown to be particularly useful in determining the depths at which rocks were irradiated.

5.2 Uniform Mixing Model - Depth of the Regolith

Upon examining the neutron fluences (Table 4-2) of the lunar surface soils, one notices that the soils from each mission tend to group in a narrow fluence range, but that the fluences vary greatly from one site to another. One would like to establish how much of the variation between sites is due to chemical effects on the neutron capture rates, how much is due to actual differences in the depositional history of the regolith at the various sites, and what the fluences imply about regolith history.

These questions are most easily approached in terms of the *uniform mixing model* [2]. In this model (Fig. 5-1), the regolith is assumed to be well-mixed to some depth, L, such that the average neutron flux to depth L multiplied by the age of the site, T, equals the observed neutron fluence of the surface sample.

$$\psi = \frac{T}{L}\int_0^L \Phi(x)dx$$

In this model, the ages of the sites are taken to be the ages of the rocks as determined by Papanastassiou and Wasserburg [3], which are between 3.3 and 4.0 $\times$ 10^9 yr. The neutron flux is taken from the LCH calculations adjusted for the effect of the chemical composition of the site. The mixing depth, L, is the parameter which can be used to compare the relative exposures of the sites. Because the depth dependence of the flux $\Phi(x)$ has a maximum and because the fluence of the surface samples is higher than would be expected for a sample irradiated on the surface for 3-4 $\times$ 10^9 yr, there are, in general, two values of L which will satisfy the model. The shallower solution would allow mixing only in the upper $\sim$ 10 cm of the regolith which is unreasonable because, as will be shown below, the core samples indicate much deeper mixing. The deeper solutions (Fig. 5-2) are interesting in two ways. First, the calculated mixing depths are all very similar except for the Luna 16 sample and the sample from the edge of Hadley Rille (15601), which undoubtedly had a different history than typical soils as will be discussed below. The other ten samples indicate depths between 10-15 m

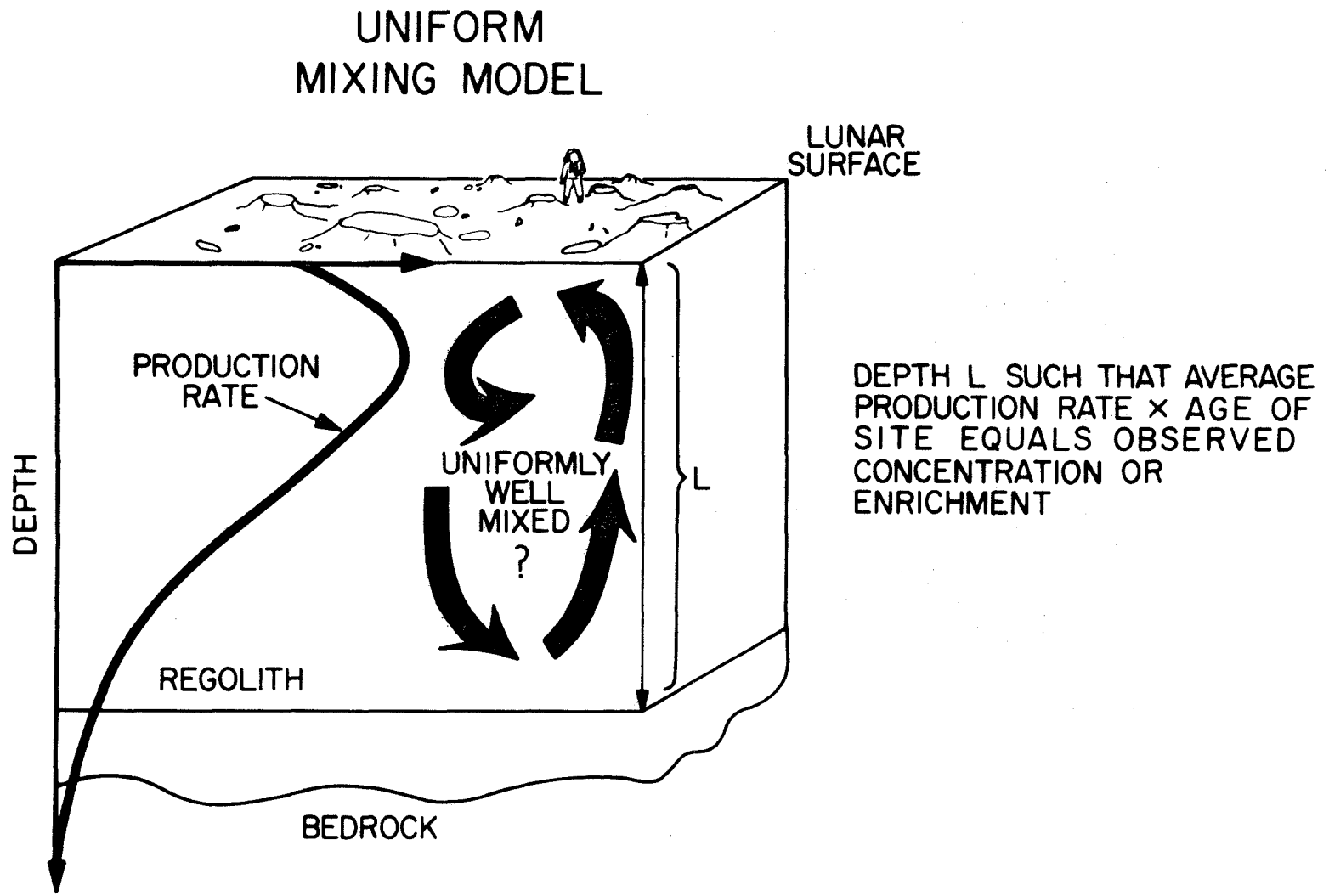

Figure 5-1. Schematic illustration of the uniform mixing model (after an unpublished figure of G. J. Wasserburg and J. C. Huneke).

Figure 5-2

Lunar soil mixing depths calculated from the uniform mixing model. Soil 12033 is from the bottom of a ~ 15 cm deep trench. 15601 is from the edge of Hadley Rille and 15221 and 15231 are from the side of St. George Crater.

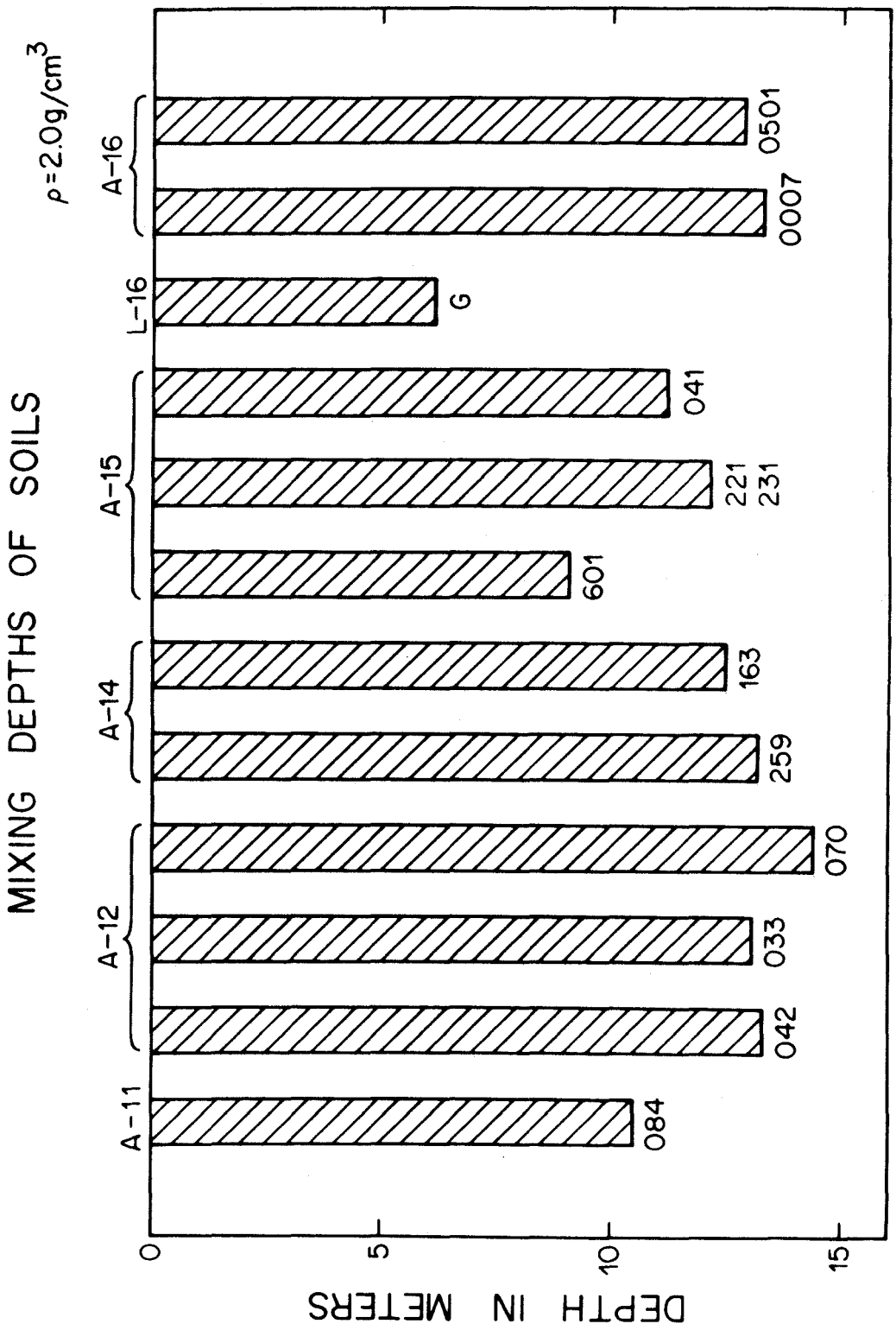
MIXING DEPTHS OF SOILS
ρ=2.0g/cm³
A-16
0501
0007
L-16
G
A-15
041
221
231
601
A-14
163
259
A-12
070
033
042
A-11
084
0
5
10
15
DEPTH IN METERS

Figure 5-2

(assuming ρ = 2.0 g/cm^3) which implies that the regolith depositional processes have been similar over a large part of the moon. The second point of interest is the calculated mixing depths themselves which can be interpreted as lower limits to the thickness of the regolith. The thicknesses calculated on the basis of crater populations and morphology are generally lower than estimated from the neutron data. For the mare sites Apollo 11, 12, 14, and 15, the cratering estimates for the regolith thickness are 3-6 [4], ~ 3 [5], 10-20 m [6], and 5 m [7], respectively. Estimates for the Apollo 16 site vary from 7 m [8] to 15 m [9]. The Active Seismic Experiment has added additional evidence for the highland sites, Apollo 14 and Apollo 16, which indicates regolith thicknesses of 8.5 and 12.2 m [10] for Apollos 14 and 16, respectively. Watkins and Kovach [10] have argued from these data that the regolith at the highland sites is deeper than on the mare because of a higher cratering rate before the maria were formed. The neutron fluence data show no such distinction between the highland and mare sites, and the only site for which the neutron data imply the same thickness as the other methods is Apollo 16. At some of the sites, *e.g.*, Apollos 12 and 14, the samples were collected on or near the ejecta blankets of relatively young craters which presumably penetrated into bedrock and excavated unirradiated material. This *fresh* material would tend to lower the neutron fluence measured in the soils and thereby increase the calculated regolith depth; however, it is unappealing to invoke this special condition at every site. If the cratering and seismic data yield the correct regolith depth, if the measured soils are representative of the site, and if the cosmic ray intensity has been nearly

constant over the last 4×10^9 yr, the necessity of diluting the surface with fresh material to satisfy the fluence data leads to the conclusion that the lower layers of the regolith must be highly irradiated because the total number of neutrons captured per cm^2 column must be conserved. Cratering theorists, *e.g.*, [11], however, believe that the cratering rate was higher in the past which would imply that fresh material was added to the regolith more rapidly in the past. For this reason, one would expect the lower layers of the regolith to be *less* irradiated. The difference in the regolith depths implied by the various techniques is not understood and remains a basic problem of regolith dynamics.

Some insight into the problem of whether the soil samples represent materials which have been irradiated at a variety of depths and mixed, or primarily material which was unirradiated when deposited and irradiated only at the surface, can be obtained by comparing the neutron fluence to the concentration of some other nuclear interaction product for which the depth dependence of the production rate is distinct from that for the low energy neutron flux.

Solar flare particle tracks and solar wind rare gases are useful in estimating the surface exposure of samples and soil accretion times, but they are not useful for determining the effective irradiation depth of samples because they are insensitive below the upper 0.1 mm. Galactic cosmic ray tracks are limited to the upper $\sim$ 10 cm, and, in general, cannot be measured in soils because of the high density of solar flare tracks. Spallation recoil tracks are produced at greater depths but have been studied in only a limited number of cases. Rare

gas nuclides produced by high energy spallation reactions caused by cosmic rays are more useful because these nuclides are produced in a depth range comparable to that of neutrons, and because they have been extensively studied. The depth dependence of rare gas production rates is distinct from that of the low energy neutron flux because the spallation reactions occur at much higher energies ($\gtrsim$100 MeV). By comparing the concentration of such a spallogenic nuclide, *e.g.*, ^{126}Xe, to the neutron fluence as measured by Gd, one can estimate the effective depth at which a soil was irradiated.

5.3 Spallogenic ^{126}Xe and Soil Irradiation Depths

The magnitude and depth dependence of the ^{126}Xe production rate from spallation reactions can be estimated as described in Appendix III. The relative depth dependences of the ^{126}Xe and ^{158}Gd production rates in material of uniform chemical composition are illustrated in Figure 5-3. The ^{126}Xe curve is seen to have a peak near the surface, which is caused by the buildup of secondary particles produced in the regolith, while the ^{158}Gd curve peaks at a greater depth because of surface neutron leakage. However, at depths beyond the peaks, the production rates decrease with similar attenuation lengths reflecting the decreasing cosmic ray flux. The ratio of the two production rates (Fig. 5-3) is a monotonically increasing function of depth which approaches a constant value at depths beyond the peaks of the production curves. If the ^{126}Xe curve is correct, it should be possible to specify the depth within the upper $\sim$ 400 g/cm^2 at which a sample was irradiated provided it was exposed at only one depth and recently brought

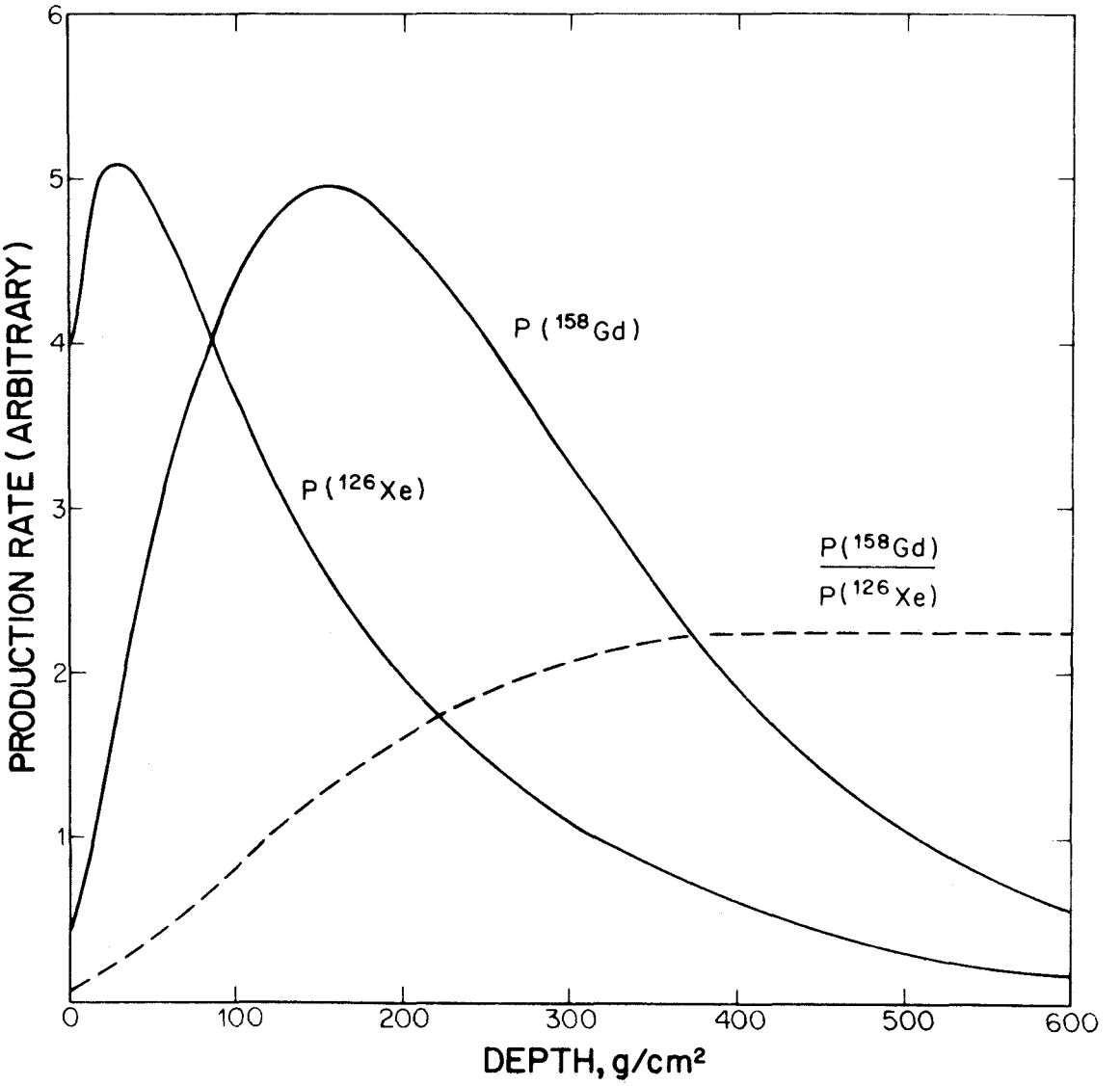

Figure 5-3

The depth profile of the ^{158}Gd production rate as calculated by LCH and that for ^{126}Xe by the model presented in Appendix III. With increasing depth, the ratio of the ^{158}Gd production rate to that for ^{126}Xe rises monotonically from its minimum value at the surface to a constant value below a depth of ~ 400 g/cm^2.

to the surface. If soils are composed of particles which have been irradiated at a variety of depths and mixed as a result of cratering events, it should be possible from the ^{126}Xe to fluence ratio to define an effective mixing depth for these grains, which is not dependent on a specific mixing model. If a soil has been excavated from a highly shielded position and subsequently irradiated only near the surface, the ^{126}Xe (spallation) to neutron fluence ratio should be lower than in a soil which is composed of grains which have been irradiated at depths throughout the regolith.

The experimental ^{126}Xe concentrations per target atom (calculated as Ba + 1.65 Ce [44]) for soil samples have been plotted against the neutron fluence in Figure 5-4. Because the neutron flux is different at each of the sites, the fluences have been normalized to the flux at the Apollo 12 site. This allows one to compare the data from all the samples on a single plot. For the moment, ignore the calculated irradiation depths and look at the data points. All the Apollo 11, 12, and 14 and the Luna 16 samples fall in a fairly narrow band with positive slope which appears to pass through the origin. (The distance of a sample from the origin is a measure of its exposure age.) This is the behavior expected if all of the samples have had similar depth histories during their irradiation; however, because all the rare gas data from these sites were not obtained by the same workers, they may contain systematic differences. The situation is somewhat complicated for the Apollo 15 and 16 samples because of experimental uncertainties. In several cases, duplicate samples (not splits but samples from the same depth in the drill stem) yielded significantly different ^{126}Xe

Figure 5-4

Correlation of cosmogenic, *i.e.*, spallogenic, ^{126}Xe per unit target atom (calculated as Ba + 1.65 Ce [44]) with the low energy neutron fluence, ψ, normalized to the fluence which would have been measured in an Apollo 12 sample. The normalization takes into account the differences in the neutron fluxes at the various sites. The longer dashed lines are correlations expected for continuous exposure at the surface, 100 g/cm^2, and $\geq$400 g/cm^2. The shorter dashed lines are the correlations expected for samples which have been recently or frequently mixed to 200 g/cm^2 (~1 m) and to depths below the zone in which significant production occurs. The vertical dashed lines connect duplicate analyses of Apollo 15 points. The xenon data were taken from Huneke [12] - Apollo 11, 12, and 14; Bogard and Nyquist [13] and Bogard *et al.* [14] - Apollo 15 and 16; and Kaiser [15] - Luna 16. Ba and Ce concentrations were taken from references [16, 17, 18, 19, 20, 21] or were estimated where no data were available. The quoted uncertainties on the ^{126}Xe concentrations are $\pm$ 10%. The typical error for a ψ measurement is somewhat smaller than that shown for the sample near the origin (14141). A similar figure for Apollo 11 and 12 rocks was published by Burnett *et al.* [27].

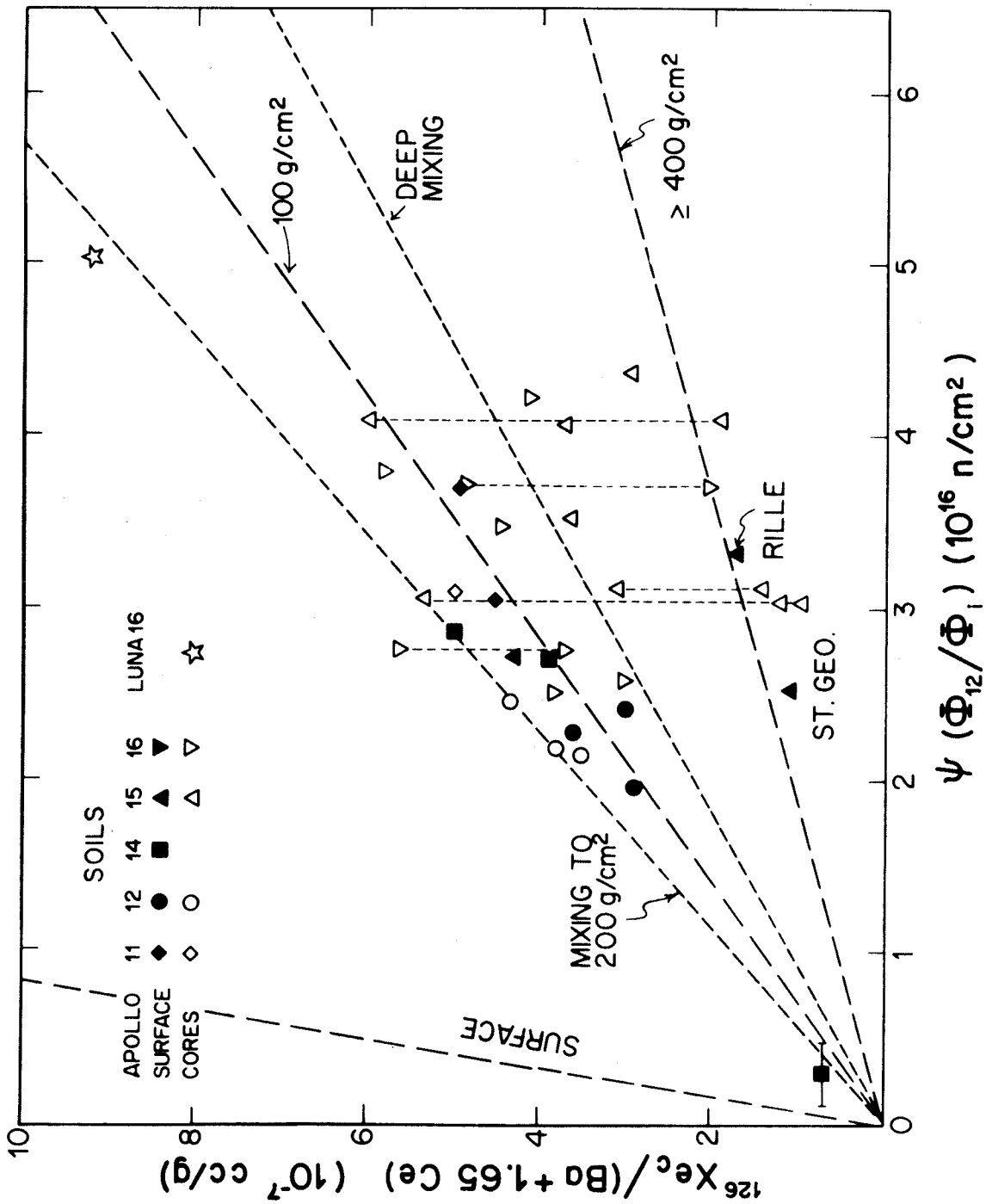
$^{126}Xe_c/(Ba + 1.65\ Ce)$ (10^{-7} cc/g)
$\psi\ (\Phi_{12}/\Phi_i)$ (10^{16} n/cm^2)
SURFACE
100 g/cm^2
DEEP MIXING
≥ 400 g/cm^2
MIXING TO 200 g/cm^2
RILLE
ST. GEO.
SOILS
APOLLO 11 12 14 15 16 LUNA 16
SURFACE CORES

Figure 5-4

concentrations [14]. It seems unlikely that these variations, which are larger than the overall variation throughout the drill stems, could be due to real differences in gas content. For all the Apollo 15 and 16 samples on which duplicate analyses were made, at least one value falls in the grouping observed for the earlier sites. The points which fall outside this grouping may represent samples with different exposure histories or may be the result of bad data.

Using the model developed above for the ^{126}Xe depth dependence and production rate, the ^{126}Xe vs. ψ correlation lines expected for exposures at various depths have been calculated (Fig. 5-4). Alternatively, one may consider the soils to be well mixed to some depth and calculate the correlation expected for such a sample (Fig. 5-4). With the exception of some of the Apollo 15 and 16 samples for which the ^{126}Xe data are questionable, all of the surface soil and core samples are compatible with having been irradiated at a depth of ~100 g/cm^2, or more reasonably, since most of them are now at the surface, with having been mixed to a depth of greater than ~200 g/cm^2. It should be remembered that the ^{126}Xe production curve is not well established; therefore, these depths should only be considered as approximations. There is, however, no evidence (except possibly for the Cone Crater soil 14141, which plots near the origin) for soils which have been irradiated predominantly near the surface, *i.e.*, in the upper $\sim \frac{1}{4}$ meter. The fact that none of the soils appear to have been irradiated only near the surface implies that the differences between the "uniform mixing" depths calculated above and

the regolith depths estimated from cratering theory cannot be explained by invoking deposition of layers of unirradiated material unless this material has been mixed throughout the upper 1-2 meters after its initial deposition. Because the ratio of ^{126}Xe to ψ is relatively insensitive to changes in the mixing depth below $\sim$ 1 m, this ratio cannot be used to estimate the actual depth of the regolith. The fact that the measured points plot somewhat above the line predicted for deep mixing means that model regolith depths calculated from ^{126}Xe by the uniform mixing model would be somewhat less than those calculated from the neutron fluences. The ^{126}Xe depths would, however, be deeper than those predicted by photogeology.

The Cone Crater soil 14141 is a special case in that it was collected near the rim of this crater. One would expect it to be fresh material ejected by the cratering event and irradiated only at the surface. This sample, however, appears to have been irradiated somewhat below the surface (Fig. 5-4). As discussed by Burnett, Huneke, Podosek, Russ, Turner, and Wasserburg [22], this observation may be explained in two ways. Either some material ($\sim$ 10% of the sample) was transported to the crater rim from the surrounding smooth areas, or one may be observing residual surface material which existed at the site before the impact and was mixed with unirradiated material during the formation of the crater.

5.4 Core Samples - Neutron Stratigraphy

5.4.1 Models

A more detailed picture of the developmental history of the regolith at a given spot can be obtained by studying the variation of neutron fluence, rare gas concentration, track density, and stratigraphic units with depth in core tube samples. The neutron fluence has been measured as a function of depth in the 13 cm core from Apollo 11, the double core ($\sim$ 60 cm) from Apollo 12 and the drill stems from Apollos 15 and 16. These drill stems each penetrated over 2 m into the regolith.

In order to describe the history of the regolith at the various sites, one must develop a model which predicts the depth dependence of the fluence for various possible depositional histories. Models for soils which have been rapidly deposited and otherwise undisturbed, well mixed, gradually accreting, *i.e.*, material being deposited, or eroding have been developed and are presented in Sections 8.4.3 and 9.4.3. They will be used here without further elaboration to discuss the fluence profiles observed in the four cores.

In the models presented in this work and those of others, *e.g.*, [14,23,24], the concept of mixing is invoked to explain certain features of the depth profiles observed for the various reaction products. To understand the meaning of *mixing* in the lunar context, one must consider the process which does the mixing. One is not dealing with eggbeaters or worms which homogenize the soil particles and destroy all records of layering. The almost certain cause of regolith mixing is impact-produced cratering.

Consider an area where there has recently been an impact. This area will be topographically low, and the ejecta from nearby impacts will tend to gradually refill the depression. The material which fills it may have been buried and excavated in previous impacts and each layer may have a unique pre-irradiation history and fragmental composition. If the materials deposited in the various layers have themselves undergone many cycles of ejection and accumulation, they may, on the average, have experienced similar irradiations while still maintaining subtle textural and/or compositional differences. This is particularly true for products which are produced over a wide depth range, *e.g.*, ^{158}Gd. Products which accumulate only at the surface, *e.g.*, solar flare tracks, may show larger variations from layer to layer because they are produced only under very restricted conditions.

If one takes a core which samples an area where an old crater has been filled, one may find discernible layering, but these layers may have had similar irradiations. The stratigrapher would, therefore, say that the area had been subject to discrete events which deposited the layers. A person modeling the irradiation history would say the regolith was well-mixed. Mixing in this work will be taken to mean the result of repetitive excavation and deposition where these processes take place on a time scale which is short compared to the ability of a technique to measure changes.

5.4.2 Apollo 11 Core 2

Eugster *et al.* [2] measured the gadolinium isotopic composition

in two samples from the Apollo 11 core 10004. From their data, one can calculate the neutron fluences to which these samples have been exposed (Table 4-2) and can use these values (2.44 ± 0.13 and 2.47 ± 0.16 × 10^{16} n/cm^2 - top and bottom, respectively) to set a limit on how long this core could have been stratified in its present configuration. Assuming that the samples had the same fluence when deposited and that the deposition was rapid, one calculates from the extremes of the errors that this core could not have been unmixed for more than 2 × 10^8 yr. Eugster *et al.* [2] set a more restrictive limit of 1 × 10^8 yr, but their value was based on a thermal flux spectrum which does not obtain on the moon. The observed densities of solar flare tracks in this core and core 10005 [24,25,26] also imply mixing and/or pre-irradiation. Because of the shallow depth involved (~ 13 cm) and the fact that there are only two fluence measurements for 10004, no attempt has been made to construct more detailed or alternate models of this core.

5.4.3 Apollo 12 Double Core

The first core for which detailed fluence data were obtained was the Apollo 12 Double Core (12025 and 12028 — upper and lower sections, respectively). Burnett, Huneke, Podosek, Russ, and Wasserburg [27] analyzed six core samples and Lugmair and Marti [28] analyzed three. In addition, Burnett *et al.* [27] analyzed the trench soil 12033 and two surface soils 12042 and 12070. The fluence is quite constant from the surface to a depth of ~ 50 g/cm^2 (Fig. 5-5). Below this depth, it is apparently slightly higher, but again constant to the bottom at a depth

Figure 5-5

Neutron fluence and spallogenic ^{126}Xe concentration as a function of depth in the Apollo 12 Double Core and the depth profiles expected for material deposited instantaneously with a uniform isotopic composition recently, 50 my, and 100 my ago. The open circles are the data of Lugmair and Marti (Table 4-2). The x's labeled A + B are sized fractions of sample 12028,110. The samples are all assumed to have been deposited with the ψ and ^{126}Xe indicated by the 0 my curves. The dashed line labeled 3,300 my is the profile expected for a core stratified for that period of time.

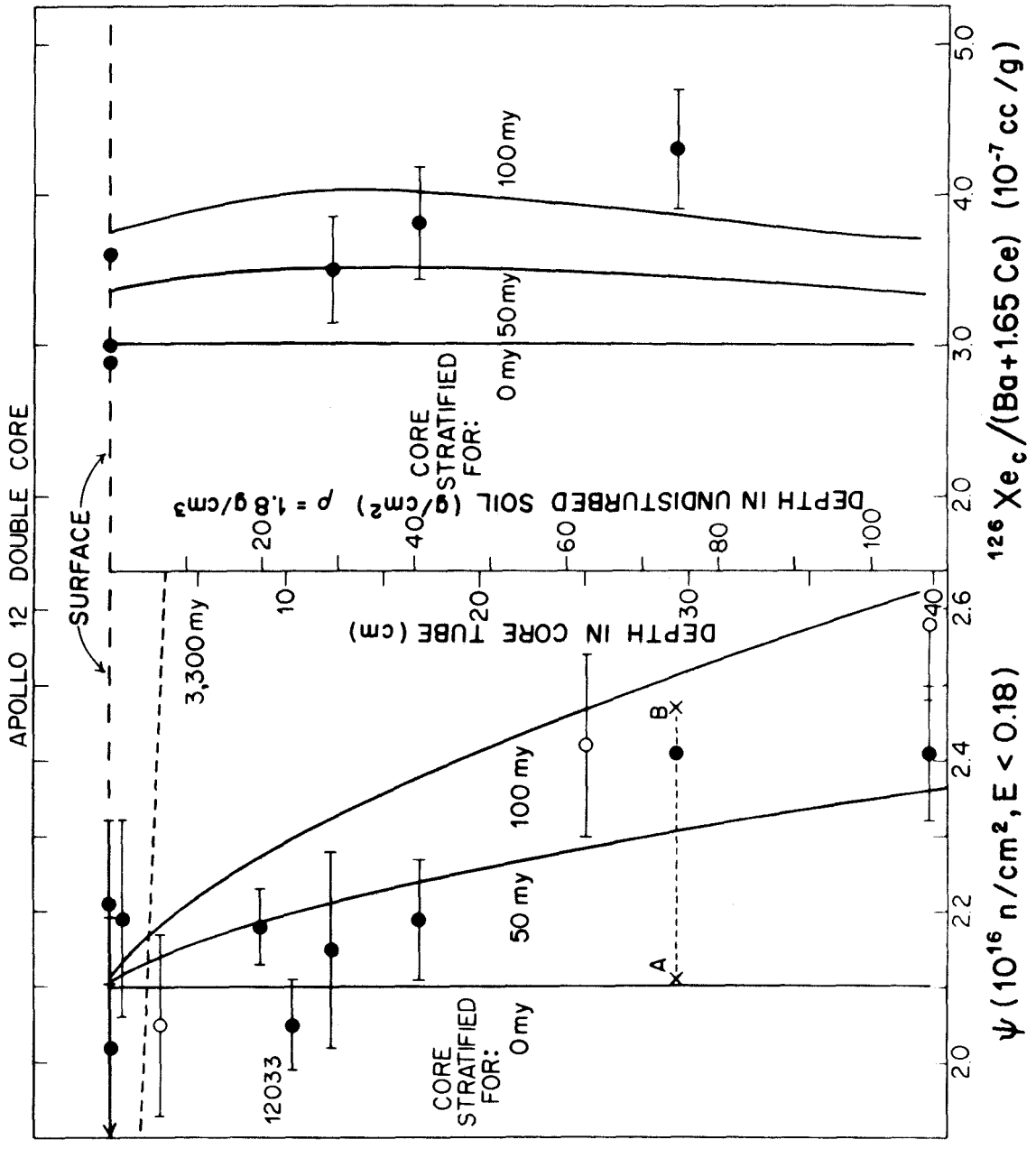
APOLLO 12 DOUBLE CORE
SURFACE
3,300 my
12033
CORE STRATIFIED FOR: 0 my
50 my
100 my
A
B
DEPTH IN CORE TUBE (cm)
DEPTH IN UNDISTURBED SOIL (g/cm²) ρ = 1.8 g/cm³
CORE STRATIFIED FOR: 0 my 50 my 100 my
ψ (10¹⁶ n/cm², E < 0.18)
¹²⁶Xe_c/(Ba+1.65 Ce) (10⁻⁷ cc/g)

Figure 5-5

of ~ 110 g/cm^2. The data do not, however, exclude a smooth variation in fluence throughout the core. It should be noted that the surface soils are actually scoop samples which sampled the upper ~ 10 g/cm^2 rather than the actual surface. In addition to the neutron fluence, the concentration of ^{126}Xe produced by spallation reactions was also measured by Burnett *et al.* [27] for three depths in the core and for three sized fractions of 12042. In the following discussion, the fluence and ^{126}Xe data will be used to model the depositional history of the regolith at this site, and the conclusions will be compared to those based on tracks and layering.

Because the fluence and ^{126}Xe concentration are essentially constant throughout the core, one can consider a model in which the material was deposited rapidly with a constant degree of pre-irradiation and has been undisturbed subsequently (see Sec. 8.4.3). From the limit on the variation of the fluence and/or ^{126}Xe, one can set an upper limit on the time elapsed since the material was deposited. This time may also be considered as the time since the core was last mixed. If the fluences of the samples were $\sim 2.1 \times 10^{16}$ n/cm^2 when they were deposited, the data are compatible with a subsequent irradiation of ~ 50 my (Fig. 5-5). An undisturbed irradiation of 100 my would be compatible with the data if the initial fluence was assumed to be somewhat lower, but the undisturbed period could not appreciably exceed 100 my. The ^{126}Xe data are roughly compatible with this model if the concentration is assumed to have been $\sim 3 \times 10^{-7}$ cc/g (target, *i.e.*, Ba + 1.65 Ce [44]) when the regolith was deposited. The ^{126}Xe data do, however, appear to indicate a deeper concentration peak than predicted.

There is at least one very well defined layer in this core [31]. The presence of such a distinct layer implies that the material sampled was not deposited in a single event because of the necessity of more than one source. It is therefore reasonable to consider accretional models and attempt to set a limit on the rate of accretion of the material sampled. The increase in fluence and ^{126}Xe with depth, although slight, is compatible with such models.

Consider a model in which it is assumed that there has been no mixing by small impacts of the material once it has been deposited, and that the material being deposited has been irradiated at various depths for the age of the site as given by the ^{87}Rb-^{87}Sr age (3.3×10^9 yr for Apollo 12 [3]). If the material being deposited is typical soil, its degree of pre-irradiation, *i.e.*, exposure to cosmic rays prior to this deposition, will depend on the age of the site at the time of deposition and the effective depth to which the material has been mixed. In order to match the observed surface fluence, this depth must be the uniform mixing depth discussed above (Sec. 5.2). To the extent that the regolith is well-mixed, this depth may be used to describe the pre-irradiation of all the layers. By this model, the degree of pre-irradiation of the layers will decrease with increasing depth because the deeper layers were deposited earlier. With these assumptions about the material being deposited, one can calculate the accretion rate which matches the observed depth dependence of the fluence. As shown in Figure 5-6, for an assumed mixing depth of 2900 g/cm^2 ($\sim$ 16 m) the data can be fitted reasonably well for accretion rates of 90 g/(cm$^2 \cdot 10^8$yr) or

Figure 5-6

Model ψ and ^{126}Xe depth profiles for the Apollo 12 Double Core calculated for a continuously accreting regolith. The material is constrained to accumulate at the rate V and to be excavated from a 3.3×10^9 yr old source which has been mixed to a depth L. The data symbols are the same as in Figure 5-5.

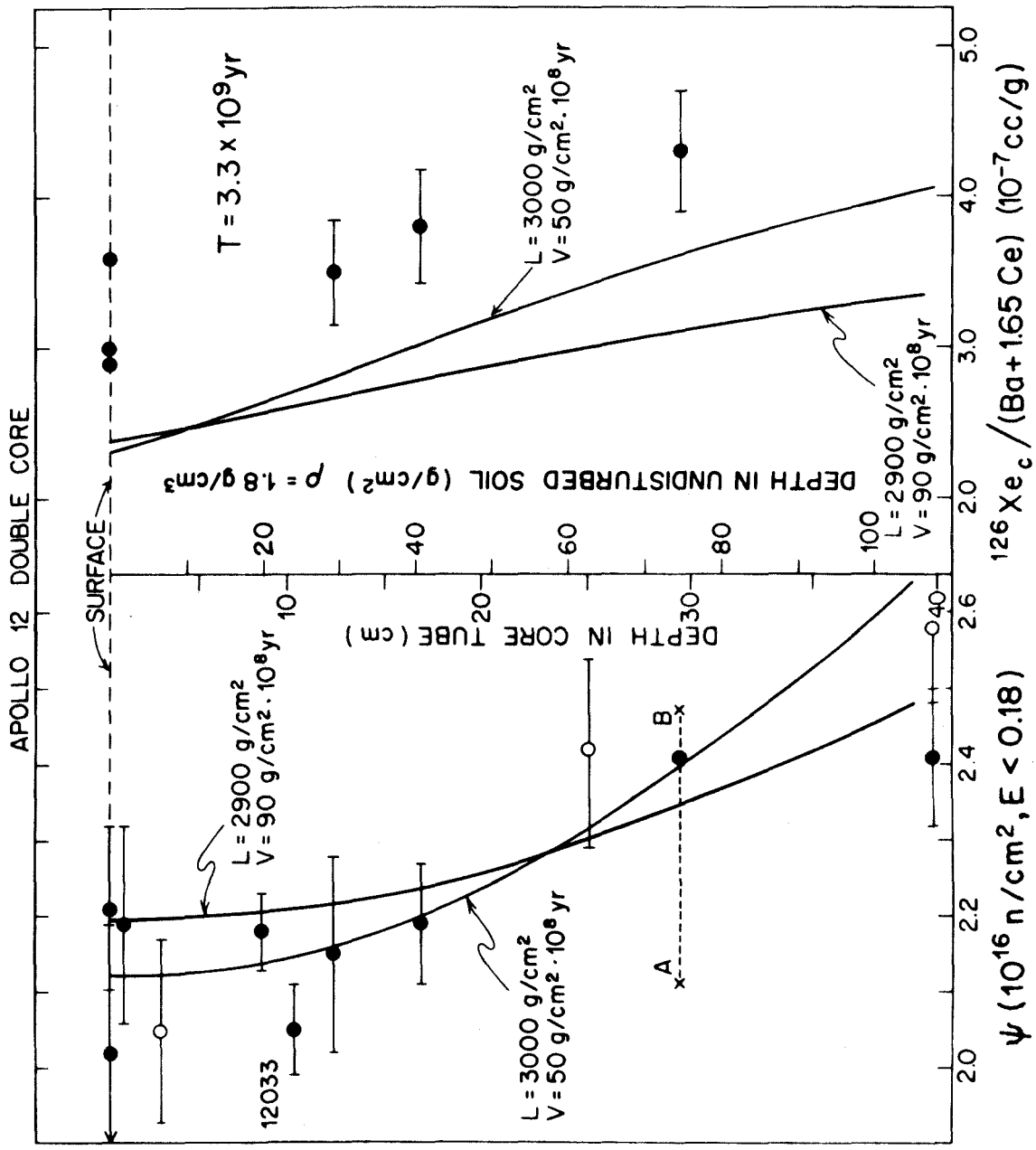
APOLLO 12 DOUBLE CORE
SURFACE
T = 3.3 x 10⁹yr
L = 3000 g/cm²
V = 50 g/cm².10⁸yr
L = 2900 g/cm²
V = 90 g/cm².10⁸yr
DEPTH IN UNDISTURBED SOIL (g/cm²) ρ = 1.8 g/cm³
DEPTH IN CORE TUBE (cm)
12033
A
B
ψ (10¹⁶ n/cm², E < 0.18)
¹²⁶Xe_c /(Ba+1.65 Ce) (10⁻⁷cc/g)

Figure 5-6

more. By increasing the mixing depth of the source material to 3000 g/cm^2, the accretion rate could be lowered to ~50 $g/(cm^2 \cdot 10^8$ yr). This lower rate implies a total time of $\leq$200 my during which the material was deposited. (If, instead of taking the age of the rocks as the time during which the source material had been irradiated, one had assumed that all the Gd was added in the KREEP component [29] ~ 800 my ago [30], the implied mixing depth for the Apollo 12 site would be decreased to ~ 4 m. Because the pre-irradiation time of the lower layers would be small under this assumption, the accretion rate could be reduced somewhat.)

Using the first two sets of parameters given above, the expected ^{126}Xe profiles were calculated for the accretion model. As one could predict from the discussion of the ^{126}Xe model (Sec. 5.3), the mixing depths which fitted the neutron fluences underestimate the measured ^{126}Xe concentrations. The shapes of the profiles, however, are in good agreement with the experimental data.

This core was not deep enough to establish whether this has generally been an area of accretion, or whether only recently mixed surface layers were sampled.

Ten separate stratigraphic units have been identified in this core [31]. The lithology, grain size distribution, and other physical characteristics of these units have been exhaustively studied. These studies have led to the conclusion that this has generally been an area of accretion with new layers being added before the older surfaces *matured* [32]. Quaide, Oberbeck, Bunch, and Polkowski [33] have

suggested that the presence of layers may indicate that the core was taken in a filled crater where the rate of deposition had been rapid. Arrhenius *et al.* [34] reported that the upper portion of several of the morphologic units had higher cosmic ray track densities than the lower part, and concluded from this and the assumption of little pre-irradiation that the units had been deposited at intervals of 5 to 50 my. On the other hand, Comstock *et al.* [23] found no significant depth variation to the cosmic ray or spallation track densities and concluded the regolith was well mixed if the grains were not pre-irradiated. This conclusion was also reached by Crozaz, Walker and Woolum [35]. The content of ^{132}Xe from the solar wind was also found to be essentially constant in three core samples [27] supporting the mixed model. Other solar wind gases, however, showed a peak at a depth of $\sim$ 12 cm [28] which is near the depth reported by Arrhenius *et al.* [34] to have the highest track density.

The stratigraphic units are good evidence that the sampled stratigraphy resulted from an accretional process, *i.e.*, deposition of discrete layers. However, with the possible exception of layer VI, which was clearly morphologically anomalous [32] and which had a low track density [34] (but which was unfortunately not analyzed for neutron fluence), the units represent fairly typical regolith materials; therefore, although the section was deposited as discrete layers, it may be considered mixed in the sense described above (Sec. 5.4.1) and most of the neutron fluence, spallogenic rare gas, and spallation tracks almost certainly represent pre-irradiations rather than production during the

latest accretional cycle. This may also be true for the solar flare and cosmic ray tracks and solar wind rare gases.

5.4.4 Apollo 15 Drill Stem

The Apollo 15 drill stem, which penetrated the regolith to a depth of ~ 2.4 m, provided the first samples which showed definite depth variations in the neutron fluence. It has been shown in the paper which constitutes Chapter 8 and which should be read at this time, that the smooth peak observed in the fluence in this core requires that this material has not been disturbed for at least 400 my except in the upper ~50 g/cm^2. The fluence data are, however, compatible with a wide variety of possible depositional histories. By varying the amount of pre-irradiation and the deposition rate, models are possible for which the whole section sampled could have been deposited instantaneously if the material were pre-irradiated, or it could have been deposited layer by layer over a period as long as 400 my if the material were unirradiated. Models in which the amount of pre-irradiation increased with time were also presented, but the above conclusions remained unchanged. All of the models require that the upper ~ 50 g/cm^2 be added after the main mass was deposited, or at least that some typical soil be mixed in to explain the fluence near the surface.

The core was taken in the area of a long (several km), low ridge which has a higher albedo than the surrounding mare material. This ridge has been interpreted as a ray from the crater Autolycus and/or Aristillus [7]. One would expect that material ejected from craters of

this size (> 10 km in diameter) would on the average be unirradiated, but no evidence was seen in the fluence data for a thick, rapidly deposited layer with no pre-irradiation. The preferred interpretation of the fluence data (see Sec. 8.5) was that this core was drilled in an area which had been topographically low more than 400 my ago, which had been subsequently filled to the normal regolith level, and which had not been disturbed thereafter except near the surface.

Shoemaker [36] has suggested a model which seems to reconcile the idea about the ray and the measured fluence data. Assume that the ridge is in fact a ray from Autolycus, that its fluence was essentially zero when deposited, and that the site which was eventually sampled by the drill stem was topographically low. This low spot could have resulted simply from irregularities in the deposition of the ray or from a subsequent crater. The rate of filling of such a depression will depend on its size and shape, but, in general, the rate will be fastest when the depression is deepest and will slow as it is filled. This is particularly true for a conical crater in which the filling rate will be very fast at first and systematically decrease as the crater is filled because a given volume of material will fill a greater depth near the bottom than near the top. In Shoemaker's view [36], the drill stem sampled a depression on the ray which had been filled by the deposition of layers of material which proceeded at a decreasing rate until the depression was filled and the accretional process stopped. Prior to being deposited in the depression, the material was being increasingly pre-irradiated as it was mixed in the upper $\sim$ 1 m of the ray. After the depression was filled, the regolith remained undisturbed except for near surface mixing until the core was taken.

Although the models discussed in Chapter 8 are for accretion at constant rates, the fluence data are shown (Sec. 8.4.3) to be compatible with the regolith having been accreted in two stages where the first stage is characterized by a faster accretion rate than the second, and where the amount of pre-irradiation increases with time. Such two-stage models approximate the model suggested by Shoemaker in which the accretion rate is continuously decreasing. It, therefore, seems that his model is compatible with the neutron fluence data.

If the decreasing accretion rate model is applicable to this site, the concentration of solar wind rare gases and the solar flare and cosmic ray track densities should be lower in the lower sections of the core than near the surface because the lower layers were deposited before the pre-irradiation was as significant as in the material added later, and because the lower layers were buried faster thereby reducing the near surface *in situ* irradiation. These effects should be particularly evident if the source of the material being deposited was unirradiated when the bottom of the depression was filled, as might be the case if the high albedo ridge is a ray.

High track densities have been reported at all depths sampled by Crozaz *et al.* [37] and Phakey, Hutcheon, Rajan, and Price [38]. Bhandari, Goswami and Lal [39] have conducted detailed studies of sections 15004 and 15002 and one sample of 15001. They find that the average track density increases in going from the deepest samples toward the surface. The fraction of grains with high track densities ($>10^8 cm^{-2}$) also increases. Wszolek, Jackson, and Burlingame [40] have reported an essentially linear decrease with increasing depth in the concentration

of carbon compounds and solar wind ^{20}Ne and ^{36}Ar. All their samples, however, have high concentrations of these gases. High, variable concentrations of solar wind gases were reported by Bogard *et al.* [14] who saw no clear trend with depth. The spallogenic rare gases reported by Bogard *et al.* [14] are compatible with models involving an undisturbed period of $\sim$ 400 my plus an accretional period or pre-irradiation.

The track and rare gas data are somewhat ambiguous with respect to variations with depth and the high concentrations of tracks and solar wind gases do not seem to support the Shoemaker model. This model may, however, be essentially correct because the ray may have been deposited considerably earlier than the material collected by the bottom of the core. This could be because the core did not penetrate to what was the bottom of the now-filled depression (or crater) and/or because the depression was formed significantly after the ray. If the high albedo ridge is a ray from Autolycus, and if this material was deposited before the layers sampled by the drill stem, Autolycus must be at least 400 my and possibly more than a billion years old.

5.4.5 Apollo 16 Drill Stem

The Apollo 16 drill stem samples, for which the fluence data is described and interpreted in Chapter 9, have had a distinctly different recent irradiation history than those from the Apollo 15 drill stem. The fluence data for the Apollo 16 drill stem show that this site has been dominated by regolith accretion. At least two slabs of material have been involved in this process of deposition, but the number could

be much larger. Continuous accretion models are also compatible with the data if a variable pre-irradiation is assumed to explain the relatively high fluences observed in the samples from section 60004. The spallogenic rare gas data of Bogard *et al.* [14] show a depth profile very similar to that observed for the neutron fluence (Fig. 9-5), including the bump at section 60004. The track density measurements of Behrmann *et al.* [41] show more variation with depth than previously observed by these workers, and the sample from near the top of section 60004 has the highest track density they have observed in a soil. These data, and the observation of Hörz *et al.* [42] of a fine layer near the top of this section, support models which treat this section as a distinct layer. This implies that at least three distinct depositional events were sampled, and that the upper part of 60004 may have had an unusually long near-surface irradiation or a distinct source.

5.4.6 Generalizations

A feature common to all four cores studied is that the neutron fluence appears to be essentially constant throughout the upper $\sim$ 100 g/cm^2 even though the neutron flux increases rapidly with depth in this region. One can only say "appears to be constant" because detailed near-surface studies were done only on the Apollo 12 core. In the other cores, only two or three analyses were made in this depth region. The relative constancy of the near-surface fluences suggests that the regolith is mixed to a depth of 50-100 g/cm^2 on a time scale of $< 10^8$ yr. Because mixing implies rapid excavation and slower deposition

(Sec. 5.4.1), mixing to 100 g/cm^2 in 10^8 yr indicates that material at low areas is accreted at a rate of ~ 5 mm/my. This is also the rate implied for the accretion of the layers sampled by the drill stems. The drill stems, however, imply that the regolith is not mixed to a depth of 2 m for 500 my or more. Gault [43] has recently calculated that a given spot on the regolith should, on the average, be cratered to a depth of 2 m about once every 500 my. If this is true, then depth profiles like that observed in the Apollo 16 drill stem should be more common than the one observed at Apollo 15, which may not have been cratered to 2 m for 10^9 yr.

As explained in the definition of mixing given above, regolith stratigraphy is almost certainly controlled by cratering and the ejecta associated therewith; therefore, it is not surprising that one finds accretional areas with discrete layers. Because the cores were collected in relatively flat areas, it is also not surprising that erosional profiles were not observed. In such terrain material will be removed in one event, but many events will be needed to replace it. Consequently, one sees accretional surfaces most often.

5.5 Lunar Rocks

5.5.1 Introduction

The low energy neutron fluence has been measured for a large number of Apollo 11 and 12 rocks. This work, which was done mostly by Eugster *et al.* [2] and Marti and Lugmair [28], has shown that the fluences of rocks are generally less than those of the associated

regolith material (see Table 4-2). This relationship is consistent with the generally held idea that the regolith is composed of rock fragments which have been repeatedly eroded by impacts. Rocks are presumed to be excavated from bedrock by cratering events. These rocks are then mixed in the regolith and gradually eroded and/or broken by impacts. The longer they are exposed to cosmic rays and meteoritic impacts, the smaller and more irradiated they become. A notable exception is rock 10017, which has nearly twice the fluence of the surrounding soil. The relatively low fluences of the rocks require that they have been buried at depths of at least several meters throughout most of their history.

In order to understand the exposure history of a rock to particle irradiations, *i.e.*, cosmic ray, solar wind, and solar flare particles, it is necessary to know the burial and/or excavation history of the rock. As discussed above for soils, information about exposure depths can be obtained from the ratio of the concentrations of two products whose production rates have different depth dependences. Following the model given for soils, attempts were made to calculate ^{126}Xe-ψ exposure depths for rocks. This proved to be a useless approach because it was necessary to use ^{126}Xe concentration data from several laboratories which, presumably because of a lack of inter-laboratory standardization, obtain Xe concentrations in significant disagreement. This difficulty was also encountered in trying to compare the measured ^{131}Xe excesses, which appear to result from neutron capture on ^{130}Ba, to those predicted from the amount of Gd neutron capture (see Sec. 4.9). The following model,

which depends on the $^{131}Xe/^{126}Xe$ ratio and not absolute concentrations of rare gases, was therefore developed to estimate exposure depths.

5.5.2 $(^{131}Xe/^{126}Xe)_{Ba}$ Depth Model

The xenon in lunar samples is composed of several components including fission products, trapped solar wind, and a cosmogenic component. The cosmogenic component includes the products of spallation reactions and, in the case of ^{131}Xe, the product of neutron capture by ^{130}Ba. Standard data handling techniques exist for separating the fissiogenic and trapped components from the cosmogenic component. Because ^{131}Xe is produced by both neutron capture and spallation reactions while the cosmogenic ^{126}Xe is produced only by spallation reactions, and because neutron capture reactions have a different depth dependence than spallation ones, the cosmogenic ratio $^{131}Xe/^{126}Xe$ can be used to determine the effective irradiation depth of a sample. A model for the production of ^{126}Xe as a function of depth was discussed above (Sec. 5.3). Assuming that the spallogenic $^{131}Xe/^{126}Xe$ ratio is independent of depth, one can calculate the production rate of ^{131}Xe (spallation) as a function of depth if the spallogenic $^{131}Xe/^{126}Xe$ ratio is known. The LCH calculations allow one to predict the depth dependence of the ^{130}Ba neutron capture rate (Sec. 4.9). Combining these functions one can calculate the depth dependence of the cosmogenic $^{131}Xe/^{126}Xe$ ratio. (One could also calculate the $^{131}Xe(neutron)/^{126}Xe(spallation)$ depth dependence and use this ratio to determine depths. Such a model would differ from the one developed here only in that the data would have

to be corrected individually for the spallogenic ratio, whereas in the model which will be used, the spallogenic ratio is included in the model and the data need not be adjusted.)

Spallogenic Xe is produced mainly from Ba and the rare earth elements. Because the ratio of these elements varies in lunar samples and the spallogenic $^{131}Xe/^{126}Xe$ ratio varies accordingly, variations in chemical composition must be taken into account in the depth model. A convenient way to do this is to subtract the rare earth contribution and base the model on the $^{131}Xe/^{126}Xe$ ratio produced from Ba where both spallation and neutron capture are included. This ratio will be designated $(^{131}Xe/^{126}Xe)_{Ba}$.

To construct the model depth profile, one must know the $^{131}Xe/^{126}Xe$ ratio produced by spallation reactions on Ba in lunar rocks. This ratio cannot be measured directly, but it can be estimated from the measured cosmogenic $^{131}Xe/^{126}Xe$ ratio in a rock, which was exposed only at the surface and therefore has the least neutron capture component; the spallation systematics of Huneke, Podosek, Burnett, and Wasserburg [44]; and the $^{131}Xe/^{126}Xe$ ratio for spallation by the rare earth elements, as measured in the laboratory. As will be shown, the calculations are not highly sensitive to the ratio used for rare earth spallation. Rock 10049 has been taken as the standard because of its low $^{131}Xe/^{126}Xe$ ratio and because it has apparently been exposed only at the surface [44]. Huneke *et al.* [44] have shown that the yield of ^{126}Xe from spallation can be described by the relationship

$$^{126}Xe = [Ba]\cdot[1+1.65(Ce/Ba)]\cdot P_{126}(Ba)$$

where the contribution from the rare earth elements is described by the Ce term, $P_{126}(Ba)$ is the production rate from Ba, and typically Ce/Ba ≈ 0.25. Using this equation, the Xe data for 10049 of Bogard, Funkhauser, Schaeffer and Zähringer [45], as reduced by Burnett [46], the Ce/Ba ratio of Gast, Hubbard, and Wiesmann [47], and the Hohenberg and Rowe [48] ratio for $^{131}Xe/^{126}Xe$ from Ce spallation ($^{131}Xe/^{126}Xe = 1.15$), the $^{131}Xe/^{126}Xe$ ratio for spallation reactions on Ba has been calculated to be 4.46. This value has then been combined with the ^{126}Xe depth dependence and the depth dependence of the neutron flux to calculate the $(^{131}Xe/^{126}Xe)_{Ba}$ depth dependence shown in Figure 5-7. If the Ce spallation ratio had been taken as 2, as inferred from Huneke *et al.* [44], rather than 1.15, the predicted $(^{131}Xe/^{126}Xe)_{Ba}$ ratios would be changed by only about 10%.

In order to use this model, measured Xe isotopic compositions must be decomposed by subtracting the contributions from fission, solar wind, and air. The resulting cosmogenic ratio, $(^{131}Xe/^{126}Xe)_c$, must then be corrected for the Ce contribution. This can be accomplished by means of the following equation which can be derived from the $(^{131}Xe/^{126}Xe)_{Ce}$ ratio and the Huneke *et al.* [44] equation given above.

$$(^{131}Xe/^{126}Xe)_{Ba} = (^{131}Xe/^{126}Xe)_c \cdot [1+1.65(Ce/Ba)] - (^{131}Xe/^{126}Xe)_{Ce} \cdot [1.65(Ce/Ba)]$$

The data and results for $^{131}Xe/^{126}Xe$ are given in Table 5-1.

Using the ratios in Table 5-1 and the model depth dependence from Figure 5-7, a histogram of model irradiation depths has been plotted

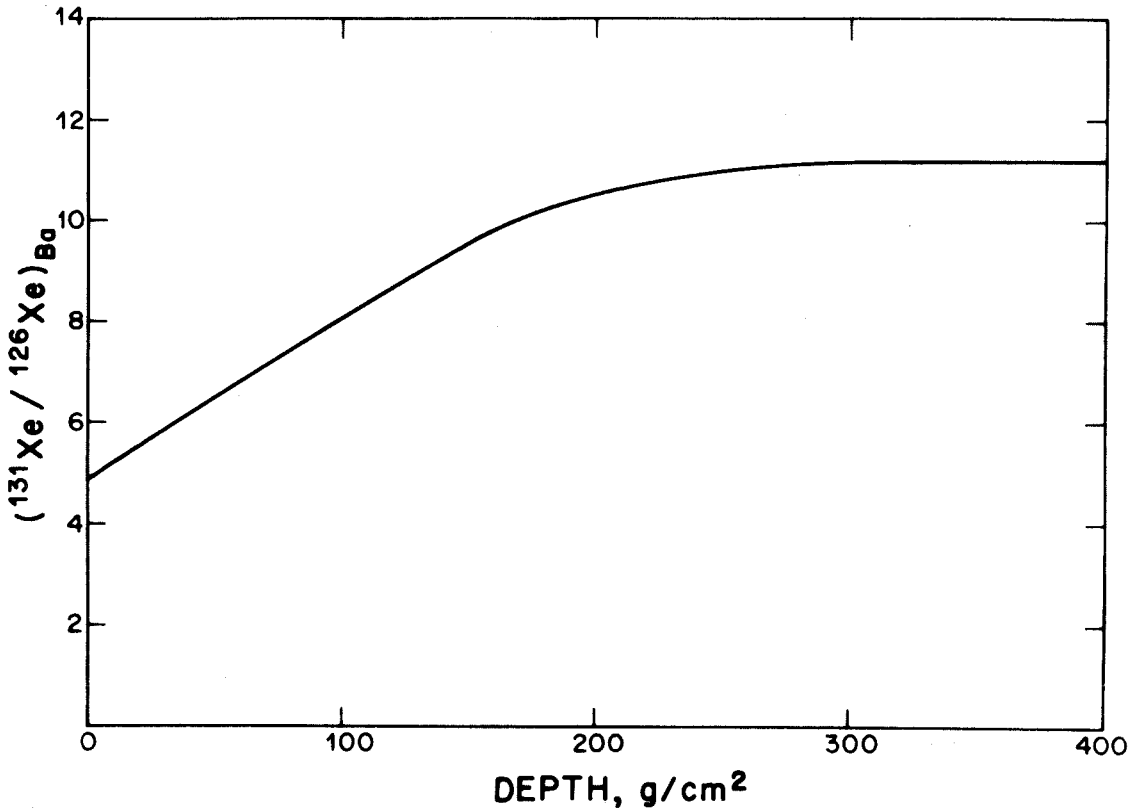

Figure 5-7

Model depth profile for $(^{131}Xe/^{126}Xe)_{Ba}$.

Table 5-1

$^{131}Xe/^{126}Xe$ Produced from Barium

Sample	$\left(\frac{^{131}Xe}{^{126}Xe}\right)_C$	$\frac{Ce}{Ba}$	$\left(\frac{^{131}Xe}{^{126}Xe}\right)_{Ba}$
10017	7.86[a]	0.26[j]	10.8
10020	4.12[b]	0.32[k]	5.7
10022	6.8 [c]	0.30[l]	9.6
10044	3.54[a]	0.27[j]	4.6
10045	4.26[b]	0.23[m]	5.4
10047	3.9 [c]	0.55[n]	6.4
10049	3.5 [c]	0.25[k]	4.5
10057	7.75[d]	~ 0.26[o]	10.6
10058	3.56[b]	0.35[k]	5.1
10069	6.8 [a]	0.26[p]	9.2
10071	5.69[b]	0.26[k]	7.6
10072	7.08[b]	0.31[n]	10.1
12002	5.67[e]	0.25[q]	7.5
12004	2.8 [f]	0.27[r]	3.5
12009	7.12[e]	~ 0.26[o]	9.7
12013 (light)	4.8 [g]	0.05[s]	5.1
12018	6.41[e]	0.26[t]	8.7
12021	5.18[e]	0.28[t]	7.0
12040	8.0 [f]	0.27[t]	11.0
12051	4.8 [f]	0.26[q]	6.4
12052	7.55[e]	0.25[t]	10.2
12053	9.2 [f]	0.25[q]	12.5
12063	7.69[e]	~ 0.26[o]	10.5
14310	~7.1 [h]	0.22[u]	9.3
15021	8.0 [i]	~ 0.25[o]	10.8

Footnotes to Table 5-1

[a] Huneke *et al.* [44].

[b] Data from Pepin *et al.* [51], reduced by Podosek [52].

[c] Data from Bogard *et al.* [45], reduced by Burnett [46].

[d] Data from Hohenberg *et al.* [53], reduced by Podosek [52].

[e] Data from Marti and Lugmair [28], reduced by Podosek [52].

[f] Geiss *et al.* [54].

[g] Lunatic Asylum [55].

[h] Lugmair and Marti report $^{131}Xe_n/^{126}Xe_{sp} = 3.6$ [56].
It is assumed that $(^{131}Xe/^{126}Xe)_{sp} = 3.5$.

[i] Bogard and Nyquist [13].

[j] Philpotts and Schnetzler [57].

[k] Gast *et al.* [47].

[l] Haskin *et al.* [58].

[m] Goles *et al.* [59].

[n] Compston *et al.* [60].

[o] Estimated.

[p] Goles *et al.* [61].

[q] Hubbard and Gast [62].

[r] Wakita *et al.* [63].

[s] Hubbard *et al.* [64].

[t] Schnetzler and Philpotts [65].

[u] Philpotts *et al.* [66].

in Figure 5-8. The most striking feature of this histogram is that unlike the soils (*cf.*, Fig. 5-4), the rocks have a wide range of irradiation depths. The Apollo 11 low-K rocks [49] all appear to have experienced near-surface irradiations while the high-K rocks [49] appear to have been irradiated at a variety of depths. This relationship was noted previously by Eberhardt *et al.* [50] on the basis of $^{78}Kr/^{83}Kr$ vs. $^{131}Xe/^{126}Xe$ correlations. The Apollo 12 rocks also seem to each have distinct histories.

One soil (15021) has been shown as a comparison with the ^{126}Xe-ψ depth model presented above in Section 5.3. The neutron fluence has not been determined for this sample, but it was determined for 15041 which was collected in the same area. The ratio of ^{126}Xe (15021) to ψ(15401) is typical of lunar soils (Fig. 5-4) and implies an effective irradiation depth (assuming no mixing) of ~ 250 g/cm^2, which is in good agreement with the depth indicated by the $(^{131}Xe/^{126}Xe)_{Ba}$ model. Because of the large component of trapped (air + solar wind) Xe in soils, the errors associated with the spectrum stripping generally restricts the use of the $(^{131}Xe/^{126}Xe)_{Ba}$ model to rocks.

Huneke *et al.* [44] have devised a relative shielding sequence for Apollo 11 rocks which is based on the $^{38}Ar/^{21}Ne$ and $^{3}He/^{21}Ne$ ratios. High values of these ratios are taken to mean little shielding. The sequence which they give in order of increasing depth of irradiation is 49, 44, 69, 57, 72, 71, 45, 20, 17, 22, and 47, where a difference in depth is significant only for samples separated by 3-4 places on the list. The depth sequence determined from the $(^{131}Xe/^{126}Xe)_{Ba}$ model for

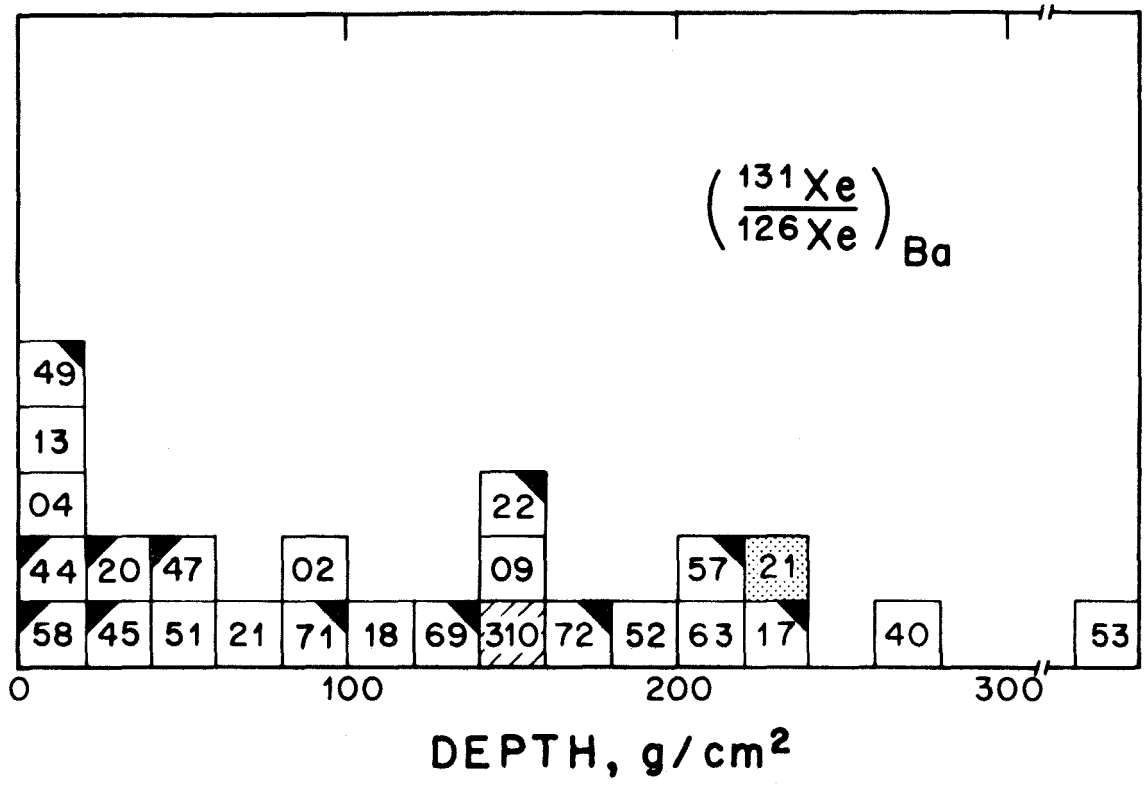

Figure 5-8

Histogram of effective irradiation depths for lunar rocks calculated from the $(^{131}Xe/^{126}Xe)_{Ba}$ model. The Apollo 11 low-K rocks are indicated by shading in the upper left corner. The Apollo 11 high-K rocks are marked by shaded upper right corners. Apollo 12 samples are unshaded. The diagonally scored box is for an Apollo 14 rock and the shaded box is for an Apollo 15 soil which has been included as a comparison with the depth model based on the $^{126}Xe/\psi$ ratio (Sec. 5.3).

the Apollo 11 rocks is 49,44,58 < 20,45 < 47 < 71 < 69,22 < 72 < 57 < 17. This sequence is in reasonable agreement with that of Huneke *et al.* [44] except for rocks 47, 57, and 69. Part of the disagreement between these models may be due to problems associated with comparing the concentrations of Ar and Ne and part may result from variations in the ratios of the target elements in the samples analyzed for Ar and Ne. Rock 57, however, presents a problem because it has a relatively high ratio of spallogenic gas to neutron fluence [2], which would indicate a near-surface irradiation.

The wide range of apparent exposure depths means that exposure ages calculated from the concentration of spallogenic rare gases assuming that the rocks have been exposed only near the surface should be used with great caution. Depth corrected exposure histories for selected samples will be discussed in the following sections.

5.5.3 Rock 14310

Rock 14310 has a comparatively high neutron fluence ($\sim 2.7 \times 10^{16}$ n/cm^2) which is similar to that for the soils from Apollo 14. In addition, an exterior piece (#100) has received a slightly higher fluence than an interior piece (#88) (see Table 4-2). The "surface" exposure age of this rock has been measured by ^{38}Ar to be 300 my [22] and by ^{81}Kr-^{83}Kr to be 259 my [56]. Furthermore, the Lugmair and Marti [56] ^{126}Xe data imply an exposure age of 262 my. Because this time period would be insufficient to produce the measured fluence, one concludes that this rock received most of its cosmic ray irradiation while buried. The depth at which the rock was irradiated can be estimated in several

ways. To produce the observed neutron fluence at the surface would require ~3.8 x 10^9 yr which is ~13 times longer than the exposure ages. The ^{126}Xe depth model developed above (Sec. 5.3) can be used to estimate the depth which would give concordant rare gas and neutron fluence exposure ages. This depth is ~150 g/cm^2. The exposure time necessary to produce the measured ^{126}Xe concentration and fluence at this depth would be ~700 my. An irradiation depth of ~150 g/cm^2 was also estimated from the $(^{131}Xe/^{126}Xe)_{Ba}$ model (Fig. 5-8). It should be noted, however, that this depth was based on an assumed value of 3.5 for the spallogenic $^{131}Xe/^{126}Xe$ ratio in this rock. This assumption, which is based on the value for rock 10049 [45], was necessary because Lugmair and Marti [56] reported only the $^{131}Xe(neutron)/^{126}Xe(spallation)$ value.

Rock 14310 is unique because a depth can also be calculated from the fluence gradient. In Figure 5-9, the fractional change in the ^{158}Gd production rate per unit depth has been plotted against depth. This curve is the derivative of the LCH depth dependence of the flux divided by the flux so that the change is expressed as a fraction of the flux. This calculated curve applies to samples in the most favorable orientation, *i.e.*, vertical, and is therefore an upper limit to the gradient which could be measured in a rock which had been irradiated at a given depth. If the samples were actually in a less favorable orientation, the measured gradient would be less. For a sample collected at the surface, one has no way to know what its orientation was while it was buried; therefore, any depth for which the calculated gradient is greater than or equal to the measured gradient is compatible with this

model. From the measured difference in fluence, which is apparent in both the Gd and Sm data, and the separation of the samples which was ~ 15 g/cm^2, the gradient per g/cm^2 has been calculated to be 0.6%. As shown in Figure 5-9, this gradient is compatible with exposure at any depth not in the range 100-300 g/cm^2. This result is in direct conflict with the depths calculated from the other two models, but it may not mean that any of the models is incorrect.

In calculating model irradiation depths, it has been assumed that the rock has had a simple history which can be treated as irradiation at a single depth followed by recent transportation to the surface. This assumption is probably incorrect and this rock has probably had a complex irradiation history. This is also implied by the track data [67] which do not show gradients with depth. Although detailed calculations have not been made, the data can probably be fitted by a three-stage model. This rock may have been irradiated at a depth of ≥ 500 g/cm^2 for a period on the order of 10^9 yr, during which the bulk of the irradiation and the fluence gradient was received. It may then have been irradiated near the surface for about 10^8 yr. This period would serve to lower the neutron capture to spallation ratio such that the rock would appear to have been irradiated at a depth of ~ 150 g/cm^2. The third period would be the time the rock has actually been on the surface. Bhandari *et al.* [68] have shown from the solar flare track density that this most recent period has lasted only about one million years.

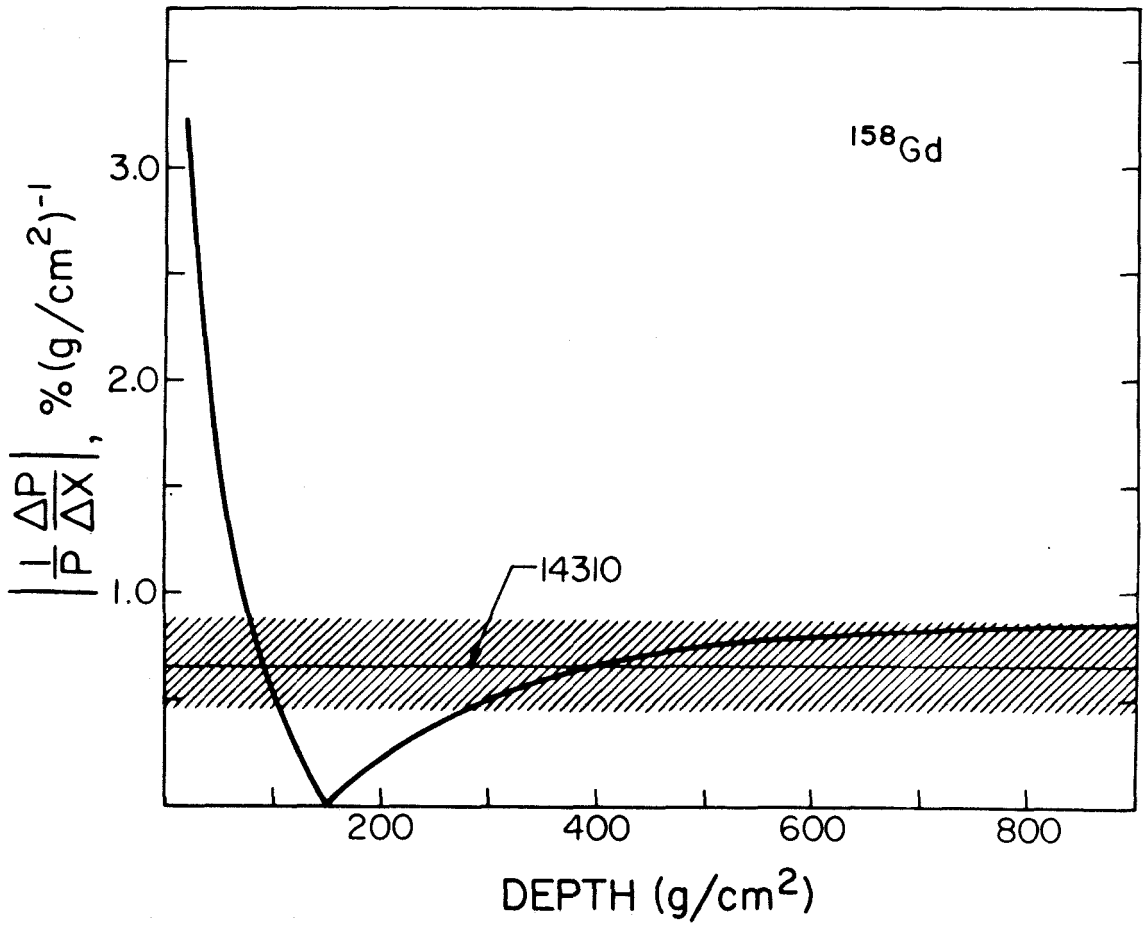

Figure 5-9

Percentage difference in the ^{158}Gd production rate for samples separated in depth by 1 g/cm^2 as a function of depth. The horizontal line and the shaded area are the observed differences and the error bar for two samples from rock 14310.

5.5.4 Rock 10017

Rock 10017 has the highest neutron fluence yet measured in a rock and is the only rock to have a fluence significantly higher than that found in the soils at the same site. It also has a high $^{131}Xe/^{126}Xe$ ratio indicating irradiation at depth. One would like to know this depth and the chemical composition of the material in which rock 10017 was irradiated. The latter point is important because this rock has a significantly different composition than the Apollo 11 soils. If the sample was irradiated in the Apollo 11 soil ($\Sigma_{eff} = 0.0103$ cm^2/g), the neutron capture rate (Fig. 4-3) would have been higher than if it was irradiated in material of its own composition ($\Sigma_{eff} = 0.0134$ cm^2/g).

The $(^{131}Xe/^{126}Xe)_{Ba}$ indicates that rock 10017 was irradiated at a depth of ~230 g/cm^2. Because the Xe concentration data for this rock {3.9×10^{-7} cc(STP)/g(Ba + 1.65 Ce)} are well documented [44], they are probably reliable and can be used to estimate an irradiation depth from the ^{126}Xe-ψ model. Because the fluence represented by a given ^{158}Gd enrichment (Table 4-2) depends on the composition of the material, two depths can be calculated for this model. One is for the rock having been irradiated in the Apollo 11 soil. This depth is 250 g/cm^2, which is in good agreement with the $(^{131}Xe/^{126}Xe)_{Ba}$ depth. On the other hand, one can in principle calculate a depth for the rock having been irradiated in material of its own composition. The $^{126}Xe/\psi$ ratio calculated under this assumption would plot below the "≥ 400 g/cm^2" line of Figure 5-4. Because such a ratio is incompatible with the model, one concludes that if the model is correct, rock 10017 could not have received the bulk of its irradiation in material of its own composition. This means

that this rock was not irradiated as part of bedrock, as a large boulder, or in a soil of its own composition and subsequently transported to the Apollo 11 site.

If one assumes that this rock was, in fact, irradiated at a depth of ~ 250 g/cm^2 in the Apollo 11 soil, one calculates that the irradiation must have lasted 1.3×10^9 yr to produce the observed ^{126}Xe concentration and neutron fluence. This time may not be unreasonably long for a sample to be undisturbed at a depth of ~ 1.5 m because the Apollo 15 and 16 drill stems indicate that cratering to such depths occurs less frequently than at least 500 my. On the other hand, like rock 14310, this rock may have had a more complicated history.

The recent history of 10017 has been studied by Fleischer *et al.* [25] and Crozaz *et al.* [26] who have measured a steep galactic cosmic ray track gradient which indicates that the rock had been in the orientation from which it was collected for about 3 my. Before that, it was exposed for an additional ~ 3 my in a bottom-up position.

5.5.5 Rock 15595 - Erosion Rate of Hadley Rille

Rock 15595 is a chip from a large rock protruding from the regolith at the edge of Hadley Rille which has been interpreted as bedrock [69] and is one of many such rocks which are exposed along the edge of the rille. The fluence has been measured in two samples from chip 15595. An interior sample (15595,20) had a fluence of $(0.85 \pm 0.09) \times 10^{16}$ n/cm^2, while an exterior sample (15595,19), which was separated from 15595,20 by ~ 5 cm had a fluence of $(0.94 \pm 0.10) \times 10^{16}$ n/cm^2 (Table 4-2). If this rock was deeply buried and then excavated by a

single event, the fluence of the surface sample would indicate an exposure time of 2×10^9 yr. This is unreasonably long and implies a more complicated exposure history for this rock. A 10^9 yr exposure age is also incompatible with the rare gas data of Behrmann *et al.* [70] which indicate an exposure age of 100 my. Their track densities are, however, anomalously low for a surface exposure lasting 100 my.

Because of the possibility that 15595 is bedrock, a reasonable model might be that the surface has been undergoing essentially a continuous erosion and that this erosion has ultimately excavated the rocks which now rim the rille. If this erosion has been operable over a long enough time period for the rock to have traveled upwards through the entire nuclear active zone, *i.e.*, the surface fluence is in equilibrium, an erosion rate of 2.6 $g \cdot cm^{-2} \cdot my^{-1}$ ($\sim$ 8 $mm \cdot my^{-1}$) is necessary to match the total measured fluence. If the surface fluence is not in equilibrium for the continuous erosion model, slower erosion rates would be possible.

The rate of 2.6 $g \cdot cm^{-2} \cdot my^{-1}$ is in reasonable agreement with the value of 1.5 $g \cdot cm^{-2} \cdot my^{-1}$ obtained by Burnett *et al.* [22] from ^{38}Ar data for rock 15555. It is somewhat higher than the rate of 0.6 $g \cdot cm^{-2} \cdot my^{-1}$ which can be calculated for soil 15601 by assuming the fluence of the soil is in erosional equilibrium. (This soil was also collected near the edge of the rille.) The lower value for 15601 probably reflects contamination of the soil with more highly irradiated material from the adjacent mare surface.

If one assumes that the erosion rate of 2.6 $g \cdot cm^{-2} \cdot my^{-1}$ is

applicable, one can calculate the depth of the material which has been transported to the bottom of the rille. Assume that the rille can be treated as a parabola which is 1 km wide at the rim and 300 m deep [69]. If the material eroded from the walls is all deposited downslope, which should be approximately true for cratering on steep slopes, and if the rille is assumed to maintain a parabolic shape, one can calculate the change in depth as the rim widens as a result of erosion because the area of the cross section of the rille must remain constant. From the equilibrium erosion rate, which is equivalent to the erosion of $\sim$ 1 cm of rock per million years, and the age of the site ($\sim 3 \times 10^9$ yr [3]), one calculates that the rille has widened $\sim$ 30 m on each side. This implies that the depth of the material deposited at the bottom is $\sim$ 30 m where this material is assumed to have a typical regolith density of ~ 1.7 g/cm^3.(Fig. 5-10).

An interesting feature of the continuous erosion model is that if the erosion is considered to take place at a constant rate, the ratio $^{126}Xe/\psi$ or $(^{131}Xe/^{126}Xe)_{Ba}$ measured in a surface sample will be the same as if the sample had been uniformly mixed throughout the nuclear active zone. This is true because as the sample is being excavated from a shielded depth, it spends equal times at each depth and therefore averages over depth. Xe concentration data have not been reported for this rock, but Behrmann *et al.* [70] have measured the spallation Xe spectrum. Using their data and an estimated Ce/Ba ratio in the range 0.20 - 0.25, which seems reasonable on the basis of the analyses of Taylor *et al.* [71] for other Apollo 15 samples, one cal-

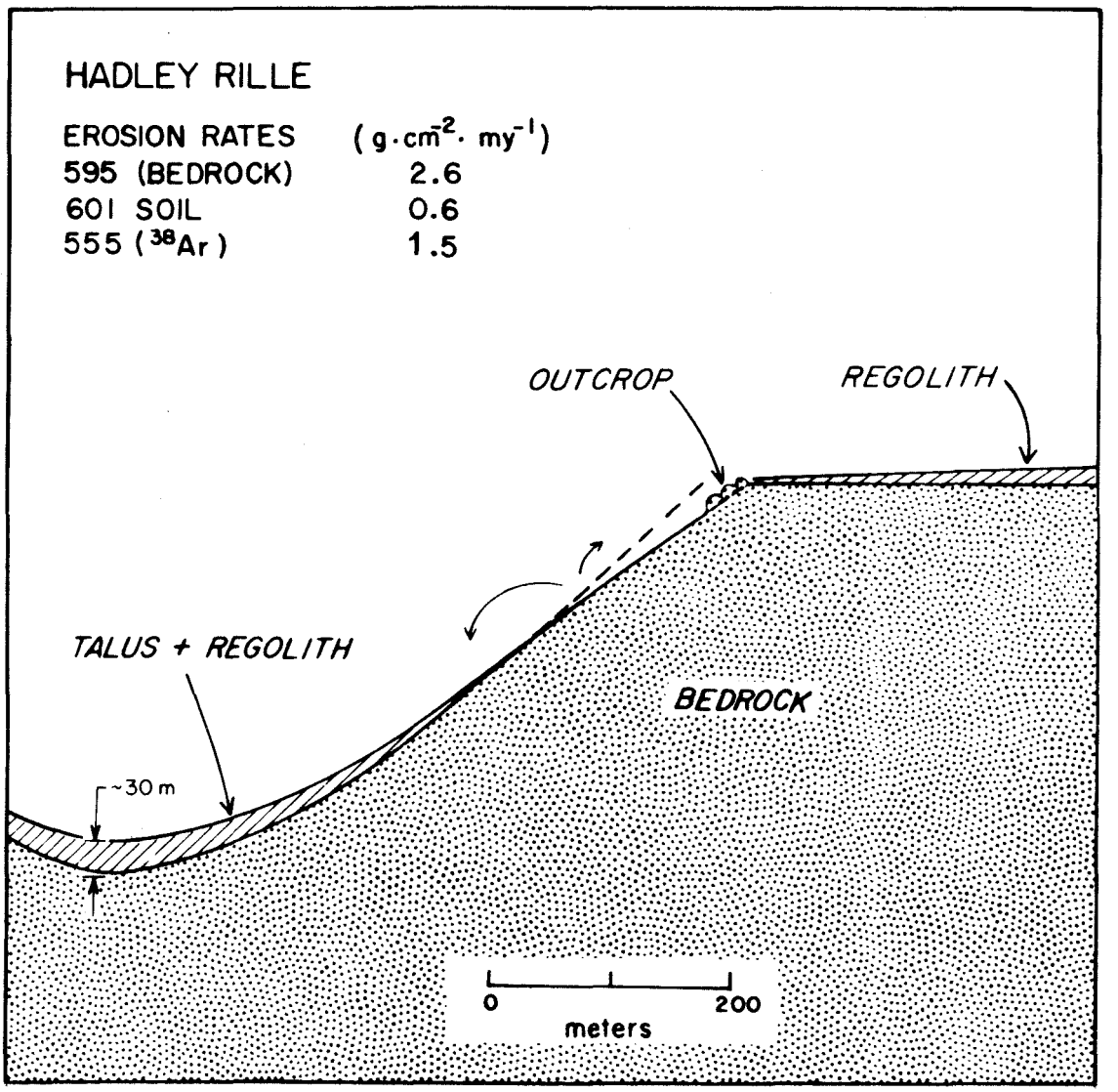

Figure 5-10

Schematic profile of Hadley Rille. The rille is assumed to have originally had the profile described by the dashed line and the bottom of the talus deposit. Impacts are assumed to have eroded the rille to the profile described by the curve connecting the outcrop to the top of the talus deposit. The erosion rate calculated from rock 15595 implies the talus at the bottom of the rille should be ~ 30 m thick.

culates that the $(^{131}Xe/^{126}Xe)_{Ba}$ ratio must be between 6.7 and 7.1. This ratio implies a burial depth of $\sim$ 60 g/cm^2 and is intermediate between those expected for continuous erosion ($\sim$ 11) and surface exposure ($\sim$ 5). The actual history for this rock is therefore inferred to be intermediate between the two extreme models.

5.6 Meteorites

5.6.1 Norton County

The Norton County achondrite is unique and interesting in several ways. (1) With a mass of 1050 kg, it is the largest "stone" meteorite existing as a single piece [72]. (2) Although its exposure age has recently been remeasured and determined to be $\sim$ 104 my [73] rather than 240 my [74], it still has the highest exposure age of the stone meteorites. (3) It is the only meteorite in which cosmic ray produced neutrons have been found to have induced changes in the isotopic composition of Gd [75] and K [76]. Eugster, Tera, Burnett, and Wasserburg [75] have shown that the differences between the Gd composition in Norton County and in terrestrial samples and several other meteorites could be explained by Norton County having been exposed to a fluence of 6×10^{15} *thermal* neutrons.

In this work, the Gd isotopic composition was redetermined on a 1.2 g sample of Norton County (Nininger Meteorite Collection: Breccia IX, Interior 523.3X). The Sm isotopic composition was also determined for this sample. By comparing the magnitudes of the neutron capture effects in Sm and Gd, as was done for the lunar samples (see Sec. 4.4),

one can put constraints on the low energy neutron spectrum to which the meteoroid was exposed. One can then interpret the neutron capture effects more realistically than in terms of *thermal* neutrons.

From the isotopic data in Tables 2-5 and 2-6, one calculates that the $\varepsilon_{Sm}/\varepsilon_{Gd}$ ratio (see Sec. 4.4) for Norton County is 0.39 ± 0.03, which is intermediate between the lowest lunar ratios of ~ 0.6 and the value of ~ 0.2 expected for thermal neutrons (200°K). This indicates that the low energy neutron spectrum in the meteoroid was not thermal but was also less hard than that experienced by lunar samples. In order to explore the implications of this ratio for interpreting the neutron fluence to which the sample was exposed, one must consider the chemical composition of the meteorite.

Norton County is composed mostly of enstatite ($MgSiO_3$) with about 10% normative olivine ($Mg_{1.8}Fe_{0.2}SiO_4$). In addition, there is a minor iron-nickel metallic phase [77]. Because the sample is to a large extent Si, O, and Mg, the average energy loss per collision and the scattering cross section are not very different in Norton County than in the lunar samples. One should therefore be able to use the LCH calculations and the parameter Σ_{eff} to describe the low energy neutron spectrum. This spectrum can then be used to calculate the neutron fluence to which the sample has been exposed. One can compare the measured $\varepsilon_{Sm}/\varepsilon_{Gd}$ ratio to the ratio predicted by LCH as a test of the applicability of the calculations. If one assumes that the metallic phase is negligible, one calculates from the chemical composition as given by Beck and LaPaz [77] that $\Sigma_{eff} = 0.0021\ cm^2\ g^{-1}$. If one

assumes that the metallic phase constitutes 2% of the meteorite, which is more than the total iron content of the meteorite as given by Wiik [78], Σ_{eff} would be raised to 0.0025. In Figure 4-6, the experimental point is seen to lie on the extrapolation of the LCH curve for silicate materials at 200°K and somewhat below the trend of the lunar samples. Assuming that the slopes, if not the exact values, of the LCH curves are correct, it would appear that Norton County had a cooler average temperature during its cosmic ray exposure than the lunar samples. The average lunar temperature is known to be ~ 250°K [79], which implies that Norton County was irradiated at a temperature of ~ 100°K. This is in reasonable agreement with the temperature of ~ 150°K calculated by Butler [80] for chondritic meteoroids in orbits midway between Mars and Jupiter. Alternatively, one could conclude that the slopes of the predicted lines are incorrect and that the measured points more correctly define the true correlation with Σ_{eff}, but the data do not seem well enough correlated to justify this conclusion.

In the temperature range 100-200°K, the average ^{157}Gd capture cross section for neutrons with E < 0.18 eV and the ^{157}Gd capture rate (see Figs. 4-2 and 4-3) vary by ≤ 20% for materials of the composition of Norton County. It is therefore reasonable to use the 200°K calculation of LCH to estimate the fluence and flux of neutrons to which this meteorite was exposed. Using $\langle^{157}\sigma\rangle_{<0.18} = 1.45 \times 10^{-19} cm^2$, one calculates that the total neutron fluence to which the sample was exposed was 1.2×10^{16} n/cm^2 (E < 0.18 eV). The Herzog and Anders [73] exposure age of ~ 104 my implies that the average neutron flux to which

this sample was exposed was 3.8 $n \cdot cm^{-2} \cdot sec^{-1}$.

This flux can be compared to the neutron slowing down densities calculated by Eberhardt, Geiss, and Lutz [81] as a function of neutron *age* (Sec. 3.3) in chondritic meteorites. The slowing down density, $q(\ell n\, E)$, is related to the flux per unit energy, $\phi(E)$ by the relation $q(\ell n\, E) = E\phi(E)\Sigma_s \xi$ where Σ_s is the macroscopic scattering cross section and ξ is the average logarithmic energy decrement per collision. The flux per unit energy at energy E can be related to the total flux below energy E, by assuming a neutron energy spectrum. The Eberhardt *et al.* [81] calculations are not detailed enough in the energy regions below 0.18 eV for which the above flux of 3.8 $n \cdot cm^{-2} \cdot sec^{-1}$ applies, but using the LCH 200° spectrum, the slowing down density at 0.18 eV can be shown to have been ~0.06 n cm^{-3} sec^{-1} during the exposure history of Norton County. This slowing down density can be related to the Eberhardt *et al.* [81] calculations if the differences in their parameters and those applicable to Norton County are taken into account. The slowing down density in the meteorite is equal to the slowing down density assuming no absorption multiplied by the resonance escape probability (see Sec. 3.2). The slowing down density without absorption is a function of the scattering properties of the samples. Making the necessary adjustments for the scattering cross section appropriate to Norton County and calculating the resonance escape probability (~0.85 to 0.18 eV), one finds that the experimentally determined slowing down density is compatible with the Eberhardt *et al.* [81] calculations for a sample being irradiated at a depth of ~10 cm in a body with a radius of $\geq$50 cm.

This is quite reasonable in that the present mass of the main stone of Norton County corresponds to a radius of ~40 cm. It also agrees with the conclusions reached by Eugster *et al.* [75], but this agreement results only because the decrease in the cross section used here relative to that used by Eugster *et al.* [75] is offset by the difference in the exposure ages used in the two calculations.

5.6.2 Allende

The carbonaceous chondrite Allende, which fell in 1969, has been the subject of a number of investigations (see, *e.g.*, [82-87]).

Inclusions from this meteorite, enriched in refractory elements, have been shown to have very primitive $^{87}Sr/^{86}Sr$ ratios [86]. This observation implies that this meteorite, or at least these inclusions, may be an early solar system condensate. Allende might therefore contain evidence of particle irradiations in the early phases of solar system formation, which would not be detectable in less primitive, more equilibrated meteorites. Allende also contains samples with high ^{60}Co activities (up to 226 dpm/kg(rock)) [85]. It was therefore of interest to see whether Gd anomalies, due either to primordial irradiations or cosmic ray produced neutrons, could be measured in this meteorite.

The Gd isotopic composition was determined on a 1 g sample of the piece designated NMNH 3525, which had a measured ^{60}Co activity of 127 dpm/kg [85]. The $^{158}Gd/^{157}Gd$ ratio for this sample was measured to be 1.58676 ± 0.00011, which is not statistically distinct from the terrestrial ratio of 1.58660 ± 0.00011 (see Tables 2-5 and 2-1, respec-

tively). One would, however, like to set an upper limit for the fluence and flux of neutrons to which the sample was exposed.

Using the chemical composition data tabulated by Clarke *et al.* [82], one can show that the scattering cross section and average logarithmic energy decrement per collision for Allende are similar to those used in the LCH calculations. (The H_2O content is < 0.1% [82]). Because of the high iron content of Allende, the absorption cross section is also similar to the absorption cross section of the Apollo 11 samples. The LCH spectrum for materials of the composition of the Apollo 11 soil samples can therefore be used to estimate the average ^{157}Gd cross section for neutrons with energies below 0.18 eV. From this value and the upper limit of the error for the $^{158}Gd/^{157}Gd$ ratio, one calculates that the Allende sample analyzed was exposed to less than 1.4×10^{15} n/cm^2 (E < 0.18 eV). The cosmic ray exposure age of Allende has been reported by Fireman and Goebel [88] to be 5.2 my. The upper limit of the neutron flux to which this meteorite could have been exposed during this period is therefore 8.5 n(E < 0.18)$\cdot$cm$^{-2}\cdot$sec^{-1}.

Because the LCH calculations should apply to the neutron energy spectrum in Allende, one can use this spectrum to compare the low energy flux implied by the measured ^{60}Co activities to the flux limit calculated above. For a Co concentration of 650 ppm [82], the measured ^{60}Co activity of 127 dpm/kg yields a specific activity of 197 dpm/g (Co). From the ^{60}Co production rate calculated in Section 4.6, and the LCH spectrum, one calculates that the flux of neutrons with energies below 0.18 eV to which this sample was exposed during the period measured by ^{60}Co ($\sim$ 10 yr) was 2.3 n$\cdot$cm$^{-2}\cdot$sec^{-1}. This is compatible with the upper

limit of 8.5 $n \cdot cm^{-2} \cdot sec^{-1}$ set from the Gd measurements. By similar reasoning, it can be shown that in the sample with the highest measured ^{60}Co activity (designated "2" [85]) the neutron fluence (E < 0.18 eV) would be expected to be $\sim 7 \times 10^{14}$ n/cm^2, which corresponds to a change in the ratio $^{158}Gd/^{157}Gd$ of 0.0002. This change in $^{158}Gd/^{157}Gd$ is only twice the uncertainty in the terrestrial ratio.

One can also ask what is the highest flux of neutrons with energies below 0.18 eV which could be expected in any meteoroid with the composition of Allende. The calculations of Eberhardt *et al.* [81] indicate that the highest flux (E < 0.18 eV) would occur at the center of a meteoroid with a radius of 75-100 cm. Taking into effect the differences in the scattering and absorption parameters used by Eberhardt *et al.* [81] from those applicable to Allende, one calculates that the maximum flux (E < 0.18 eV), which would be expected to occur in such a meteoroid, would be ~ 9 $n \cdot cm^{-2} \cdot sec^{-1}$.

Taking the upper limit of the low energy neutron flux (E < 0.18 eV) as 9 $n \cdot cm^{-2} \cdot sec^{-1}$, one sets an upper limit of $< 2 \times 10^{15}$ n/cm^2 for the maximum neutron fluence which could be expected from the recent cosmic ray exposure of an Allende sample assuming its pre-atmospheric radius had the optimum value of ~ 75 cm. This fluence would correspond to a change in the $^{158}Gd/^{157}Gd$ ratio which would be < 3 times the error associated with a typical measurement.

The recovered mass of Allende is 2×10^3 kg [82] which would correspond to a radius of ~ 50 cm. A pre-atmospheric radius of 75 cm would require a mass of 5×10^3 kg. Because of the large number of

fragments which fell, the large area over which they fell, and the effects of atmospheric ablation, it seems likely that the pre-atmospheric radius of Allende was indeed near 75 cm. If the Eberhardt *et al.* [81] calculations are correct, it should therefore be possible to find samples with higher ^{60}Co activities (normalized to the date of fall) than those thus far reported [85]. Such samples might have measurable Gd isotopic anomalies caused by cosmic ray produced neutrons.

5.6.3 Differential Primordial Irradiations

Throughout this work, it has been assumed that all lunar, meteoritic, and terrestrial samples were formed with the same isotopic composition, and that all variations in the isotopic composition of Gd and Sm were the result of neutrons produced by galactic cosmic rays. It is conceivable, however, that these bodies were formed from materials which had been differentially irradiated and which had differing isotopic compositions. Two extreme irradiation mechanisms were considered by Eugster *et al.* [75]. (1) The materials which formed these bodies were irradiated while in a diffuse state such that all material was irradiated. In such a case, differences in the Gd or Sm isotopic compositions of the bodies would represent differences in the magnitude of the flux at the different locations in the protosolar system. (2) A fraction of the solar system material was intensely irradiated (see, *e.g.*, Fowler, Greenstein, and Hoyle [89]) so that the ^{157}Gd, ^{155}Gd, ^{149}Sm, and other nuclides with large cross sections were totally depleted. In this case, differences in isotopic composition would

reflect differences in the fraction, q, of irradiated material which had subsequently been mixed with that which was unirradiated. To explain the terrestrial D/H ratio, Burnett, Fowler, and Hoyle [90] concluded that approximately 5% of the material which makes up the earth had been irradiated. Eugster *et al.* [75] were able to show from their Gd isotopic composition measurements, that the value of q in the meteorites they studied, except Norton County, differed from the terrestrial q by less than 0.001. As discussed in Section 5.6.1, the differences in the Gd compositions of Norton County and terrestrial samples can be explained by cosmic ray produced neutrons without invoking primordial irradiations.

These considerations can now be extended to include Allende and the lunar samples. It can be shown from a mass balance equation that for small changes in q, near $q = 0.05$, the fractional difference in the $^{158}Gd/^{157}Gd$ ratio of a sample from the terrestrial ratio is equal to ~ 1.7 times the change in q. From the upper limit of 1.58696 for the $^{158}Gd/^{157}Gd$ ratio of the sample analyzed from Allende, and the lower limit on the terrestrial ratio, one concludes that the difference in q between this sample and the earth is < 0.0003. Therefore, if 5% of the material of the solar system was intensely irradiated, the fraction of this material incorporated into the Allende sample analyzed differed from the fraction incorporated into the earth by less than 0.6%. This limit is a factor of three lower than set by Eugster *et al.* [75] for the meteorites they analyzed. It does not, however, preclude the possibility that certain "primitive" chondrules and/or aggregates of the types discussed by Grossman [83] and Gray, Papanastassiou, and

Wasserburg [86] might have been more extensively irradiated because the fraction of these materials in the bulk sample analyzed is unknown.

As noted in Section 2.6, no lunar sample has a Gd or Sm isotopic composition indicating that it has been exposed to less neutrons than the terrestrial standards. There are, however, samples, *e.g.*, 14321 [22], which have been brought to the lunar surface recently enough that one would not expect their Gd or Sm isotopic compositions to have been altered by cosmic ray produced neutrons. Within the assigned errors, these samples are found to have the terrestrial isotopic composition. The measured isotopic composition of all other lunar samples can be explained in terms of the cosmic ray produced neutron flux. There is, therefore, no evidence from these data that the materials which compose the earth, the moon, and the meteorites were subjected to differing primordial irradiations beyond the limits set by Eugster *et al.* [75].

5.7 Summary

High precision measurements of the isotopic composition of Gd have been made on a wide variety of lunar samples. The observed variations in the Gd composition have been shown to be due to neutron capture, and the fluence of neutrons to which the samples have been exposed have been calculated for a realistic, non-thermal neutron spectrum. Neutron induced variations in the isotopic composition of Sm have been reported for the first time and, on a quantitative basis, the ratio of the Gd variations to those in Sm has been shown to be

approximately compatible with the LCH neutron energy spectrum which was used to calculate fluences. The LCH spectrum and flux have also been shown to be compatible with most of the other effects attributed to neutrons in the lunar literature.

The Gd neutron fluence measurements have been shown to be useful in establishing the time scale for the deposition of the lunar regolith. In particular, it has been established that the areas sampled by the Apollo 15 and 16 drill stems have not been disturbed to a depth of 2 m for ~ 500 my. On the other hand, the upper ~ 50 cm of every core studied have been disturbed within the last 100 my. It has also been demonstrated that within ~ 30%, the variations observed in the isotopic anomalies in Gd in lunar soils can be explained by variations in the neutron capture rate among the sites, and that the surface soils collected from widely separated sites have experienced similar mixing histories. For rock samples, models based on the ratio of the neutron fluence to spallation products have been developed and used to tentatively establish the effective depths at which selected rocks were irradiated by cosmic rays.

5.8 References

[1] R. E. Lingenfelter, E. H. Canfield, and V. E. Hampel, The lunar neutron flux revisited, Earth Planet. Sci. Letters 16 (1972) 355.

[2] O. Eugster, F. Tera, D. S. Burnett, and G. J. Wasserburg, The isotopic composition of Gd and the neutron capture effects in samples from Apollo 11, Earth Planet. Sci. Letters 8 (1970) 20.

[3] D. A. Papanastassiou and G. J. Wasserburg, The Rb-Sr age of a crystalline rock from Apollo 16, Earth Planet. Sci. Letters 16 (1972) 289.

[4] Lunar Sample Preliminary Examination Team, Preliminary examination of lunar samples from Apollo 11, Science 165 (1969) 1211.

[5] E. M. Shoemaker, R. M. Batson, A. L. Bean, C. Conrad, Jr., D. H. Dahlem, E. N. Goddard, M. H. Hait, K. B. Larson, G. G. Schaber, D. L. Schleicher, R. L. Sutton, G. A. Swann, and A. C. Waters, Preliminary geologic investigation of the Apollo 12 landing site, Apollo 12 Preliminary Science Report (NASA SP-235, 1970) 113.

[6] G. A. Swann, N. G. Bailey, R. M. Batson, R. E. Eggleton, M. H. Hait, H. E. Holt, K. B. Larson, M. C. McEwen, E. D. Mitchell, G. G. Schaber, J. P. Schafer, A. B. Shephard, R. L. Sutton, N. J. Trask, G. E. Ulrich, H. G. Wilshire, and E. W. Wolfe, Preliminary geologic investigations of the Apollo 14 landing site, Apollo 14 Preliminary Science Report (NASA SP-272, 1971) 39.

[7] Apollo Lunar Geology Investigation Team, Geologic setting of the Apollo 15 samples, Science 175 (1972) 407.

[8] V. R. Oberbeck, Implications of regolith thickness in Apollo 16 landing site, NASA Technical Memorandum (TM X-62, 089, 1971).

[9] Apollo Field Geology Investigation Team, Apollo 16 exploration of Descartes: a geologic summary, Science 179 (1973) 62.

[10] Joel S. Watkins and Robert L. Kovach, Seismic investigation of the lunar regolith, preprint (1973).

[11] Ronald Greeley and Donald E. Gault, Crater frequency age determinations for the proposed Apollo 17 site at Taurus-Littrow, Earth Planet. Sci. Letters 18 (1973) 102.

[12] J. C. Huneke, personal communication.

[13] D. D. Bogard and L. E. Nyquist, Noble gas studies on regolith materials from Apollo 14 and 15, Proc. Third Lunar Sci. Conf. 2 (M.I.T. Press, 1972) 1797.

[14] D. D. Bogard, L. E. Nyquist, W. C. Hirsch, and D. R. Moore, Trapped solar and cosmogenic noble gas abundances in Apollo 15 and 16 deep drill stems, preprint (1973)

[15] W. A. Kaiser, Rare gas studies in Luna-16-G-7 fines by stepwise heating technique. A low fission solar wind Xe, Earth Planet. Sci. Letters 13 (1972) 387.

[16] F. Tera, personal communication.

[17] J. A. Philpotts, personal communication.

[18] M. K. Carron, C. S. Annell, R. P. Christian, Frank Cuttitta, E. J. Dwornik, D. T. Ligon, Jr., and H. J. Rose, Jr., Elemental analyses of lunar soil samples from Apollo 15 mission, The Apollo 15 Lunar Samples (Lunar Sci. Inst., 1972) 198.

[19] H. Wänke, H. Baddenhausen, A. Balacescu, F. Teschke, B. Spettel, G. Dreibus, H. Palme, M. Quijano-Rico, H. Kruse, F. Wlotzka, and F. Begemann, Multielement analyses of lunar samples and some implications of the results, Proc. Third Lunar Sci. Conf. 2 (M.I.T. Press, 1972) 1251.

[20] J. A. Philpotts, C. C. Schnetzler, M. L. Bottino, S. Schumann, and H. H. Thomas, Luna 16: some Li, K, Rb, Sr, Ba, rare-earth, Zr, and Hf concentrations, Earth Planet. Sci. Letters 13 (1972) 429.

[21] J. A. Philpotts, S. Schuhmann, A. L. Bickel, and R.K.L. Lum, Luna 20 and Apollo 16 core fines: large-ion lithophile trace-element abundances, Earth Planet. Sci. Letters 17 (1972) 13.

[22] D. S. Burnett, J. C. Huneke, F. A. Podosek, G. P. Russ III, G. Turner, and G. J. Wasserburg, The irradiation history of lunar samples, Lunar Science III (Lunar Sci. Inst. Cont. No. 88, 1972) 105.

[23] G. W. Comstock, A. O. Evwaraye, R. L. Fleischer, and H. R. Hart, Jr., The particle track record of lunar soil, Proc. Second Lunar Sci. Conf. 3 (M.I.T. Press, 1971) 2569.

[24] D. Lal, D. Macdougall, L. Wilkening, and G. Arrhenius, Mixing of the lunar regolith and cosmic ray spectra: evidence from particle-track studies, Proc. Apollo 11 Lunar Sci. Conf. 3 (Pergamon Press, 1970) 2295.

[25] R. L. Fleischer, E. L. Haines, H. R. Hart, Jr., R. T. Woods, and G. M. Comstock, The particle track record of the Sea of Tranquillity, Proc. Apollo 11 Lunar Sci. Conf. 3 (Pergamon Press, 1970) 2103.

[26] G. Crozaz, U. Haack, M. Hair, M. Maurette, R. Walker, and D. Woolum, Nuclear track studies of ancient solar radiations and dynamic lunar surface processes, Proc. Apollo 11 Lunar Sci. Conf. 3 (Pergamon Press, 1970) 2051.

[27] D. S. Burnett, J. C. Huneke, F. A. Podosek, G. Price Russ III, and G. J. Wasserburg, The irradiation history of lunar samples, Proc. Second Lunar Sci. Conf. 2 (M.I.T. Press, 1971) 1671.

[28] K. Marti and G. W. Lugmair, Kr^{81}-Kr and K-Ar^{40} ages, cosmic-ray spallation products, and neutron effects in lunar samples from Oceanus Procellarum, Proc. Second Lunar Sci. Conf. 2 (M.I.T. Press, 1971) 1591.

[29] N. J. Hubbard, C. Meyer, Jr., P. W. Gast, and H. Wiesmann, The composition and derivation of Apollo 12 soils, Earth Planet. Sci. Letters 10 (1971) 341.

[30] Leon T. Silver, U-Th-Pb isotope systems in Apollo 11 and 12 regolithic materials and a possible age for the Copernicus impact event, Trans. Am. Geophys. Union 52 (1971) 534 *(abstract)*.
P. Eberhardt, O. Eugster, J. Geiss, N. Grögler, J. Schwarzmüller, A. Stettler, and L. Weber, When was the Apollo 12 KREEP ejected?, Lunar Science III (Lunar Sci. Inst. Cont. No. 88, 1972) 206.

[31] Lunar Sample Preliminary Examination Team, Preliminary examination of lunar samples from Apollo 12, Science 167 (1970) 1325.

[32] George A. Sellers, Ching Chang Woo, Melvin L. Bird, and Michael B. Duke, Composition and grain-size characteristics of fines from the Apollo 12 double-core tube, Proc. Second Lunar Sci. Conf.1 (M.I.T. Press, 1971)665.

[33] William Quaide, Verne Oberbeck, Theodore Bunch and George Polkowski, Investigations of the natural history of the regolith at the Apollo 12 site, Proc. Second Lunar Sci. Conf. 2 (M.I.T. Press, 1971) 701.

[34] G. Arrhenius, S. Liang, D. Macdougall, L. Wilkening, N. Bhandari, S. Bhat, D. Lal, G. Rajagopalan, A. S. Tamhane, and V. S. Venkatavaradan, The exposure history of the Apollo 12 regolith, Proc. Second Lunar Sci. Conf. 3 (M.I.T. Press, 1971) 2583.

[35] G. Crozaz, R. Walker, and D. Woolum, Nuclear track studies of dynamic surface processes on the moon and the constancy of solar activity, Proc. Second Lunar Sci. Conf. 3 (M.I.T. Press, 1971) 2543.

[36] Eugene M. Shoemaker, personal communication.

[37] G. Crozaz, R. Drozd, C. M. Hohenberg, H. P. Hoyt, Jr., D. Ragan, R. M. Walker, and D. Yuhas, Solar flare and galactic cosmic ray studies of Apollo 14 and 15 samples, Proc. Third Lunar Sci. Conf. 3 (M.I.T. Press, 1972) 2917.

[38] P. P. Phakey, I. D. Hutcheon, R. S. Rajan, and P. B. Price, Radiation effects in soils from five lunar missions, Proc. Third Lunar Sci. Conf. 3 (M.I.T. Press, 1971) 2905.

[39] Narendra Bhandari, Jitendra Goswami, and Devendra Lal, Surface irradiation and evolution of the lunar regolith, preprint (1973).

[40] P. C. Wszolek, R. F. Jackson, and A. L. Burlingame, Carbon chemistry of the Apollo 15 deep drill stem and a glass-rich sample related to the uniformity of the regolith and lunar surface processes, The Apollo 15 Lunar Samples (Lunar Sci. Inst., 1972) 324.

[41] C. Behrmann, G. Crozaz, R. Drozd, C. Hohenberg, C. Ralston, R. Walker, and D. Yuhas, Radiation history of the Apollo 16 site, Lunar Science IV (Lunar Sci. Inst., 1972) 54.

[42] Friedrich Hörz, W. D. Carrier III, J. W. Young, C. M. Duke, J. S. Nagle, and R. Fryxell, Apollo 16 special samples, Apollo 16 Preliminary Science Report (NASA SP-315, 1972) 7-24.

[43] Donald E. Gault, personal communication.

[44] J. C. Huneke, F. A. Podosek, D. S. Burnett, and G. J. Wasserburg, Rare gas studies of the galactic cosmic ray irradiation history of lunar rocks, Geochim. Cosmochim. Acta 36 (1972) 269.

[45] D. D. Bogard, J. G. Funkhauser, O. A. Schaeffer and J. Zähringer, Noble gas abundances in lunar material, cosmic ray spallation products and radiation ages from the Sea of Tranquility and the Ocean of Storms, J. Geophys. Res. 76 (1971) 2757.

[46] D. S. Burnett, personal communication.

[47] P. W. Gast, N. J. Hubbard, and H. Wiesmann, Chemical composition and petrogenesis of basalts from Tranquillity Base, Proc. Apollo 11 Lunar Sci. Conf. 2 (Pergamon Press, 1970) 1143.

[48] C. M. Hohenberg and M. W. Rowe, Spallation yields of xenon from irradiation of Cs, Ce, Nd, Dy, and a rare earth mixture with 730-MeV protons, J. Geophys. Res. 75 (1970) 4205.

[49] F. Tera, O. Eugster, D. S. Burnett, and G. J. Wasserburg, Comparative study of Li, Na, K, Rb, Cs, Ca, Sr, and Ba abundances in achondrites and in Apollo 11 lunar samples, Proc. Apollo 11 Lunar Sci. Conf. 2 (Pergamon Press, 1970) 1637.

[50] P. Eberhardt, J. Geiss, H. Graf, N. Grögler, U, Krähenbühl, H. Schwaller, J. Schwarzmüller, and A. Stettler, Correlation between rock type and irradiation history of Apollo 11 igneous rocks, Earth Planet. Sci. Letters 10 (1970) 67.

[51] R. O. Pepin, L. E. Nyquist, Douglas Phinney, and David C. Black, Rare gases in Apollo 11 lunar material, Proc. Apollo 11 Lunar Sci. Conf 2 (Pergamon Press, 1970) 1435.

[52] F. A. Podosek, personal communication.

[53] C. M. Hohenberg, P. K. Davis, W. A. Kaiser, R. S. Lewis, and J. H. Reynolds, Trapped and cosmogenic rare gases from stepwise heating of Apollo 11 samples, Proc. Apollo 11 Lunar Sci. Conf. 2 (Pergamon Press, 1970) 1283.

[54] H. Schwaller, P. Eberhardt, J. Geiss, H. Graf, and N. Grögler, The $(^{78}Kr/^{83}Kr)_{sp}$ - $(^{131}Xe/^{126}Xe)_{sp}$ correlation in Apollo 12 rocks. Earth Planet. Sci. Letters 12 (1971) 167.

[55] Lunatic Asylum, Mineralogic and isotopic investigations on lunar rock 12013, Earth Planet. Sci. Letters 9 (1970) 137.

[56] G. W. Lugmair and Kurt Marti, Exposure ages and neutron capture record in lunar samples from Fra Mauro, Proc. Third Lunar Sci. Conf. 2 (M.I.T. Press, 1972) 1891.

[57] John A. Philpotts and C. C. Schnetzler, Apollo 11 lunar samples: K, Rb, Sr, Ba, and rare-earth concentrations in some rocks and separated phases, Proc. Apollo 11 Lunar Sci. Conf. 2 (Pergamon Press, 1970) 1471.

[58] Larry A. Haskin, Ralph O. Allen, Philip A. Helmke, Theodore P. Paster, Michael R. Anderson, Randy L. Korotev, and Kathleen A. Zweifel, Rare earths and other trace elements in Apollo 11 lunar samples, Proc. Apollo 11 Lunar Sci. Conf. 2 (Pergamon Press, 1970) 1213.

[59] Gordon G. Goles, Keith Randle, Masumi Osawa, David J. Lindstrom, Dominique Y. Jérome, Terry L. Steinborn, Robert L. Beyer, Marilyn R. Martin, and Sheila M. McKay, Interpretations and speculations on elemental abundances in lunar samples, Proc. Apollo 11 Lunar Sci. Conf. 2 (Pergamon Press, 1970) 1177.

[60] W. Compston, B. W. Chappell, P. A. Arriens, and M. J. Vernon, The chemistry and age of Apollo 11 lunar material, Proc. Apollo 11 Lunar Sci. Conf. 2 (Pergamon Press, 1970) 1007.

[61] Gordon G. Goles, Keith Randle, Masumi Osawa, Roman A. Schmitt, Hiroshi Wakita, William D. Ehmann, and John W. Morgan, Elemental abundances by instrumental activation analyses in chips from 27 lunar rocks, Proc. Apollo 11 Lunar Sci. Conf. 2 (Pergamon Press, 1970) 1165.

[62] Norman J. Hubbard and Paul W. Gast, Chemical composition and origin of nonmare lunar basalts, Proc. Second Lunar Sci. Conf. 2 (M.I.T. Press, 1971) 999.

[63] H. Wakita, P. Rey, and R. A. Schmitt, Abundances of the 14 rare-earth elements and 12 other trace elements in Apollo 12 samples; five igneous and one breccia rock and four soils, Proc. Second Lunar Sci. Conf. 2 (M.I.T. Press, 1971) 1319.

[64] N. J. Hubbard, P. W. Gast, and H. Wiesmann, Rare earth, alkaline and alkali metal and $^{87}/^{86}Sr$ data for subsamples of lunar sample 12013, Earth Planet. Sci. Letters 9 (1970) 181.

[65] C. C. Schnetzler and John A. Philpotts, Alkali, alkaline earth, and rare-earth element concentrations in some Apollo 12 soils, rocks, and separated phases, Proc. Second Lunar Sci. Conf. 2 (M.I.T. Press, 1971) 1101.

[66] John A. Philpotts, C. C. Schnetzler, David F. Nava, Michael L. Bottino, Paul D. Fullagar, Herman H. Thomas, Shuford Schuhmann, and Charles W. Kouns, Apollo 14: some geochemical aspects, Proc. Third Lunar Sci. Conf. 2 (M.I.T. Press, 1972) 1293.

[67] D. E. Yuhas, R. M. Walker, H. Reeves, G. Poupeau, P. Pellas, J. C. Lorin, G. C. Chatrit, J. L. Berdot, P. B. Price, I. D. Hutcheon, H. R. Hart, Jr., R. L. Fleischer, G. M. Comstock, D. Lal, J. N. Goswami, and N. Bhandari, Track consortium report on rock 14310, Proc. Third Lunar Sci. Conf. 3 (M.I.T. Press, 1972) 2941.

[68] N. Bhandari, J. N. Goswami, S. K. Gupta, D. Lal, A. S. Tamhane, and V. S. Venkatavaradan, Collision controlled radiation history of the lunar regolith. Proc. Third Lunar Sci. Conf. 3 (M.I.T. Press, 1972) 2811.

[69] G. A. Swann, N. G. Bailey, R. M. Batson, V. L. Freeman, M. H. Hait, J. W. Head, H. E. Holt, K. A. Howard, J. B. Irwin, K. B. Larson, W. R. Muehlberger, V. S. Reed, J. J. Rennilson, G. G. Schaber, D. R. Scott, L. T. Silver, R. L. Sutton, G. E. Ulrich, H. G. Wilshire, and E. W. Wolfe, Preliminary geologic investigation of the Apollo 15 landing site, Apollo 15 Preliminary Science Report (NASA SP-289, 1972) 5-1.

[70] C. Behrmann, G. Crozaz, R. Drozd, C. M. Hohenberg, C. Ralston, R. M. Walker, and D. Yuhas, Rare-gas and particle track studies of Apollo 15 samples: Hadley Rille and special samples, The Apollo 15 Lunar Samples (Lunar Sci. Inst., 1972) 329.

[71] S. R. Taylor, M. Gorton, P. Muir, W. Nance, R. Rudowski, and N. Ware, Composition of the lunar highlands II - the Apennine Front, The Apollo 15 Lunar Samples (Lunar Sci. Inst., 1972) 262.

[72] M. H. Hey, Catalogue of Meteorites (British Museum, 1966 - 3rd ed.).

[73] G. F. Herzog and Edward Anders, Radiation age of the Norton County meteorite, Geochim. Cosmochim. Acta 35 (1971) 239.

[74] F. Begemann, J. Geiss, and D. C. Hess, Radiation age of a meteorite from cosmic ray-produced He^3 and H^3, Phys. Rev. 107 (1957) 540.

[75] O. Eugster, F. Tera, D. S. Burnett, and G. J. Wasserburg, Isotopic composition of gadolinium and neutron-capture effects in some meteorites, J. Geophys. Res. 75 (1970) 2753.

[76] D. S. Burnett, H. J. Lippolt, and G. J. Wasserburg, The relative isotopic abundance of K^{40} in terrestrial and meteoritic samples, J. Geophys. Res. 71 (1966) 1249.

[77] Carl W. Beck and Lincoln LaPaz, The Nortonite fall and its mineralogy, Am. Mineral. 36 (1951) 45.

[78] H. B. Wiik, The chemical composition of some stony meteorites, Geochim. Cosmochim. Acta 9 (1956) 279.

[79] Marcus G. Langseth, Jr., Sydney P. Clark, Jr., John L. Chute, Jr., Stephen J. Keihm, and Alfred E. Wechaler, Heat-flow experiment, Apollo 15 Preliminary Science Report (NASA SP-289, 1972) 11-1.

[80] Clay P. Butler, Temperature of meteoroids in space, Meteoritics 3 (1966) 59.

[81] P. Eberhardt, J. Geiss, and H. Lutz, Neutrons in meteorites, Earth Science and Meteorites - J. Geiss and E. D. Goldberg (ed.) (North-Holland Pub. Co., 1963) 143.

[82] Roy S. Clarke, Jr., Eugene Jarosewich, Brian Mason, Joseph Nelen, Manuel Gómez, and Jack R. Hyde, The Allende, Mexico, Meteorite Shower, Smithsonian Cont. Earth Sci. 5 (1970).

[83] Lawrence Grossman, Condensation, Chondrites, and Planets (Ph.D. thesis, Yale Univ., 1972).

[84] E. L. Fireman, J. DeFelice, and Elinor Norton, Ages of the Allende meteorite, Geochim. Cosmochim. Acta 34 (1970) 873.

[85] Phillip J. Cressey, Jr., Cosmogenic radionuclides in the Allende and Murchison carbonaceous chondrites, J. Geophys. Res. 77 (1972) 4905.

[86] C. M. Gray, D. A. Papanastassiou, and G. J. Wasserburg, The identification of early condensates from the solar nebula, Icarus 20 (1973) in press.

[87] F. A. Podosek, and R. S. Lewis, ^{129}I and ^{244}Pu abundances in white inclusions of the Allende meteorite, Earth Planet. Sci. Letters 15 (1972) 101.

[88] E. L. Fireman and R. Goebel, Argon 37 and Argon 39 in recently fallen meteorites and cosmic-ray variations, J. Geophys. Res. 75 (1970) 2115.

[89] W. A. Fowler, J. L. Greenstein, and F. Hoyle, Nucleosynthesis during the early history of the solar system, Geophys. J. 6 (1962) 148.

[90] D. S. Burnett, William A. Fowler and F. Hoyle, Nucleosynthesis in the early history of the solar system, Geochim. Cosmochim. Acta 29 (1965) 1209.

Chapter 6

EARTH AND PLANETARY SCIENCE LETTERS 13 (1971) 53–60. NORTH-HOLLAND PUBLISHING COMPANY

NEUTRON CAPTURE ON ^{149}Sm IN LUNAR SAMPLES *

G.P. RUSS III, D.S. BURNETT, R.E. LINGENFELTER **
and G.J. WASSERBURG
The Lunatic Asylum of the Charles Arms Laboratory, Division of Geological and Planetary Sciences, California Institute of Technology, Pasadena, California 91109, USA

Received 28 September 1971
Revised version received 13 November 1971

High precision isotopic composition measurements of Sm have been carried out for two terrestrial and seven lunar samples from three Apollo sites. The lunar samples, selected to show a wide variation in cosmic ray exposure ages, have a wide range of enrichments in ^{150}Sm/^{154}Sm (up to 0.8%) and depletions in ^{149}Sm/^{154}Sm which are due to neutron capture. The ratio of the number of neutrons captured per atom by ^{149}Sm to ^{157}Gd is 0.9 and reflects a hardened lunar neutron spectrum. This ratio is in reasonable but not exact agreement with that obtained from the theoretical lunar neutron energy spectrum of Lingenfelter, Canfield and Hampel. The average composition for terrestrial samarium is ^{144}Sm : ^{147}Sm : ^{148}Sm : ^{149}Sm : ^{150}Sm : ^{152}Sm : ^{154}Sm = 3.074 : 14.995 : 11.243 : 13.820 : 7.380 : 26.739 : 22.749%.

1. Introduction

Previous measurements have established that Gd isotopic variations are present in lunar samples [1–4] and in the Norton County meteorite [5] which can be ascribed unambiguously to neutron capture on ^{157}Gd and ^{155}Gd, predominantly around the strong resonances in both these nuclei at ~0.03 eV. Theoretical calculations [6, 7] have shown that the lunar neutron energy spectrum in the energy range $\lesssim$ 0.2 eV differs greatly from the Maxwell–Boltzmann distribution for neutrons in thermal equilibrium at ambient lunar temperatures ($kT \sim 0.02$ eV). The maximum in the neutron energy spectrum is shifted distinctly to higher (~ 0.1 eV) energies ('hardened') because of the relatively strong neutron absorbing properties of lunar material. The existence of such spectra has long been recognized (e.g., in the earth's atmosphere [14]). The hardness of the spectrum suggests that comparable neutron capture should also occur in the strong resonance in ^{149}Sm at 0.1 eV. The relative magnitude of the neutron capture isotopic variation in ^{150}Sm/^{149}Sm compared to ^{158}Gd/^{157}Gd can give a quantitative measure of the hardness of the spectrum.

2. Experimental

2.1. *Samples*

Lunar samples were chosen in order to determine whether the ratio of the Sm isotopic variations to those for Gd varied due to differences in neutron absorbing properties (chemical composition) between the various sites and to determine whether differences in this ratio were present between soil and rock samples. Soil samples from all three sites have been analyzed for both Sm and Gd along with lunar rocks 14310, 14321, and 10017, which were picked because of their spread in exposure ages. Sample 10084,12 was sieved and only the particles smaller than 37 μm were used. For 12042,44 the 'total' soil was washed in acetone and only those very fine particles which remained in suspension (acetone floats) were taken for

* Division of Geological and Planetary Sciences, contribution no. 2067.

** Institute of Geophysics and Planetary Physics, University of California, Los Angeles, California 90024, USA.

this analysis. Particles larger than 300 μm were removed from soil 14163,110 and a split of the remainder was analyzed.

Since sized fractions of the soils were used, the measured isotopic shifts of these samples are not necessarily representative of the 'total' soils. Two pieces of rock 14310 were analyzed. An exterior sample 14310,100 was from the side of the rock while 14310,88 came from the interior near the center. The typical sample size was ~ 30 mg. Reagent Sm and the Knippa basalt have been analyzed as terrestrial reference samples and to define the precision of our analyses.

2.2. *Chemistry*

Chemical separations were carried out by the procedures of Eugster et al. [5], which, as shown by fig.1 in ref. [5], give excellent separations of both Gd and Sm from other elements. In this procedure two cation exchange resin columns are used. The second of these separates the rare earth elements, permitting Gd to be isolated from Sm. ^{160}Tb tracer was added to monitor the column elutions. For two samples, which had accumulated noticeable amounts of NH_4Cl because the sample solutions containing NH_4^+ were allowed to stand in the laboratory where HCl vapors were present, an additional cation exchange step (0.2 × 4 cm column) was added before filament loading to remove NH_4^+. In this step, the sample in a drop of H_2O was loaded on a strong acid cation resin in the H^+ form. The NH_4^+ was eluted with 2N HCl, then the Sm or Gd was eluted with 4N HCl. Blanks have not yet been determined for Sm but these should be negligible since the Gd blank is ~ 10^{-11} g. The Knippa basalt sample was processed through the chemical separation procedure in order to test for any spurious effects on the Sm isotopic abundances due to our chemical separations.

2.3. *Mass spectrometry*

The dried Sm sample was dissolved in a small drop of dilute hydrochloric acid and bonded onto a V-shaped filament of zone refined rhenium which had previously been outgassed at 5 amps for 2 hr at about 10^{-6} Torr. After the filament was heated briefly to dull red to burn off hydrocarbons, a layer of rhenium powder (−325 mesh, Electronic Space Products) was added. Phosphoric acid was then mixed in and evaporated. This seemed to improve the bonding of the powder to the filament. Finally, the filament was again heated briefly to an orange color. The sample of 14163 was analyzed on a single flat rhenium ribbon without rhenium powder. All other samples were analyzed using the V-filament technique by which stable beams of ~4×10^{-12} amps of $^{154}Sm^+$ could be obtained for several hours in the temperature range of 1350–1400°C for samples of ~ 300 ng. With the exception of the 14163 sample (see below) all data were taken using ^{154}Sm as the reference isotope. Sm ions were measured rather than SmO ions, which also give large signals, because SmF^+ interference was found to be as large as the ^{18}O corrections. In the temperature range where data were taken, SmO^+ is from 2 to 0.2 times the Sm^+ beam intensity and the SmO^+/Sm^+ decreases with time.

Sm isotopic analyses were made on the Lunatic III mass spectrometer using a Faraday cup and a 10^{11} ohm resistor. This mass spectrometer is similar to the Lunatic I described by Wasserburg et al. [8]. Gd analyses were made on the Lunatic I using the procedures of Eugster et al. [5].

All seven Sm isotopes have been measured and the data screened such that only individual ratios which satisfied two criteria were included in the final average. First, for a set of 10 ratios, the standard deviations for $^{148-152}Sm/^{154}Sm$ were required to be less than 0.25%. All ratios belonging to sets failing this criterion were rejected. Second, for three sequential readings *A*, *B* and *C* of mass 154, the time-interpolated mean of *A* and *C* was required to agree with *B* to within 0.1% (cf. ref. [8]). If this obtained, the ratios formed for other isotopes by interpolating *A* and *B* were retained. Only a few sets of data failed to meet criterion I, but criterion II eliminated from 10% to 60% of the ratios, depending on the stability of the ion beam. All ratios meeting both criteria have been normalized to $^{147}Sm/^{154}Sm = 0.65918$ (averaged from refs. [9] and [10]), which agrees within 2‰ with our average uncorrected value for the normal runs. The corrected ratios have been averaged and two standard deviations of the mean calculated. The results are tabulated in table 1. No significant differences were observed for the average values if the unscreened data were used rather than those which satisfied the criteria given above.

In order to reduce the effect of any variable inter-

Table 1
Isotopic composition of terrestrial and lunar Sm*.

Sample	Run no.	No. of ratios $^{150}Sm/^{154}Sm$	$^{152}Sm/^{154}Sm$	$^{150}Sm/^{154}Sm$	$^{149}Sm/^{154}Sm$	$^{148}Sm/^{154}Sm$	$^{144}Sm/^{154}Sm$
Reagent	318	102	1.175 49	0.32 447	0.60 751	0.494 21	0.135 21
			± 8	± 4	± 5	± 5	± 3
Reagent	319	87	1.175 39	0.32 442	0.60 750	0.494 22	0.135 12
			± 10	± 5	± 10	± 6	± 5
Reagent	325	194	1.175 33	0.32 441	0.60 749	0.494 22	0.135 10
			± 9	± 5	± 7	± 6	± 5
Knippa basalt	324	100	1.175 45	0.32 441	0.60 751	0.494 28	0.135 18
			± 19	± 10	± 13	± 11	± 10
Terrestrial average		483	1.175 40	0.32 442	0.60 750	0.494 23	0.135 14
			± 6	± 3	± 4	± 4	± 3
12042,44 (acetone floats)	320	114	1.175 33	0.32 566	0 60 635	0.494 32	0.135 17
			± 13	± 7	± 9	± 9	± 5
10084,12 (−37 μm)	321	219	1.175 11	0.32 589	0.60 610	0.494 23	0.135 16
			± 8	± 4	± 5	± 5	± 4
14163,110	307	70		0.32 601	0.60 581	0.494 21	
				± 6	± 10	± 10	±
14321,161	322	116	1.175 23	0.32 441	0.60 740	0.494 11	0.135 17
			± 12	± 6	± 7	± 7	± 5
14310,100	323	220	1.175 15	0.32 598	0.60 594	0.494 24	0.135 20
			± 6	± 3	± 4	± 4	± 3
14310,88	327	116	1.175 12	0.32 579	0.60 602	0.494 20	0.135 16
			± 14	± 8	± 13	± 8	± 6
10017,32	326	121	1.175 22	0.32 696	0.60 508	0.494 25	0.135 23
			± 16	± 7	± 10	± 7	± 11

* Data are corrected for mass discrimination by normalizing to ($^{147}Sm/^{154}Sm$) = 0.65918. Quoted errors are two standard deviations of the mean.

ference at mass 154, a $^{150}Sm/^{149}Sm$ value was calculated from each ratio of $^{150}Sm/^{154}Sm$ and $^{149}Sm/^{154}Sm$ corrected for fractionation using the nearest $^{147}Sm/^{154}Sm$ ratio. These values were then averaged for the total run. If $^{150}Sm/^{149}Sm$ were calculated from the average $^{150}Sm/^{154}Sm$ and $^{149}Sm/^{154}Sm$ for the run, an interference at mass 154 would tend to enlarge the apparent error in $^{150}Sm/^{149}Sm$.

The data for 14163 in table 1 were based on an early analysis in which ^{152}Sm was used as the reference isotope and $^{154}Sm/^{152}Sm$ ratios were not measured. In this case we have normalized the data to $^{147}Sm/^{152}Sm = 0.56081$ based on our average value for terrestrial Sm. This should produce discrimination-corrected $^{148-150}Sm/^{152}Sm$ ratios which are internally consistent with the other analyses. The $^{148-150}Sm/^{154}Sm$ values tabulated in table 1 were calculated by multiplying the corrected $^{148-150}Sm/^{152}Sm$ by 1.17540 (our average value for terrestrial $^{152}Sm/^{154}Sm$). The error in the terrestrial $^{152}Sm/^{154}Sm$ has been included in the tabulated errors for 14163 in table 1.

2.4. *Interfering ions*

The chemical separations used are quite good, but the possibility of interference from spurious ions was monitored by scanning the magnetic field from the Ba^+ region to above the SmO^+ region and by observing the constancy of the normalized ratios $^{152,148,144}Sm/^{154}Sm$. Barium can interfere at mass 154 either as

$^{138}Ba^{16}O$ or $^{135}Ba^{19}F$. In either case the contamination at mass 154 would be ~ 10 times that at other Sm masses, so that only 154 need be considered for small corrections. $Ba^{16}O$ is difficult to observe directly because of Eu which tends to obscure BaO^+ at masses 151 and 153. BaF can be monitored at mass 157, Gd, which could tail into the Sm fraction during the chemical separation, has interfering isotopes at masses 154 and 152, but again the 154 interference is 10 times larger. Peaks at masses 158, 157, 156 and 155 would indicate Gd. Nd can interfere at masses 144, 148 and 150. The presence of Nd can be confirmed by peaks at 142, 143, 145 and 146. However, because ^{144}Nd is ~ 15 times more significant in a Sm spectrum than ^{148}Nd and ~ 9 times more than ^{150}Nd, the absence of positive anomalies at 144 would argue against the presence of significant Nd signals. Nd and Ba are strongly held in the chemical procedure so that any interference from either probably would be from the blank. On one occasion (run 322) an anomalous peak was observed at mass 136. This is attributed to $^{89}Y^{31}P^{16}O$. YPO_2 would produce an interference at mass 152 which cannot be ruled out in this run. At operating temperatures no evidence of hydrocarbons was seen in the adjacent mass region and the background between the Sm peaks was smooth.

Although the beam intensity typically varied by a factor of three during the data taking period, no discernible changes were found in the normalized ratios and the data appear to be normally distributed. Small discrepancies (1–3 parts in 10^4 or about 2 times the quoted statistical errors) were observed (table 1) between the terrestrial and lunar $^{152}Sm/^{154}Sm$ values which we attribute to a small interference at mass 154 from $^{138}Ba^{16}O$, $^{135}Ba^{19}F$ and/or ^{154}Gd. In general runs with high Ba^+ have relatively low $^{152}Sm/^{154}Sm$ but the statistical variation from reading to reading is too large to resolve any correlation between Ba^+ and $^{152}Sm/^{154}Sm$ within a run. For such an interference $^{152}Sm/^{154}Sm$ is the most sensitive ratio. The errors in $^{150}Sm/^{154}Sm$ and $^{149}Sm/^{154}Sm$ are less because when an interference is present at mass 154 the normalization procedure generates a false discrimination correction which tends to cancel the effect of the interference. In $^{150}Sm/^{149}Sm$, which is the ratio of greatest interest, the errors introduced by the observed interferences are negligible (< 5 parts in 10^5).

The choice of 154 as the reference isotope was made at an early stage before the interference problem had become evident. Since the effect on the ratios of prime interest is small the data were not reprocessed relative to another isotope. However, in the future, if samples with fluences large enough to cause significant ^{151}Eu neutron capture are not encountered (see section on lunar data), it might be better to analyze the data relative to mass 152.

3. Results

3.1. *Terrestrial Sm*

The four analyses of reagent Sm and Sm separated from the Knippa basalt agree within the quoted errors

Table 2
Percentage abundances for terrestrial Sm.

Source \ Isotope	144	147	148	149	150	152	154
Inghram et al. [9]	3.16 ±0.1	15.07 ±0.15	11.27 ±0.11	13.84 ±0.14	7.47 ±0.07	26.63 ±0.26	22.53 ±0.22
Aitken et al. [10]	3.02 ±0.02	14.87 ±0.04	11.22 ±0.03	13.82 ±0.04	7.40 ±0.02	26.80 ±0.05	22.88 ±0.06
Collins et al. [11]	3.15 ±0.03	15.09 ±0.1	11.35 ±0.09	13.96 ±0.1	7.47 ±0.06	26.55 ±0.2	22.43 ±0.2
This work *	3.074 ±0.001	14.995 ±0.001	11.243 ±0.001	13.820 ±0.001	7.380 ±0.001	26.739 ±0.002	22.749 ±0.001

* These data are normalized to $^{147}Sm/^{154}Sm = 0.65918$ and do not include errors due to mass fractionation.

(table 1) for all isotopes except for $^{144}Sm/^{154}Sm$ for which the quoted error limits just fail to overlap. These data indicate that the calculated statistical errors are a relatively reliable measure of the precision of a single analysis. The 'terrestrial average' values were obtained by averaging the discrimination corrected isotopic ratios (483 points) for the four runs. The quoted error is two standard deviations of the mean. As shown in table 2, the isotopic abundances of terrestrial Sm reported here are considerably more precise than earlier literature values [9–11]. Both the present data and those reported in the literature are not absolute in that they are subject to systematic errors, which are difficult to evaluate, due to mass discrimination in the surface ionization process. Because of the considerably higher precision of the data reported here, our values should best represent the relative abundances of the Sm isotopes with the understanding that we have normalized our measured ratios to $^{147}Sm/^{154}Sm = 0.65918$. This choice is somewhat arbitrary but it is close to the average of our uncorrected measured $^{147}Sm/^{154}Sm$ ratios.

3.2. *Lunar data*

Inspection of table 1 shows that the Sm isotopic abundances in lunar samples show variations which correspond to the pattern expected for neutron capture. There are large and variable decreases in lunar $^{149}Sm/^{154}Sm$ which are an order of magnitude larger than experimental errors and correspondingly large increases in $^{150}Sm/^{154}Sm$. In contrast the ratios $^{144}Sm/^{154}Sm$, $^{148}Sm/^{154}Sm$ and $^{152}Sm/^{154}Sm$ are essentially equal to the terrestrial values. Although there are some small discrepancies for $^{152}Sm/^{154}Sm$ (see section on interfering ions), they are negligible for this discussion. In pure Sm the neutron fluence

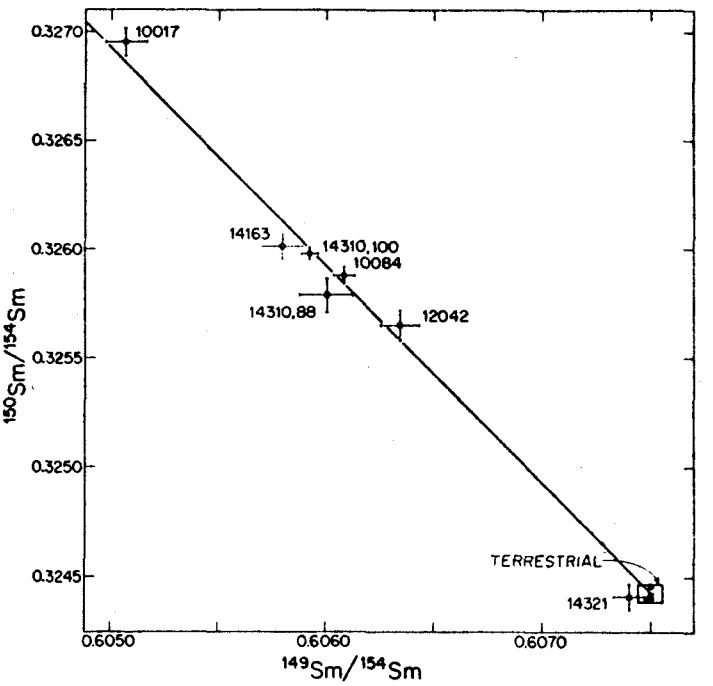

Fig. 1. $^{150}Sm/^{154}Sm$ versus $^{149}Sm/^{154}Sm$ correlation diagram. The ratios vary along the line predicted for neutron capture by ^{149}Sm. Errors are $2\sigma_{mean}$.

necessary to produce the observed effects on ^{149}Sm and ^{150}Sm would cause negligible changes in the ratios $^{144}Sm/^{154}Sm$, $^{148}Sm/^{154}Sm$, and $^{152}Sm/^{154}Sm$. The correlated variations in $^{149}Sm/^{154}Sm$ and $^{150}Sm/^{154}Sm$ can be explored quantitatively by means of a correlation diagram (fig. 1) analogous to that employed previously for Gd [1–5]. For a series of samples exposed to varying neutron fluences, the measured $^{149}Sm/^{154}Sm$ and $^{150}Sm/^{154}Sm$ should plot along a correlation line of slope −1. As shown in fig.1, the data do plot on such a line, which establishes unambiguously that the measured isotopic variations are due to neutron capture. The box indicates the limits set on the terrestrial values. The points in the box are averages for separate runs of terrestrial Sm.

Sample 14321 has no significant enrichment in $^{150}Sm/^{154}Sm$ which is consistent with its known low exposure age [12]. Sample 10017, which has a high exposure age [13], shows the largest effect. Two samples of rock 14310 have an intermediate neutron exposure and show a distinct difference between the exterior [#100] and interior [#88]. The soil samples, which were known to have large neutron fluences from Gd data [1–3] also plot in the middle region of the diagram and show some variability. However, it should be noted that the soils are not representative splits.

In natural samples where mixtures of Eu and Sm are present, enrichments in $^{152}Sm/^{154}Sm$ due to neutron capture on ^{151}Eu are expected to be $\lesssim 10^{-4}$ unless samples with neutron fluences greater than 10^{17} n/cm^2 are encountered. No lunar sample with a fluence greater than 4×10^{16} n/cm^2 has been observed.

4. Discussion

The Sm isotopic ratio which is most sensitive to neutron irradiation is $^{150}Sm/^{149}Sm$. Table 3 gives the $^{150}Sm/^{149}Sm$ and the analogous $^{158}Gd/^{157}Gd$ ratios measured in this laboratory on the same lunar samples. The enrichments in the lunar $^{150}Sm/^{149}Sm$ compared to the terrestrial ratio are a measure of the neutron fluence to which a given sample has been exposed. Lunar $^{158}Gd/^{157}Gd$ ratios have previously been used to estimate fluences (n/cm^2). In this paper we focus on the ratio of the variations in $^{150}Sm/^{149}Sm$ to those in $^{158}Gd/^{157}Gd$ in order to draw conclusions about

Table 3
Comparison of neutron capture anomalies in Sm and Gd.

Sample	$^{150}Sm/^{149}Sm$	$^{158}Gd/^{157}Gd$*	$\epsilon_{Sm}/\epsilon_{Gd}$**
Average terrestrial	0.53403 ± 5	1.58660 ± 11	
10084,12 (−37 μm)	0.53768 ± 7	1.59426 ± 26	0.83 ± 4
10017,32	0.54035 ± 11	1.59881 ± 14	0.89 ± 2
12042,44 (Acetone Floats)	0.53708 ± 11	1.59275 ± 28	0.84 ± 5
14163,110	0.53815 ± 13	1.59452 ± 13	0.89 ± 3
14321,161	0.53410 ± 9	1.58653 ± 14	
14310,88	0.53760 ± 10	1.59373 ± 15	0.86 ± 3
14310,100	0.53798 ± 6	1.59432 ± 68	0.88 ± 7
Theoretical values for Apollo 11 soil			
0°K			0.60
200°K			0.72
400°K			0.80

* The Gd isotopic composition is normalized to $^{156}Gd/^{160}Gd = 0.9361$. This introduces a fluence dependent false discrimination correction into $^{158}Gd/^{157}Gd$ [5]. This ratio is high by 2 parts in 10^4 for 10017.

** Corrected for the false discrimination in $^{158}Gd/^{157}Gd$.

the lunar neutron energy spectrum in the region below 0.2 eV. The correlation between the measured $^{150}Sm/^{149}Sm$ and $^{158}Gd/^{157}Gd$ is shown in fig. 2. The data show a rather precise linear relationship between the terrestrial abundances (and 14321), and extending up to 10017. It follows that the ratio of the isotopic variations in Sm and Gd is essentially constant.

The percentage enhancements in $^{150}Sm/^{149}Sm$ are larger than those observed for $^{158}Gd/^{157}Gd$. These large enrichments are in themselves a clear demonstration of the hardness of the lunar neutron spectrum.

For the purposes of the present paper, the comparison between experiment and theory is the relative magnitude of the neutron anomalies in Sm and Gd. We define ϵ to be the number of neutrons captured per atom of a particular isotope; ϵ is equal to the product of the cross section weighted over the energy spectrum

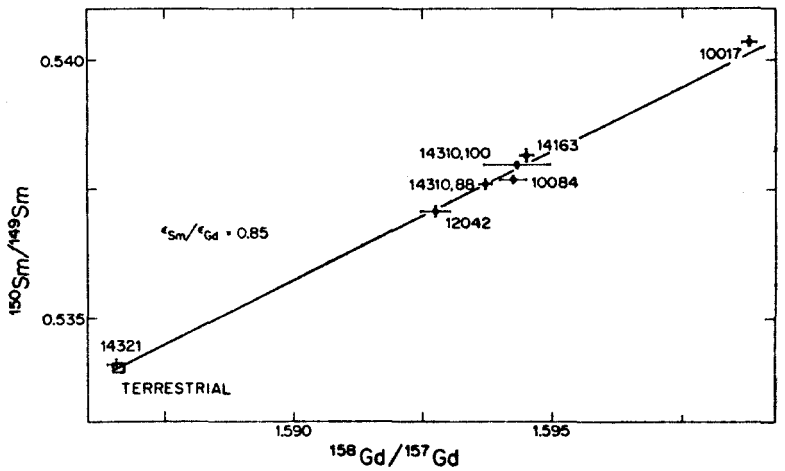

Fig. 2. Correlated variations in $^{150}Sm/^{149}Sm$ and $^{158}Gd/^{157}Gd$. The samples fall in a nearly linear array indicating exposure to essentially the same neutron spectrum. $\epsilon_{Sm}/\epsilon_{Gd}$ is the ratios of the average cross sections. A typical value ($\epsilon_{Sm}/\epsilon_{Gd}$ = 0.85) is shown for reference.

and the fluence. This is directly related to experimental quantities by

$$\epsilon_{Sm} = \frac{(^{150}Sm/^{149}Sm)_M - (^{150}Sm/^{149}Sm)_O}{[1 + (^{150}Sm/^{149}Sm)_M]}$$

where the subscripts M and O refer to the measured and terrestrial ratios respectively. An analogous definition of ϵ_{Gd} is made by replacing $^{150}Sm/^{149}Sm$ with $^{158}Gd/^{157}Gd$.

The ratio of the experimental values of ϵ for Sm and Gd can be compared directly with the average capture cross sections for ^{149}Sm and ^{157}Gd calculated for the proper neutron energy spectrum: $\epsilon_{Sm}/\epsilon_{Gd} = \langle\sigma_{149}\rangle/\langle\sigma_{157}\rangle$. Here $\langle\sigma_m\rangle$ is the capture cross section for the isotope of mass m averaged over the lunar neutron energy spectrum. These average cross sections are dependent on both the temperature and, more importantly, the composition of the lunar soil as discussed by LCH II [7], and are essentially depth independent except very near the surface.

Using the cross sections calculated by LCH II, theoretical values of $\langle\sigma_{149}\rangle/\langle\sigma_{157}\rangle$ = 0.60, 0.72 and 0.80 are obtained for Apollo 11 soil for temperatures of 0°, 200° and 400°K respectively. For the soils 12042 and 14163, this ratio is calculated to be the same, but it is lower than the ratio calculated for 10084 by about 7% and 4% for temperatures of 0°K and 400°K respectively.

The experimental values $\epsilon_{Sm}/\epsilon_{Gd}$ shown in table 3 are typically ~0.9 and are in reasonable agreement with the theoretical range of 0.6–0.8. Any differences among the Apollo sites are smaller than our errors (~4%). In comparison $(\sigma_{149}/\sigma_{157})_{2200\,m/sec}$ is 0.17. This is grossly different from both the observed values and the values calculated by LCH II, and clearly demonstrates the sensitivity of the quantity $\epsilon_{Sm}/\epsilon_{Gd}$ to the shape of the neutron spectrum in the sub eV region.

The determination of $\epsilon_{Sm}/\epsilon_{Gd}$ places constraints on the lunar neutron spectrum at low energies. The calculations of LCH II appear to describe the observations reasonably well in the energy region monitored by Gd and Sm neutron capture. However, for the 200°K case, which is closest to the actual lunar temperature below the zone of diurnal variation, the calculated values are low by ~20%. This implies that either the adopted Sm cross section data are not accurate or the lunar spectrum neutron is somewhat harder than calculated by LCH II. Refinements in the model for calculating neutron scattering at low energies and better cross sections might resolve the differences.

The discussion so far has concentrated on the shape of the neutron spectrum and not the actual flux. This latter matter is of considerable importance in unravelling the mixing rates of the lunar regolith. Estimates of the neutron fluence in the sub 0.2 eV region can be obtained by using the observed isotopic effects and the average cross sections $\langle\sigma_{149}\rangle$ or $\langle\sigma_{157}\rangle$ calculated using the energy spectrum of LCH II. Typical fluence values of $\sim 2 \times 10^{16}$ n/cm^2 ($E < 0.2$ eV) are obtained for soils. In situ measurements of neutron capture rates from which fluxes can be inferred will greatly enhance the use of isotopic measurements to unravel lunar surface mixing problems.

Acknowledgements

Discussions with F. Tera and J. Huneke were very beneficial. This work was supported by the National Science Foundation under Grant GP-28027 and in part by NASA Contract NGL-05-002-188. One of us (G.P.R.) is supported by a National Defense Education Act, Title IV, Fellowship and his wife.

References

[1] A.L. Albee, D.S. Burnett, A.A. Chodos, O.J. Eugster, J.C. Huneke, D.A. Papanastassiou, F.A. Podosek, G.P. Russ III, H.G. Sanz, F. Tera and G.J. Wasserburg, Ages, irradiation history, and chemical composition of lunar rocks from the Sea of Tranquillity, Science 167 (1970) 463.

[2] O. Eugster, F. Tera, D.S. Burnett and G.J. Wasserburg, The isotopic composition of Gd and neutron capture effects in samples from Apollo 11, Earth Planet. Sci. Letters 8 (1970) 20.

[3] D.S. Burnett, J.C. Huneke, F.A. Podosek, G. Price Russ III and G.J. Wasserburg, The irradiation history of lunar samples, Proc. Apollo 12 Lunar Sci. Conf. (MIT Press, 1971) 1671.

[4] K. Marti and G.W. Lugmair, Kr^{81}-Kr and K-Ar^{40} ages, cosmic-ray spallation products and neutron effects in lunar samples from Oceanus Procellarium, Proc. Apollo 12 Lunar Sci. Conf. (MIT Press, 1971) 1591.

[5] O. Eugster, F. Tera, D.S. Burnett and G.J. Wasserburg, Isotopic composition of gadolinium and neutron capture effects in some meteorites, J. Geophys. Res. 75 (1970) 2753.

[6] R.E. Lingenfelter, E.H. Canfield and W.N. Hess, The lunar neutron flux, J. Geophys. Res. 66 (1961) 2665.

[7] R.E. Lingenfelter, E.H. Canfield and V.H. Hampel, The lunar neutron flux revisited, to be submitted to Earth Planet. Sci. Letters.

[8] G.J. Wasserburg, D.A. Papanastassiou, E.V. Nenow and C.A. Bauman, A programmable magnetic field mass spectrometer with on-line data processing, Rev. Sci. Inst. 40 (1969) 288.

[9] M.G. Inghram, D.C. Hess and R.J. Hayden, Isotopic composition of Sm, Phys. Rev. 73 (1948) 180.

[10] K.L. Aitken, J. Littler, E.E. Lockett and G.H. Palmer, The pile-neutron absorption cross-section of Sm^{149}, J. Nucl. Energy 4 (1957) 33.

[11] T.L. Collins, F.M. Rourke and F.A. White, Mass-spectrometric investigation of the rare earth elements for the existence of new stable isotopes, Phys. Rev. 105 (1957) 196.

[12] G. Turner, J.C. Huneke, F.A. Podosek and G.J. Wasserburg, ^{40}Ar-^{39}Ar ages and cosmic ray exposure ages of Apollo 14 samples, Earth Planet. Sci. Letters 12 (1971) 19.

[13] J.C. Huneke, F.A. Podosek, D.S. Burnett and G.J. Wasserburg, Rare gas studies of the galactic cosmic ray irradiation history of lunar rocks, to be published in Geochim. Cosmochim. Acta.

[14] H.A. Bethe, S.A. Korff, G. Placzek, On the interpretation of neutron measurements in cosmic radiation, Phys. Rev. 57 (1940) 573.

Chapter 7

EARTH AND PLANETARY SCIENCE LETTERS 13 (1972) 384 - 386. NORTH-HOLLAND PUBLISHING COMPANY

NEUTRON CAPTURE ON Gd AND Sm IN THE LUNA 16, G-2 SOIL*

G. P. RUSS π

Lunatic Asylum, Division of Geological and Planetary Sciences, California Institute of Technology, Pasadena, California 91109, USA

Received 3 December 1971

The Gd and Sm isotopic compositions have been measured in the Luna 16, G-2 soil. This sample has the largest low energy neutron fluence $\{\psi = 5.9 \times 10^{16}$ n/cm^2 $(E < 0.18$ eV$)\}$ yet observed in a lunar sample. The ratio of the number of neutrons captured per atom by ^{149}Sm to ^{157}Gd is 0.76 which is distinct from the value of 0.86 observed at the Apollo 11, 12 and 14 sites. This indicates a softer neutron energy spectrum at the Sea of Plenty.

Both Gd and Sm in lunar samples have been shown to exhibit variations in isotopic composition which are unambiguously attributable to neutron capture [1–4]. The magnitude of these variations in Gd has been used to estimate low energy neutron fluences which set limits on possible models for lunar soil mixing processes and irradiation histories for lunar rocks [2–4]. The ratio of the Sm isotopic variations to those for Gd is an indicator of the shape of the neutron energy spectrum, which is dependent on the chemical composition and temperature of the lunar soils.

A 35 mg sample of soil G-2 from the lower part of the drill tube returned by Luna 16 was made available to this laboratory for determining the isotopic composition of Sm and Gd. The chemical procedures, mass spectrometry and data reduction were carried out as described in refs. [1, 5].

The Gd isotopic composition for Luna 16, G-2 and our average terrestrial values are listed in table 1. The terrestrial averages result from averaging the data obtained from six mass spectrometer runs and include the data of Eugster, Tera, Burnett and Wasserburg [5]. The Luna 16 sample is clearly seen to be enriched in ^{158}Gd/^{160}Gd and depleted in ^{157,155}Gd/^{160}Gd, and the ratios plot on the correlation lines expected for neutron capture by ^{155}Gd and ^{157}Gd (cf., ref. [4]). These variations are the largest yet seen in a lunar sample.

The Luna 16, G-2 and average terrestrial [1] Sm isotopic compositions are shown in table 2. The enrichment in ^{150}Sm/^{154}Sm and corresponding depletion of ^{149}Sm/^{154}Sm is evident. These values also plot on the correlation line expected for neutron capture (cf., ref. [1]).

The isotopic ratios most sensitive to neutron capture, ^{150}Sm/^{149}Sm and ^{158}Gd/^{157}Gd, are listed in table 3. We define the measured quantity

$$\epsilon_{Sm} \equiv \frac{(^{150}Sm/^{149}Sm)_{measured} - (^{150}Sm/^{149}Sm)_{terrestrial}}{1 + (^{150}Sm/^{149}Sm)_{measured}}$$

and similarly for Gd [1]. The ratio $\epsilon_{Sm}/\epsilon_{Gd}$ is equal to the ratio of the number of neutrons captured per atom by ^{149}Sm to the number captured per atom by ^{157}Gd, i.e., to the ratio of the average cross sections for the lunar neutron energy spectrum. Since ^{157}Gd has a strong resonance near 0.03 eV and ^{149}Sm has one near 0.1 eV, a higher $\epsilon_{Sm}/\epsilon_{Gd}$ indicates a harder (i.e., higher energy) spectrum.

As seen in table 3, $\epsilon_{Sm}/\epsilon_{Gd} = 0.76$ for Luna 16, G-2. This is distinctly lower than the values measured for the Apollo 11, 12 and 14 sites which, within the precision of our analyses, were the same in $\epsilon_{Sm}/\epsilon_{Gd}$ (0.83–0.89). This result is best interpreted as indicating

* Division of Geological and Planetary Sciences, Contribution No. 2102.

Table 1
Gadolinium isotopic composition [a]

Sample	$^{158}Gd/^{160}Gd$	$^{157}Gd/^{160}Gd$	$^{155}Gd/^{160}Gd$	$^{154}Gd/^{160}Gd$	$^{152}Gd/^{160}Gd$
Luna 16, G-2 [b]	1.13926 ± 16	0.71133 ± 14	0.67514 ± 16	0.09960 ± 5 [c]	0.009435 ± 28 [c]
Terrestrial average	1.13582 ± 5	0.71588 ± 4	0.67687 ± 5	0.09974 ± 3	0.009285 ± 8

a) Normalized to ($^{156}Gd/^{160}Gd$) = 0.9361. Errors are $2\sigma_{mean}$. For samples with measurable fluences the normalization procedure introduces a false discrimination correction because of the enrichment of ^{156}Gd. These effects have been discussed by Eugster et al. [5].
b) Data from sixteen sets of ten ratios.
c) When $^{152,154}Gd/^{160}Gd$ are corrected for the false discrimination correction introduced by the normalization procedure, Sm interference (cf. ref. [4]), and $^{151}Eu(n,\gamma)^{152}Eu(\beta^-)^{152}Gd$, the corrected $^{154}Gd/^{160}Gd$ = 0.09967 and agrees with the terrestrial average within the errors.

Table 2
Samarium isotopic composition [a]

Sample	$^{152}Sm/^{154}Sm$	$^{150}Sm/^{154}Sm$	$^{149}Sm/^{154}Sm$	$^{148}Sm/^{154}Sm$	$^{144}Sm/^{154}Sm$
Luna 16, G-2 [b]	1.17531 ± 8	0.32698 ± 4	0.60485 ± 6	0.49418 ± 5	0.13518 ± 4
Terrestrial average	1.17540 ± 6	0.32442 ± 3	0.60750 ± 4	0.49423 ± 4	0.13514 ± 3

a) Normalized to ($^{147}Sm/^{154}Sm$) = 0.65918. Errors are $2\sigma_{mean}$.
b) Data from sixteen sets of ten ratios.

Table 3
Summary of neutron capture effects

	$^{150}Sm/^{149}Sm$	$^{158}Gd/^{157}Gd$	$\epsilon_{Sm}/\epsilon_{Gd}$		$\psi(10^{16}$ n/cm^2)
			Measured	Calculated	($E < 0.18$ eV)
Terrestrial average [a]	0.53403 ± 5	1.58660 ± 11	-	-	-
Luna 16, G-2 [a]	0.54059 ± 6	1.60121 ± 38 [b]	0.76 ± 0.01	0.68	5.9 ± 0.2
Apollos 11, 12 and 14	-	-	0.86 ± 0.03 [c]	0.68–0.72 [c]	2.0–2.8 [d]

a) Errors are $2\sigma_{mean}$.
b) Corrected for false discrimination. (See footnotes to table 1.)
c) From ref. [1].
d) From ref. [2] and published data.

that the neutron energy spectrum is softer in material with the chemical composition of the Sea of Plenty than in material of the composition found at the three Apollo sites. This is qualitatively reasonable in that the contribution to the average macroscopic cross section by the non-resonant absorbers (i.e., major elements) is similar at the Apollo 12 and Luna 16 sites while the rare earth contributions are lower in the Luna 16 soil [6–8].

Table 3 also shows that the $\epsilon_{Sm}/\epsilon_{Gd}$ for Luna 16, G-2 is close to the value of 0.68 derived from the calculations by Lingenfelter, Canfield and Hampel (LCH) [9] of the neutron energy spectrum in material of the Luna 16 soil composition at a temperature of 200 K.

The agreement with the calculations may be misleading in that the three Apollo sites were predicted theoretically to have $\epsilon_{Sm}/\epsilon_{Gd} = 0.72$ for Apollo 11 and 0.68 for Apollos 12 and 14, whereas the measured values were all in the range of 0.83 to 0.89.

For the chemical composition of the G layer, the LCH energy spectrum yields an average cross section of 9.5×10^4 b for ^{157}Gd in the region below 0.18 eV, where 95% of the ^{157}Gd neutron captures occur. This cross section yields a neutron fluence of 5.9×10^{16} n/cm^2 which is ~ 25% higher than previously observed in any lunar sample and up to a factor of three higher than for the soils of Apollo 11, 12 and 14 which are all grouped between 2.0 and 2.8×10^{16} n/cm^2. The LCH calculations indicate that the ^{158}Gd production rate for soil of the Luna 16 composition is ~ 40% higher than at the three Apollo sites. Therefore, the higher fluence cannot be accounted for by chemical differences. One explanation for the higher fluence of Luna 16 soil is that the degree of mixing has been much less at this site. Soil 15221 (St. George crater) also has a high fluence ($\psi \sim 4 \times 10^{16}$ n/cm^2) [10]. Even though the St. George terrain is not typical of the mare, the data from these sites indicate that soil mixing processes may not be as uniform as was suggested by the measurements on soils from the first three Apollo sites. If the G layer is representative of a uniformly mixed soil [4], as appeared to be the case with the Apollo 12 double core, rather than a layer which has been at a constant depth, an average mixing depth of ~ 1200 g/cm^2 (~ 6 m) is calculated for a total exposure time of 3.45×10^9 y [11]. This is less by a factor of three than the mixing depths calculated for the Apollo 11 and 12 sites [2, 4] and is consistent with the suggestion of a shallow regolith at this site [8].

Acknowledgements

I thank the Soviet Academy of Sciences and The National Aeronautics and Space Administration for arranging for the exchange of lunar samples and the Lunar Sample Analysis Planning Team for entrusting the Lunatic Asylum with this sample. I am indebted to G. J. Wasserburg and D. S. Burnett for their continuing support, supervision, and consultation. This work was supported by NASA Contract NGL-05-002-188 and National Science Foundation grant GP-28027. The author is supported by an NDEA Fellowship.

References

[1] G. P. Russ III, D. S. Burnett, R. E. Lingenfelter and G. J. Wasserburg, Neutron capture on ^{149}Sm in lunar samples, Earth Planet. Sci. Letters 13 (1971) 53.

[2] D. S. Burnett, J. C. Huneke, F. A. Podosek, G. P. Russ III and G. J. Wasserburg, The irradiation history of lunar samples, The Proceedings of the Second Lunar Science Conference, MIT Press (1971) 1671.

[3] K. Marti and G. W. Lugmair, ^{81}Kr-Kr and K-^{40}Ar ages, cosmic-ray spallation products and neutron effects in lunar samples from Oceanus Procellarum, The Proceedings of the Second Lunar Science Conference, MIT Press (1971) 1591.

[4] O. Eugster, F. Tera, D. S. Burnett and G. J. Wasserburg, The isotopic composition of Gd and neutron capture effects in samples from Apollo 11, Earth Planet. Sci. Letters 8 (1970) 20.

[5] O. Eugster, F. Tera, D. S. Burnett and G. J. Wasserburg, Isotopic composition of gadolinium and neutron capture effects in some meteorites, J. Geophys. Res. 75 (1970) 2753.

[6] R. A. Schmitt, personal communication.

[7] L. E. Nyquist, personal communication.

[8] A. P. Vinogradov, Preliminary data on luna ground brought to earth by automatic probe "Luna-16", Proceedings of the Second Lunar Science Conference, MIT Press (1971) 1.

[9] R. E. Lingenfelter, E. H. Canfield and V. H. Hampel, The lunar neutron flux revisited, manuscript to be submitted to Earth Planet. Sci. Letters.

[10] Unpublished data.

[11] J. C. Huneke, F. A. Podosek and G. J. Wasserburg, Gas retention and cosmic-ray exposure ages of a basalt fragment from Mare Fecunditatis, Earth Planet. Sci. Letters 13 (1972) 375.
D. A. Papanastassiou and G. J. Wasserburg, Rb-Sr age of a Luna 16 basalt and the model age of lunar soils, Earth Planet. Sci. Letters 13 (1972) 368.

Chapter 8

EARTH AND PLANETARY SCIENCE LETTERS 15 (1972) 172–186. NORTH-HOLLAND PUBLISHING COMPANY

6

LUNAR NEUTRON STRATIGRAPHY

G. Price RUSS III, D.S. BURNETT, G.J. WASSERBURG
The Lunatic Asylum of the Charles Arms Laboratory, Division of Geological and Planetary Sciences, California Institute of Technology, Pasadena, California 91109, USA*

Received 4 April 1972
Revised version received 12 May 1972

Variations in the isotopic ratios $^{158}Gd/^{157}Gd$ and $^{150}Sm/^{149}Sm$ in the Apollo 15 deep drill stem show that the neutron fluence is a smoothly varying function of depth with a relatively symmetric peak at a depth of 190 g/cm^2. The peak fluence is about 60% greater than the surface value. The observed peak is at a depth comparable to the theoretically calculated peak in the neutron flux. These data may be quantitatively explained by a model in which a blanket of pre-irradiated material was deposited rapidly 450×10^6 yr ago which has remained essentially undisturbed since, i.e., the material was deposited during terrestrial Cambro-Ordovician time. The upper several cm of the drill stem represents soil which has been mixed and transported to the drill site by shallow impacts.

Other models quantitatively compatible with the data are those for a regolith continuously accreting for a time as long as 400×10^6 yr and subsequently irradiated for $\sim 500 \times 10^6$ yr as an unmixed section. This would allow the base of the drill stem to be as old as 900×10^6 yr.

These results show that at this site the turnover time to 2.5 m depth is significantly greater than about 500 my. No positive evidence of ray material from Aristillus or Autolycus was observed in the fluence data.

Studies of a variety of cosmic-ray nuclei from deep cores from several sites should permit the determination of detailed depositional histories. If deeper core samples could be obtained, it should be possible to study over a billion years of lunar stratigraphy. However, the determination of absolute stratigraphic ages will require that neutron capture rates be determined in situ by accurate methods.

1. Introduction

The isotopic composition of gadolinium has been measured in four soils (15601, 15221, 15231 and 15041) and seven drill stem samples (from 15001–15006) returned by the Apollo 15 mission. In addition, the isotopic composition of samarium was determined for four of these samples (15601, 15041, 15004 and 15001). Variations in the composition of these elements can be used to estimate fluences (time-integrated fluxes) of low energy neutrons [1–7]. These fluences taken in conjunction with the depth dependence of the lunar neutron flux as calculated by Lingenfelter et al. (LCH) [8] can be used to set limits on the depth and rate of soil mixing. The ratio of the Gd isotopic variations to those in Sm is a measure of the energy dependence of the neutron spectrum which is dependent on the chemical composition and temperature [8,9]. The drill stem samples, which come from as deep as 2.4 m [10] below the regolith surface, provide a unique opportunity to study the history of the regolith in the Hadley Rille area. We reported previously, on the basis of two samples, that the drill stem seemed to have sampled material which had not been mixed for around 5×10^8 yr [6]. Model fits to the fluences determined for the seven drill stem samples will be shown to support this conclusion.

*Contribution no. 2158.

2. Experimental

The soil samples analyzed were collected from widely separated areas [11]. Sample 15601 was collected

at station 9A near the rille edge. Soils 15231 and 15221 are both from station 2 near St. George Crater. Sample 15041, which was scooped at station 8 near the site where the drill was deployed, will be taken to represent the material from the top of the drill stem which penetrated to a depth of 2.4 m. Samples were taken from the bottom of each of the six drill stem sections and from near the middle of section 15005. The depths of these samples (table 3) were calculated in g/cm^2 from the weights of the sections and the cross sectional area of the tubing as given by Carrier et al. [10]. There is some discrepancy between these data and those of the Lunar Sample Information Catalog [12], but the difference is small for our purposes.

For the surface samples, up to 75 mg were dissolved. Approximately 35 mg each were used for the drill stem samples. The chemical and mass spectrometric procedures were carried out as described previously [1,9]. Gd and Sm were analyzed as GdO^+ and Sm^+ ions. The Gd data were reduced by methods similar to those described previously [1], except that in the present work the Gd data were screened such that only the means of those sets of 10 ratios for which the standard deviations of $^{158}Gd/^{160}Gd$ and $^{157}Gd/^{160}Gd$ were less than 0.125 % and the standard deviations of $^{156}Gd/^{160}Gd$ and $^{155}Gd/^{160}Gd$ of less than 0.25% were used. No screening was applied to the $^{154}Gd/^{160}Gd$ and $^{152}Gd/^{160}Gd$ data, but in most cases these data were acquired in sets satifying the screening procedure described above. These screening procedures also apply to the data previously reported [3,5,6,9]. The values reported in table 1 are the discrimination corrected averages of the screened sets and the quoted errors represent two standard deviations of the mean of the distribution of the set averages, i.e. quoted error =

$$2\left\{\frac{\sum_{i=1}^{n}(SA_i - GA)^2}{(n)(n\text{-}1)}\right\}^{\frac{1}{2}},$$

Table 1
Gadolinium isotopic composition.[a]

Sample	No. of Sets[b] $\frac{^{158}Gd}{^{160}Gd}$	$\frac{^{158}Gd}{^{160}Gd}$	$\frac{^{157}Gd}{^{160}Gd}$	$\frac{^{155}Gd}{^{160}Gd}$	No. of Sets $\frac{^{154}Gd}{^{160}Gd}$	$\frac{^{154}Gd}{^{160}Gd}$	$\frac{^{152}Gd}{^{160}Gd}$
15601,65	24	1.13 818 ± 10	0.71 272 ± 8	0.67 566 ± 9	13	0.099 68 ± 5	0.009 338 ± 32
15221,46	19	1.13 833 ± 8	0.71 276 ± 6	0.67 572 ± 7	8	0.099 67 ± 4	0.009 322 ± 22
15231,47	19	1.13 830 ± 8	0.71 271 ± 6	0.67 569 ± 8	14	0.099 64 ± 6	0.009 323 ± 17
15041,54	22	1.13 799 ± 9	0.71 316 ± 8	0.67 587 ± 8	8	0.099 61 ± 8	0.009 314 ± 39
15006,27	16	1.13 827 ± 11	0.71 282 ± 11	0.67 571 ± 11	5	0.099 63 ± 14	0.009 341 ± 35
15005,222	27	1.13 866 ± 8	0.71 219 ± 4	0.67 546 ± 6	16	0.099 67 ± 5	0.009 353 ± 25
15005,26	13	1.13 891 ± 14	0.71 173 ± 11	0.67 525 ± 9	3	0.099 67 ± 18	0.009 364 ± 31
15004,27	17	1.13 920 ± 9	0.71 153 ± 8	0.67 518 ± 14	5	0.099 59 ± 12	0.009 325 ± 27
15003,29	25	1.13 893 ± 11	0.71 193 ± 8	0.67 530 ± 7	16	0.099 56 ± 7	0.009 336 ± 29
15002,27	14	1.13 852 ± 12	0.71 257 ± 13	0.67 562 ± 15	7	0.099 70 ± 2	0.009 357 ± 48
15001,31	25	1.13 806 ± 7	0.71 294 ± 5	0.67 576 ± 5	14	0.099 67 ± 5	0.009 344 ± 19
Terrestrial average	92	1.13 582 ± 5	0.71 588 ± 4	0.67 687 ± 5	52	0.099 74 ± 3	0.009 285 ± 8

[a] Normalized to $^{156}Gd/^{160}Gd = 0.9361$. Errors are 2 σ_{mean}
[b] A set consists of ten ratios for a given pair of isotopes.

Table 2
Samarium isotopic composition.[a]

Sample	No. of Ratios $\frac{^{150}Sm}{^{154}Sm}$	$\frac{^{152}Sm}{^{154}Sm}$	$\frac{^{150}Sm}{^{154}Sm}$	$\frac{^{149}Sm}{^{154}Sm}$	$\frac{^{148}Sm}{^{154}Sm}$	$\frac{^{144}Sm}{^{154}Sm}$
15601,65	220	1.175 27	0.32 619	0.60 562	0.494 18	0.135 18
		± 5	± 2	± 3	± 3	± 2
15041,54	87	1.175 05	0.32 596	0.60 591	0.494 13	0.135 14
		± 18	± 9	± 17	± 13	± 4
15001,31	106	1.175 40	0.32 617	0.60 574	0.494 08	0.135 16
		± 28	± 10	± 14	± 10	± 7
15004,27	99	1.175 28	0.32 700	0.60 515	0.494 21	0.135 21
		± 25	± 16	± 37	± 20	± 10
Terrestrial[b] average	483	1.175 40	0.32 442	0.60 750	0.494 23	0.135 14
		± 6	± 3	± 4	± 3	± 3

[a]Errors are $2\sigma_{mean}$.
[b]From Russ et al. [9].

where n is the number of sets, GA is the grand average and SA_i is the average ratio for the i^{th} set. The Sm data (table 2) were reduced as described in Russ et al. [9].

3. Results

The Gd isotopic data are shown in table 1. Our average terrestrial values result from averaging the screened data sets of six mass spectrometer runs. Four of these, including the best analysis reported by Eugster et al. [1], were for reagent Gd. The other two runs were on a sample of Knippa basalt to which reagent Gd was added before processing through the chemical separation procedure. The experimental data are plotted on a $^{158}Gd/^{160}Gd$–$^{157}Gd/^{160}Gd$ correlation diagram in fig. 1. The heavy line is the calculated correlation line for the variation in the Gd isotopic composition caused by neutron capture in Gd of terrestrial composition (cf. Eugster et al. [1]). The points fall on this line within the quoted errors.

All of the data in table 1 have been normalized to $^{156}Gd/^{160}Gd = 0.9361$ to correct for discrimination in the mass spectrometer. This normalization procedure introduces a false discrimination correction of $\frac{1}{4}\left[^{155}\sigma\Psi\left(^{155}Gd/^{156}Gd\right)_{terr}\right]$ per mass unit where $^{155}\sigma$ is the cross section for neutron capture by ^{155}Gd and Ψ is the neutron fluence [1]. This is responsible for the apparent depletion of the $^{154}Gd/^{160}Gd$ ratios as compared with the terrestrial value in table 1. When this effect is taken into account, the $^{154}Gd/^{160}Gd$ agrees with the terrestrial value for all samples except 15002 (and marginally 15005) where the ratio is slightly high. This difference may be due to a Sm interference. After taking the effect of the normalization procedure into account, the $^{152}Gd/^{160}Gd$ ratios are all found to be higher than the terrestrial value. This may result from the reaction $^{151}Eu(n,\gamma)^{152}Eu(\beta^-)^{152}Gd$ and/or from $^{152}Sm^{16}O$ interference. The errors in $^{154}Gd/^{160}Gd$ and $^{152}Gd/^{160}Gd$ are too large to permit an accurate separation of these effects.

In table 2 the results for Sm are shown. The enrichments in $^{150}Sm/^{154}Sm$ and depletions in $^{149}Sm/^{154}Sm$ correspond to those expected for neutron capture by ^{149}Sm. As discussed in Russ et al. [9], there are small variations in the $^{152}Sm/^{154}Sm$ averages which are not understood. In addition to the possibility discussed previously of interferences at mass 154 [9], ^{152}Sm may be depleted by $^{152}Sm(n,\gamma)^{153}Sm(\beta^-)^{153}Eu$ for which the neutron capture reaction has a 2.1×10^5 barn resonance at 8.03 eV [13]. However, due to the smallness of the $^{152}Sm/^{154}Sm$ variations ($< 4 \times 10^{-2}$%), we cannot attribute them to a specific cause.

In order to check whether the cause of the $^{152}Sm/^{154}Sm$ variations also affected $^{150}Sm/^{149}Sm$, which is the ratio of prime interest, we re-analyzed our data,

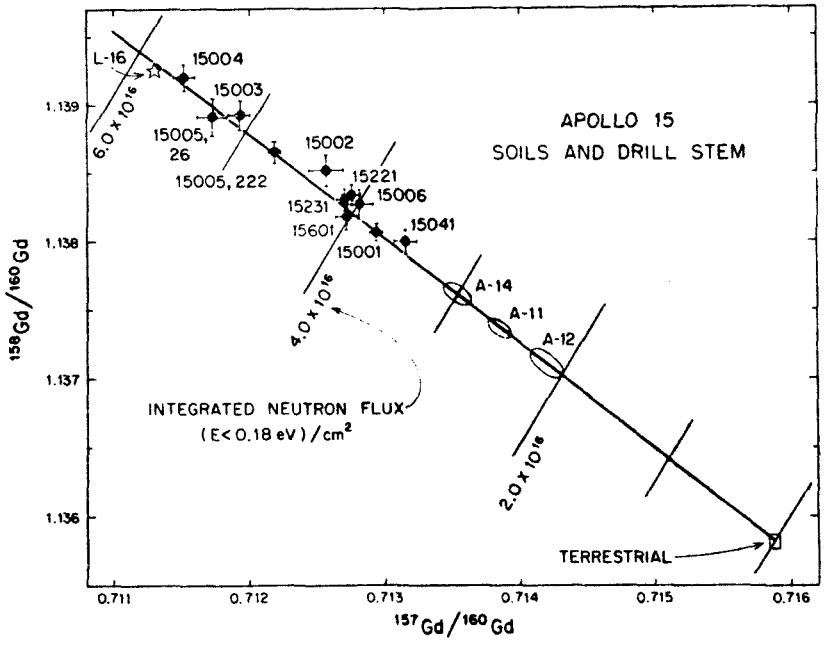

Fig. 1. $^{158}Gd/^{160}Gd$ vs. $^{157}Gd/^{160}Gd$ correlations diagram. The Apollo 15 soil samples are indicated by solid points. Approximate fields are also shown for soils from the earlier Apollo and Luna 16 missions. The integrated flux lines are calculated for a material with the chemical composition of 15601 and apply only approximately to the soils from the other sites.

including those reported by Russ [5] and Russ et al. [9], in several ways. We have formed ratios relative to ^{n}Sm where n is 154, 152 or 148 and in each case have corrected for mass fractionation first by normalizing to $^{147}Sm/^{n}Sm$ and then to $^{144}Sm/^{n}Sm$. No appreciable variation ($< 2 \times 10^{-2}\%$) was introduced in the $^{150}Sm/^{149}Sm$ by any of the six methods of data analysis.

The data needed for regolith mixing and spectral shape calculations are summarized in table 3. The depths from which the drill stem samples were obtained are given in units of g/cm^2. The $^{158}Gd/^{157}Gd$ ratios, which most sensitively reflect the neutron capture by ^{157}Gd, have been corrected for the effect of the false discrimination correction described above. Using the cross sections for neutron capture by ^{157}Gd (and ^{155}Gd) predicted by the LCH calculations for materials of the various chemical compositions [14–16], the fluence of neutrons below 0.18 eV has been calculated for each sample by eq. (9) of Eugster et al. [1]:

$$\Psi = \{[(^{158}Gd/^{157}Gd)_{meas} - (^{158}Gd/^{157}Gd)_{terr}]\} \Big/ \{^{157}\sigma[1+(^{158}Gd/^{157}Gd)_{terr}] + \tfrac{1}{4}\,^{155}\sigma(^{158}Gd/^{157}Gd)_{terr}\,(^{155}Gd/^{156}Gd)_{terr}\}.$$

The cross sections used for ^{157}Gd capture ($^{157}\sigma$) are listed in footnote b of table 3 and $^{155}\sigma$ is taken as $(0.24)\cdot(^{157}\sigma)$ [1]. The ratio $^{150}Sm/^{149}Sm$ is also tabulated for those samples where the data are available. The ratio $\epsilon_{Sm}/\epsilon_{Gd}$ [9] given in table 3 is an experimental quantity equal to the ratio of the cross section of ^{149}Sm averaged over the lunar neutron energy spectrum to the average ^{157}Gd cross section.

In terms of measured quantities the ratio is

Table 3
Summary of neutron capture effects.

Sample	Depth (g/cm^2)	$\frac{^{158}Gd}{^{157}Gd}$[a]	$\frac{^{150}Sm}{^{149}Sm}$	$\Psi(10^{16} n/cm^2)$[b] (E < 0.18 eV)	$\frac{\epsilon_{Sm}}{\epsilon_{Gd}}$
Soils					
15601,65	surface	1.59668	0.53861	4.02	0.77
(Sta. 9A)		± 23[e]	± 4[e]	± 0.09	± 0.02
15221,46	surface	1.59708		3.84	
(Sta. 2)		± 17		± 0.07	
15231,47	under	1.59715		3.57	
(Sta. 2)	boulder	± 18		± 0.07	
15041,54	surface	1.59547	0.53796	3.51	0.75
(Sta. 8)		± 22	± 15	± 0.09	± 0.04
Drill Stem (Sta. 8)					
15006,27	65	1.59659		3.94	
		± 28		± 0.11	
15005,222	109	1.59850		4.69	
		± 14		± 0.05	
15005,26	138	1.59984		5.24	
		± 32		± 0.12	
15004,27	208	1.60069	0.54037	5.57	0.76
		± 22	± 32	± 0.09	± 0.04
15003,29	276	1.59942		5.06	
		± 24		± 0.09	
15002,27	341	1.59747		4.30	
		± 33		± 0.13	
15001,31	412	1.59603	0.53846	3.72	0.79
		± 15	± 17	± 0.06	± 0.04
Terrestrial average		1.58660 ± 11	0.53403 ± 5	≡ 0	–
Luna 16 G[c]				5.94 ± 0.15	0.76 ± 0.01
Apollos 11,12,14[d]				2.2–3.1	0.83–0.89

[a]Corrected for the effect of fluence on the normalization isotope.
[b]Calculated from $^{157}\sigma$'s predicted by the LCH calculations–9.7×10^4 (15601), 1.02×10^5 (15221, 15231, 9.8×10^4 (15041, 15001-6), 9.6×10^4 (L-16), 8.9×10^4 (A-11) and 9.4×10^4 barns (A-12,14).
[c]From Russ [5].
[d]From Burnett et al. [6] and Russ et al. [9].
[e]Errors are $2\sigma_{mean}$ for isotopic ratios. The error in Ψ and $\epsilon_{Sm}/\epsilon_{Gd}$ are calculated quadratically from the errors of the isotopic ratios.

$$\frac{\epsilon_{Sm}}{\epsilon_{Gd}} = -\frac{\dfrac{\left(\frac{^{150}Sm}{^{149}Sm}\right)_{meas} - \left(\frac{^{150}Sm}{^{149}Sm}\right)_{terr}}{1 + \left(\frac{^{150}Sm}{^{149}Sm}\right)_{meas}}}{\dfrac{\left(\frac{^{158}Gd}{^{157}Gd}\right)_{meas} - \left(\frac{^{158}Gd}{^{157}Gd}\right)_{terr}}{1 + \left(\frac{^{158}Gd}{^{157}Gd}\right)_{meas}}}$$

Variations in the shape of the neutron spectrum in the sub-eV region are reflected by changes in this ratio.

4. Discussion

4.1. *Soils*

In the top band of fig. 2. we have plotted the $^{158}Gd/^{157}Gd$ observed in surface soil samples from the Apollo 11–15 missions and the Luna 16-G layer. The lower portion of this figure shows the Apollo 15 drill stem results plotted as a function of depth. The Apollo 15 surface soils are more highly irradiated than soils from the earlier Apollo sites but less irradiated than the G. layer from Luna 16. The soils analyzed all have similar fluences (cf., table 3 and fig. 2), even though they were collected from rather distinct areas. This similarity in fluence suggests that similar soil mixing processes are operative over an area of many square kilometers. However, the situation is complicated by the fact that, because of differences in chemical composition, the production rate of ^{158}Gd is calculated to be 30% higher at St. George Crater than at the rille edge. If this is true, the tight grouping of the fluences must be regarded as fortuitous. The terrain at St. George Crater is considered to be the oldest visited during the mission and the rille edge one of the youngest [17,29]. However, this variation in 'age' is not apparent in the neutron fluence data. The similarity in these results may reflect an erosion rate on the slope at St. George which is comparable to that at the rille edge, or possibly that lateral transport from the adjacent flat areas has added more highly irradiated material to the soil at the rille edge.

Soil 15601 was collected within 25 m of the rille edge where the thin regolith has been interpreted as an erosional surface [11]. If this is the case and if lateral transport of material from upslope has not been significant at this spot, then an erosion rate of 60 g/cm^2 10^8 yr is indicated (cf. sect. 4.3.).For comparison, an erosion rate of 150 g/cm^2 10^8 yr has been calculated from ^{38}Ar data by Podosek et al. [28].

Soil 15231 was obtained from beneath a large boulder. Soil 15221 was collected approximately a meter away. If we assume that 15221 and 15231 had equal neutron fluences when the boulder was deposited on top of 15231, the difference in the ^{158}Gd production rate between the surface and covered soil allows us to set an upper limit on the time when the boulder was emplaced even though there is no difference in the Gd isotopic composition of the two

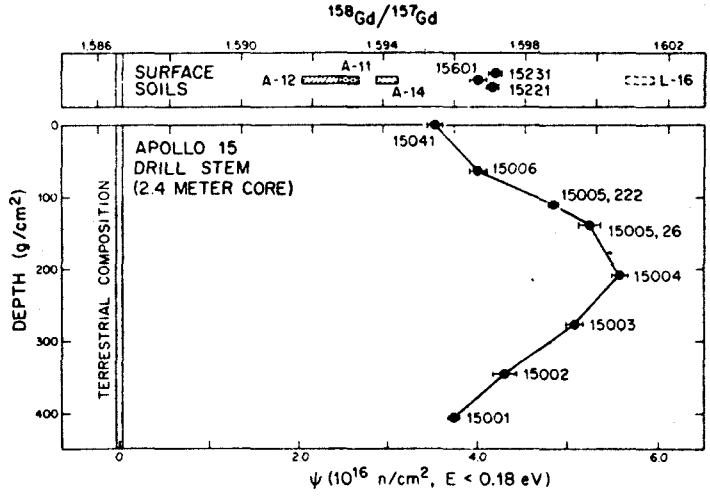

Fig. 2. The spread in $^{158}Gd/^{157}Gd$ observed in surface soils and the Luna 16-G layer is indicated in the upper band. The soils from Apollo 15 (including 15041) have been more highly irradiated than the soils returned by the earlier Apollo missions. In the bottom portion drill stem data, connected by straight lines, are presented as a function of depth. The calculated neutron fluences are indicated as well as the $^{158}Gd/^{157}Gd$ ratios. The fluence is seen to peak between samples 15005 and 15004.

samples today. As soil 15231 was covered by $\gtrsim \frac{1}{4}$m of rock in all directions, it seems reasonable to take 50 g/cm^2 as a conservative shielding depth. At these depths the production rate rises rapidly so this choice will give us an upper limit for the deposition time of the boulder. Using the LCH production curve and the extremes of the error bars we calculate that the boulder could not have been in place for more than 5×10^7 yr. A much stronger limit of 1×10^6 yr has been set by Rancitelli et al. [18] from ^{26}Al and ^{22}Na data.

4.2. *Neutron energy spectrum*

The ratio of the average cross section of ^{149}Sm to that for ^{157}Gd, defined as $\epsilon_{Sm}/\epsilon_{Gd}$ is a measure of the neutron energy spectrum. The spectral shape is dependent on the chemical composition of the medium and its temperature. According to the LCH calculations, it is only slightly dependent on the burial depth of the sample. In fig. 3 we have plotted $\epsilon_{Sm}/\epsilon_{Gd}$ (cf. sect. 3 of this paper and Russ et al. [9]) against the effective macroscopic cross section Σ_{eff}, which describes the neutron absorbing properties of a material. A more complete description of Σ_{eff} can be found in LCH. The important point for this discussion is that Σ_{eff} increases with the concentration of elements which strongly absorb neutrons, e.g., Fe, Ti and rare earths. The experimental points, including those of Russ et al. [9], fall in the region of $\epsilon_{Sm}/\epsilon_{Gd} \sim$ 0.8. The Apollo 15 and Luna 16 samples have slightly lower $\epsilon_{Sm}/\epsilon_{Gd}$ values than the others. Since the ^{149}Sm resonance is near 0.1 eV while the ^{157}Gd resonance is near 0.03 eV, the lower values of $\epsilon_{Sm}/\epsilon_{Gd}$ for Apollo 15 and Luna 16 indicate lower energy spectra at these sites. This is qualitatively what the LCH calculations predict, but in all cases the spectrum is slightly more energetic than predicted. For comparison the $\epsilon_{Sm}/\epsilon_{Gd}$ ratio for a thermal spectrum, which would be independent of the chemical composition, has also been shown in the figure.

Among the Apollo 15 samples no variations in $\epsilon_{Sm}/\epsilon_{Gd}$ were observed. In particular the ^{149}Sm/^{150}Sm depth profile appears to be the same as that measured for ^{157}Gd/^{158}Gd. Thus, there is no evidence for any variations in the neutron energy spectrum with depth. However, as shown in sect. 4.3, only about 63% of the exposure of 15004 and 43% for 15001 was produced by in situ irradiation at a given depth.

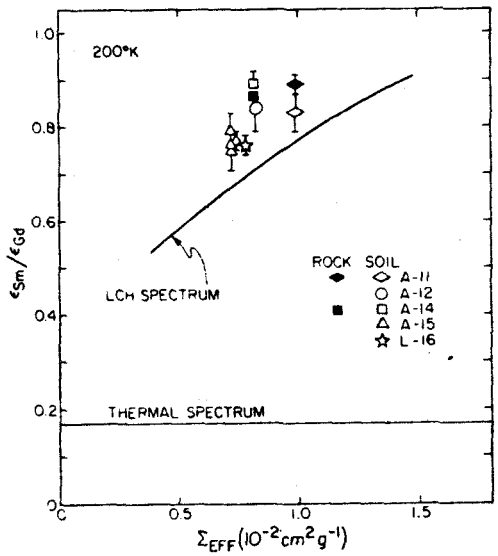

Fig. 3. Variation of the ratio of the average neutron capture cross section for ^{149}Sm to that for ^{157}Gd as a function of the average neutron absorption cross section. An increase in Σ_{eff} indicates an increase in the concentration of the major neutron absorbing elements and should be accompanied by an increase in $\epsilon_{Sm}/\epsilon_{Gd}$ which indicates a higher energy spectrum. The measured $\epsilon_{Sm}/\epsilon_{Gd}$'s are in all cases somewhat higher than predicted by LCH and much higher than expected for a thermal spectrum. The neutron spectrum in the rocks has been assumed to be controlled by the soils in which they were found. Consequently the rock points are plotted at the Σ_{eff} values of the soils. If the Apollo 11 rock (10017) had been plotted at $\Sigma_{eff} \sim 1.4$ the point would lie closer to the predicted line. The drill stem samples are all assumed to have the same Σ_{eff} as 15041.

4.3. *Deep drill stem samples*

In this section we show that the measured neutron fluence profile can place strong bounds on the depositional history of the Apollo 15 deep drill stem material and that those samples provide a record of lunar stratigraphy reaching back to at least terrestrial Cambro-Ordovician time.

The drill stem samples show a definite peak in fluence at a depth of $\sim$ 190 g/cm^2 (fig. 2). The peak fluence is $\sim$ 60% greater than the surface value as measured by ^{158}Gd/^{157}Gd and ^{150}Sm/^{149}Sm. This is the first core in which a marked depth variation has been observed. The Apollo 12 double core showed

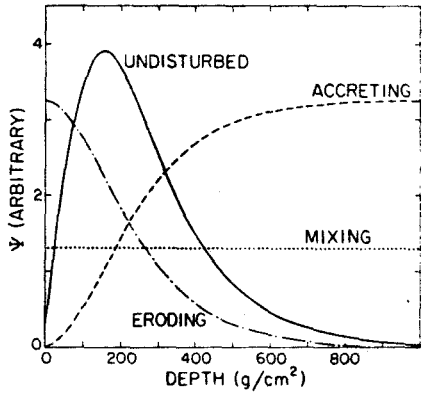

Fig. 4. Diagram showing the neutron fluence as a function of depth for different cases. Note the distinctive shapes of the various curves. The curve labelled undisturbed is the fluence for a slab which has been unstirred for the total period of irradiation. The horizontal line labelled mixing is the fluence for the case of uniform mixing down to a depth of 1000 g/cm^2 for the same period of time as the undisturbed curve. The eroding and accreting curves are for uniform erosion or accretion. For illustrative purposes we have taken the time required for the erosion or accretion of 1000 g/cm^2 as two and a half times the irradiation time which was assumed for undisturbed and mixing cases.

an increase with depth in $^{158}Gd/^{157}Gd$ and in spallation ^{126}Xe, but the increases were only slightly greater than the experimental errors [3]. Within the resolution afforded by the limited sampling, the variations are smooth and no discontinuities are obvious in the neutron fluence. This is surprising because one might expect chaotic variations if the drill stem sampled layers which had large random variations in predepositional neutron fluences. The smooth nature of the curve indicates a simple irradiation history throughout the depth sampled by the drill stem.

In order to explore the meaning of this smoothly varying and distinctly peaked neutron fluence profile, it is useful to consider some simple soil models based on the depth dependence of the neutron flux (fig. 4). The neutron flux $\Phi(x)$, as calculated by LCH, rises sharply from the surface to a peak at ~ 155 g/cm^2 and then drops exponentially at larger depths, so that essentially all production takes place in the upper 600 g/cm^2 of the regolith. In an undisturbed stratigraphic section of soil (or rock) which has not been previously irradiated, the neutron fluence Ψ as a function of depth will just be the flux multiplied by the irradiation time. Therefore the undisturbed soil curve of fig. 4 may be taken to represent the depth dependence of the neutron flux.

Fig. 4 also illustrates several other simple model soil histories based on initially unirradiated material. If an otherwise undisturbed soil has been recently or continuously mixed to some depth l, then in the mixed layer Ψ will be a constant equal to the average of the flux from the surface to the mixing depth multiplied by the irradiation time T of the material:

$$\Psi = \frac{T}{l}\int_0^l \Phi(x)\,dx$$

where $\Phi(x)$ is the flux of neutrons with energies less than 0.2 eV. This corresponds to the uniform mixing model which we have previously discussed [2,3,6]. Let us now consider the case of deposition of unirradiated material at a constant rate Vg/cm^2 sec. As we go deeper into the section, we encounter older material which has increasingly larger fluences because of their greater exposure time and because burial has brought them into regions of higher neutron flux. Since a given layer spends equal time at every depth, when it reaches a depth lg/cm^2 at time l/V, it will have a fluence

$$\Psi(l) = \frac{1}{V}\int_0^l \Phi(x)dx.$$

Layers deeper than ~600 g/cm^2 will have already passed through the region of appreciable neutron flux and additional ^{157}Gd neutron capture with additional burial becomes small. This causes the fluence to reach a plateau as shown by the accretion curve in fig. 4. We can also consider the complementary case of erosion by continuous removal of material at a rate V from the surface of a slab which was initially unirradiated. As material is removed from the surface, the material at depth moves closer to the surface. A given layer, approaching the surface at a rate V, will monotonically build up a neutron fluence. When it has reached a depth l below the surface, its fluence will be

$$\Psi(l) = \frac{(-1)}{V}\int_{\infty}^{l} \Phi(x)dx,$$

as shown by the erosional case in fig. 4. The fluence will continue to increase until the layer reaches the surface (l=0) and is removed.

Models which assume that the drill stem section was formed from materials which had been uniformly pre-irradiated to an initial fluence Ψ_0, do not change the shapes of the curves shown in fig. 4. The pre-irradiation would simply add a constant Ψ_0 to the fluence developed during the processes discussed above. For such cases the base line of fig. 4 would no longer be $\Psi = 0$ but rather $\Psi = \Psi_0$.

In summary, the theoretical fluence curves for the simple models shown in fig. 4 are quite distinct. Only the undisturbed soil case has a peak below the surface similar to the experimental fluence profile. Thus, models culminating in an undisturbed period are the most reasonable to consider in attempting to fit the measurements.

From the observed peak in fluence (fig. 2), it is possible to calculate bounds on the amount of time the material sat undisturbed in the upper few meters of the regolith and to set a lower limit to the rate of accretion. The observed peak of the fluence occurs at ~ 190 g/cm^2 which is in the range of peak depths (150–200 g/cm^2) calculated for various models by LCH and similar to the 175 g/cm^2 peak depth of Armstrong and Alsmiller [19]. The observed peak is similar in shape to the calculated ones. If we assume the LCH production rates based on a exponentially decreasing neutron source spectrum are valid, the discrepancy in the observed peak depths and that calculated theoretically (155 g/cm^2) is most simply explained by the recent addition of a surface layer to an otherwise undisturbed slab. For the calculations in this paper we have used the LCH calculations which assume that neutron production drops exponentially with depth.

Let us assume that the material sampled, with the exception of that near the surface, represents a slab which was deposited instantaneously from material with a uniform initial fluence Ψ_0 and which subsequently remained undisturbed for a time T. The limits on the possible Ψ_0 are zero and 4×10^{16} neutrons/cm^2 (the fluence of 15001). If we try to fit the data starting with an unirradiated slab, $\Psi_0 = 0$, then the curve whose peak fits samples 15004 drops much too sharply to fit the other data points. The points cannot be fit for $\Psi_0 = 4 \times 10^{16}$ either. However, as shown in fig.5, the 7 drill stem points can be fitted reasonably well for a slab emplaced 450 my ago with $\Psi_0 = 2.1 \times 10^{16}$ n/cm^2. If we vary T by $\pm 100 \times 10^6$ yr and Ψ_0 correspondingly, the fit is seen to be poorer. These fits imply that there is a surface layer of about 10–40 g/cm^2 which was added recently (< 150 my). If we consider this thin surface layer to have grown continuously throughout the time since the main slab was emplaced, rather than being added recently, the required Ψ_0 and T values would not be significantly altered. The precise thickness of such a layer depends on the model used for the depth dependence of the neutron flux.

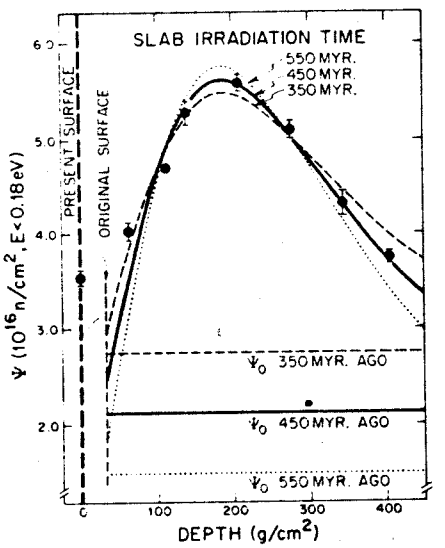

Fig. 5. Calculated fits to the observed neutron fluence profile for uniformly pre-irradiated material allowed to sit as a slab for various time intervals following instantaneous deposition. The present surface is interpreted as representing the recent addition of about 35 g/cm^2 of soil to the original surface.

In these fits and those discussed below we have not attempted to account for the fluence of the surface samples and have allowed 15006 to fall somewhat off the model curves. We have been willing to ignore the near surface region because it is the most likely to have been disturbed by shallow mixing and lateral transport and is therefore the most difficult region to interpret. Since the observed surface fluence is between that of 15006 and that predicted for the surface, it is most easily explained by the deposition of material with dosages similar to other local soils (e.g. 15601) by lateral transport. Vertical mixing alone cannot ac-

count for the surface fluence because it would be necessary to mix below the level of 15006 in order to match the surface fluence. This would tend to make the 15006 fluence fall below the model curves, contrary to what is observed. A more detailed investigation of the fluence of samples from section 15005 and 15006 will help reveal the details of the history of the near surface region.

The previous discussion has shown that the data can be quantitatively described by the instantaneous deposition of a pre-irradiated, well-mixed layer which then remains as an undisturbed slab for 450 my. However, the question arises as to the maximum amount of time over which the 400 g/cm^2 of the drill stem could have accreted. We have considered two accretion models:

A. Accretion from material with a constant initial fluence, Ψ_0.

B. Accretion from material in which $\Psi_0(\tau)$ increases with time.

A. As material is added to the surface at the rate V and subsequently buried to depth l, it builds up a fluence as described above for the simple accreting case:

$$\Psi(l) = \Psi_0 + \frac{1}{V}\int_0^l \Phi(x)\,dx.$$

Subsequent to the accretion period, the section remains undisturbed for time T until the present and develops an additional fluence $T{\cdot}\Phi(l)$. The present day fluence profile is then:

$$\Psi(l) = \Psi_0 + \frac{1}{V}\int_0^l \Phi(x)\,dx + T{\cdot}\Phi(l).$$

The effect of the accretion term is to flatten the profile and increase the depth of the peak compared to the undisturbed soil case. Therefore, in order to fit the observed data using this model, it is necessary to increase the in situ irradiation time and decrease Ψ_0 relative to the undisturbed soil case in order to counteract the flattening introduced by the finite accumulation rate. Consequently, the maximum accretion time for the drill stem (L/V for L = 400 g/cm^2) will be obtained by setting $\Psi_0 = 0$. As shown in fig. 6, for an in situ irradiation time of 600 my, the slab could have accumulated over a period of 350 my. This combination matches the observed Ψ as a function of depth. If we try to increase the accretion time by taking a shorter in situ exposure time, the calculated curve does not drop off fast enough for larger depths. For this case, it is not necessary to have a recently added surface layer in order to fit the peak position as was necessary for the instantaneously deposited slab. However, at least a thin layer of irradiated material would still have to be added in order to explain the fluence of the surface sample.

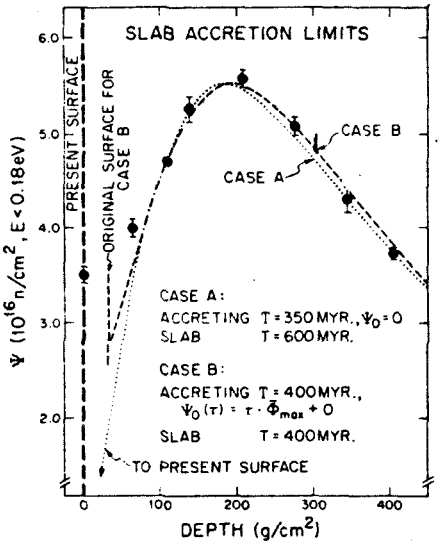

Fig. 6. Calculated fits to the observed neutron fluence profiles for continuously accreting models. These models, set lower limits on the possible accretion rates for the drill stem material. Both cases require that the whole section was accreted within about 400 my and has since remained undisturbed as a slab for around half a billion years. In case A the curve is calculated relative to the present lunar surface and in case B, a 35 g/cm^2 surface layer is assumed to have been recently added in order to fit the observed maximum. The observed fluences in the upper 50–80 g/cm^2 are not described by these models but appear to be mixed material transported in by local impacts.

B. For the case where the initial fluence of the accreting material is changing with time, we want to find the maximum effect of this time variation on the allowable accretion rate. Therefore we want to allow $\Psi_0(\tau)$ to increase at the *maximum rate*. A plausible maximum time variation for Ψ_0 can be obtained by assuming that the accreted material is primarily produced by cratering into an irradiated regolith where the cratering mixes down to some depth D such that

the average flux $\bar{\Phi}$ in the mixed material is maximized i.e.,

$$\bar{\Phi}_D = \frac{1}{D}\int_0^D \Phi(x)dx \equiv \bar{\Phi}_{max}.$$

The fluence in the mixed material is then $\Psi_0(\tau) = \tau \cdot \bar{\Phi}_{max} + \Psi_0(0)$ where $\Psi_0(0)$ is the fluence at $\tau = 0$. The optimum value of D is ~ 250 g/cm^2 ($\bar{\Phi}_{max} = 6 \times 10^{15}$ n/cm^2 10^8 yr) for a cylindrical crater; however in the range 125–500 g/cm^2, $\bar{\Phi}$ decreases by only 20% from its maximum value. Consequently using the maximum value of $\bar{\Phi}$ not only maximizes the variation in $\Psi_0(\tau)$ but is realistic if the major transport and mixing of material is from a wide variety of shallow impacts (1–4 m depth). The fluence at depth l in the accreted material is described by

$$\Psi(l) = \frac{1}{V}\int_0^l \Phi(x)dx + \Psi_0(\tau)$$

where τ is the time between the start of accretion and the deposition on the surface of the material now at depth l.

For this type of continuous accretion model, it is possible to produce a peak in the fluences without post-depositional irradiation. The shape of this peak will depend on the mixing depth and accretion rate. However, it is distinguishable from the peak of the undisturbed soil case in that it is broader and reaches a maximum at greater depth; therefore,we must still invoke a period of undisturbed irradiation in which most of the observed peak shape is developed. At the end of this period of T years the observed fluence at depth l will be

$$\Psi(l) = \frac{1}{V}\int_0^l \Phi(x)dx + \Psi_0(\tau) + T \cdot \Phi(l).$$

In order to find the maximum change in $\Psi_0(\tau)$, we define $\tau = 0$ as the time at which the layer now at the bottom of the drill stem was deposited, assume the accretion at $\tau = 0$ to start with $\Psi_0(0) = 0$, and let the neutron fluence of the material added to the surface be given by $\Psi_0(\tau) = \tau \cdot \bar{\Phi}_{max}$. For the deposition of material at the rate of $V \geq 100$ g/cm^2 10^8 yr, the resulting $\Psi(l)$ is nearly constant throughout the deposited slab at the end of accretion (i.e. when 400 g/cm^2 have been accreted). This means that the peak must be developed almost totally during the undisturbed period, T, after deposition and the in situ irradiation time of the slab must be similar to that found for the case of an instantaneously deposited slab (~ 450 my). As shown in fig. 6, the accretion of the slab could have taken up to 400 my followed by an additional 400 my period during which the slab was undisturbed. If the slab had accumulated at a rate slower than 100 g/cm^2 10^8 yr, the effect would have been to produce larger fluences at the end of the accumulation period and thereby decrease the time possible for the undisturbed irradiation which would not fit the data. As for the case of the instantaneously deposited slab, we must assume that the upper ~ 35 g/cm^2 has been added to the area recently or gradually over the last 400 my.

If the fluence in the accreting material actually changed at a rate between that of cases A and B,(i.e., less than $\tau \cdot \bar{\Phi}_{max}$) an intermediate solution would be obtained for the allowable accretion time. Since the maximum accretion time is similar in the extreme cases A and B, the effect of letting $\Psi_0(\tau)$ be a function of time is small.

The soil deposition models considered above show that the material sampled, with the possible exception of the upper drill stem section, has been essentially undisturbed for at least 400 my and possibly 600 my and that the drill stem material could have been deposited continuously over a period ranging from 400 my to instantaneously. Furthermore, the lowest layer sampled must represent material deposited between one billion and 400 million years ago.

4.4 *Comparison with track data*

Interpretation of both the rates of deposition and the stratigraphy of the drill stem samples must depend on the record of various processes which are preserved in this section. In particular the tracks of solar flare heavy ions, which penetrate only to depths of ~ 50 μm, are important in establishing whether materials in the drill stem were derived from depth, possibly from a single deep cratering event in bedrock, or whether they had a significant residence time in the very upper millimeter of the regolith. In the latter case these materials were deposited with a relatively slow accretion rate or from previously irradiated regolith material. Preliminary studies by Crozaz et al. [20] and Phakey et al. [21] have shown that relatively high track densities are found in the Apollo 15 drill stem samples and that there is no appreciable

variation of track density with depth for the same samples as we analyzed. Crozaz et al. [20] found an average track density of $\sim 10^9/cm^2$ for feldspar grains of $\sim 100\,\mu m$ diameter and reported no grains with densities less than $10^8/cm^2$. Phakey et al. [21], in a similar experiment, reported lower densities; nevertheless, over 50% of the grains examined by them had track densities greater than $10^8/cm^2$. It follows, therefore that material from the Apollo 15 drill stem has been highly irradiated in the upper mm of the lunar surface either prior to, or during, deposition. There is no evidence for a significant admixture of unirradiated bedrock material, thus it appears that the samples are similar to typical lunar surface soils. This is compatible with the interpretation that the section sampled by the drill stem was derived from shallow impacts into older, well mixed regolith. It may also be compatible with a uniform accretion model if the rate of accretion was slow enough to permit the accumulation of sufficient solar particle bombardment. Using the production rate for solar particle tracks of $10^4/cm^2$ yr at $50\,\mu m$ depth, as determined on the Surveyor III camera lens [22–24] and an average track density of $10^9/cm^2$ in $100\,\mu m$ plagioclase grains, we calculate an effective residence time of 10^5yr and an accretion rate of 0.2 g/cm^2 per my. This is somewhat lower than the minimum accretion rate of ~ 1 g/cm^2 per m.y determined by the fluence results for an accreting model based on deposition of unirradiated material (fig. 6A). This discrepancy could be explained if the larger grains have a longer residence time at the surface than the average soil grains. However, if the discrepancy is real, we would have to reject the particular case of uniform accretion of unirradiated material and would instead require some previous irradiation in the regolith prior to deposition in order to simultaneously account for both the track and neutron fluence data.

5. Implications for lunar surface processes

It is of great interest to establish what limitations can be set on the mechanisms of deposition and on the sources of the material deposited at the drill stem site from the range of permitted depositional histories. Although bounds can be set on the times of deposition, the necessity for an undisturbed period of irradiation following deposition tells us nothing about the depositional processes per se. This in situ irradiation primarily indicates the absence of major impacts on this spot in the last $\sim 500 \times 10^6$ yr. Information on the depositional processes is contained in the permitted range of accretion rates and initial fluences. In principle, a complete depositional history can be constructed by interrelating the neutron fluence, track and other particle exposure results with chemical and petrological data on discrete strata within the drill core.

In the following discussion we shall assume, as required by most of the permitted depositional histories (figs. 5 and 6), that the stratigraphic section is composed of materials that were rather heavily pre-irradiated at the time of their deposition. This model also provides the simplest explanation of the particle track data which indicate that the amount of unirradiated material in the drill stem samples is small. Therefore, except for the in situ irradiation in the last 500×10^6 yr, the stem samples appear to have the irradiation history of typical lunar surface soil samples. A model in which the deposited material was unirradiated at the time of deposition is discussed in sect. 4.3. However, the calculations show (see fig. 6A) that the time for accumulation of the section would have to be about 350 my. We consider it unlikely that the accumulated debris blanket represents a steady rain of *primary* ejecta from *deep* craters over this long time period.

The requirement of a comparatively large amount of pre-irradiation does not permit layers of 20 cm or larger in the drill stem material to be *undisturbed* ejecta from a deep crater. However, it is possible that a large quantity of fresh ejecta from a deep crater was deposited at this site prior to ~ 500 my and was then subject to irradiation and mixing which ceased at ~ 450 my.

It follows from the above discussion that there is no evidence in either the fluence or particle track data for a component which can be identified with the ray from Autolycus or Aristillus which is visible at the Apollo 15 site [17]. Therefore, we cannot establish any limits on the age of the ray solely from our data. However, the fluence and track data can be used to impose bounds on specific models for the deposition of the ray. For example, if the ray occurred within the last $\sim 300 \times 10^6$ yr and produced an appreciable ($\sim 100 - 200$ g/cm^2) amount of erosion or deposition of ma-

terial at the drill stem site, the observed fluence profile would have been different from that observed. Consequently, for models of this type, the deposition time of the ray is required to be greater than the slab irradiation time of $\sim 400 \times 10^6$ yr.

If the broad physiography of the Apollo 15 LM-ALSEP site, particularly the ridge, was produced by the Aristillus or Autolycus impacts, then it is evident that these craters were formed prior to $\sim$ 450 my. If the ray is older than 450 my, it is not clear why the 'ray material' is so readily visible in photographs of the landing site considering the fact that there has been mixing and deposition to depths of over 2 m in this time period.

The portion of the drill stem below 30–60 g/cm^2 is best interpreted as ejecta from local craters in the regolith which deposited pre-irradiated, well-mixed material at this site. We have considered two models:

A. The drill site is considered to be on a thick part of the ejecta blanket of a crater of about 30–100 m in diameter or possibly the intersection of the ejecta blankets of a few craters of 20–100 m in diameter. Such craters would mostly excavate regolith and could yield mixed, pre-irradiated material. Because of the low frequency of occurrence of impacts producing craters with diameters of over 3 m, this debris blanket could remain relatively stable without major erosion for periods of $\sim 5 \times 10^8$ yr. These craters would have to be relatively close to the drill stem site. The presence of a large number of visible strata within the drill stem material [16] would not rule out this hypothesis because it is possible that such strata can be formed during different phases in the throwout of ejecta from a single impact.

B. We consider it unreasonable that a 2.5 m high lunar 'sand dune' (i.e. a statistical accumulation of material on a level surface) produced by small impacts (craters less than 3 m diameter), would have a lifetime comparable with 5×10^8 yr. However, a model utilizing small impacts is suggested if we note that this site has been an area of accretion for at least the last 450×10^6 yr. Thus in the period $450–950 \times 10^6$ yr ago, this spot was probably topographically low, e.g., near the bottom of a crater of 10 m diameter or larger. Such a crater will be filled in by small impacts in or near the crater walls. The rate of filling would be rapid at first, but, once the crater had filled in, the small impacts would not affect the deeper strata, and a long period of in situ irradiation could result. It is possible that some vestige of this ancient crater would be visible at present in high resolution photos of the ALSEP site.

Our data show that no impacts yielding craters greater than $\sim$ 2 m diameter have disturbed the drill stem section in the last $\sim$ 500 my. Assuming the average impact rate for 2 m diameter craters on the lunar surface estimated by Shoemaker et al. [25], the probability that the drill stem section would remain undisturbed for 500 my is low. Therefore, our data provide additional support for a decrease in the rate of impact on the lunar surface in the last 4×10^9 yr. Our data provides evidence that, in addition to the flux of km-sized objects, the impact rate of objects producing 1–10 m craters has also dropped off.

Physical examination and detailed chemical and petrological examination of the 15006 section will be necessary in order to see if there is any independent evidence for the upper surface layer required by many of the fits to the observed fluence profile. However, the presence of a dense layer at $\sim$ 55 g/cm^2 was noted by the astronauts during drilling and digging the soil mechanics trench [11]. This dense layer is responsible for the high average density for section 15005. It is possible that this well-defined boundary is the transition between our 'surface layer' and the zone of 'in situ irradiation'.

6. Epilogue

This study shows that it is possible to date sedimentary processes on the lunar surface for time scales of around 10^8 yr. This innovation is possible because of the particular dependence of neutron capture reactions on depth. The neutron flux has a distinct peak as a function of depth. This peak appears to lie below the level of shallow cratering for time scales of less than 10^9yr and consequently forms a readily identified marker layer of both depth and time.

It should be emphasized that since the product nuclei studied (^{158}Gd, ^{150}Sm) are stable, they are total time integrators and preserve a record of the total irradiation history of the sample.

The measured neutron fluences alone place rather tight bounds on the depositional history of the Apollo 15 deep drill stem. The available particle track data

reinforce these conclusions. Eventually, comparison with other laboratory data and more detailed field observations will provide strong checks on the conclusions drawn in this paper and should permit the depositional processes to be more closely delineated. Of particular interest will be measurements of other neutron capture products such as ^{131}Xe and stable cosmic-ray produced rare gases, especially ^{126}Xe and ^{78}Kr, because these latter nuclei are high energy nuclear reaction products and have production rate gradients which are distinct from those for neutron capture [3, 26, 27]. We would have great confidence in a depositional model which fit both the neutron fluence and rare gas concentration data well. A complication, at present, is that only theoretical production rate gradients are available for both neutron capture and spallation products. This introduces an unknown uncertainty into the above conclusions. It is important to have experimental data for these gradients. An in situ measurement of the neutron capture rates is feasible, and studies of radioactive cosmic-ray produced nuclei, particularly ^{37}Ar, ^{81}Kr, ^{53}Mn and ^{3}H, can be used to establish the spallation production rates.

Despite the uncertainties in the neutron capture rates and the range of models which fit the data presently available, it is quite clear that the Apollo 15 drill stem has obtained samples which will allow us to study the lunar surface as it existed half a billion years or more ago. This makes a variety of studies possible, in particular the analysis of 'ancient solar wind', which accumulated prior or during the deposition, as a function of time.

Acknowledgements

This paper is dedicated to Astronauts, David R.Scott, James B. Irwin and Alfred M. Worden, whose heroic efforts made Apollo 15 an extraordinary and successful scientific mission. We gratefully acknowledge many fruitful discussions with J. Huneke, E. Shoemaker, and R.E. Lingenfelter. We thank N. Hinners for his comments on the manuscript. The expertise of P.Young and A. Massey in maintaining the Lunatic mass spectrometers was invaluable. This work was supported by the National Science Foundation under grant GP-28027 and by the National Aeronautics and Space Administration under grant NASA NGL 05-002-188.

References

[1] O. Eugster, F. Tera, D.S. Burnett and G.J. Wasserburg, Isotopic composition of gadolinium and neutron capture effects in some meteorites, J. Geophys. Res. 75 (1970) 2753.

[2] O. Eugster, F. Tera, D.S. Burnett and G.J. Wasserburg, The isotopic composition of Gd and neutron capture effects in samples from Apollo 11, Earth Planet. Sci. Letters 8 (1970) 20.

[3] D.S. Burnett, J.C. Huneke, F.A. Podosek, G. Price Russ III and G.J. Wasserburg, The irradiation history of lunar samples, Proc. Second Lunar Sci. Conf. 2 (MIT Press, 1971) 1671.

[4] G.W. Lugmair and K. Marti, Neutron capture effects in lunar gadolinium and the irradiation histories of some lunar rocks, Earth Planet. Sci. Letters 13 (1971) 32.

[5] G.P. Russ π, Neutron capture on Gd and Sm in the Luna 16, G-2 soil, Earth Planet. Sci. Letters 13 (1972) 384.

[6] D.S. Burnett, J.C. Huneke, F.A. Podosek, G.P. Russ III, G. Turner and G.J. Wasserburg, The irradiation history of lunar samples, Lunar Sci. III (Lunar Sci. Inst. Cont. No. 88, 1972) 105.

[7] G.W. Lugmair and K. Marti, Neutron and spallation effects in Fra Mauro regolith, Lunar Sci. III (Lunar Sci. Inst. Cont. No. 88, 1972) 495.

[8] R.E. Lingenfelter, E.H.Canfield and V.H. Hample, The lunar neutron flux revisited, unpublished manuscript.

[9] G.P. Russ III, D.S. Burnett, R.E. Lingenfelter and G.J. Wasserburg, Neutron capture on ^{149}Sm in lunar samples, Earth Planet. Sci. Letters 13 (1971) 53.

[10] W. David Carrier III, Stewart W. Johnson, Lisimaco H. Carrasco and Rolf Schmidt, Core sample depth relationships: Apollo 14 and 15, to be published in Proc. Third Lunar Sci. Conf. (1972).

[11] G.A. Swann, M.H. Hait, G.G. Schaber, V.L. Freeman, G.E Ulrich, E.W. Wolfe, V.S. Reed and R.L. Sutton, Interagency report 36: Preliminary description of Apollo 15 samples environment, U.S.G.S. (1971).

[12] Lunar Receiving Laboratory, Lunar Sample Information Catalog, Apollo 15 (MSC 03209) (1971).

[13] Br. A. Bernabei, L.B. Borst and V.L. Sailor, Neutron resonance in samarium, Nucl. Sci. Eng. 12 (1962) 63.

[14] N. Hubbard, personal communication.

[15] L. Haskin, personal communication.

[16] Apollo 15 Preliminary Examination Team, The Apollo 15 lunar samples: A preliminary description, Science 175 (1972) 363.

[17] Apollo Lunar Geology Investigation Team, Geologic setting of the Apollo 15 samples, Science 175 (1972) 407.

[18] L.A. Rancitelli, R.W. Perkins, W.D. Felix and N.A. Wogman, Cosmic ray flux and lunar surface processes characterized from radionuclide measurements in Apollo 14 and 15 lunar samples, Lunar Sci. III.(Lunar Sci. Inst. Cont. No 88, 1972) 630.

[19] T.W. Armstrong and R.G. Alsmiller, Jr., Calculation of cosmogenic radionuclides in the Moon and comparison

with Apollo measurements, Proc. Second Lunar Sci. Conf. 2 (MIT Press, 1971) 1729.

[20] G. Crozaz, R. Drozd, C.M. Hohenberg, H.P. Hoyt, Jr., D. Ragan, R.M. Walker and D. Yuhas, Solar flare and and galactic cosmic ray studies of Apollo 14 Samples, Lunar Sci. III (Lunar Sci. Inst. Cont. No. 88, 1972) 167.

[21] P.P. Phakey, I.D. Hutcheon, R.S. Rajan and P.B. Price, Radiation damage in soils from five lunar missions, Lunar Sci.III (Lunar Sci. Inst. Cont. No. 88, 1972) 608.

[22] G. Crozaz and R.M. Walker, Solar particle tracks in glass from the Surveyor 3 spacecraft, Science 171 (1971) 1237.

[23] D.J. Barber, R. Cowsik, I.D. Hutcheon, P.B. Price and R.S. Rajan, Solar flares, the lunar surface, and gas-rich meteorites, Proc. Second Lunar Sci. Conf. 3 (MIT Press, 1971) 2705.

[24] R.L. Fleischer, H.R. Hart, Jr. and G.M. Comstock, Very heavy solar cosmic rays: energy spectrum and implication for lunar erosion, Science 171 (1971) 1240.

[25] E.M. Shoemaker, M.H. Hait, G.A. Swann, D.L. Schleicher G.G. Schaber, R.L. Sutton, D.H. Dahlem, E.N. Goddard and A.C. Waters, Origin of the lunar regolith at Tranquillity Base, Proc. of the Apollo 11 Lunar Sci. Conf. 3 (Pergamon, Lunar Sci. Conf. 3 (Pergamon, 1970) 2399.

[26] J.C. Huneke, F.A. Podosek, D.S. Burnett and G.J. Wasserburg. Rare gas studies of the galactic cosmic ray irradiation history of lunar rocks, Geochim. Cosmochim. Acta 36 (1972) 269.

[27] P. Eberhardt, J. Geiss, H.Graf, N. Grögler, U. Krähenbühl, H. Schwalles, J. Schwarzmuller and A. Stettler, Correlation between rock types and irradiation history of Apollo 11 igneous rocks, Earth Planet. Sci. Letters 10 (1970) 67.

[28] F.A. Podosek, J.C. Huneke and G.J. Wasserburg, Gas-retention and cosmic-ray exposure ages of lunar rock 15555, Science 175 (1972) 423.

[29] P.A. Baedecker, C.L. Chou, J.Kimberlin and J.T. Wasson, Trace element studies of lunar rocks and soils, Lunar Science III (Lunar Sci. Inst. Cont. No. 88, 1972) 35.

Chapter 9

EARTH AND PLANETARY SCIENCE LETTERS 19 (1973) 275–289. NORTH-HOLLAND PUBLISHING COMPANY

2

APOLLO 16 NEUTRON STRATIGRAPHY

G. PRICE RUSS III

The Lunatic Asylum of the Charles Arms Laboratory, Division of Geological and Planetary Sciences, California Institute of Technology, Pasadena, California 91109, USA*

Received 16 December 1972
Revised version received 16 March 1973

The Apollo 16 soils have the largest low energy neutron fluences (up to 10^{17} n/cm^2, $E < 0.18$ eV) yet observed in lunar samples. Variations in the isotopic ratios ^{158}Gd/^{157}Gd and ^{150}Sm/^{149}Sm (up to 1.9% and 2.0% respectively) indicate that the low energy neutron fluence in the Apollo 16 drill stem increases with depth throughout the section sampled. Such a variation implies that accretion has been the dominant regolith "gardening" process at this location. The data may be fit by a model of continuous accretion of pre-irradiated material at a rate of ~70 g/(cm^2 · 10^8yr) or by models involving as few as two slabs of material in which the first slab could have been deposited as long as 10^9 yr ago.

The ratio of the number of neutrons captured per atom by Sm to the number captured per atom by Gd is lower than in previously measured lunar samples, which implies a lower energy neutron spectrum at this site. The variation of this ratio with chemical composition is qualitatively similar to that predicted by Lingenfelter, Canfield and Hampel.

Variations are observed in the ratio ^{152}Gd/^{160}Gd which are fluence correlated and probably result from neutron capture by ^{151}Eu.

1. Introduction

The isotopic composition of Gd has been measured in seven samples from various depths in the Apollo 16 drill stem (60007–60001) and soil 60501. For five of these samples, the Sm isotopic composition has also been measured. Variations in the isotopic composition of Gd and Sm in lunar samples can be used to calculate the energy spectrum and fluence (time integrated flux) of low energy neutrons to which the samples have been exposed [1–4]. If the depth dependence and magnitude of the neutron flux is known, it is possible to determine the "mixing" history of lunar soils by measuring the neutron fluence as a function of depth in drill stem samples. Using the depth dependence and flux calculated by Lingenfelter et al. [5] (hereafter referred to as LCH), the regolith sampled by the Apollo 15 drill stem, in which the neutron fluence showed a distinct peak, was shown to have been essentially undisturbed for ~ 5 × 10^8 yr [3].

During the Apollo 16 mission to the Descartes region, astronauts Young and Duke also obtained a drill stem which penetrated more than 2 m into the lunar regolith. In this paper, models for the development of the regolith at the Apollo 16 site are fit to the isotopic data for Gd and Sm from the drill stem, and the layering implied by these models is compared with geological descriptions of the site and the layers observed in the cores by X-ray radiography.

* Contribution No. 2276.

2. Experimental

Samples were analyzed from each of the five junctions of the six 40 cm long drill stem sections, from the upper surface of the drill sample, and from the drill bit (fig. 1). Soil 60501, which was collected at station 10 about 40 m from the drill site, was selected to determine whether the neutron exposure of the soil changed significantly over this distance.

All the samples were sieved to a grain size of less than 300 μm. Approximately 80% of the < 1 mm fines were also smaller than 300 μm. They were then dissolved, and the Gd and Sm were isolated as described previously [4, 6]. For each of the seven drill stem samples, 30–50 mg of sieved material were used.

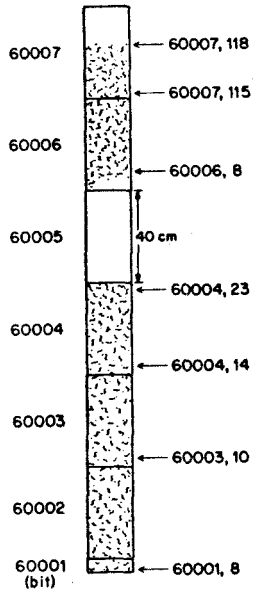

Fig. 1. Depth relationships of the samples analyzed. The drill stem sections (40 cm long) and the drill bit are labeled on the left. The sample numbers and locations are indicated on the right. When the tubes were opened, section 60005 and part of 60006 were nearly empty. The diameter of the drill stem has been exaggerated in this cartoon.

In the case of 60501, 90 mg were used to ensure a good quality mass spectrometric analysis.

Gd was analyzed on the Lunatic I mass spectrometer as GdO^+ ions [6]. Ratios were taken relative to $^{160}Gd^{16}O$ and averaged in sets of ten. These set averages were converted to Gd isotopic ratios by correcting for the ^{17}O and ^{18}O contributions and where then normalized to $^{156}Gd/^{160}Gd = 0.9361$ [6]. The set averages were screened for iron beam stability as described by Russ et al. [3], and those sets satisfying the stability criteria were averaged for the final result. Ion current of $1 - 2 \times 10^{-12}$ amps $^{160}Gd^{16}O^+$ were obtained for several hours. In a typical analysis, 24 sets of ten ratios of $^{155-158}Gd/^{160}Gd$ data were collected using a Faraday cup and a 10^{11} ohm resistor. In addition, ten to fifteen sets of $^{152, 154, 156}Gd/^{160}Gd$ data were collected at the end of the analysis by using an electron multiplier with a gain of $\sim 3 \times 10^3$ and a 10^9 ohm resistor.

Sm was analyzed on the Lunatic III mass spectrometer as Sm^+ ions according to the procedure of Russ et al. [4]. Ratios were taken relative to ^{154}Sm and normalized to $^{147}Sm/^{154}Sm = 0.65918$. A typical analysis consisted of ~ 300 scans of the Sm isotopes at an ion current of $\sim 2 \times 10^{-12}$ amps of $^{154}Sm^+$. These data were screened and averaged as described previously [4]. In order to speed data acquisition and reduce the interpolation time between successive readings of the ^{154}Sm reference peak during analyses where ion beam stability was a problem, ^{152}Sm, ^{148}Sm, and ^{144}Sm were omitted during some of the scans.

During the course of this work three aliquots of a Knippa basalt sample, which had been doped with reagent Gd, were analyzed. Each aliquot contained ~ 300 ng of Gd. They yielded $^{158}Gd/^{157}Gd$ values of 1.58650 ± 0.00016, 1.58645 ± 0.00020, and 1.58661 ± 0.00031, which are in agreement with the previously published value of 1.58660 ± 0.00011 [3]. Two samples of reagent Sm (~ 400 ng each) gave $^{150}Sm/^{149}Sm$ ratios of 0.53391 ± 0.00007 and 0.53401 ± 0.00005. Although one of these agrees with our previous value of 0.53403 ± 0.00005 [4] only at the extremes of the error bars, this discrepancy ($\sim 2 \times 10^{-2}$%) is small compared to the neutron induced effects (up to 2%) in the lunar samples (cf. table 3).

3. Results

3.1. Isotopic data

The Gd isotopic composition data are shown in table 1. The samples are listed in order of increasing depth (cf. fig. 1). The number of sets of $^{155-158}Gd/^{160}Gd$ which satisfied the screening criteria and were therefore included in the final average is indicated. Because the $^{152, 154}Gd/^{160}Gd$ data are collected separately, the number of sets of $^{152, 154}Gd/^{160}Gd$ included in the final average is also tabulated. The $^{158}Gd/^{160}Gd$ values are seen to be distinctly higher than the terrestrial average and increase with depth, whereas the $^{157}Gd/^{160}Gd$ and $^{155}Gd/^{160}Gd$ ratios are lower than the terrestrial averages and decrease with increasing depth. As shown in fig. 2, the variations in $^{158}Gd/^{160}Gd$ and $^{157}Gd/^{160}Gd$ are corre-

TABLE 1
Gadolinium isotopic composition[a]

Sample	Number of sets[b] $\frac{^{155-158}Gd}{^{160}Gd}$	$\frac{^{158}Gd}{^{160}Gd}$	$\frac{^{157}Gd}{^{160}Gd}$	$\frac{^{155}Gd}{^{160}Gd}$	Number of sets[b] $\frac{^{152,154}Gd}{^{160}Gd}$	$\left(\frac{^{154}Gd}{^{160}Gd}\right)_{norm}$[d]	$\left(\frac{^{152}Gd}{^{160}Gd}\right)_{norm}$	$\left(\frac{^{154}Gd}{^{160}Gd}\right)_{corr}$[e]	$\left(\frac{^{152}Gd}{^{160}Gd}\right)_{corr}$
60501,31	24	1.14 000 ± 8	0.71 024 ± 6	0.67 479 ± 8	15	0.099 67 ± 4	0.009 381 ± 13	0.099 85 ± 4	0.009 403 ± 13
60007,108	22	1.14 002 ± 10	0.71 053 ± 10	0.67 490 ± 11	13	0.099 49 ± 7	0.009 383 ± 25	0.099 66 ± 7	0.009 405 ± 25
60007,115	9	1.14 023 ± 36	0.71 040 ± 10	0.67 485 ± 17	0	–	–	–	–
60006,8	8	1.14 041 ± 19	0.70 992 ± 14	0.67 457 ± 25	15	0.099 57 ± 16	0.009 383 ± 21	0.099 77 ± 16	0.009 407 ± 21
60004,23	26	1.14 164 ± 9	0.70 840 ± 8	0.67 409 ± 8	13	0.099 66 ± 7	0.009 407 ± 19	0.099 90 ± 7	0.009 438 ± 19
60004,14	21	1.14 210 ± 12	0.70 772 ± 13	0.67 373 ± 13	13	0.099 56 ± 9	0.009 422 ± 29	0.099 82 ± 9	0.009 454 ± 29
60003,10	12	1.14 186 ± 19	0.70 779 ± 18	0.67 369 ± 21	0	–	–	–	–
60001,8	23	1.14 282 ± 10	0.70 675 ± 7	0.67 344 ± 10	12	0.099 53 ± 7	0.009 414 ± 28	0.099 83 ± 7	0.009 451 ± 28
Terrestrial[c] average	92	1.13 582 ± 5	0.71 588 ± 4	0.67 687 ± 5	52	0.099 74 ± 3	0.009 285 ± 8		

(a) Normalized to $^{156}Gd/^{160}Gd = 0.9361$. Errors are 2σ mean.
(b) A set consists of ten ratios for a given pair of isotopes.
(c) From Russ et al. [3].
(d) norm ≡ normalized, cf. footnote (a).
(e) corr ≡ corrected for the effect of fluence on the normalization isotope.

lated as expected for neutron capture by ^{157}Gd [6]. Since the data are normalized to a constant ^{156}Gd/^{160}Gd to correct for mass fractionation in the mass spectrometer, a plot of ^{155}Gd/^{160}Gd vs. ^{156}Gd/^{160}Gd is not possible, but if ^{155}Gd/^{160}Gd is plotted against ^{157}Gd/^{160}Gd [6], the measured values all fall on the correlation line expected for neutron capture by ^{155}Gd and ^{157}Gd. The ratios are not normalized to an isotope which is unaffected by neutron capture because of the low abundances of these isotopes.

Since ^{156}Gd is enriched by the reaction ^{155}Gd $(n, \gamma)^{156}$Gd, the procedure of normalizing to a constant ^{156}Gd/^{160}Gd causes a false discrimination correction of $\frac{1}{4}[^{155}\sigma\psi(^{155}\mathrm{Gd}/^{156}\mathrm{Gd})_{\mathrm{terr}}]$ per mass unit [1] where $^{155}\sigma$ is the cross section for neutron capture by ^{155}Gd, ψ is the neutron fluence, and the subscript 'terr' indicates the terrestrial ratio. This effect is responsible for the values of $(^{154}\mathrm{Gd}/^{160}\mathrm{Gd})_{norm}$ in table 1 being lower than the terrestrial ratio. When this effect is taken into account for the ^{154,152}Gd/^{160}Gd data, the values tabulated in the last two columns of table 1 are obtained. With two exceptions, 60004, 23 and 60501,31, where the ratio is high by 0.16% and 0.11% respectively, the corrected ^{154}Gd/^{160}Gd values agree with the terrestrial average within the extremes of the errors. However, the ^{152}Gd/^{160}Gd values are about two percent above the terrestrial average. These enrichments may result from the reaction $^{151}\mathrm{Eu}(n, \gamma)^{152}\mathrm{Eu}(\beta^-)^{152}\mathrm{Gd}$ which will be discussed in sect. 4.2.

The Sm data (table 2) show that, compared to the terrestrial values the ^{150}Sm/^{154}Sm ratios are enriched while the ^{149}Sm/^{154}Sm ratios are depleted in the lunar samples. If these data are plotted on a ^{150}Sm/^{154}Sm vs. ^{149}Sm/^{154}Sm diagram [4], the points all fall on the line predicted for neutron capture by ^{149}Sm. The other Sm isotopes are in the same relative abundances as in terrestrial samples. In previous work [3, 4], small depletions, which were not explained, were noted in the ^{152}Sm/^{154}Sm ratios of some lunar samples. Because such depletions are not observed in these data, we infer that they were probably due to an interference at mass 154 rather than neutron capture.

For the Apollo 16 samples, approximately 98% of the Gd neutron captures are calculated to occur below 0.18 eV; therefore, the neutron fluence below this energy (table 3) to which the samples have been exposed is

TABLE 2
Samarium isotopic composition[a]

Sample	No. of ratios ^{150}Sm/^{154}Sm	^{152}Sm/^{154}Sm	^{150}Sm/^{154}Sm	^{149}Sm/^{154}Sm	^{148}Sm/^{154}Sm	^{144}Sm/^{154}Sm
60007,108	187	1.175 50 ± 14	0.32 703 ± 6	0.60 500 ± 11	0.494 25 ± 8	0.135 21 ± 5
60004,23	105	1.175 55 ± 27	0.32 791 ± 11	0.60 400 ± 23	0.494 33 ± 17	0.135 14 ± 10
60004,14	84	1.175 24 ± 30	0.32 816 ± 15	0.60 378 ± 27	0.494 20 ± 15	0.135 13 ± 7
60003,10	118	1.175 43 ± 18	0.32 829 ± 8	0.60 364 ± 13	0.494 14 ± 10	0.135 17 ± 7
60001,8	151	1.175 38 ± 30	0.32 871 ± 9	0.60 322 ± 13	0.494 28 ± 14	0.135 14 ± 9
Terrestrial[b] average	483	1.175 40 ± 6	0.32 442 ± 3	0.60 750 ± 4	0.494 23 ± 4	0.135 14 ± 3

(a) Normalized to ^{147}Sm/^{154}Sm = 0.65918. Errors are $2\sigma_{mean}$.
(b) From Russ et al. [4].

TABLE 3
Summary of neutron capture effects

Sample	Depth (g/cm^2)		$^{158}Gd/^{157}Gd$(a)	$^{150}Sm/^{149}Sm$	(10^{16} n/cm^2)(b)	$\epsilon_{Sm}/\epsilon_{Gd}$
	No loss	180 g loss			($E < 0.18$ eV)	
60501,31	surface		1.60460 ± 18(c)		6.06 ±.06	
60007,108	surface		1.60399 ± 27	0.54055 ± 12(c)	5.86 ±.09	0.634 ±.016(d)
60007,115	32.4		1.60457 ± 56		6.05 ±.18	
60006,8	83.1		1.60588 ± 42		6.49 ±.14	
60004,23	106.4	161.5	1.61093 ± 21	0.54290 ± 27	8.17 ±.07	0.617 ±.019
60004,14	168.4	223.5	1.61307 ± 35	0.54352 ± 18	8.89 ±.11	0.604 ±.015
60003,10	234.4	289.5	1.61258 ± 49	0.54384 ± 14	8.72 ±.16	0.639 ±.012
60001,8	308.5	363.6	1.61621 ± 22	0.54492 ± 13	9.93 ±.07	0.623 ±.009
Terrestrial average			1.58660 ± 11	0.53403 ± 5	≡0	

(a) Corrected for the effect of fluence on the normalization isotope, ^{156}Gd.
(b) $\langle^{157}\sigma\rangle_{0.18} = 1.13 \times 10^5$ barns. Errors are calculated from the error in the $^{158}Gd/^{157}Gd$ of the sample only.
(c) Errors are $2\sigma_{mean}$.
(d) Errors are calculated quadratically from the errors in the isotopic ratios including the errors in the terrestrial ratios.

$$\psi = 0.98\{(^{158}Gd/^{157}Gd)_{corr} - (^{158}Gd/^{157}Gd)_{terr}\}/\langle^{157}\sigma\rangle_{0.18} \cdot \{1 + (^{158}Gd/^{157}Gd)_{corr}\}$$
$$\approx 0.98\ \{(^{158}Ge/^{157}Gd)_{norm} - (^{158}Gd/^{157}Gd)_{terr}\}/\langle^{157}\sigma\rangle_{0.18} \cdot \{1 + (^{158}Gd/^{157}Gd)_{terr}$$
$$+ \tfrac{1}{4}\langle^{155}\sigma\rangle_{0.18} \cdot (^{158}Gd/^{157}Gd)_{terr} \cdot (^{155}Ge/^{156}Gd)_{terr}\}$$

where the subscripts 'norm', 'terr', and 'corr' indicate the normalized sample ratio, the normalized terrestrial ratio, and the normalized sample ratio corrected for the false discrimination effects, respectively. The average ^{157}Gd and ^{155}Gd capture cross sections, $\langle^{157}\sigma\rangle_{0.18}$, and $\langle^{155}\sigma\rangle_{0.18}$, are calculated for the LCH spectrum at energies below 0.18 eV in material with the major element composition of 60600 [9] and the rare earth concentration of 60001 [10]. The value of $\langle^{157}\sigma\rangle_{0.18}$ is 1.13×10^5 barns, and $\langle^{155}\sigma\rangle_{0.18}$ is taken as $0.24 \cdot \langle^{157}\sigma\rangle_{0.18}$ [6]. The Apollo 16 samples with fluences ranging up to $\sim 10^{17}$ n/cm^2 are the most irradiated natural samples yet analyzed (fig. 2).

Differences in the neutron energy spectrum in the sub-eV range are reflected by the ratio of the number of neutrons captured per atom by Gd to the number captured per atom by Sm. This is just the ratio of the average cross sections, $\langle\sigma\rangle$, for ^{157}Gd and ^{149}Sm where the average is carried out over the total energy spectrum. The ratio $\langle^{149}\sigma\rangle/\langle^{157}\sigma\rangle$ is equal to an experimentally de-

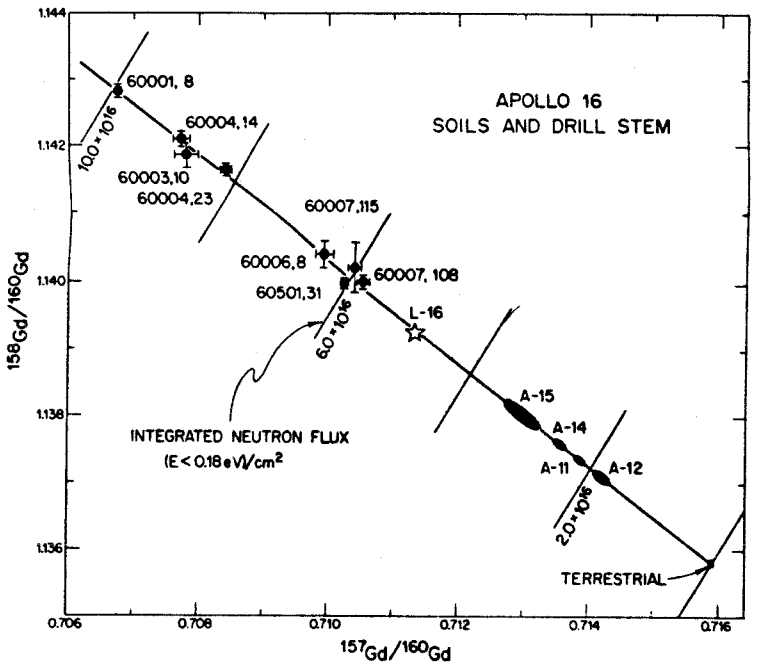

Fig. 2. $^{158}Gd/^{160}Gd$ vs $^{157}Gd/^{160}Gd$ correlation diagram. The slope of the correlation line is that calculated for neutron capture by ^{157}Gd and ^{155}Gd [6]. The distance of a sample point from the terrestrial value is a measure of its neutron fluence. Approximate fields are indicated for surface soils from previous Apollo missions and for the Luna 16 G layer [1, 3, 4, 7, 8]. The fluence scale is calculated for materials of the composition of the Apollo 16 soils and applies only approximately to the soils from the other sites.

terminable ratio defined as $\epsilon_{Sm}/\epsilon_{Gd}$ [4]. The $\epsilon_{Sm}/\epsilon_{Gd}$ values of the Apollo 16 samples (table 3) are all quite similar, but they may be slightly lower in the samples from 60004 than in the other three samples.

3.2. Sample depths

On the lunar surface, the filled drill stem was uncoupled in the middle, between sections 60005 and 60004, and the ends were capped. The two halves were then returned to Earth. When the upper half was opened at the Lunar Receiving Laboratory, its lower third (60005) was found to be nearly empty. Several hypotheses have been advanced to explain how this gap in the sample could have occurred and its effect on the depth relationships of the strata sampled [11].

Because of the uncertainty in the depth relationships of the samples, the depths in the regolith from which they were obtained have been calculated in two ways. In the first case, it is assumed that a negligible amount of material was lost when the two halves of the drill stem were separated on the lunar surface and that section 60005 is empty (fig. 1) because the soil shifted in the tubes, without the stratigraphy being altered, either when the stem was extracted from the drill hole or during transportation. In the alternate case, it is assumed that the gap resulted from material being lost during the uncoupling of the halves of the drill stem. In order to calculate depths for this case one must estimate the amount of material lost. In units of g/cm^2, the depth of a sample is simply the mass of material above it in the drill tube divided by the cross-sectional area of the

tube. The lower three sections (60002–60004), which were returned full, contain between 203 and 216 g each [11]. Assuming that the partially filled sections (60006 and 60005) contained 210 g each when extracted from the drill hole, the difference between 420 g and the mass returned in these two sections must be the amount spilled. This implies 180 g were lost. Correcting for this loss, the depths in g/cm^2 can then be calculated for the lower sections. The depths calculated for each model using a cross sectional area of 3.27 cm^2 [12] are shown in table 3.

4. Discussion

4.1. Neutron energy spectrum

The absorption cross section of ^{157}Gd is dominated by a resonance near 0.03 eV while the ^{149}Sm cross section has a large resonance near 0.1 eV. The ratio $\epsilon_{Sm}/\epsilon_{Gd}$ (cf. sect. 3.1) is therefore an indicator of the shape of the neutron spectrum. The shape of the energy spectrum below $\approx$ 10 eV is controlled by the concentration of neutron absorbers (e.g., Fe, Ti, and rare earths) and the temperature of the medium [5]. As the concentration of absorbers is increased, the fraction of neutrons moderated to the low energy region is decreased. The relatively low $\epsilon_{Sm}/\epsilon_{Gd}$ ratios determined for the Apollo 16 samples (fig. 3) indicate a lower energy spectrum than observed at the earlier sites. This reflects the lower concentration of neutron absorbers in the Apollo 16 samples.

In all cases the measured $\epsilon_{Sm}/\epsilon_{Gd}$ ratios are somewhat higher than predicted by LCH (fig. 3) for lunar materials at a temperature of 200° K which implies a harder spectrum than predicted. With the exception of the Apollo 14 and, to a lesser extent, Apollo 12 samples, the variation of the experimental $\epsilon_{Sm}/\epsilon_{Gd}$ values with the effective macroscopic absorption cross section, Σ_{eff} (cf. [5]), does however parallel the curve predicted by LCH. The Apollo 14 samples, which show the greatest deviation from the theoretical curve, have the highest fractional contribution (38%) of the rare earth elements to Σ_{eff}. Rare earth neutron absorption is also important for the Apollo 12 soil. Thus, it may not be possible to represent the effects of chemical variations by a single parameter such as Σ_{eff}. As would be expected if the LCH treatment using Σ_{eff} has not properly accounted for the effects of rare earth absorption on the shape of the energy spectrum, the fractional deviation of the measured values from those predicted is correlated with the fractional contribution of the rare earths to Σ_{eff}.

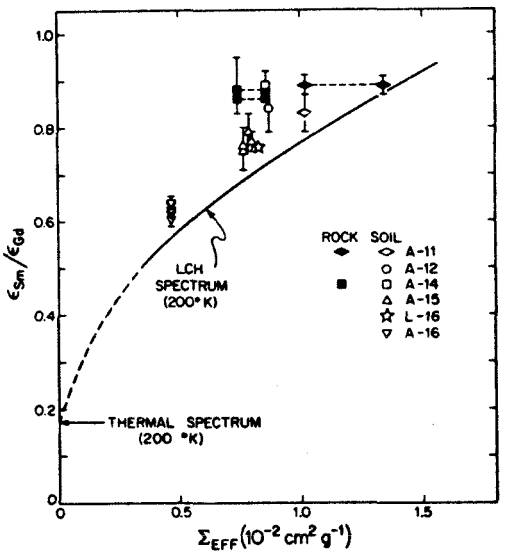

Fig. 3. Variation of $\epsilon_{Sm}/\epsilon_{Gd}$ as a function of the effective macroscopic neutron absorption cross section, Σ_{eff}, of the sample. The Apollo 16 samples are all assumed to have the major element composition of 60600 [9] and rare earth concentration of 60001 [10]. The rock points are plotted at both the Σ_{eff} value of the soils from which they were collected and at the Σ_{eff} corresponding to their own composition, because it is not known in which environment they received the bulk of their neutron exposure. Where error bars would overlap, they are indicated on only one side of the points. This figure differs slightly from the previous version of this plot [3]. In the earlier version Σ_{eff} was calculated by including the contributions from Si, Ti, Al, Fe, Mg, Ca, Gd, Sm, Eu, and O. In this work the contributions of Mn, Cr, Na, and K have also been included in the Σ_{eff} of each sample.

If the LCH spectrum is too soft, then the average cross sections for ^{157}Gd used to calculate fluences of neutrons with $E < 0.18$ eV are too high and the fluences are correspondingly low. The effect on the fluences should be on the order of 10%. The effect on the neutron flux and consequently on the calculated exposure times will be somewhat greater although it is not possible to make quantitative estimates of the uncertainties.

In pure anorthite ($CaAl_2Si_2O_8$), $\epsilon_{Sm}/\epsilon_{Gd}$ would be ~0.5, whereas values of ~0.8 were typical in the soils from the previous missions in which the concentration of neutron absorbers was higher than at the Apollo 16 site. The lack of significant variation in $\epsilon_{Sm}/\epsilon_{Gd}$ from the intermediate value of ~0.62 throughout the Apollo 16 drill stem implies that the chemical composition of the soil is not very different throughout the sampled layers. The slightly lower $\epsilon_{Sm}/\epsilon_{Gd}$ ratios of section 60004 may indicate a somewhat more anorthositic composition for these samples.

4.2. $^{151}Eu(n, \gamma)^{152}Eu(\beta^-)^{152}Gd$

The fractional change in $^{152}Gd/^{160}Gd$ due to this reaction has been predicted by LCH to be larger than in $^{158}Gd/^{160}Gd$. The low intensity of the ^{152}Gd signal in the mass spectrometer and the possibility of ^{152}Sm interference, however, have prevented this effect from being clearly resolved in previous work. The Apollo 16 samples have been more heavily irradiated by neutrons than any previously studied samples. These samples also have a more favorable target to product ratio, i.e., Eu/Gd, than previous lunar samples [10]. These factors should enhance the effect in $^{152}Gd/^{160}Gd$. In spite of these advantages, the low rare earth concentrations and small sample sizes provided to us from the drill stem made it difficult to obtain good $^{152, 154}Gd/^{160}Gd$ data. However, as noted earlier, the measured $^{152}Gd/^{160}Gd$ ratios are distinctly higher than the terrestrial value after the effect of the false discrimination correction is taken into account (table 1).

If these enrichments are due to neutron capture, the magnitude of the effect should be proportional to the neutron fluence. In fig. 4, $^{152}Gd/^{160}Gd$ and $^{154}Gd/^{160}Gd$ have been plotted against the fluence of neutrons with energies less than 0.18 eV. Although the errors are large, the $^{152}Gd/^{160}Gd$ variations seem to be correlated with the fluence, while the $^{154}Gd/^{160}Gd$ ratios appear to be independent of fluence. There is, however, some scatter in the $^{154}Gd/^{160}Gd$ values beyond the statistical errors. If this scatter is caused by $^{154}Sm^{16}O$ interference, then the $^{152}Gd/^{160}Gd$ ratios must be corrected for $^{152}Sm^{16}O$ interference, which is about ten times more significant than the interference with ^{154}Gd. Such a correction would seriously scatter the $^{152}Gd/^{160}Gd$ data. A potential check on SmO^+ is the Sm^+ intensity, which should be at least as large as the SmO^+. However, in these analyses, the Sm^+ signal was too small ($\lesssim 3 \times 10^{-16}$ amps) to resolve because of the slope of the baseline in this mass region. If the $^{154}Gd/^{160}Gd$ and $^{152}Gd/^{160}Gd$ ratios were subject to a common source of interference, they would be expected to vary proportionately. This does not seem to be the case; therefore neutron capture on ^{151}Eu appears to be the more probable cause of the enrichments in ^{152}Gd, and the observed effects should thus be compared to the LCH predictions.

For the LCH neutron spectrum, resonances at 0.321 and 0.460 eV dominate the capture cross section of ^{151}Eu. For materials of Apollo 16 soil composition, only about 50% of the neutron captures are predicted to occur below 0.18 eV where essentially all of the $^{157, 155}Gd$ absorption occurs. In principle ^{151}Eu, therefore, provides a third experimental window through which the spectrum can be constrained. Using the Eu and Gd concentrations of Philpotts [10] and the spectral calculations of LCH, the predicted correlation line between the fluence of $E < 0.18$ eV neutrons and the $^{152}Gd/^{160}Gd$ ratio has been calculated (fig. 4). The agreement between the calculated line and the experimental points is reasonably good, but the apparent amount of ^{151}Eu capture relative to the ^{157}Gd capture is somewhat higher than predicted. This discrepancy might be due to a slight interference at mass 152. However, if it is real, then the spectrum is harder than predicted, which is consistent with the deviations in $\epsilon_{Sm}/\epsilon_{Gd}$ from the LCH calculations. ^{152}Sm is produced by ~55% of the ^{152}Eu decays [5], but the target to product ratio is much less favorable than in the ^{152}Gd case. For 60001, the most irradiated sample, the ratio $^{152}Sm/^{154}Sm$ is predicted to be enriched by only 2×10^{-2}%, which is within the errors of the measurement.

4.3. Interpretation of the Apollo 16 drill stem data

In order to interpret the drill stem data, it is first necessary to establish the correct depth relationship for the samples from above and below the essentially empty section (60005). If the fluence was a smooth

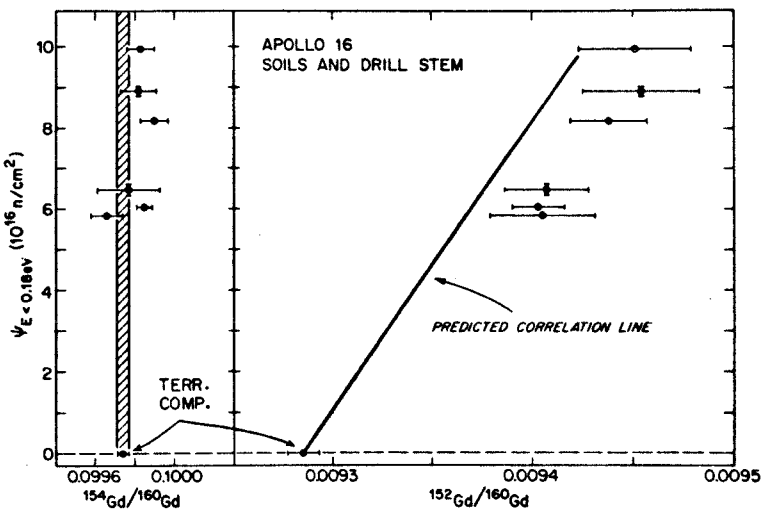

Fig. 4. Variation of ^{152}Gd/^{160}Gd with neutron fluence. The ^{152}Gd/^{160}Gd ratios of the lunar samples are clearly higher than the terrestrial value ($\psi = 0$) and appear to be correlated with the neutron fluence. The ^{154}Gd/^{160}Gd ratios scatter somewhat from the terrestrial value, but the ^{152}Gd/^{160}Gd variations are not proportional to those in ^{154}Gd/^{160}Gd. The "predicted correlation line" is the LCH prediction for the variation in ^{152}Gd/^{160}Gd due to the reaction ^{151}Eu (n, γ)^{152}Eu(β^-)^{152}Gd.

simple* function of depth everywhere except across section 60005, it could be argued that one of the possible depth scales given in table 3 was preferable. As shown in fig. 5, the fluence does not vary simply with depth on either end of section 60004 for either depth scale; therefore, neither depth scale can be eliminated by these data. The mission transcript indicates that some material was lost during the uncoupling of the sections [14], but this is believed to have been only a few grams [15]. ^{37}Ar data of Davis and Stonner [16] show that the activity of this isotope is essentially the same on opposite ends of the gap. This supports the idea that a negligible quantity of material was spilled on the surface. We will therefore attempt to fit the fluence data using the assumption that no material has been lost from the middle of the drill stem.

Although the variation may not be monotonic for Gd, the ratios ^{158}G/^{157}Gd and ^{150}Sm/^{149}Sm, and therefore the fluence, generally increase with depth (fig. 5). The drill bit sample (60001), which has the maximum fluence, was obtained from a depth of at least 300 g/cm^2 which is significantly below the calculated peak in the ^{158}Gd production curve (150–200 g/cm^2 depending on the model used [5, 13]) and below the peak observed at 190 g/cm^2 in the Apollo 15 drill stem [3]. The depth dependence of the neutron fluence for a variety of simple models in which the soil was undisturbed, mixed, eroded, and accreted has been discussed [3]. Only those models involving accretion, i.e., the addition of soil to the site with time, resulted in an increase in fluence below the peak in the production curve. Therefore, it is reasonable to attempt to fit the data with accretional models in order to discuss limits on the possible histories for this site.

Some simple models involving accretion are illustrated in fig. 6. The model for a soil continuously accreting at a constant rate V was treated previously [3]. If the material has a constant fluence ψ_0 when deposited, then the fluence at depth l will be:

$$\psi(l) = \frac{1}{V}\int_0^l \Phi(x)\,dx + \psi_0$$

* 'Simple' in this context is defined as second degree or less.

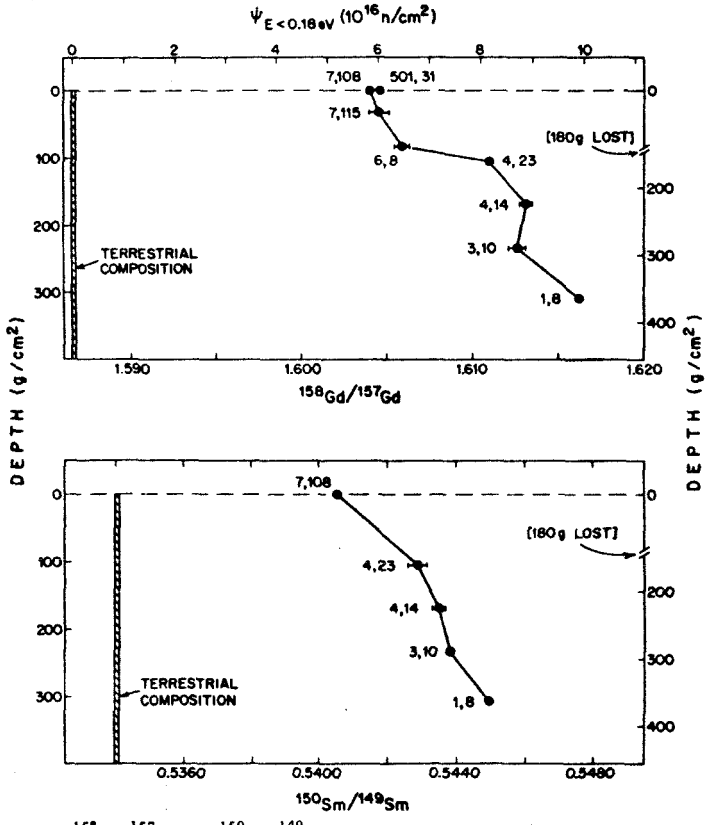

Fig. 5. Depth dependence of $^{158}Gd/^{157}Gd$ and $^{150}Sm/^{149}Sm$. The depth scale on the left assumes no material was lost when the drill stem halves were decoupled on the lunar surface. The one on the right assumes 180 g (55 g/cm^2) were lost at the indicated depth. A neutron fluence scale has been included on the Gd portion, and applies only to that portion of the figute. The $^{158}Gd/^{157}Gd$ values have been corrected for the false discrimination effect introduced by the normalization procedure.

where $\Phi(x)$ is the neutron flux at depth x. As shown in fig. 6, this is a strictly increasing function of depth. If the accretion stops and the regolith remains undisturbed for a time T, then the fluence at depth l will be:

$$\psi(l) = T\Phi(l) + \frac{1}{V}\int_0^l \Phi(x)\,dx + \psi_0$$

This function describes a broadly peaked ~~shape~~ *depth* profile (fig. 6). As T increases the peak moves to shallower depths, narrows, and approaches the shape of the undisturbed slab curve. If T is too short for a peak to develop within the depth sampled, it is difficult to distinguish this case from simple continuous accretion, and the accretion rate calculated in such a situation must be regarded as a lower limit. These models allow the fluence to increase below the depth of maximum neutron flux, but they cannot account for the increase in slope observed experimentally below sample 60003,10 (fig. 5) for both Gd and Sm except by changes in ψ_0. The discontinuity between samples 60006,8 and 60004,23 could be attributed to mixing, either on the lunar surface or resulting from sampling and/or transporting of the drill stem.

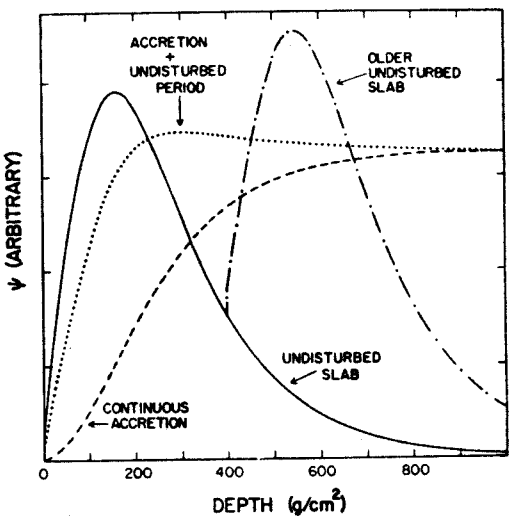

Fig. 6. Depth dependence of the neutron fluence, ψ, for various models involving accretion. The initial fluence of the materials at the time of deposition has been taken as zero. For illustrative purposes, the time required for the accretion of 1000 g/cm^2 in the "continuous accretion" case has been taken as two and a half times the irradiation time of the "undisturbed slab". The "older undisturbed slab" has been taken as having been at the surface for a time equal to the time since the upper slab was deposited. As illustrated, the "accretion plus undisturbed slab" case was accreted at the rate of the "continuous accretion" case and then remained undisturbed for half of the time represented by the "undisturbed slab" case.

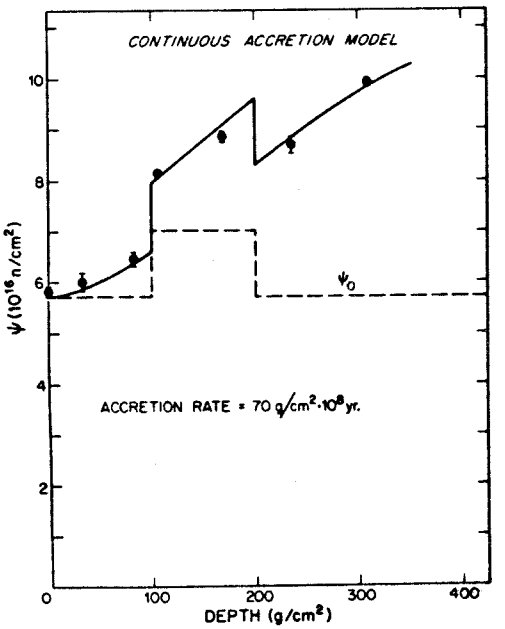

Fig. 7. Calculated fluence profile for continuous accretion of material at the rate of 70 g/(cm^2 · 10^8 yr). The fluence of the material at the time of deposition is assumed to have varied as indicated by the dashed curve.

The similar slopes of the lines connecting point 60004,23 to point 60004,14 and point 60003,10 to point 60001,8 in fig. 5 suggest that we may attempt to fit the data with a continuous accretion model by letting ψ_0 be different in the material of section 60004. The fact that the two 60004 samples have slightly lower $\epsilon_{Sm}/\epsilon_{Gd}$ values than the other samples may support the idea of a different origin for this "layer". By letting ψ_0 be ~ 20% higher in this layer than elsewhere, the data can be fit reasonably well for an accretion rate of 70 g/(cm^2 · 10^8 yr) (fig. 7). By this model the bottommost sample, 60001, was deposited nearly 500 my ago. If we adopted the other depth scale discussed above in which material is assumed to have been lost, an accretion rate of 85 g/(cm^2 · 10^8 yr) would be indicated. These are simple models which fit the data, but the solutions are not unique. If ψ_0 is allowed to vary freely, the deposition could have been instantaneous. Likewise, by introducing mixing near the surface and a low ψ_0 for the deeper points, the rate of deposition could be lowered.

It should be noted that these and all "gardening" rates calculated in this work are based on the LHC estimate of the lunar neutron flux, to which they attach a 30% uncertainty. A more direct estimate of the ^{157}Gd capture rate should be possible when the results of the Apollo 17 Lunar Neutron Probe Experiment are evaluated.

If the soil was not built by an essentially continuous rain of material on the site, we would like to find the minimum number of events which could have deposited the layers sampled. A single layer is not tenable because the observed fluence does not peak to a depth

of at least 300 g/cm^2, whereas the peak of the neutron flux occurs at ~ 150 g/cm^2.

Let us consider a two slab case where the older slab, which was emplaced T_1 years ago, has been buried to a depth of D g/cm^2 by a second slab T_2 years ago, and let us assume that the initial fluence was uniform throughout the slabs when they were emplaced. The fluence measured today in the second and newer slab will be

$$\psi(x) = T_2\,\Phi(x) + \psi_0(2)$$

where $\psi_0(2)$ indicates the initial fluence of the second slab. Below the depth D, the fluence will be described by

$$\psi(x) = T_2\,\Phi(x) + (T_1 - T_2)\,\Phi(x - D) + \psi_0(1)$$

This model is illustrated in fig. 6 for the case where $T_2 = \frac{1}{2}T_1$ and $D = 400$ g/cm^2. Above 400 g/cm^2 the solid curve applies, whereas below 400 g/cm^2, the dot-dash curve holds. This model has the interesting property that the fluence can have two maxima. This may be useful in explaining the experimental fluence data which appear to have two maxima, at least for Gd (fig. 5).

Although a slab of regolith may experience a negligible amount of net accretion or erosion, its surface will be subjected to mixing caused by impacts. The constancy with depth of the neutron fluences in cores from Apollo 11 and 12 [1, 8] suggests that surface mixing must be included in slab models. In a layer which has undergone mixing (not necessarily isotopic homogenization) to a depth l, without exchange of material with regions which have different exposure histories, the integral over depth of the function, which we will call $f(x)$, which describes the fluence above depth l must equal the area under the fluence profile for the case of no mixing, i.e.,

$$\int_0^l f(x)\,dx = T\int_0^l \Phi(x)\,dx + \psi_0 .$$

Physically, mixing increases ψ near the surface and reduces ψ at depth.

Since the upper slab has the simpler history, we will attempt to fit it to the data first. A slab ~ 200 g/cm^2 thick which was deposited 450 my ago with an initial fluence of 3.3×10^{16} n/cm^2 (fig. 8) approximately fits the two data points from section

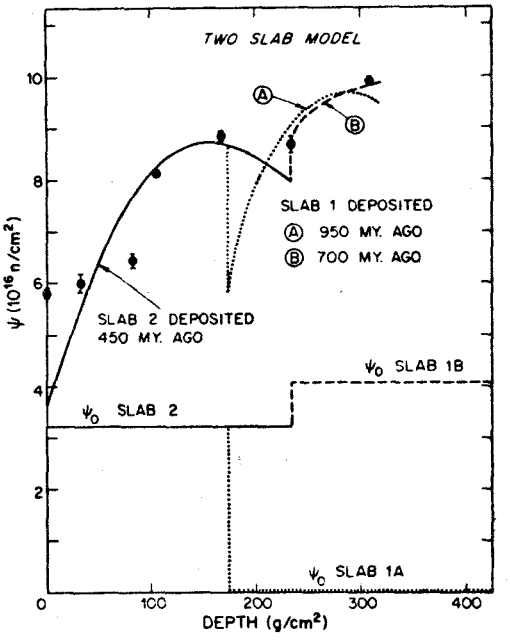

Fig. 8. Two-slab model for the evolution of the regolith. The deviation of the three near surface points from the calculated curve may be explained by the soil having been mixed to a depth of ~ 100 g/cm^2. The time of deposition of the older (deeper) slab may be between 700 and 950 my ago depending on its initial fluence, which may vary from 0 to 4×10^{16} n/cm^2, and the thickness of slab 2.

60004. Furthermore, the area under the line segments connecting the data points from the surface to a depth of ~ 100 g/cm^2 (60004,23) is essentially equal to the area under the curve calculated for the 450 my old undisturbed slab. This is consistent with recent ($\lesssim$ 50 my) mixing of the upper 100 g/cm^2.

In order to fit the data points below ~ 200 g/cm^2 an additional older slab is required. This slab may start at any depth between that of 60004,14 and 60003,10 (165 – 235 g/cm^2). If the first slab was unirradiated when it was deposited, the closest fit will be obtained by assuming that the boundary between the layers is slightly below sample 60004,14. As shown by the dotted curve in fig. 8, the data can be approximately fitted if slab 1 was deposited 950 my ago. If the interface of the slabs occurs just above sample 60003,10, the initial fluence of the older slab

could have been as high as 4.1×10^{16} n/cm^2. In this case, the first slab was laid down 700 my ago. This is the most recent time of deposition of the lower slab possible for the two slab model. For the case where the initial fluence of the two slabs is taken to have been the same at the times at which they were laid down, a good fit to the deeper points could be obtained for the first slab having been deposited 775 my ago and subsequently buried with 225 g/cm^2 of material 325 my later. In summary, a two slab model is compatible with the data if the upper ~ 100 g/cm^2 is allowed to be mixed. The upper slab must have been emplaced ~ 450 my ago. The lower slab could have been deposited 700–950 my ago. For this model it has been assumed that the older slab (slab 1) was not mixed or otherwise disturbed when it was at the surface. If mixing of the slab is included in the model, the age of slab 1 may be older. For instance, if the ψ_0 of slab 1B (fig. 8) resulted from mixing of the surface of the slab rather than being a property of the material when deposited and if this mixing averaged the fluence over a depth of ~ 100 g/cm^2, then the apparent fluence was developed in ~ 500 my. This means that the slab could have been deposited as long as 1.2×10^9 yr ago. Similar models are possible for the alternative depth relationships, which assume a significant amount of material was lost when the stem sections were separated.

Many models for three or more slabs can undoubtedly be fit to the data. Two of these will be discussed briefly. If the upper ~ 25 g/cm^2 is considered as a separate layer of relatively recent origin ($\lesssim 10^8$ yr) then a second layer extending to 300 g/cm^2 with an age of ~ 400 my is possible. The deepest layer (below 300 g/cm^2) is restricted only by the total fluence of the deepest point and could be several billion years old. This model moves the upper boundary of the lower slab below sample 60003,10 (235 g/cm^2) and reduces the depth of mixing required to fit the near surface data. The other three slab model which seems reasonable to discuss, assumes the material of section 60004 (105–170 g/cm^2) constitutes a distinct slab. In this model, the near surface material is not required to be mixed. The material from the surface through section 60006 (~ 100 g/cm^2) may represent a layer deposited ~ 50 my ago with a uniform initial fluence of $\sim 6 \times 10^{16}$ n/cm^2. The middle layer, encompassing section 60004, would be ~ 100 my older if it had a uniform initial fluence of $\sim 8 \times 10^{16}$ n/cm^2. If near surface mixing is allowed, these layers could be older. Because of the large number of possible solutions, no attempt has been made to fit the lowest layer for the three stage models.

A feature common to all the models discussed is that a boundary of two layers (slab-slab or mixed zone-slab boundary) is required between 25 and 105 g/cm^2 and between 170 and 305 g/cm^2. Because the neutron flux is a smooth function of depth, any discontinuity in the fluence must reflect either the addition of a new layer (normally with a different initial fluence) or mixing. In either case, assuming the depth relationships are well known, a discontinuity in the fluence vs. depth curve is unambiguous evidence for a stratigraphic boundary.

From the above discussion, one sees that the general increase in fluence throughout the length of the drill stem implies that in the area around the drill stem the regolith has been accreting. This accretion could have been continuous or could have resulted from the deposition of as few as two slabs of soil. The material sampled by the deepest part of the drill stem may have been deposited as long ago as 10^9 yr if the material was deposited in only two slabs or 450 my ago if the accretion has been due to many thin layers with similar initial fluences.

The fluence of soil 60501 is very similar to that of the core top. This implies that in the LM-ALSEP area at least the surface layers have had similar histories over a distance of ~ 50 m.

4.4. Mixing lengths of soils

If the total exposure age of the soil is taken as the crystallization age of the local rocks, the quantity of unirradiated material which has been mixed into the surface soil can be estimated by assuming that the soil has been uniformly mixed, i.e., isotopically homogenized, to some depth L such that the fluence multiplied by the depth will equal the total flux of neutrons in the layer multiplied by the age of the site.

$$\psi \cdot L = T \int_0^L \Phi(x)\, dx .$$

In general, there are two values of L which satisfy this

equation for a given ψ and T. Using the age of rock 68415 ($T = 3.84 \times 10^9$ yr [17]) as the age of the site and the LCH curve of $\Phi(x)$, it follows that the surface fluence could be accounted for by mixing to only 11 g/cm^2 or by mixing to 2.7×10^3 g/cm^2 in a soil which was not subject to any exchange of material with outside sources. The shallow solution seems unreasonable but the larger solution is interesting in that the depth of 2.7×10^3 g/cm^2 falls in the rather narrow total range of $1.8 - 3.0 \times 10^3$ g/cm^2 calculated for nine other surface soils analyzed in this laboratory from previous Apollo missions. The Luna 16-G2 soil gives a lower value of 1.3×10^3 g/cm^2.

One interpretation of these mixing lengths is that they represent lower limits for the thickness of the regolith. In general, these depths are greater than those estimated from cratering theory, e.g., see [18] and [19]. However, at the Apollo 16 site the depth inferred from the fluence (~ 16 m) is not greatly different from the 10–15 m depth estimated by the Field Geology Investigation Team [20] or the 12.2 m depth calculated by Kovach and Watkins [21] from seismic refraction data. Alternatively, the similarity among surface samples can be taken to imply that the rate of dilution of irradiated material with fresh material excavated from depths of several meters is fairly constant over the lunar surface. In either case, the high fluences of the Apollo 16 soils result from the higher neutron flux in these soils rather than longer exposures.

5. Correlation with field geology and X-ray radiography

If South Ray and North Ray craters contributed appreciable amounts of material to the drill site, as is implied by the abundant white soils which are presumably from South Ray; and if the cratering events were separated by $\gtrsim 10^8$ yr, then their deposits should be distinguishable by a discontinuity in fluence in the drill stem. If these layers on the average represent material ejected from $\lesssim 15$ m depth, the initial fluence of the layers should have been near zero. However, if the cratering events mixed the ejecta and the craters are considered as parabolic with a diameter to depth ratio of 5/1, then the fluence of the ejected material should have been $\approx 2 \times 10^{16}$ n/cm^2. There is no evidence in the fluence data for layers deposited with near zero initial fluences except possibly for the lower slab in the two-slab model. This argues for the ejecta being mixed, or of shallow origin, unless it is too thin to have been measured in this work.

The apparent discontinuities at opposite ends of 60004 imply stratigraphic boundaries. Assuming that North Ray is older than South Ray and that the ejecta from these events is thick enough at the drill site to have been sampled in this work, this observation leads to several possible interpretations. For the two-slab model, the lower slab may represent North Ray ejecta and the upper one may be South Ray material, or the surface mixing may have been caused by the addition of a very small amount of South Ray ejecta to a larger slab, possibly from North Ray. The former case implies that these craters were formed more than 450 my ago. This may be unreasonable. Both of these hypotheses require that the initial fluence be $\sim 3 \times 10^{16}$ n/cm^2 in the material represented by the upper slab of the two-slab model. This may not be unreasonable if the ejecta which formed the slab was mixed or from the upper layers of pre-impact terrain. Alternatively, section 60004 may be North Ray ejecta, and 60005 – 60007 may be from South Ray; or if the ejecta from both craters had essentially identical initial fluences, they could both be in sections 60005–60007. If North Ray and South Ray ejecta are not the only materials sampled by the drill stem, it may also contain ejecta from Spook, Kiva, Palmetto and/or Gator craters.

Using X-ray radiographs and penetrometer readings, Hörz et al. [15, 22] have been able to describe layers in the drill stem and core tubes and to correlate the major stratigraphic units among the various cores.

If the stratigraphic interpretation of Hörz et al. [15] is correct, then surface sample 60501 and the upper two drill stem samples (60007,108 and 60007,115) are predominantly South Ray ejecta. The upper drill stem samples may also contain some additional material excavated by nearby craters. Sample 60006,8 falls in the North Ray unit. This interpretation implies that the ejecta from these two large craters had essentially identical fluences when deposited. Although this would be surprising, this objection may be overcome by assuming that the contribution of material from the primary crater is small, and that what we observe is mostly a local accumulation of ejecta from small craters. If both North Ray and South Ray ejecta are

contained in the upper 100 g/cm^2 of the drill stem, then this suggests that a large number of events may have been necessary to build the regolith, and that the continuous accretion model may best represent the history of this site.

Alternatively, the observation by Hörz et al. [15] of a fine layer at the top of section 60004 could be taken as evidence of an old surface near the top of this section. This would support the models which treat this section as a separate slab, perhaps from North Ray.

The fluence data tell us that the "gardening" history of the regolith at the Apollo 16 drill site has been dominated by accretion throughout the layers sampled by the drill, but these data are not sufficient to locate the ejecta associated with given craters. Because of this, no strong preference can be given to any one of the possible interpretations discussed above. When complete data on spallation products, track densities, chemical composition, grain size distributions and petrology become available, it should be possible to correctly model the development of the regolith at this site.

Acknowledgments

It is a pleasure to acknowledge the advice and support offered by D.S. Burnett and G.J. Wasserburg throughout this and previous investigations. This work was supported by National Science Foundation grant GP 28027 and National Aeronautics and Space Administration grant NAS 9-8074.

References

[1] O. Eugster, F. Tera, D.S. Burnett and G.J. Wasserburg, The isotopic composition of Gd and neutron capture effects in samples from Apollo 11, Earth Planet. Sci. Letters 8 (1970) 20.

[2] G.W. Lugmair and K. Marti, Neutron capture effects in lunar gadolinium and the irradiation histories of some lunar rocks, Earth Planet. Sci. Letters 13 (1971) 32.

[3] G. Price Russ III, D.S. Burnett and G.J. Wasserburg, Lunar neutron stratigraphy, Earth Planet. Sci. Letters 15 (1972) 172.

[4] G.P. Russ III, D.S. Burnett, R.E. Lingenfelter and G.J. Wasserburg, Neutron capture on ^{149}Sm in lunar samples, Earth Planet. Sci. Letters 13 (1971) 53.

[5] R.E. Lingenfelter, E.H. Canfield and V.H. Hampel, The lunar neutron flux revisited, Earth Planet. Sci. Letters 16 (1972) 355.

[6] O. Eugster, F. Tera, D.S. Burnett and G.J. Wasserburg, Isotopic composition of gadolinium and neutron capture effects in some meteorites, J. Geophys. Res. 75 (1970) 2753.

[7] G.P. Russ III, Neutron capture on Gd and Sm in the Luna 16, G-2 soil, Earth Planet. Sci. Letters 13 (1972) 384.

[8] D.S. Burnett, J.C. Huneke, F.A. Podosek, G. Price Russ III and G.J. Wasserburg, The irradiation history of lunar samples, Proc. Second Lunar Sci. Conf. 2 (MIT Press, 1971) 1671.

[9] Apollo 16 Preliminary Examination Team, The Apollo 16 lunar samples: a petrographic and chemical description of samples from the lunar highlands, Science 179 (1973) 23.

[10] J. Philpotts, personal communication.

[11] W.D. Carrier, personal communication.

[12] W. David Carrier III, Stewart W. Johnson, Lisimaco H. Carrasco and Rolf Schmidt, Core sample depth relationships: Apollo 14 and 15, Proc. Third Lunar Sci. Conf. 3 (MIT Press, 1972) 3213.

[13] T.W. Armstrong and R.G. Alsmiller, Jr., Calculation of cosmogenic radionuclides in the Moon and comparison with Apollo measurements, Proc. Second Lunar Sci. Conf. 2 (MIT Press, 1971) 1729.

[14] Apollo Lunar Geology Investigation Team, Interagency Report: Astrogeology 51, Documentation and environment of the Apollo 16 samples, A preliminary report, U.S. Geological Survey, 1972.

[15] Friedrich Horz, W.D. Carrier, J.W. Young, C.M. Duke, J.S. Nagle and R. Fryxell, Apollo 16 special samples, Apollo 16: Preliminary Science Report (to be published).

[16] R. Davis and R.W. Stonner, personal communication.

[17] D.A. Papanastassiou and G.J. Wasserburg, The Rb-Sr age of a crystalline rock from Apollo 16, Earth Planet. Sci. Letters 16 (1972) 289.

[18] The Lunar Sample Preliminary Examination Team, Preliminary examination of lunar samples from Apollo 11, Science 165 (1969) 1211.

[19] Apollo Lunar Geology Investigation Team, Geologic setting of the Apollo 15 samples, Science 175 (1972) 407.

[20] Apollo Field Geology Investigation Team, Apollo 16 exploration of Descartes: A geological summary, Science 179 (1973) 62.

[21] Robert L. Kovach and Joel S. Watkins, The velocity structure of the lunar crust, preprint (1972).

[22] J.S. Nagle, personal communication.

Appendix O

Calculation of Neutron Fluences from Gadolinium Isotopic Ratios and the Effect of Fluence on the Normalization of Gadolinium Isotopic Ratios

In this appendix, the equations relating the *normalized* ratios obtained as described in Section 2.3 to the *correct* ratios, *i.e.*, those normalized to $^{156}Gd/^{160}Gd$ taking into account the amount of ^{156}Gd produced by neutron capture, and the equation for calculating neutron fluences, ψ, from $^{158}Gd/^{157}Gd$ ratios - correct or normalized - will be derived. The elemental symbol Gd will be omitted to conserve space. "156" is to be read ^{156}Gd.

For a sample with no neutron capture effect, the measured ratio $(156/160)_M$ can be related to the defined terrestrial ratio, $(156/160)_T$, by the equation

$$(156/160)_M \; / \; (156/160)_T = 1 + 4\alpha \qquad (1)$$

where α is the fractionation factor per mass unit. Henceforth, the subscript T will be used to refer to terrestrial ratios.

In a sample which has been exposed to neutrons, 156 will be enriched due to the reaction 155(n,γ)156, and this enrichment will be $155_T\sigma_5\psi$ where σ_5 is the cross section for capture by 155 and ψ is the neutron fluence. In such a sample, one has

$$\frac{(156/160)_M}{(156/160)_T} = \frac{(156/160)_T + \left[(155/160)_T\sigma_5\psi\right]\,[1+4\alpha]}{(156/160)_T} \qquad (2)$$

The term $4\alpha(155/160)_T\sigma_5\psi$ is insignificant for the observed range of α and ψ; therefore one can write

$$\frac{(156/160)_M}{(156/160)_T} = 1 + 4\alpha + (155/156)_T\sigma_5\psi \qquad (3)$$

If as is done in practice, $(156/160)_M / (156/160)_T = 0.9361$ is used to normalize the data, a *false discrimination correction* of $\frac{1}{4}(155/156)_T\sigma_5\psi$ per mass unit will result. For convenience, this quantity will be called β in the following discussion.

For the ratio of isotope X to 160, the *correct* ratio denoted by a subscripted C will be related to the measured ratio by the equation

$$(X/160)_C = (X/160)_M / (1 + n\alpha) \qquad (4)$$

where $n \equiv 160 - X$; whereas the normalized ratio $(X/160)_N$ will be

$$(X/160)_N = (X/160)_M (1+n\alpha+n\beta) \qquad (5)$$

$$\therefore (X/160)_C = (X/160)_N \cdot \frac{1+n\alpha+n\beta}{1+n\alpha} \cong (X/160)_N(1+n\beta) \qquad (6)$$

This says that if the fluence is known, the correct ratio may be obtained from the normalized ratio.

The fluence is also related to the 158/157 ratio because of the reaction 157(n,γ)158. By analogy to the above treatment for capture by 155, one can write

$$\left(\frac{158}{157}\right)_C = \frac{158_T + 157_T\sigma_7\psi}{157_T - 157_T\sigma_7\psi} \qquad (7)$$

Rearranging this expression to solve for ψ, one obtains

$$\psi = \frac{(158/157)_C - (158/157)_T}{\sigma_7[1+(158/157)_C]} \tag{8}$$

One does not know $(158/157)_C$, but it can be related to $(158/157)_N$ by

$$\left(\frac{158}{157}\right)_C = \frac{(158/160)_C}{(157/160)_C} = \frac{(158/160)_N(1+2\beta)}{(157/160)_N(1+3\beta)} \tag{9}$$

$$= (158/157)_N(1-\beta+3\beta^2 \cdots) \tag{10}$$

$$\therefore \quad \psi = \frac{(158/157)_N(1-\beta+3\beta^2\ldots) - (158/157)_T}{\sigma_7[1+(158/157)_N(1-\beta+3\beta^2\ldots)]} \tag{11}$$

If β is small, one can simplify this expression. Consider a sample with a fluence of 10^{17} n/cm^2, which is the highest yet observed, and take σ_5 as 2.5×10^4 barns (see Sec. 4.2). For such a case

$$\beta = \tfrac{1}{4}(0.6769/0.9361)(2.5 \times 10^{-20})(1 \times 10^{17}) = 4.5 \times 10^{-4}$$

which is negligible in the denominator. The β^2 term can also be ignored in the numerator. From equation 11, one has

$$\psi = \frac{(158/157)_N(1-\beta) - (158/157)_T}{\sigma_7[1+(158/157)_N]} \qquad (12)$$

Recalling that $\beta = \frac{1}{4}(155/156)_T\sigma_5\psi$, one now has a linear equation in ψ which, by rearranging, is

$$\psi = \frac{(158/157)_N - (158/157)_T}{\sigma_7[1+(158/157)_N] + \frac{1}{4}\sigma_5(158/157)_N(155/156)_T} \qquad (13)$$

The second term in the denominator is equal to 3% of the first term. Because $(158/157)_N$ differs from $(158/157)_T$ by < 5% in the most irradiated case, the above expression can be further simplified, with < 1% error being introduced in ψ to

$$\psi = \frac{(158/157)_N - (158/157)_T}{\sigma_7[1+(158/157)_T] + \frac{1}{4}\sigma_5(158/157)_T(155/156)_T} \qquad (14)$$

In this work fluences have been calculated from equation 13 and the correct ratios have then been calculated by equation 6. The details of the numerical values of the cross sections and the energy range involved in Gd neutron capture are discussed in Sections 4.2 and 4.3.

When Gd isotopic data are discussed (*e.g.*, Sec. 2.6), it is convenient to use an isotope correlation diagram in which 158/160 is plotted against 157/160. For the correct ratios, the correlation line describing the increase in 158/160 and decrease in 157/160 with increasing fluence would have a slope of -1 for variations of the magnitude observed. This will not be the case for the normalized ratios because of the false discrimination effect.

For a sample with fluence ψ, the line connecting its isotopic composition to the terrestrial composition will have slope

$$\frac{\Delta(158/160)_N}{\Delta(157/160)_N} = \frac{(158/160)_N - (158/160)_T}{(157/160)_N - (157/160)_T} \tag{15}$$

$$= \frac{(158/160)_C/(1+2\beta) - (158/160)_T}{(157/160)_C/(1+3\beta) - (157/160)_T} \tag{16}$$

Let the amount of 158 produced by neutron capture be 158*, then

$$\psi \cong \frac{158^*}{157_T \sigma_7}$$

and

$$\frac{\Delta(158/160)_N}{\Delta(157/160)_N} = \frac{\left(\frac{158_T+158^*}{160_T}\right)\left[1+\frac{1}{2}\sigma_5(155/156)_T\left(\frac{158^*}{157_T\sigma_7}\right)\right] - (158/160)_T}{\left(\frac{157_T-158^*}{160_T}\right)\left[1+\frac{3}{4}\sigma_5(155/156)_T\left(\frac{158^*}{157_T\sigma_7}\right)\right] - (157/160)_T} \tag{17}$$

$$= -\frac{\dfrac{1-\frac{1}{2}(\sigma_5/\sigma_7)(155/156)_T(158/157)_T}{1+\frac{1}{2}(\sigma_5/\sigma_7)(155/156)_T(158^*/157_T)}}{\dfrac{1+\frac{3}{4}(\sigma_5/\sigma_7)(155/156)_T}{1+\frac{3}{4}(\sigma_5/\sigma_7)(155/156)_T(158^*/157_T)}} \tag{18}$$

For $\psi = 10^{17}$ n/cm^2, $\sigma_7 = 1 \times 10^5$ barns, and $\sigma_5 = 0.24\sigma_7$, 158* is only 1% of 157_T. This means that for the fluence range observed, the above equation can be simplified to the following:

$$\frac{\Delta(158/160)_N}{\Delta(157/160)_N} = -\frac{1-\frac{1}{2}(\sigma_5/\sigma_7)(155/156)_T(158/157)_T}{1+\frac{3}{4}(\sigma_5/\sigma_7)(155/156)_T} = -0.763 \qquad (19)$$

The error introduced by this simplification is only 4×10^{-2}% for $\psi = 10^{17}$ n/cm^2. Therefore, to the extent that this slope is independent of fluence, which is a very good approximation for the range of fluences observed in the lunar samples, the isotopic composition of any sample must lie on the line segment through the terrestrial composition point with slope -0.76.

APPENDIX I

Detailed Experimental Procedures

I.1 Chemical Procedures

In this appendix, an attempt will be made to record the complete experimental procedure employed in isolating Gd and Sm and in determining their isotopic compositions. Some of the procedures described here may seem trivial and/or ritualistic, but it is intended that they be presented as completely as possible for the benefit of one wanting to extend this work.

If one is dealing with a rock sample, it should first be crushed with a mortar and pestle (normally stainless steel) to a grain size of < 1 mm. This will make it easier to dissolve the sample. Soil samples need not be crushed. However, for the lunar samples, it has been customary to sieve soils in order to exclude grains larger than 300 μm across. The ground or sieved sample is carried to the chemical laboratory in a vial and transferred to a 30 ml Teflon beaker. In order to reduce the chance of grains flying out of the beaker as a result of static charging, $\sim \frac{1}{2}$ ml of dilute HCl should be put in the beaker before the sample is poured in. (The preparation of the HCl used in these procedures will be described below.) The grains can then be poured directly into the liquid. If the vial was made of stainless steel, the grains should pour out readily. For plastic vials, it may be necessary to tap the bottom in order to force the grains out. If the weight of the sample is desired, the vial can be weighed before and

after the transfer. Stainless steel vials will corrode if left in the laboratory for long periods of time; therefore, samples should be transferred to beakers and dissolved as soon as practical.

To dissolve the sample, a mixture of HF and $HClO_4$ (typically 1 ml each for a 50 mg sample) is added to the sample beaker. (The HF was purified by M. Tatsumoto of the U. S. Geological Survey. The $HClO_4$, twice distilled, was obtained from G. Frederick Smith Chemical Co.) The beaker is normally covered with Parafilm (American Can Co.) and allowed to react overnight at room temperature. The cover is then removed and the beaker is placed in a covered Teflon *pot* through which filtered dry nitrogen is passed. The mixture is cooked on a hot plate at a temperature of $\sim$ 120°C. When the solution is clear, the temperature is increased to $\sim$ 180°C and the solution is evaporated to dryness. The nitrogen flow must be sufficient to prevent condensation from occurring on the interior walls of the pot. The dry residue is then dissolved in 2 ml of 1.5*N* HCl. A clear solution should result. If this is not the case, evaporate the solution and retreat the residue with HF and $HClO_4$ as before. The clear solution is centrifuged in a SiO_2 glass tube. This centrifuged solution is now ready for the first ion exchange column.

As described in Section 2.1, the isolation of Gd and Sm involves two ion exchange columns. The first column, which is made of SiO_2 glass, has a 1 cm diameter and is approximately 30 cm long. It is topped by a 100 ml reservoir. The resin is held in the column by a *frit* near the bottom. This column is packed with Dowex 50 × 8,

100-200 mesh, resin. Before loading the sample, the resin is washed with ≥ 300 ml of 4*N* HCl. After this conditioning, the height of the resin is 17 cm. Two milliliters of 5 times distilled H_2O are then passed through the column. (Unless otherwise specified, all references to H_2O imply 5 times distilled). Two 5 ml portions of 1.5*N* HCl are then passed through. The sample is loaded onto the column from the centrifuge tube with a disposable pipette. In this and all steps, the solution is allowed to drain completely before more liquid is added to the top of the column. Next, 5 ml of 4*N* HCl are passed through. This is followed by 35 ml of 4*N* HCl. The elutant from these stages is normally discarded. The rare earth elements are eluted with 25 ml more 4*N* HCl. Collect this elutant in a clean Teflon beaker. (The beaker cleaning procedure is described below.) If one desires to collect the alkali and alkaline earth elements, a more complicated elution scheme involving 1.5 and 2.5*N* HCl can be used. This procedure has been described by Tera, Eugster, Burnett, and Wasserburg [1].

The rare earth fraction is evaporated in a Teflon pot through which nitrogen is again passed. In this case, because there is no HF present, a SiO_2 glass cover is used, and the solution is heated with lamps. Before the solution dries, add enough ^{60}Tb to be able to detect its elution from the second column with a γ-ray counter. An effort should be made to avoid cooking the dried residue because it contains organic material from the ion exchange resin which will decompose and make it difficult to redissolve the sample.

The second column, which is used to separate the rare earth

elements, is made from a SiO_2 glass capillary tube with an inside diameter of 0.2 cm. The total length of this tube is 33 cm. At the top of the capillary, there is a reservoir with a volume of 10 ml. This reservoir is capped by a ball joint. The mate to this ball joint is attached to a Teflon stopcock which is used to control the application of air pressure to the column. This is necessary to increase the flow rate of the elutant. Air pressure is applied by means of two $\sim$ 1 liter bottles connected at their bottoms by a plastic tube such that one can be filled with water (not necessarily distilled) and raised $\sim$ 8 ft above the other which contains only air. A tube from the top of the lower bottle is connected to the stopcock to supply air pressure to the column. The leakage of air from the ball joint is small enough that pressure can be maintained with this arrangement throughout the separation procedure which takes $\sim$ 5 hours. Moistening the ball joint with high purity H_2O helps detect leaks due to improper alignment. The bottom of the column is ground smooth and fits into a machined Teflon nipple with a hole $\sim$ 1 mm in diameter. The resin is held in the capillary by a disc of filter paper which can be cut to the proper size with a cork borer. This disc is inserted between the bottom of the capillary and the nipple. This filter should be changed approximately every 10 runs or whenever there is any chance that it may have been damaged, *e.g.*, when changing the resin, as described below. Note that filter paper which has been exposed to the acidic atmosphere of the laboratory may be rotten and should not be used. Returning to the column, the nipple is held in place by two Teflon-coated steel plates.

One is drilled so that the tip of the nipple fits through. The other fits around the upper part of the reservoir. These plates are bolted together with three rods which also serve to protect the column.

The resin for this column is changed for each separation. New resin is prepared in batches sufficient for ~ 40 separations and stored in a propyethylene bottle. The resin, AG50W-X4, was initially sized to 50-90 μm diameter grains but later unsized < 400 mesh resin was used. About 50 ml of this resin is prepared in a large exchange column in the following way. The resin is first washed by passing through one liter of 4*N* HCl to remove Ba and rare earth elements. The resin is then converted to the NH_4^+ form by passing through a liter of 0.4 M 2-hydroxy-2-methyl-propanoic acid (Eastman Organic Chemicals) which has been adjusted to pH 4.6 with concentrated NH_3 solution. The NH_3 solution is prepared by bubbling NH_3 gas into high purity H_2O.

As described by Eugster *et al.* [2], the 4.6 pH is high enough to prevent rare earth absorption on the resin but any Ba present will be strongly held. The resin, now in the ammonium form, is then washed with water to remove the reagent and the upper third which might be contaminated with Ba is discarded. The remaining resin is stored in a bottle under H_2O.

The evening before a rare earth separation is to be performed, the column is prepared by changing the resin. The old resin is sucked out of the column with the aid of a 1 mm O.D. thin wall capillary which is long enough to penetrate the entire length of the column. This capillary is attached to a disposable syringe by means of a rubber

bulb of the type used for micropipettes. Care should be taken that any sharp points on the end of the thin capillary do not puncture the filter paper which retains the resin. (This thin tubing is not readily available on the market at this time, but it can be prepared by a glass blower.) After the resin has been removed, the column is rinsed by filling it with H_2O, and then using the thin capillary to suck out this water. The column is again filled with H_2O and new resin is introduced with a disposable pipette. The resin settles slowly and should be introduced in small quantities to attempt to avoid gravitational sizing. The column should be filled to a height of $\sim$ 32 cm. After the resin has settled, remove the excess water and fill the reservoir with 0.2 M 2-hydroxy-2-methyl propanoic acid adjusted to pH 4.10 with NH_3 solution. A supply of this solution can be prepared at the same time as the resin and stored for long periods in a Teflon bottle. Cover the top of the column with a beaker or Parafilm, and allow the column to drip overnight. In the morning apply sufficient air pressure to achieve a flow rate of 1-2 drops per minute until 60 more drops have been eluted. After this, use a disposable pipette to adjust the height of the resin to exactly 30 cm. (A reproducible volume can be achieved by permanently marking the column at the appropriate height.) Now remove the remaining solution with the pipette. Fill the column to the top of the capillary with H_2O (0.15 ml) and use air pressure to force this through the column. The change in pH will cause the resin to swell slightly.

The evaporated sample should now be dissolved in 4 drops of 0.75 *N* HCl and loaded on the column with a pipette. Some of the organic

residue may not dissolve, but it may be loaded with no harmful effect. Loading the column must be done with care to avoid getting air bubbles trapped between the sample and the resin. Bubbles can usually be avoided by touching the tip of the pipette to the edge of the capillary where it joins the reservoir and expelling the liquid slowly. This also keeps the sample restricted to a smaller area and thereby reduces the chance of *smearing* it on the column. If air bubbles do get trapped in the capillary, they can be sucked out or sometimes *goosed* out with the tip of the pipette. Avoid disturbing the resin. Allow the sample solution to drain through the column without applying pressure. After this has occurred, use a Kimwipe to remove the drop hanging from the bottom of the column and reset the drop counter. Use a clean pipette to fill the capillary to the bottom of the reservoir with the pH 4.10 solution. Use air pressure to force this solution through, then refill the capillary and reservoir with the same solution. Use air pressure to achieve a flow rate of 1-2 drops per minute. Throughout these steps use caution to avoid getting air bubbles in the capillary.

At some earlier time the column will have been calibrated with a mixture of radioactive Tb, Sm, and Gd tracers to determine the volume factors between the elution of the Tb activity and the Gd and Sm peaks. For the conditions described, Tb will typically be eluted near drop number 58 while the drop with the highest Gd concentration will be eluted at $\sim$ 1.4 times this volume. The factor for Sm will be $\sim$ 2.8. The first $\sim$ 45 drops need not be collected separately but after drop 45 each one should be collected in a vial suitable for the γ counter.

Number "0" hollow Nalgene stoppers are convenient for this. They need not be clean. Because one will need to count the activity in these drops as soon as they are eluted, it is essential to have an automatic drop counter and a sample changer to change the vials while the operator is at the γ counter. Count the activity of the drops until the peak of the ^{160}Tb activity is detected; then multiply by the appropriate factors to determine in which drops the Gd and Sm activities will peak. For Gd start collecting the sample in a clean beaker 10 drops before the calculated peak and collect for 6 drops after. The asymmetrical cutoff is used to avoid Eu contamination. The Eu fraction, which is eluted between Gd and Sm, can be saved in the dirty sample beaker as a safeguard against missing the Gd and Sm peaks. Sm is collected in another beaker in the 40 drop band centered at the calculated elution peak. The Gd and Sm solutions should be evaporated in the nitrogen flow pots under heatlamps within 24 hours. This prevents the buildup of NH_4Cl in the solutions which will occur because of the HCl fumes in the laboratory.

It should not be necessary to do so, but if the samples have been allowed to stand for long periods without being evaporated, NH_4Cl can be removed by a third column. This column which is also made of SiO_2 glass has an inside diameter of 2 mm and is $\sim$ 5 cm long. The resin is held in by a plug of SiO_2 glass wool. The capillary is topped by a reservoir with a volume of $\sim$ 2 ml. This column is filled to a height of 4 cm with Dowex 50 x 8, 200-400(?) mesh, resin suspended in H_2O. Two ml of 2*N* HCl are passed through, then the sample dissolved in a drop of H_2O is loaded. Next 1.5 ml of H_2O is passed through. This is followed by 1.5 ml of 2*N* HCl. The rare earth, Gd or Sm, is then eluted

with 1.5 ml of 4*N* HCl. Finally this solution is evaporated in the nitrogen flow pot under the heatlamp. The beaker should be allowed to cool while still in the covered pot, covered with Parafilm to which a label can be attached, and stored in a plastic box to protect it from lint and dust.

The sample is now ready to be loaded on the mass spectrometer filament, but for completeness the procedures for cleaning labware and preparing HCl will be described before discussing the mass spectrometric procedures.

Dirty beakers are first inspected for sticky spots caused by gummed labels or in the case of new beakers for imperfections in the Teflon. Sticky spots can be removed with acetone, but as a policy it is better not to label the beakers directly. (They can be labelled on the Parafilm covers used to protect the samples from dust.) After removing any sticky material, the beakers are soaked and scrubbed with a brush in a solution of Laboratory Glassware Cleaner. The washed beakers are then rinsed thoroughly in tap water. At this stage, water should flow freely over the surface of the Teflon. If it does not, scrub again and/or use more acetone. The beakers are now placed in a large beaker of 8*N* HNO_3 which is brought to a boil. Once the solution has boiled, turn off the hotplate and allow the liquid to cool. The boiled beakers, preferably still warm, are rinsed individually several times with a flow of distilled water and finally with multiply distilled water (normally 5 times distilled). The clean beakers should be allowed to dry on Kimwipes. First cover the table with clean plastic wrap, *e.g.*, Vitafilm,

then cover this with Kimwipes and place the beakers on the Kimwipes. Use another layer of Kimwipes to protect the beakers from dust. The dry beakers can be stored inverted on Kimwipes in an all plastic box, or they may be wrapped in Parafilm. Do not wrap them in Vitafilm. It becomes sticky with age. While this washing procedure has been written explicitly for beakers, it is also used for other labware which comes in contact with the sample, *e.g.*, disposable pipettes. Plasticware cannot be boiled. It is soaked in warm acid instead.

The HCl used in these ion exchange procedures is made by bubbling HCl gas into five times distilled H_2O. This procedure was not developed for this work, but it has never been described elsewhere. Because of the danger involved in handling HCl gas, the whole procedure should be carried out in a non-metallic fume hood and gas masks should be available both at the work area and at the door of the laboratory. Any metal items used, *e.g.*, stands, wrenches, and valves, are likely to corrode; so the use of such items should be minimized. A spare needle valve for the HCl tanks should be available. The gas flows from this valve, which is attached directly to the tank, through Tygon tubing to a coarse sintered glass frit. This tubing should be securely attached because it is exposed to considerable pressure. The purpose of the frit is to trap solid particles. Care should be taken to watch for clogging. If it becomes clogged the plastic tube or the glass around the frit may explode! After the frit, a pull-apart plastic connector should be installed as a safety valve in case of backflow. It can also be used as a pressure relief valve. Beyond the frit only Teflon tubing is used.

The filtered gas is passed through a ~ 4 liter bottle which is set up as a backflow trap. It is then bubbled through ~ 25 ml of concentrated reagent grade H_2SO_4 in a 125 ml gas washing bottle. Finally, it is bubbled through ~ 1 liter of five times distilled H_2O saturated with HCl in a ~ 4 liter gas washing bottle. This final wash must be saturated and allowed to cool to ambient temperature before passing the gas to the collection bottle. From the HCl wash, the gas is bubbled into a ~ 10 liter polyethylene bottle which contains a known weight of H_2O (5 times distilled). The amount of HCl dissolved can be determined by weighing the bottle. The tubing which carries the gas to this bottle should be long enough to have several loops ~ 20 cm in diameter in it and to still reach the bottom of the collection bottle. These extra coils make it easier to insert the tube into the bottle. Great care should be taken to insure that the part of the tube which will be inserted into the bottle is clean and that it touches nothing but the inside of this bottle. An inverted beaker with a hole in the bottom through which the tube is passed and secured makes a good dust cover and defines the part of the tube which will go into the bottle. Because the dissolving HCl will liberate heat, the collecting bottle must be placed in an ice bath. Care must be taken to avoid splashing this dirty water on the mouth of the collecting bottle or in it. When the acid in the collecting bottle reaches the desired concentration, the gas flow is stopped and the acid is weighed, transferred to a 6-gallon polyethylene bottle and diluted to the proper normality. Do not try to saturate the solution in the collecting bottle. This will waste gas. When the gas

tank is exhausted, the flow will of course stop. This should not present any difficulty.

I.2 Mass Spectrometric Procedures

I.2.1 Gadolinium

The sample, prepared as described above, is now ready to be loaded on a mass spectrometer filament. The filament is a ribbon of zone refined Re (Rembar Co.) which is 0.0012 in. thick, 0.030 in. wide, and ~ 0.5 in. long. This ribbon is spot welded to covar feedthroughs (Elecpac), and the assembly is aligned and secured in a filament mounting block, which ultimately serves to hold the filament in the mass spectrometer. (This block should have previously been cleaned by boiling it in 8*N* HNO_3, rinsing it in distilled water and drying it in an oven. The clean block, covars, and filament ribbon are handled with non-powdered plastic gloves at all times.) This assembly is placed in a vacuum chamber and evacuated to a pressure of ~ 10^{-6} Torr. While under vacuum, the filament is *outgassed* by passing an electrical current of 5 amps through it for 2 hours. This current is sufficient to heat the filament to ~ 2000°C, which is ~ 500° hotter than the temperatures used in the mass spectrometer. By inserting an outgassed filament into the mass spectrometer, it can be shown that no rare earth or hydrocarbon signals are obtained from the filament under normal operating conditions.

The outgassed filament is now ready for the sample. It has been found that thin polyethylene tubing is convenient for loading the sample

on the filament. About 2 in. of 0.030 in. I.D. tubing (Intramedic, P.E. 60) is attached to a *pipette control* (Hamilton 605 CH) by means of a hypodermic needle. This pipette control has a threaded insert to the plunger which allows one to precisely control the amount of liquid drawn into or pushed out of the tubing. The tubing is cleaned by drawing up and expelling 4*N* HCl three times. Because of the possibility of BaCl interference in the Gd mass spectrum, it is desirable to add a spike of ^{134}Ba to the sample. (If BaCl is a problem, the $^{134}Ba^{35}Cl$ signal can then be monitored at mass 169 where only $^{152}Gd^{17}O$ normally occurs.) This spike is used to dissolve the sample and load it on the filament. Only about 0.05 ng of ^{134}Ba spike is necessary.

If the spike is prepared appropriately, this amount may be drawn up directly into the P.E. 60 tubing. For the C.I.T. S_2Ba 134 solution, $\sim$ 1 cm of solution in the P.E. 60 tubing is sufficient. This solution is expelled from the tubing into the sample beaker. The end of the tubing can be used to mix it with the sample. In the meantime, the outgassed filament is mounted in a jig so that an electrical current can be passed through it. The sample solution is drawn into the tubing and the pipette control is adjusted so that a hemisphere of liquid protrudes beyond the end of the tubing. This solution is touched to the center of the filament. A small drop should be left on the filament. This drop can be evaporated by passing a current of $\sim$ 0.5 amps through the filament. After the drop dries, repeat the procedure until all of the sample has been loaded. It is desirable to restrict the load to as small a spot as possible; so care should be taken to use small drops.

Usually the sample will spread over the middle ~1/3 of the length of the filament. The sample must now be oxidized. To insure even heating of the filament, it is necessary to protect it from air currents. This can be done by covering the assembly with a cylinder of plexiglass. By wrapping the plexiglass with black paper and covering the top except for a $\sim \frac{1}{4}$ in. wide slit, one can also block out light and improve the visibility of the hot filament. It is also helpful in this capacity to dim the room lights. Heat the covered filament to an orange color (~ 800°C) by passing a current of 1.9 - 2.0 amps through it. This heating should last for one minute unless there are signs that the ribbon is weakening. These signs are a drop in current and/or the development of hot spots. Watch the filament and the ammeter carefully! Some batches of Re will not withstand this treatment while others present no problem. Try to get a good batch and stick with it. Throughout this heating, the whole length of the filament should be a dull orange. At the end of the minute, the current can be <u>briefly</u> increased by ~ 20% in one or two pulses. Load the oxidized filament into the mass spectrometer and *bake* overnight at 1200°C (1.6 - 1.9 amps).

In the morning, increase the temperature by 50° at hourly intervals until reaching 1350°C. After reaching 1350°, turn on the mass spectrometer. Using the electron multiplier, find the peak at mass 176 ($^{160}Gd^{16}O$) and focus the beam. Find the Ba peaks at masses 138 and 134. Scan the spectrum from above mass 180 to below 134. At this temperature, a large number of peaks will probably be observed. After ~ 45 min. turn the temperature up to 1390°. (The temperature may vary

along the filament. Unless the location of the sample is well known and localized, go by the temperature of the hottest area.) At this temperature the intensity at mass 176 may exceed the range of the electron multiplier. If this is the case, the beam can be monitored at mass 170 ($^{154}Gd^{16}O$). The intensity of the Ba peaks may be very unstable and quite high. A scan of the mass region from 130-180 should show Ba and GdO peaks and probably intensities of a few mV (10^4 gain, 10^9 ohm resistor) at masses 151, 153, 155, and 157. The peaks at 153 and 157 correspond to BaF and should vary with the Ba peaks. LaO is probably responsible for the peak at mass 155. Eu contributes to masses 151 and 153 in approximately equal intensities. Scan A in Figure I-1 illustrates such a spectrum. In addition in a few cases, peaks of a few mV may be observed at masses 179 and 180. These are probably due to DyO. If they are smaller than the $^{160}Gd^{17}O$ peak, they should present no problems.

After $\sim \frac{1}{2}$ hour the Ba signal should increase rapidly; then die away. After several such pulses, it should reach a level of a few mV and remain roughly constant or die slowly away. After this has occurred, the spectrum should show only the GdO peaks and possibly small peaks ($\leq$10 mV) at masses 134, 138, 151, 153, and 155. During the course of the run, these small peaks, except possibly those due to Ba, should die away completely, and small peaks due to Gd will appear (Scan B, Fig. I-1). While waiting for the Ba to die, switch to the Faraday collector (10^{11} ohm resistor), find the field settings for the GdO peaks, focus the beam, and cycle the magnet several times through the steps corresponding

to the GdO peaks. For normal sample sizes ($\sim$ 400 ng of Gd), the intensity of the $^{160}Gd^{16}O$ peak should be $\sim$ 100 mV. A scan of the GdO mass region should show the peaks to be flat topped and symmetrical (Scan C, Fig. I-1). For a collector slit width of 25 mil, a detailed step scan over the peaks (Scans D and E, Fig. I-1) should show that to the limit of the beam stability and recorder resolution ($\leqslant 0.1\%$) there is no intensity change for $\geqslant 1.2$ gauss on either side to the center of the peak. Under actual operating conditions, the slit is normally opened to 30 mil and the field is controlled to 0.1 gauss.

If the Ba has died away, one is now ready to begin collecting data. Check the intensity of mass 138 with the multiplier. It should be less than 25 mV (10^4 gain, 10^9 ohm resistor) before data are taken, and in favorable cases, it will have dropped below 1 mV. If the Ba intensity does not die, it may be necessary to correct for the BaCl interference at mass 173. Return to the Faraday collector, and using mass 176 as the reference peak and an integration time of 1 sec. (2 sec. if the intensity is below 100 mV), collect 40 ratios for the major isotopes, ^{155}Gd - ^{160}Gd. Unless the intensity of the 176 peak is above $\sim$ 200 mV, do not take data on ^{152}Gd and ^{154}Gd. After $\sim$ 40 ratios have been collected, stop the data acquisition system, check the Ba intensity with the multiplier, recenter the peaks in the collector slit, and check the focus. Collect another 40 ratios. After $\sim$ 80 ratios have been obtained, the beam intensity can be increased by raising the filament temperature $\sim 10°$. Because the beam tends to decay with time, this increase may in effect only bring the intensity back up to an

Figure I-1

Mass spectrometer scans of the Gd mass region. In scan B, disregard the two peaks between masses 134 and 135. They are repeat sweeps over the 134 peak.

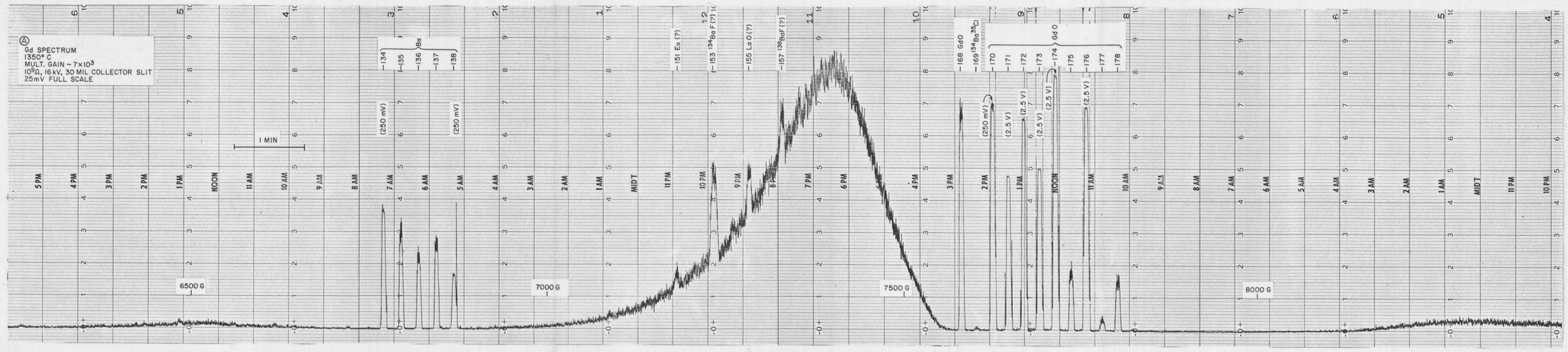
Ⓐ
Gd SPECTRUM
1350° C
MULT. GAIN ~ 7×10³
10⁹Ω, 16 kV, 30 MIL COLLECTOR SLIT
25 mV FULL SCALE
1 MIN
(250 mV)
(250 mV)
(2.5 V)
(2.5 V)
(2.5 V)
(2.5 V)
(2.5 V)
134 135 136 137 138 Ba
151 Eu (?)
153 134BaF (?)
155 La O (?)
157 138BaF (?)
168 GdO
169 134Ba35Cl
170 171 172 173 174 175 176 177 178 GdO
6500 G
7000 G
7500 G
8000 G

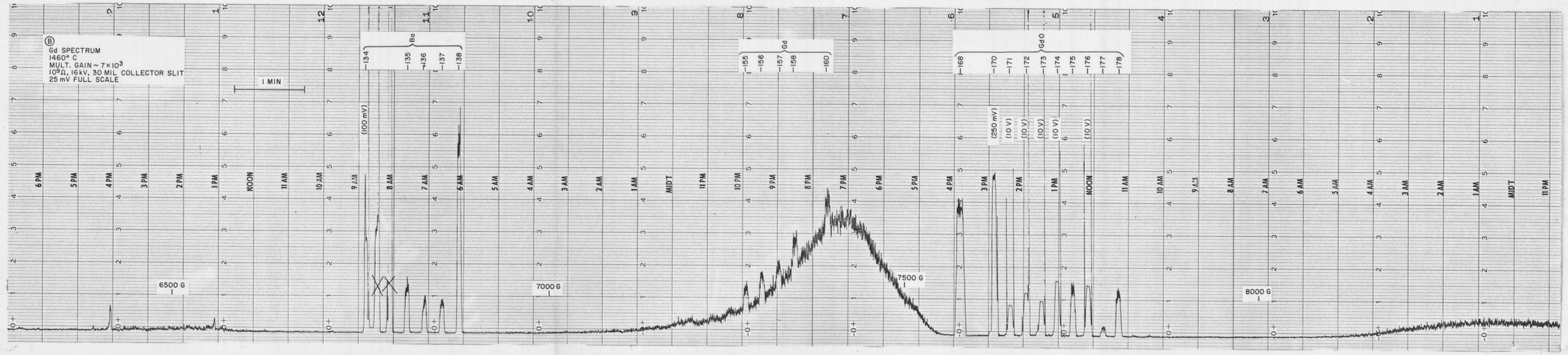
Ⓑ
Gd SPECTRUM
1460° C
MULT. GAIN ~ 7×10³
10⁹Ω, 16 kV, 30 MIL COLLECTOR SLIT
25 mV FULL SCALE
1 MIN
(100 mV)
134 135 136 137 138 Ba
155 156 157 158 160 Gd
168 170 171 172 173 174 175 176 177 178 GdO
(250 mV)
(10 V)
(10 V)
(10 V)
(10 V)
(10 V)
6500 G
7000 G
7500 G
8000 G

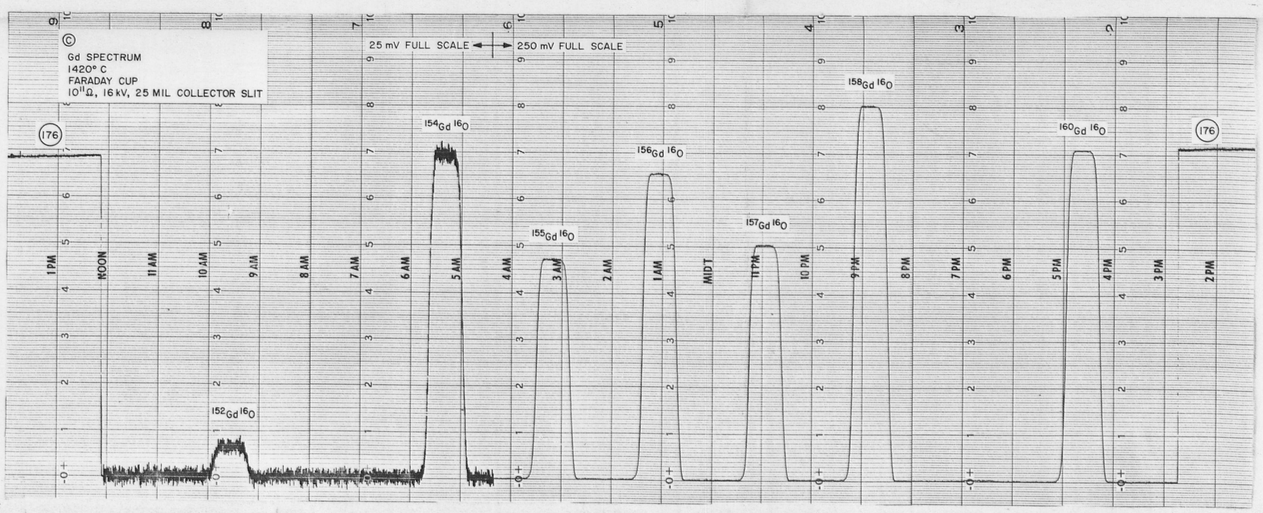
Ⓒ
Gd SPECTRUM
1420° C
FARADAY CUP
10¹¹Ω, 16 kV, 25 MIL COLLECTOR SLIT
25 mV FULL SCALE
250 mV FULL SCALE
176
152Gd 16O
154Gd 16O
155Gd 16O
156Gd 16O
157Gd 16O
158Gd 16O
160Gd 16O
176

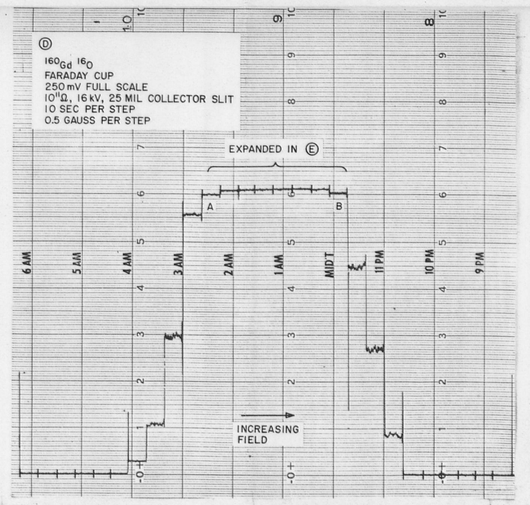
Ⓓ
160Gd 16O
FARADAY CUP
250 mV FULL SCALE
10¹¹Ω, 16 kV, 25 MIL COLLECTOR SLIT
10 SEC PER STEP
0.5 GAUSS PER STEP
EXPANDED IN Ⓔ
A
B
INCREASING FIELD

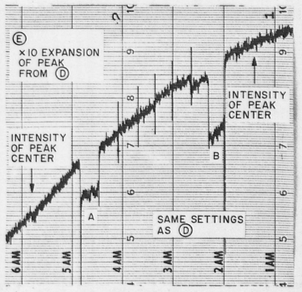
Ⓔ
×10 EXPANSION OF PEAK FROM Ⓓ
INTENSITY OF PEAK CENTER
INTENSITY OF PEAK CENTER
A
B
SAME SETTINGS AS Ⓓ

earlier level. Do not increase the temperature so rapidly that the Gd is burned off before enough data are collected. Do not exceed 1450°C! Above this temperature the beam becomes unstable. Continue taking data in blocks of 30-40 mass scans each until at least 200 scans have been made. In a typical analysis one should make ~ 240 scans. It should now be possible to use the multiplier to measure the $^{152}Gd/^{160}Gd$ and $^{154}Gd/^{160}Gd$ ratios. Remember to also measure ^{156}Gd, which is used for normalization (see Sec. 2.3). In analyses where the intensity of the $^{160}Gd^{16}O$ peak exceeds ~ 200 mV, the minor isotopes can be measured along with the major ones. This eliminates the need of using the multiplier.

The data are screened for beam stability, normalized, and averaged as described in Section 2.3.

I.2.2 Samarium

The filament used for Sm differs from that used for Gd in that it is bent along its long axis to form a V or trough with an angular opening of ~ 45°. This V is ~ $\frac{1}{4}$ inch long. At the ends of the V the ribbon is crimped nearly shut. Outside the crimps the ribbon is flattened and welded to covars. As in the Gd case, the filament is made of zone refined Re, but in this case, it need not be able to withstand oxidation. The filament is mounted and outgassed in the manner described for Gd.

The outgassed filament is mounted in a jig which allows electrical current to be passed through it, and this setup is placed under a low power binocular microscope. Using the pipette control described

above and hypodermic needles of the appropriate sizes, clean a 2-in. piece of P.E. 60 tubing and a 1-in. segment of P.E. 10 (0.011 in. I.D.) tubing which has had the end cut on an angle of $\sim 60°$ such that when the pipette control is held nearly horizontally, the natural curvature of the tubing will cause the opening to also be essentially horizontal. Drawing in and expelling $4N$ HCl three times is sufficient cleaning. Take care with the finer tubing or acid will be sucked into the needle. If this happens, throw away the tube and needle and start over. Also be sure that the finer tubing is not cut by the needle. This will result in one's being unable to expel the sample from the tubing.

Draw up between 1 and 2 mm of H_2O or dilute HCl in the P.E. 60 tubing and drop it into the sample beaker. Do not touch the tubing to the beaker because the clean tubing will be used again later. Attach the finer needle and tubing to the pipette control. Use the tubing to mix the drop of liquid with the sample; then draw up a small amount, 1-2 mm, of solution into the tube. Under the binocular microscope, touch the tubing to the center of the V, and transfer as little liquid as possible to the V. (Hold the pipette control parallel to the length of the V.) This is done because the liquid tends to spread along the length of the V and collect in the crimps at the ends. Such loads tend to give poorer peak shapes than those concentrated in the center of the trough. If the tubing was cut on an angle as described above, the tip can often be used to hold the liquid and reduce spreading. Evaporate the solution in the V by passing a current of $\sim \frac{1}{2}$ amp through the filament. Repeat this procedure until the desired quantity of sample

has been loaded. Patience is a must in this operation. Don't try to load a large drop. It will surely spread. If the sample does run into the crimps at the end of the V, it is not necessarily a disaster, but it may be difficult to focus the beam in the mass spectrometer. After the sample is loaded, slowly heat the filament by increasing the current until the organic residue burns off. Keep increasing the temperature until the filament starts to glow, but do not keep it at this temperature for more than a few seconds. Turn off the filament current.

The next step is to add Re powder to the filament. A supply of Re powder (-325 mesh, Electronic Space Products) can be stored under H_2O in a plastic, conical-bottom vial. Put the larger needle and tubing back on the pipette control, and draw up ~ 2 mm of Re powder. This mixture of powder and water can be expelled into the sample beaker, and some of the water can be drawn off and discarded. Draw the powder, now in a smaller drop, back into the tubing, and drop it in the V. It is usually helpful to do this in two small drops rather than one large one. Try to drop the powder only <u>inside</u> the V. A tungsten carbide needle, which is cleaned between uses by rubbing with Kimwipes and by streams of 4 *N* HCl and H_2O from squirt bottles, is used to spread the Re powder evenly throughout the V. The water can then be evaporated by heating with a current of ~ $\frac{1}{2}$ amp. Put a drop of 0.5 *N* H_3PO_4 in the sample beaker, and draw a few mm of the acid into the tubing (P.E. 60). Touch the tubing to the outside of one end of the V and expel enough acid to fill the V. This acid will run through the crimp into the V and tend to wash anything trapped in the crimp into the V. Use the tungsten

carbide needle to smooth the powder, and let the mixture dry without heating. Add more H_3PO_4 from the opposite end, and again redistribute the powder evenly. This time heat the filament with a current of $\frac{1}{2}$ amp. Fill the V with H_3PO_4 a third time, smooth the powder carefully, and evaporate the acid with a $\frac{1}{2}$ amp. current. When the powder appears to be dry, slowly increase the current until the powder starts to glow. Turn off the current. The filament can now be loaded into the mass spectrometer and baked overnight. Historically and arbitrarily a current of 1.4 amps has been used ($\sim$ 900°C), but this could probably be increased to $\sim$ 1100° or even higher without appreciable loss of sample.

Turn on the mass spectrometer, and locate mass 168 ($^{152}Sm^{16}O$) on the multiplier. If no signal is present, slowly increase the filament current until a beam appears. Scan the field to be sure it is set for SmO. Focus the beam, and locate masses 152 and 138 (^{152}Sm and ^{138}Ba). Continue to slowly increase the temperature, changing the 168 intensity $\sim$ 10% with each increase. If the signal *grows* without changing the temperature, let it. Below a temperature of $\sim$ 1250°C, the SmO beam will be at least a factor of 10 more intense than the Sm beam, and a scan of the mass region will show many small peaks. This is normal. When the beam at mass 168 exceeds the operational range of the multiplier switch to the Faraday collector (10^{11} ohm resistor). At this stage, it is unlikely that a peak will be resolvable with the Faraday collector at mass 152. Keep increasing the temperature until it appears. When the 152 signal is a few mV, it will tend to grow slowly without the temperature being increased. Three or four hours should have elapsed

since the run was started; so this is a good place to break for lunch. After returning, continue to increase the temperature. A 10% change every few minutes should be sufficient. About the time the Sm signal begins to grow, the Ba signal will also start growing. Monitor it from time to time. At this stage, the ratio of SmO to Sm should start to decrease. Monitor the intensities of masses 168, 152, and 138. When the SmO beam reaches an intensity of $\sim$ 200 mV, it is a good idea to start thinking about the peak shape. On the Lunatic III, the peaks tend to have shoulders which must be suppressed by focusing. Preliminary focusing should be done now on the SmO beam to avoid wasting time and Sm^+ ions. No set procedure can be given for obtaining good peak shapes. Try changing the differential voltage between the halves of the two sets of focusing plates. With patience a good peak shape can usually be obtained. (Write down the various trial settings. Often subtle changes in the focusing makes a great difference in the peak shape.) By the time the temperature reaches $\sim$ 1320°, the SmO/Sm ratio should be down to $\sim$ 2. A scan of the mass region 130-175 using the multiplier (Scan A, Fig. I-2) should reveal large peaks at the Ba, Sm, and SmO masses. (Be careful not to damage the multiplier with these large ion currents.) Eu signals will probably be observed at masses 151 and 153, and at mass 155 a small peak, presumably LaO, may appear. At mass 173, a peak, which normally has about the same intensity as the $^{154}Sm^{18}O$ peak at mass 172, will be observed. This is presumably due to SmF. It is because of this peak that isotopic ratios are not measured for the SmO beam. No other peaks should be observed between masses 130

and 180, but the baseline will vary greatly because of ions which are reflected off of the walls of the mass spectrometer tube. These reflected ions are less important for the Faraday collector because it is shielded. A scan of the mass region using the Faraday collector (Scan B, Fig. I-2) should show only the Ba, Sm, SmO, and possibly Eu peaks.

When the SmO/Sm ratio decreases to ~ 2 or no later than ~ 1340°C, make the final focusing adjustments and adjust the field controls to center the Sm peaks in the collector slit. Check the peak shape. If the peaks are symmetrical with flat tops (Scan C, Fig. I-2), it is time to start taking data. For a slit width of 25 mil, the peak top should be flat to the limit of the stability of the beam and the resolution of the recorder (~ 0.05 - 0.1%) for 1 gauss on either side of the center of the peak (Scans D and E, Fig. I-2). If there is reason to suspect that the peak is not flat, a series of 10-20 step scans should be made in which the steps are ~ 0.4 gauss each and for which digital data are collected and averaged. This will accurately define the flatness of the peak top. As an added assurance that the total beam passes through the slit, it is normally opened to 30 mil. Before starting to collect data, check the ^{138}Ba intensity. It should be ~ 20 mV or less on the Faraday collector, and should decrease throughout the run -- hopefully to < 1 mV.

Using mass 154 as the reference peak, collect ~ 40 ratios of each of the other peaks to 154. Assuming the intensity of the 154 beam is > 100 mV, a one-second integration time is sufficient for all peaks. Unless the beam is unstable, it should be possible to collect data for all 7 isotopes on each scan. After ~ 40 scans, stop scanning, recenter

the peaks, and check the Ba intensity. If any change is made in the focusing conditions, recheck the peak shape. Collect another group of ~ 40 ratios. The temperature can be increased by ~ 10° between data-taking periods. It should be possible to reach an intensity of ~ 400 mV of 154 in a typical run with ~ 400 ng of Sm. Higher intensities may be obtained, but be careful not to exhaust the sample by overheating in an attempt to get a higher beam intensity. Collect ~ 300 ratios in all. If the beam is unstable, check whether or not some other element, *e.g.*, Ba, is varying rapidly in intensity. If so, try to wait until it dies out. If not, increasing the temperature may help, but because this may kill the sample, take data before increasing the temperature. Omitting the less important isotopes — 144, 148, and 152 — will speed data acquisition and thereby avoid some of the instability problem.

The data are processed as described in Section 6.2.3.

I.3 References

[1] F. Tera, O. Eugster, D. S. Burnett, and G. J. Wasserburg, Comparative study of Li, Na, K, Rb, Cs, Ca, Sr, and Ba abundances in achondrites and in Apollo 11 lunar samples, Proc. of the Apollo 11 Lunar Sci. Conf. 2 (Pergamon Press, 1970) 1637.

[2] O. Eugster, F. Tera, D. S. Burnett, and G. J. Wasserburg, Isotopic composition of gadolinium and neutron-capture effects in some meteorites, J. Geophys. Res. 75 (1970) 2753.

Figure I-2

Mass spectrometer scans of the Sm mass region.

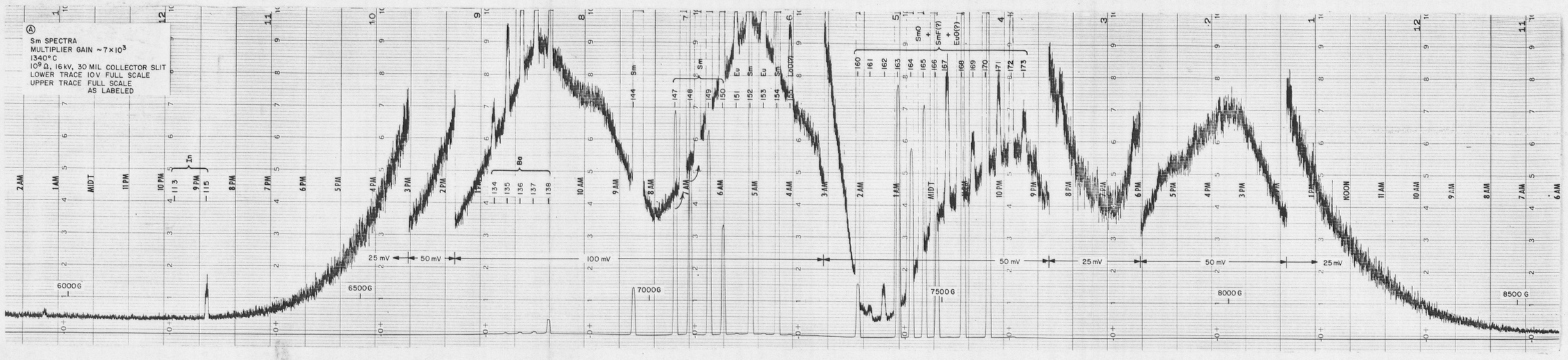
A
Sm SPECTRA
MULTIPLIER GAIN ~7×10³
1340° C
10⁹ Ω, 16 kV, 30 MIL COLLECTOR SLIT
LOWER TRACE 10 V FULL SCALE
UPPER TRACE FULL SCALE
AS LABELED
In
Ba
Sm
Eu
LaO(?)
SmO + SmF(?) + EuO(?)
25 mV
50 mV
100 mV
50 mV
25 mV
50 mV
25 mV
6000 G
6500 G
7000 G
7500 G
8000 G
8500 G

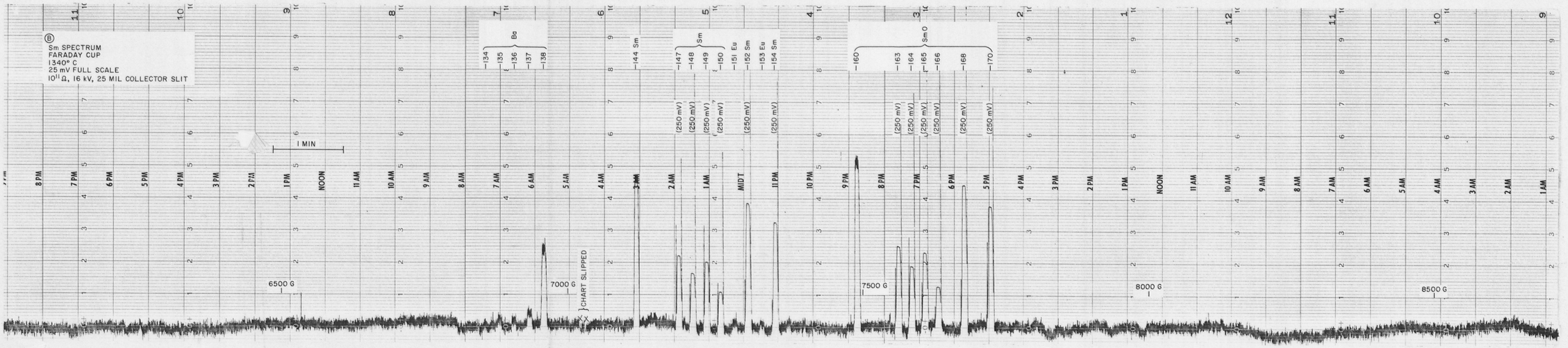
B
Sm SPECTRUM
FARADAY CUP
1340° C
25 mV FULL SCALE
10¹¹ Ω, 16 kV, 25 MIL COLLECTOR SLIT
1 MIN
Ba
Sm
Eu
SmO
6500 G
7000 G
CHART SLIPPED
7500 G
8000 G
8500 G

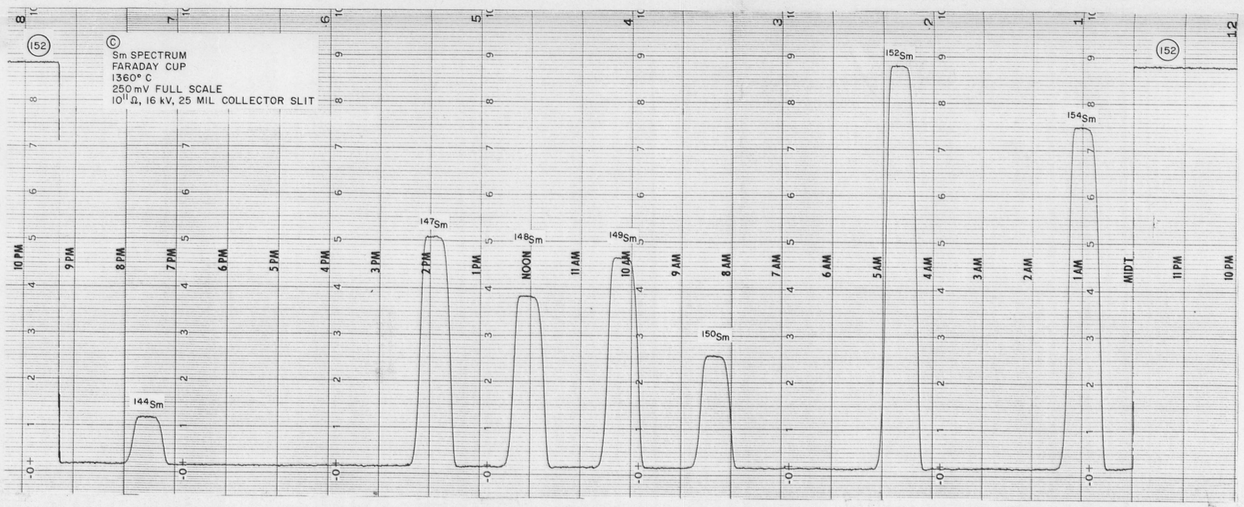
C
Sm SPECTRUM
FARADAY CUP
1360° C
250 mV FULL SCALE
10¹¹ Ω, 16 kV, 25 MIL COLLECTOR SLIT
144Sm
147Sm
148Sm
149Sm
150Sm
152Sm
154Sm

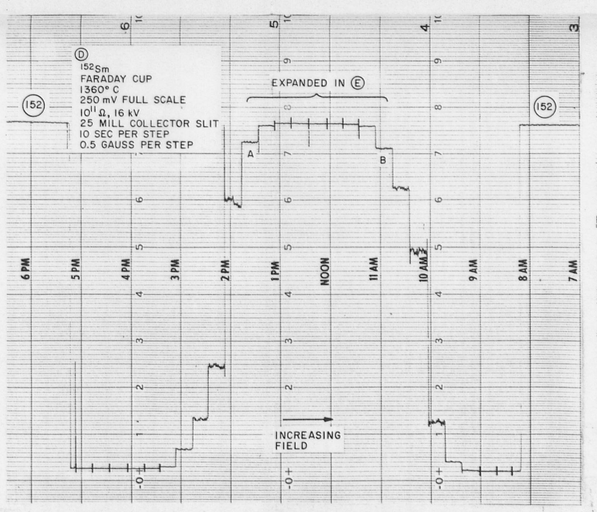
D
152Sm
FARADAY CUP
1360° C
250 mV FULL SCALE
10¹¹ Ω, 16 kV
25 MILL COLLECTOR SLIT
10 SEC PER STEP
0.5 GAUSS PER STEP
EXPANDED IN E
A
B
INCREASING FIELD

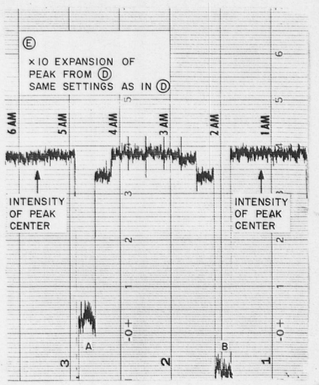
E
×10 EXPANSION OF PEAK FROM D
SAME SETTINGS AS IN D
INTENSITY OF PEAK CENTER
INTENSITY OF PEAK CENTER
A
B

Appendix II

The Breit-Wigner Formula for (n,γ) Reactions

As discussed in Section 4.1, several representations of the Breit-Wigner formula for single level capture are commonly used. Because the terms used in these various representations are often not clearly defined, confusion can result when numerical calculations are performed. In this appendix, the form derived in the text of Weinberg and Wigner [1] will be assumed and other equivalent representations will be derived from it. The neutron capture cross section, $\sigma_{n\gamma}(E)$, is

$$\sigma_{n\gamma}(E) = \frac{g\lambda^2}{4\pi} \cdot \frac{\Gamma_n(E)\Gamma_\gamma}{[(E-E_o)^2+(\Gamma/2)^2]}$$

where g is a statistical factor, λ is the de Broglie wavelength of the neutron, E is the energy of the neutron, E_o is the resonance energy, $\Gamma_n(E)$ is the neutron width, *i.e.*, the probability of re-emission of the neutron, which is a function of energy, Γ_γ is the probability of the γ-ray being ejected, and Γ is the sum of the partial widths; *i.e.*, $\Gamma = \Gamma_n(E) + \Gamma_\gamma \ldots$. Because $\Gamma_n(E)$ varies as $E^{\frac{1}{2}}$, one can define the reduced width Γ_n^o as $\Gamma_n^o \equiv \Gamma_n(\text{at } E)/E^{\frac{1}{2}}$ and $\sigma_{n\gamma}(E)$ can be written as

$$\sigma_{n\gamma}(E) = \frac{g\lambda^2}{4\pi} \cdot \frac{E^{\frac{1}{2}}\Gamma_n^o\Gamma_\gamma}{[(E-E_o)^2+(\Gamma/2)^2]}$$

Similarly, the neutron width at E_o can be expressed as $\Gamma_n^{E_o} = E_o^{\frac{1}{2}}\Gamma_n^o$ which gives

$$\sigma_{n\gamma}(E) = \frac{g\lambda^2}{4\pi} \cdot \frac{E^{\frac{1}{2}}}{E_o} \cdot \frac{\Gamma_n^{E_o}\Gamma_\gamma}{[(E-E_o)^2+(\Gamma/2)^2]}$$

Because λ is proportional to $E^{\frac{1}{2}}$, this equation can be written as

$$\sigma_{n\gamma}(E) = \frac{g\lambda\lambda_o}{4\pi} \cdot \frac{\Gamma_n^{E_o}\Gamma_\gamma}{[(E-E_o)^2+(\Gamma/2)^2]}$$

where λ_o is the de Broglie wavelength of a neutron at the resonance energy. Again, using the fact that λ/λ_o is equal to $(E_o/E)^{\frac{1}{2}}$, one can write

$$\sigma_{n\gamma}(E) = \frac{g\lambda_o^2}{4\pi} \cdot \left(\frac{E_o}{E}\right)^{\frac{1}{2}} \cdot \frac{\Gamma_n^{E_o}\Gamma_\gamma}{[(E-E_o)^2+(\Gamma/2)^2]}$$

The confusion about these forms arises from the fact that $\Gamma_n^{E_o}$ and $\Gamma_n(E)$ are both frequently written as Γ_n.

It is sometimes convenient to describe a cross section in terms of its value at the resonance energy, σ_o. From the above equations, it follows that

$$\sigma_{n\gamma}(E) = \frac{\sigma_o}{1+4(E-E_o)^2\Gamma^2} \left(\frac{E_o}{E}\right)^{\frac{1}{2}}$$

Note that when $E \ll E_o$, $\sigma_{n\gamma}(E)$ is proportional to $E^{-\frac{1}{2}}$ or $1/V$.

References

[1] Alvin M. Weinberg and Eugene P. Wigner, The Physical Theory of Neutron Chain Reactors, The University of Chicago Press (1958) 41.

Appendix III

Production Rate of Spallogenic ^{126}Xe

In order to estimate irradiation depths from the ratio of the spallation produced ^{126}Xe concentration to the neutron fluence, one must first calculate the depth dependence of the ^{126}Xe production function and the absolute production rate of ^{126}Xe. Reedy and Arnold [1] have calculated the flux of cosmic ray particles as a function of energy and depth in the regolith. Burnett [2] has estimated the energy dependence of the cross section for the production of ^{126}Xe from Ba by analogy to the ^{127}I to $^{116-118}Te$ cross sections. Burnett and Malin [3] have integrated the flux and cross section to obtain the depth dependence for ^{126}Xe production (see Fig. 5-3). This curve is similar to the Reedy and Arnold [1] curve for the production of ^{48}V from Fe except that this one has more buildup from the surface to the peak due to secondary particles than the ^{48}V curve. The exact depth dependence of the production curve depends on the variation of the cross section with energy which is not well known. The Burnett-Malin curve will be adopted for this work. The absolute production rate can be estimated by normalizing the curve at the surface to the measured ^{126}Xe production rate for rock 10049 which appears to have been irradiated only at the lunar surface [4].

The exposure age of this rock can be calculated from the spallogenic ^{21}Ne concentration [5] and the ^{21}Ne production rate calculated from the ^{22}Na activity [2]. Using this age, which is calculated to be 24.5 my, the spallogenic ^{126}Xe concentration [6], and the target element

concentrations [7], which can be expressed as Ba + 1.65Ce according to the systematics of Huneke *et al.* [4], the surface production rate of ^{126}Xe from Ba is calculated to be 8.1×10^{-10} cc(STP)·my^{-1}·g^{-1}(Ba).

Alternatively, a surface production rate can be calculated for rock 14306. This sample has a low exposure age and is probably a rock ejected from Cone Crater which has only been exposed on the surface. Ragan [8] has measured the ^{81}Kr-Kr age and Xe concentration in two portions of this breccia. If one assumes that all of the ^{132}Xe is trapped solar wind gas, one can calculate the maximum effect of the solar wind on the ^{126}Xe concentration. This effect is less than 2%, so it will be assumed that all the measured ^{126}Xe was produced by spallation. For the two samples analyzed by Ragan [8] (one light and one dark), the calculated ^{126}Xe production rates are 7.3 and 6.7×10^{-10} cc·my^{-1}·g^{-1}(Ba). The Ba and Ce concentrations used in this calculation were taken from Taylor [9] who also analyzed both light and dark samples.

For the meteorite Bruderheim, Marti, Eberhardt, and Geiss [10] calculated a production rate of 1.2×10^{-9} cc·my^{-1}·g^{-1}(Ba). Because a small rock on the lunar surface is shielded by the mass of the moon, it is exposed to roughly half of the cosmic ray flux to which a small meteoroid is exposed. The Bruderheim value therefore implies a lunar production rate of 6×10^{-10} cc·my^{-1}·g^{-1}(Ba), which is slightly lower than the estimates based on lunar rocks. This may reflect the greater probability of particles escaping from the meteoroid.

A theoretical estimate of the ^{126}Xe production rate can be made

for the cross sectional form assumed by Burnett [2]. If this cross section is normalized to the 730 MeV measurements of Funk, Podosek, and Rowe [11], one calculates a production rate of 4.1×10^{-10} cc·my^{-1}·g^{-1}(Ba).

In this work, the value calculated for rock 10049 has been used. Although this is the highest of the estimates, it is in reasonable agreement with the values calculated for rock 14306.

References

[1] R. C. Reedy and J. R. Arnold, Interaction of solar and galactic cosmic-ray particles with the moon, J. Geophys. Res. 77 (1972) 537.

[2] D. S. Burnett, personal communication.

[3] D. S. Burnett and M. C. Malin, personal communication.

[4] J. C. Huneke, F. A. Podosek, D. S. Burnett, and G. J. Wasserburg, Rare gas studies of the galactic cosmic ray irradiation history of lunar rocks, Geochim. Cosmochim. Acta 36 (1972) 269.

[5] H. Hintenberger, H. W. Weber, H. Voshage, H. Wänke, F. Begemann and F. Wlotzka, Concentrations and isotopic abundances of the rare gases, hydrogen and nitrogen in Apollo 11 lunar matter, Proc. Apollo 11 Lunar Sci. Conf. 2 (Pergamon Press, 1970) 1269.

[6] D. D. Bogard, J. G. Funkhauser, O. A. Schaeffer, and J. Zähringer, Noble gas abundances in lunar material-cosmic ray spallation products and radiation ages from the Sea of Tranquility and the Ocean of Storms, J. Geophys. Res. 76 (1971) 2757.

[7] P. W. Gast, N. J. Hubbard, and H. Wiesmann, Chemical composition and petrogenesis of basalts from Tranquillity Base, Proc. Apollo 11 Lunar Sci. Conf. 2 (Pergamon Press, (1970) 1143.

[8] Don Ragan, Apollo 14 Rare Gases; Pu-244 Xenon (Ph.D. Thesis, Washington Univ., 1972).

[9] S. R. Taylor, Maureen Raye, Patricia Muir, W. Nance, R. Rudowski, and N. Ware, Composition of the lunar uplands; chemistry of Apollo 14 samples from Fra Mauro, Proc. Third Lunar Sci. Conf. 2 (M.I.T. Press, 1972) 1231.

[10] K. Marti, P. Eberhardt, and J. Geiss, Spallation, fission, and neutron capture anomalies in meteoritic krypton and xenon, Z. Naturforschg. 21 (1966) 398.

[11] H. Funk, F. Podosek, and M. W. Rowe, Spallation yields of krypton and xenon from irradiation of strontium and barium with 730 MeV protons, Earth Planet. Sci. Letters 3 (1967) 193.

Proposition 1

Measurements of the ^{53}Mn activity in ureilites relative to that in other stony meteorites can be used to test the hypothesis that the ureilites come from orbits with perihelia appreciably less than 1 A.U.

The ureilites (named for the meteorite Novo Urei) form a rare, six membered group of stony meteorites which are part of the larger group called achondrites. Mineralogically the ureilites are predominantly olivene and clinopyropene in a carbonaceous matrix. They are distinct from other achondrites in having an appreciable iron-nickel phase and diamonds, which were presumably produced by impacts between meteoroids [1,2]. The ureilites are also distinct in that their measured $^{26}Al(t_{1/2} = 7 \times 10^5$ yr) activities are lower than predicted for meteorites with their chemical composition.

Fuse and Anders [3] have shown that for 71 chondrites the variation in the ratio of the measured ^{26}Al to that calculated for the appropriate chemical compositions, assuming saturation, was less than 30% and that only 7 chondrites have less than 80% of the calculated ^{26}Al activity. For the achondrites 7 of 19 meteorites had less than 80% of the calculated activity. The 2 ureilites measured fell in the group with low activity. The ^{26}Al measurements have been extended to the other ureilites by Cressy [4] and Wilkening, Herman and Anders [5] who have shown that only

Dyalpur with a ratio of observed ^{26}Al to calculated ^{26}Al of 0.90 ± 0.08 has close to the expected ^{26}Al activity. The other five ureilites have ratios between 0.63 and 0.77.

Although the production rate of ^{26}Al must be a function of the size of the meteoroid and depth within it, the measured ^{26}Al activities of random samples of stony meteorites and particularly chondrites do not seem to be strongly affected by depth and size. The calculations of Kohman and Bender [6] indicate that for stone meteorites with radii between ~25 and ~45cm the saturation ^{26}Al activity as a function of size and depth should vary by only ~20%.

Wilkening *et al.* [5] have argued that the low ^{26}Al activities of the ureilites can not be explained on the basis of insufficient cosmic ray exposure times for the ^{26}Al activity to reach saturation, shielding effects, errors in the calculated production rate, or errors in the experimental method. They conclude somewhat cautiously that the data can best be explained by *exotic* orbits for the ureilites. Assuming that the chondrites spend most of their cosmic ray exposure time at distances between 2 and 3.5 A.U. and that because of the effect of the solar magnetic field, the cosmic ray intensity decreases as one gets closer to the sun, Wilkening *et al.* [5] conclude that the orbits of the ureilites may have had perihelia less than 0.6 A.U. If this is the case, then as they point out, these meteorites may have experienced appreciable gas losses and their cosmic ray exposure ages may be higher than indicated by the measured ^{3}He and ^{21}Ne concentrations $\{0.1$ my (North Haig) - 19 my (Haverö)$\}$. On the other

hand, Fireman and Spannagel [7] have concluded from ^{37}Ar and ^{39}Ar data that Haverö's orbit over the last 1000 yr had a mean solar distance greater than that of the chondrites. This may, however, reflect only a recent perturbation of the orbit of this meteorite.

It is proposed that the activity of ^{53}Mn ($t_{\frac{1}{2}} = 3.7 \times 10^6$ yr [8]) be measured in the ureilites and representative chondrites by the neutron activation technique. The chondrites should be selected from those having typical ^{26}Al activities and exposure ages of at least 15 my. The latter requirement is necessary to insure that the ^{53}Mn activity has had ample time to approach saturation (>95%). Such a study would be interesting for several reasons. (1) It would establish whether the ^{53}Mn activity in the chondrites is tightly grouped as is the case with ^{26}Al. (The calculations of Kohman and Bender [6] imply that stony meteorites with radii between ~20 and ~70 cm the ^{53}Mn production rate should vary by only ~20% except in the upper ~10 cm.) (2) Over a wider range in size, the relative ^{53}Mn and ^{26}Al activities could be used to indicate the pre-atmospheric sizes of meteorites. (3) If the ^{53}Mn activities of the ureilites are lower than those of the chondrites, by the same fraction as the ^{26}Al activities, it would support the suggestion that the ureilites have spent most of their exposure time in orbits where the galactic cosmic rays are more excluded than along the orbits of the chondrites. (4) If the fractional undersaturation of ^{53}Mn in the ureilites is greater than that of ^{26}Al with respect to the chondrites and this effect can not be attributed to size differences, the recent cosmic-

ray exposure period would have to be short (~10^6 yr) and could be determined from the ^{53}Mn to ^{26}Al ratio. The presence of rare gas concentrations which could not be developed in this period would indicate a prior period of irradiation. (5) Because Mn is not volatile and because the saturation time of ^{53}Mn is long compared to the exposure ages of 4 of the ureilites as measured by ^{3}He and ^{21}Ne a correlation or the lack of one between ^{53}Mn and ^{3}He or ^{21}Ne would be evidence against or for gas loss by these meteorites. Such a loss might be expected for meteoroids traveling near the sun.

The neutron activation method of counting the ^{53}Mn activity was suggested by Millard [9] as a way to avoid the difficulties associated with counting the low energy X-rays associated with the decay of ^{53}Mn. This method, which has been developed in the laboratories of Herr [10-15], Arnold [16-18] and Honda [19], involves chemically separating Mn from a sample, irradiating the Mn with thermal neutrons (fluences ~10^{19} n/cm^2), and counting the ^{54}Mn ($t_{\frac{1}{2}}$ = 313 days) produced by the reaction ^{53}Mn(n,γ)^{54}Mn. The activity of ^{54}Mn is easier to count than the X-rays from ^{53}Mn and the disintegration rate for ^{54}Mn can be increased by ~6 x 10^3 relative to that for ^{53}Mn. This technique and direct counting of ^{53}Mn have been used to study iron meteorites [18-25], lunar samples [13-18] and a few stony meteorites [22,24,26]. However, little of the published data is readily applicable to this work because of the differences in shielding of the various iron meteorites and lunar samples.

^{53}Mn is produced only by the reactions $Fe(p,2p\chi n)^{53}Mn$ and $Fe(n,p\chi n)^{53}Mn$ [18] whereas ^{26}Al is produced from Mg, Al, Si, S, Ca, and Fe [3]. For this reason, the ^{53}Mn data are simpler to interpret than those for ^{26}Al. The only significant interferences in the activation technique arise from the reactions $^{55}Mn(n,2n)^{54}Mn$ and $^{54}Fe(n,p)^{54}Mn$. The first interference can accurately be taken into account by irradiating standards and by selecting phases rich in Fe relative to Mn. If the chemical separation is good, the $^{54}Fe(n,p)^{54}Mn$ reaction also presents no problem. Of course, the natural ^{54}Mn activity produced by cosmic rays must be taken into account for recently recovered samples.

Although it is necessary to destroy the sample in the ^{53}Mn activation method while ^{26}Al can be counted non-destructively, the high sensitivity afforded by the activation should allow better than $\pm$5% data to be obtained for 0.5g samples of the ureilites. In that the smallest ureilite - Dingo Pup Donga - has a recovered mass of 123g [1], samples of sufficient size for analysis should be obtainable.

References

[1] G. P. Vdovkin, Ureilites, Space Sci. Rev. 10 (1970) 483.

[2] Brian Mason, Meteorites (John Wiley and Sons, Inc., 1962) chapter 7.

[3] Kiyano Fuse and Edward Anders, Aluminum-26 in meteorites-VI. Achondrites, Geochim. Cosmochim. Acta 33 (1969) 653.

[4] P. J. Cressy, Jr., Cosmogenic radionuclides in the Haverö meteorite, Meteoritics 7 (1972) 533.

[5] Laurel L. Wilkening, Gerald F. Herman, and Edward Anders, Aluminum-26 in meteorites-VII. Ureilites, their unique radiation history, Geochim. Cosmochim. Acta 37 (1973) 1803.

[6] Truman P. Kohman and Michael L. Bender, Nuclide production by cosmic rays in meteorites and on the moon, High-Energy Nuclear Reactions in Astrophysics - B.S.P. Shen (ed.) (W. A. Benjamin, Inc., 1967) 169.

[7] E. L. Fireman and G. Spannagel, Argon-37, argon-39, and tritium radioactivities in the Haverö meteorite, Meteoritics 7 (1972) 559.

[8] Masatake Honda and Mineo Imamura, Half-life of Mn^{53}, Phys. Rev. C. 4 (1971) 1182.

[9] H. T. Millard, Jr., Thermal neutron activation: Measurement of cross section for manganese-53, Science 147 (1965) 503.

[10] U. Herpers, W. Herr and R. Woelfe, Determination of cosmic ray produced nuclides ^{53}Mn, ^{45}Sc, and ^{26}Al in meteorites by neutron activation and gamma coincidence spectroscopy, Radioactive Dating and Methods of Low-Level Counting (Int. At. Energy Agency, 1967) 199.

[11] U. Herpers, W. Herr and R. Woelfe, Evaluation of ^{53}Mn by (n,γ) activation, ^{26}Al, and special trace elements in meteorites by γ-coincidence techniques, Meteorite Research - P. M. Millman (ed.) (Int. At. Energy Agency, 1969) 387.

[12] W. Herr, U. Herpers, and R. Woelfe, Die Bestimmung von ^{53}Mn, welches in meteoritischen Material durch komische Strahlung erzeugt wurde, mit Hilfe der Neutronenaktivierung, J. Radioanal. Chem 2 (1969) 197.

[13] W. Herr, U. Herpers, B. Hess, B. Skerra, and R. Woelfe, Determination of manganese-53 by neutron activation and other miscellaneous studies on lunar dust, Proc. Apollo 11 Lunar Sci. Conf. 2 (Pergamon Press, 1970) 1233.

[14] W. Herr, U. Herpers, and R. Woelfe, Spallogenic ^{53}Mn ($T \sim 2 \times 10^6$ yr) in lunar surface material by neutron activation, Proc. Second Lunar Sci. Conf. 2 (MIT Press, 1971) 1797.

[15] W. Herr, U. Herpers, and R. Woelfe, Study on the cosmic ray produced long-lived Mn-53 in Apollo 14 samples, Proc. Third Lunar Sci. Conf. 2 (MIT Press, 1972) 1763.

[16] R. C. Finkel, J. R. Arnold, M. Imamura, R. C. Reedy, J. S. Fruchter, H. H. Loosli, J. C. Evans, A. C. Delany, and J. P. Shedlovsky, Depth variation of cosmogenic nuclides in a lunar surface rock and lunar soil, Proc. Second Lunar Sci. Conf. 2 (MIT Press, 1971) 1773.

[17] M. Wahlen, M. Honda, M. Imamura, J. S. Fruchter, R. C. Finkel, C. P. Kohl, J. R. Arnold, and R. C. Reedy, Cosmogenic nuclides

in football-sized rocks, Proc. Third Lunar Sci. Conf. 2 (MIT Press, 1972) 1719.

[18] M. Imamura, R. C. Finkel, M. Wahlen, Depth profile of ^{53}Mn in the lunar surface, Earth Planet. Sci. Letters 20 (1973) in press.

[19] M. Imamura, H. Matsuda, K. Horie and M. Honda, Applications of neutron activation method for ^{53}Mn in meteoritic iron, Earth Planet. Sci. Letters 6 (1969) 165.

[20] J. P. Shedlovsky, Cosmic-ray produced manganese-53 in iron meteorites, Geochim. Cosmochim. Acta 21 (1960) 156.

[21] M. Honda, J. P. Shedlovsky, and J. R. Arnold, Radioactive species produced by cosmic rays in iron meteorites, Geochim. Cosmochim. Acta 22 (1961) 133.

[22] Masatake Honda and James R. Arnold, Effects of cosmic rays on meteorites, Science 143 (1964) 203.

[23] J. H. Kaye, Cosmogenic X-Ray and β-Ray Emitters in Iron Meteorites (Ph.D. Thesis, Carnegie Inst. Tech., 1963).

[24] J. H. Kaye and P. J. Cressy, Half-life of manganese-53 from meteorite observations, J. Inorg. Nucl. Chem. 27 (1965) 1889.

[26] P. J. Cressy, Cosmogenic Radionuclides in Stone Meteorites (Ph.D. Thesis, Carnegie Inst. Tech., 1964).

Proposition 2

It is proposed that the evolution of bryozans be studied by isolating and at least partially sequencing cytochromes c from representative species of the extant orders of Bryozoa.

The phylum Bryozoa (or Polyzoa or less properly Ectoprocta) is composed of abundant small (mm size) sessile, colonial organisms with unsegmented bodies and a tentacle-bearing structure (lophophore) for feeding [1,2]. The individual animal or zooid resembles a coelenterate in having a saclike body, which may be calcified, and tentacles; however, bryozoans are more advanced. They have a digestive system with a mouth located inside the circle of tentacles, an esophagus, a stomach, an intestine, and an anus located outside the tentacles. The tentacles can be retracted by muscles and other muscles may be present. Bryozoans have a nerve ganglion and in general are bisexual. They have no vascular or excretory systems. Respiration is probably accomplished by diffusion. Bryozoans are found at all latitudes and from intertidal zones to depths of at least 5,500 m. Of the ~1200 genera which have been described ~450 are extant (~4000 species). In spite of their abundance bryozoans have been studied relatively little because of their small size.

Although earlier workers included bryozoans, brachiopods, endoprocts, and other rare animals in a single phylum, Molluscoidea,

these groups are now generally considered to be separate phyla. The bryozoans are divided into classes and orders on the basis to their structure. The classification scheme based on detailed studies of structural differences given by Ryland [2] recognizes three classes. (1) Phylactolaemata. These are non-calcareous, freshwater forms which lack mineralized tissues. Members of this class are unknown in the fossil record. (2) Stenolaemata. These are marine organisms which are calcified. Only the order Cyclostomata for which examples are known from the Paleozoic is extant. Three orders - Cystoporata, Trepostomata, and Cryptostomata - are restricted to the Paleozoic. (3) Gymnolaemata. This class consists of two orders both of which are extant. The Ctenostomata which live in brackish or fresh water are not calcified but are known in the fossil record back to the Paleozoic. The Cheilostomata are marine forms with calcified walls. They are known only since the Mesozoic but are by far the most common forms today.

The Ctenostomata, Cyclostomata, Trepostomata, and Cryptostomata first appear in the fossil record during the Ordovician period (~450 my ago) as fully separated orders. The fossil record gives no evidence for the separation of the various orders from each other (or from the brachiods and endoprocts). Although only one of the four extant orders is known from the Ordovician, it is generally considered that all of the bryozoan classes and orders differentiated at least as long ago as the early Ordovician.

Schopf and Manheim [3] have attempted to classify bryozoan

species on the basis of chemical composition. For 32 species, they have defined three groups. They describe these groups as follows:

> Group I consists of genera that have more than 50 percent organic matter (dry weight). It includes all species of the entirely freshwater Phylactolaemata and the commonly brackish-water and freshwater Ctenostomata. Group II includes Cheilostomata having from 25 to 50 percent organic matter (dry weight). These genera are bush-like in growth habit and may be anchored to fine-grained sediment bottoms. Genera in Group II contain appreciable amounts of P_2O_5 (1.0-2.0 percent) and Fe_2O_3 (0.4-1.0 percent) in the ash. Only calcite has been observed in the mineralized portion of the skeleton of Group II species. Group III includes Cheilostomata and Cyclostomata that have less than 25 percent organic matter. These forms require stable surfaces for colonization. They contain a lesser amount of P_2O_5 (0.1-0.6 percent) and of Fe_2O_3 (less than 0.4 percent) than Group II genera. About 15 percent of Group III species have aragonitic skeletons.

One sees immediately that this classification grouping does not follow that based on zooid structure; however, this does not necessarily mean that the structural classification is invalid.

Little is known about the biochemistry of the bryozoans. Schneider [4] showed that in the cuticle of a cheilostome, protein was 10 times more abundant than chitin, and Krishman and Rajulu [5] concluded that the cuticle protein is collagenous. The studies of Schopf and Manheim [3] support the conclusion of a low-chitin content. Morse [6] reported a phylactolaemate to be a rapidly growing source of non-collagen protein. Schopf and Manheim [3] measured the bulk concentrations of 28 amino acids in two cheilostomes and a cyclostome and found similar abundance patterns for the three samples. Stephens and Schinski [7] showed that a cheilostome removed large amounts of glycine from sea water but how glycine is incorporated by the zooids

is unknown. No organic compounds have been isolated from bryozoans.

The protein cytochrome c with 104-112 amino-acid residues is believed to be present in the mitochondria of every eucaryotic cell, *i.e.*, cell with a nucleus. It has been shown that cytochrome c can be isolated relatively easily (*e.g.*, [8]) and the complete amino acid sequence has been determined for over 40 species representing mammals, other vertebrates, insects, and lower and higher plants. These studies have shown that in 35 positions the same amino acid residues occur in all of the species analyzed while the sequences of the residues at the other positions vary among the species [9]. Between species the number of positions having different residues has been shown to be useful in constructing a phylogenetic tree [10] and the rate of change in the amino acid sequence has been estimated as 1% per 20 my [9]. Between samples of the various bryozoan orders, one would therefore expect differences at >20% of the positions along the cytochrome c chain.

It is proposed that an attempt be made to isolate cytochrome c from representative species of the extant orders of Bryozoa. If sufficient material can be isolated, it is proposed that the amino acid sequences be determined for these proteins. If only small amounts of cytochrome c can be isolated, more restricted studies can be undertaken which will still give valuable information about the evolution of the bryozoans. Such studies would be useful in establishing the phylogenetic relationship of the Bryozoa to other phyla, the relationship of the various orders and their time of

divergence, and the validity of current classification schemes based on zooid morphology.

The first step of this study would involve picking a single species from which to attempt a cytochrome c extraction. This organism should be abundant and one from which the organic material can be easily extracted. Because of their lack of calcification, it seems reasonable to pick either a ctenostomate, *e.g.*, a member of the genus Alcyomidium which is abundant in the North Sea [2] or a phylactolaemate, *e.g.*, a Pectinatella which Morse [6] describes as growing to a mass of ~5 kg in a few weeks. Assuming that the cytochrome c concentration in bryozoans is similar to that in oysters [11], *i.e.*, ~1 mg/kg (tissue) and that ~1% of the weight of a wet bryozoan is "tissue", it should be possible to collect and/or grow enough material {~100 kg (wet)} to attempt an isolation of the cytochrome c.

Margoliash and Schejter [8] have described an extraction procedure using aluminum sulfate, which can lead to "entirely native products", which could be used to extract the proteins from the tissue. Alternatively the $(NH_4)_2SO_4$ procedure employed by Yamanaka *et al.* [11] to isolate cytochrome c from oysters could be used. The affinity of cytochrome c for cation exchange resins, can then be utilized to concentrate the cytochrome c [8,11]. The concentrate can then be purified by ammonium sulfate fractionation and chromatography or repeated molecular exclusion and cation exchange separations.

The yield of the isolation studies from the test species will determine the practicality of proceeding to further studies. If bryozoans have high cytochrome c concentrations and it is feasible to obtain several hundred mg of pure product, then the complete sequence of the amino acid residues can be determined from tryptic and chymotryptic digests. By determining the sequences for members of each of the bryozoan orders and if possible for members of other phyla, *e.g.*, a brachiopod, it would be possible to establish the phylogenetic relationships of the bryozoan orders to each other, the times of their divergences, the relationship of the Bryozoa to other phyla, and to test the classification system normally used for bryozoans.

It may well be the case that it will be impractical to isolate more than ~10 mg of pure cytochrome c from a given species or genus. In this case more restrictive but still valuable experiments can be preformed. A determination of the amino acid content by hydrolysis and ion exchange separation would allow one to deduce the total length of the protein chain which varies among different groups of organisms and provide such information as how many methionines were present. (All vertebrates analyzed to date have two except primates which have three. Plants have two or three.) An Edman reaction would establish whether or not the NH_2 terminus is blocked as is the case with all organisms studied except insects and lower plants. A cyanogen bromide cleavage, which is specific for methionine, could be used to establish the number of methionines and the peptides from the

cleavage (excluding the NH_2 terminal peptide if it is blocked) could be isolated and at least partially sequenced by successive Edman reactions. Combination paper chromatography and electrophoresis could also be used to establish fingerprints for peptides produced by trypsin and chymotrypsin digestions. These fingerprints could be compared to those of known peptides which would give further information about the amino acid sequence of bryozoan cytochromes c. The number of such experiments which can be performed would of course depend on the amount of material available.

References

[1] Raymond C. Moore, Cecil G. Lalicker, and Alfred G. Fischer, Invertebrate Fossils (McGraw-Hill, 1952) chapter 5.

[2] J. S. Ryland, Bryozoans (Hutchinson and Co., 1970).

[3] Thomas J. M. Schopf and Frank T. Manheim, Chemical composition of ectoprocta (bryozoa), Jour. Paleontology 41 (1967) 1197.

[4] Dietrich Schneider, Normal and phototropic growth reactions in the marine bryozoan Bugula avicularia, The Lower Metoza - E. C. Dougherty, Z. N. Brown, E. D. Hanson, and W. D. Hartman (ed.) (Univ. of California Press, 1963) 357.

[5] G. Krishnan and G. Rajulu, Nature and composition of the cuticle of the Ectoproct Polyzoan Scrupocellaria bertholetti, Biol. Zentralbl. 84 (1965) 359.

[6] Withrow Morse, The chemical constitution of Pectinatella, Science 71 (1930) 265.

[7] G. C. Stephans and R. A. Schinski, Uptake of amino acids by marine invertebrates, Limnology and Oceanography 6 (1961) 175.

[8] E. Margoliash and A. Schejter, Cytochrome c, Adv. Prot. Chem. 21 (1966) 114.

[9] Richard E. Dickerson, The structure and history of an ancient protein, Sci. Am. 226 (April 1972) 58.
Richard E. Dickerson, The structure of cytochrome c and the rate of molecular evolution, J. Molec. Evolution 1 (1971) 26.

[10] E. Margoliash, W. M. Fitch, and R. E. Dickerson, Molecular expression of evolutionary phenomena in the primary and tertiary

structures of cytochrome c, Brook. Symp. Biol. 21 (1968) 259.

[11] T. Yamanaka, H. Mizushima, and K. Okunuki, Cytochrome c's purified from marine invertebrates, Biochim. Biophys. Acta 81 (1964) 223.

Proposition 3

It is proposed that the distribution of boron in plant cells be studied by the $^{10}B(n,\alpha)^{7}Li$ reaction.

Boron is one of ~16 elements which are known to be essential for the normal development of plants [1,2], and the effects of its defficiency are well documented [2]. Boron is unique in that within given species its acceptable range of concentration in the growing medium is narrow [1]. It is known to be able to help regulate carbohydrate metabolism by blocking the "pentose shunt" [3,4] and may regulate the translocation of sugars in plant tissue [5,6,7], but its exact role in plant biochemistry is not known. Boron has not been shown to be essential for animals.

The distribution of boron in tobacco plants has been studied by McIlrath and Skok [8] who analyzed various parts of the plants. They found that leaves contained more B than other parts, older leaves contained more B than younger ones, and that in stems the highest B levels occurred in the chlorophyllous cells. These authors also studied the distribution of B among cellular fractions separated from sunflower and mung bean tissue by the centrifugation of ground material [9]. These studies indicated that the boron concentration was higher in the nuclei, plastids and supernatant solution than in mitochondria and microsomes. Such studies suffer from the necessity of having to use relatively large quantities of material and having

to grind the material and extract the desired organelles.

It is proposed that the distribution of boron be studied *in situ* in thin sections of plant tissues by mapping the distribution of α recoil *tracks* produced in the reaction $^{10}B(n,\alpha)^{7}Li$. Such studies should reveal the distribution of boron within single cells and among various tissue types with a minimum of disturbance to the tissues. Profiles could also be made across single leaf or stem sections.

In this technique which as been used to study B in clam shells [10], cells are fixed and sectioned, the surface of the section is covered with a plastic sheet which serves as the track detector, the section and detector are irradiated with thermal neutrons, the detector is etched to develop the tracks cause by the α particle induced radiation damage in the plastic, the tracks are counted under an optical microscope, and the track distribution is compared to the cellular structure of the tissue section. The method is simple, highly sensitive, and precisely defines areas of boron accumulation. As noted by Skok and McIlrath [9], a knowledge of the distribution of boron among and within the organelles of the cells may not provide direct evidence for the precise role of boron in plant biochemistry, but it could contribute to a better understanding of the function of boron in plant cells.

In that there are some data for boron distribution in tobacco, sunflower and mung bean it might be reasonable to begin the study with specimens of one or more of these plants. In order to preserve the cell as nearly as possible in its normal state, it is necessary

to "fix" it. The procedure which would be most applicable to preserving the boron distribution would have to be determined experimentally but standard techniques like fixing with glutaraldehyde, freeze-drying, or freeze-substitution should be applicable. The fixed tissue could then be embedded in a methacrylate mixture or epoxy and sectioned. For determining the boron concentration in the larger organelles, *e.g.*, chloroplasts, the sections should be thick enough to act as "thick" boron targets, ~2μm; however, to determine the concentrations in organelles smaller than 2μm, *e.g.*, nuclei and mitochondria, relative to the large organelles thinner sections, ~0.5-1.0μm thick, may be desirable to avoid registering α particles from boron atoms beneath the organelle of interest.

For material with as little as 1 ppm B an irradiation with only 10^{12} thermal neutrons/cm^2 will produce a track density of ~10^3/cm^2 of detector. This track density is of the same magnitude as that expected for "background" reactions in the plastic and is roughly the lower limit of detection. (Larger neutron fluences would increase the ^{10}B and background track densities proportionately, but would improve the counting statistics.) The studies of McIlrath and Skok [8] indicate that even in the pith of the stem of tobacco plants, where the boron concentration was the lowest observed, a concentration of ~2.5 ppm can be expected. It is therefore reasonable to expect to be able to map the boron distribution by this technique providing the fixation step does not leach boron. The extent of leaching can be determined by analyzing the fixing solution. If it

should be desirable to increase the ^{10}B concentration without changing the total B level, the plants could be fed B enriched in ^{10}B. This could increase the sensitivity of the method by a factor of ~5.

The techniques for irradiation, etching the plastic detector and track counting are well developed [10] and directly applicable. Because the length of the tracks is short (<4μm) and because the direction of motion of the α particle which caused the track can be established from the track shape, the location of the B atoms which produced the α particle can be determined with approximately micrometer precision if the alignment of the sample and detector during irradiation is known. The alignment of these components can be established by putting small fiducial spots of boron on the target, pin holes, and/or the pattern of the α track map, *e.g.*, if boron were concentrated in mitochondria the distribution of high track density areas in the plastic would match the distribution of mitochondria on the target.

References

[1] Emanuel Epstein, Mineral Nutrition of Plants: Principles and Perspectives (John Wiley and Sons, 1972) chapter 11.

[2] E. J. Hewitt, The essential nutrient elements, requirements and interactions in plants, Plant Physiology - F. C. Steward (ed.) 3 (Academic Press, 1963) 137.

[3] James Bonner and J. E. Varner, The path of carbon in respiration metabolism, Plant Biochemistry - Bonner and Varner (ed.) (Academic Press, 1965) 213.

[4] S. Lee and S. Aronoff, Boron in plants: A biochemical role, Science 158 (1967) 798.

[5] H. G. Gauch and W. M. Dugger, Jr., The role of boron in the translocation of sucrose, Plant. Physiol. 28 (1953) 457.

[6] C. J. Weiser, L. T. Blaney, and P. Li, The question of boron and sugar translocation in plants, Physiol. Plantarum 17 (1964) 589.

[7] Kung-Woo Lee, Catherine M. Whittle and Herbert J. Dyer, Boron deficiency and translocation profiles in sunflower, Physiol. Plantarum 19 (1966) 919.

[8] Wayne J. McIlrath and John Skok, Distribution of boron in the tobacco plant, Physiol. Plantarum 17 (1964) 839.

[9] John Skok and Wayne J. McIlrath, Distribution of boron in cells of dicotyledonous plants in relation to growth, Plant. Physiol. 33 (1958) 428.

[10] D. S. Burnett and D. Woolum, personal communication.

Proposition 4

By measuring ^{87}Rb-^{87}Sr, ^{40}K-^{40}Ca, and ^{40}K-^{40}Ar ages of splits of the same mineral separates, indirect measurements of the half-life of ^{87}Rb and the branching ratio for ^{40}K decay can be obtained.

The rubidium-strontium method has been widely used for establishing relative ages of both terrestrial and extra-terrestrial rocks. There are however several limitations to determining absolute ages by this method. Two result from the uncertainties in the isotopic ratios measured for strontium and in the precision of the determination of the rubidium concentrations. The use of rapid digital data acquisition systems and imrpoved techniques for determining the rubidium concentration (*e.g.*, [1]) have reduced the significance of these limitations. A third and the largest limitation arises from the uncertainty of 6% in the half-life of ^{87}Rb.

The half-life of ^{87}Rb is difficult to measure because of the low energy (~275 keV) and unusual energy spectrum associated with its β^- decay. Aldrich, Wetherill, Tilton and Davis [2] determined the ^{87}Rb half-life to be $(5.0 \pm 0.2) \times 10^{10}$ yr by measuring the radiogenic strontium in mineral assemblages giving concordant U - Pb ages. This is the half-life generally used in Rb-Sr dating. By using the liquid scintillation method which eliminates the scattering and self-absorption corrections, Flynn and Glendenin [3] measured the

^{87}Rb half-life to be $(4.70 \pm 0.10) \times 10^{10}$ yr. McMullen, Fritze and Tomlinson [4] mass-spectrometrically measured the ^{87}Sr evolved in a mass of rubidium over a period of 7 years and found the ^{87}Rb half-life to be $(4.72 \pm 0.10) \times 10^{10}$ yr which is in good agreement with the counting experiments of Flynn and Glendenin [3]. The decay constants for ^{235}U and ^{238}U have recently been redetermined [5], but the revised values would only lower the ^{87}Rb half-life calculated by Aldrich *et al.* [2] by ~1%.

The importance of being able to determine absolute ages is that ages determined from different decay schemes could then be compared to establish whether certain chronometers are more reliable or record different types of metamorphic events. For instance the model age calculated for the moon from Rb-Sr data is 4.6×10^9 yr while that calculated from the U-Pb systematics is 4.5×10^9 yr [6]. This difference may relate to the early geologic history of the moon, which would be of great interest, or it could be simply an artifact of an error in the half-lives used.

An independent geological determination of the ^{87}Rb half-life can be obtained by measuring the amount of radiogenic ^{87}Sr and the decay products of ^{40}K from the same samples. Three types of ages can be determined for the products of ^{40}K decay. (1) The concentrations of ^{40}Ar and K can be determined and used to calculate an age, but because of the possibility of gas loss, this method is not highly accurate. (2) Samples can be irradiated with neutrons to make ^{39}Ar by the (n,p) reaction on ^{39}K. The Ar in the irradiated samples

can then be extracted in steps of increasing temperature and the $^{39}Ar/^{40}Ar$ ratio used to calculate the age of the sample. This method is based on the idea that the Ar released at low temperatures will be from sites most likely to have leaked gas while the Ar released at high temperatures should have originated in sites where leakage was negligible and should give the $^{39}Ar/^{40}Ar$ ratio appropriate for the age of the sample. This method has been widely used with lunar samples (*e.g.*, [7]). The results of these studies will be discussed below. (3) For samples with a sufficiently high K/Ca ratio, ^{40}K-^{40}Ca ages can be determined for the same sample used to determine the ^{87}Rb-^{87}Sr age. Measurements of the radiogenic ^{40}Ca in sylvite (KCl) were used by Inghram, Brown, Patterson, and Hess [8] to determine the branching ratio of ^{40}K, the potential of ^{40}K-^{40}Ca dating has been discussed (*e.g.*, [9]), and a few ^{40}K-^{40}Ca ages have been determined [10,11]; but the method has not been fully or widely exploited. This is largely because of the scarcity of potassium-rich, calcium-poor minerals and the fact that ^{40}Ca constitutes ~97% of all Ca while K is only 0.0118% ^{40}K. For comparative half-life studies, however, this method has the advantage of being applicable to the same sample grains used for ^{87}Rb-^{87}Sr dating, which eliminates problems of sample inhomogeneity.

The decay properties of ^{40}K have been summarized by Beckinsale and Gale [12] who urge the adoption of decay constants based on recent counting experiments. They recommend $(1.265 \pm 0.002) \times 10^9$ yr for the half-life and (89.5 ± 0.1)% for the ^{40}K-^{40}Ca branch

of the decay. These values are somewhat different from the commonly used values recommended by Wetherill [13] - $t_{\frac{1}{2}} = 1.31 \times 10^9$ yr and 89.0% for the ^{40}K-^{40}Ca branch. In that the values recommended by Beckinsale and Gale [12] are based on more recent counting experiments and in that Wetherill [13] presents no reason beyond convenience for maintaining the older values, it seems reasonable to adopt those of Beckinsale and Gale [12]. For ^{40}K-^{40}Ar ages, the use of the revised constants will raise the age of a 5 my old sample by 1% while lowering the age of a 4.5×10^9 yr old sample by 2%. For ^{40}K-^{40}Ca ages, the change in the branching ratio is relatively unimportant but the ages of all samples will be lowered by 3.4% because of the change in the half-life.

As noted above, the ^{40}Ar-^{39}Ar method has been widely used for dating lunar materials. In many cases ages were only determined relative to a sample of known age as determined by another method, but in other cases the necessary calibrations have been made so that precise ages can be determined without assuming the age of a standard. For those samples where such ^{40}Ar-^{39}Ar ages have been determined and for which ^{87}Rb-^{87}Sr ages have been measured, a comparison of these ages can be used to indicate whether or not the decay constants used are mutually compatible. For five samples from the Apollo 14 and 15 and Luna 16 missions for which both ^{40}Ar-^{39}Ar and ^{87}Rb-^{87}Sr ages have been measured in the Lunatic Asylum [1,7,14,15] the ages calculated by the two methods agree within 1% when the Aldrich *et al.* [2] half-life for ^{87}Rb and the Wetherill [13] decay

constants for ^{40}K are used. If the Beckinsale and Gale [12] decay constants for ^{40}K are used, a ^{87}Rb half-life of 4.9×10^{10} yr is implied. This value is between that based on physical determinations [3,4] and the value of Aldrich *et al.* [2]. Such a calculation of course assumes that the two "chronometers" were started simultaneously and that the systems have remained closed. In that argon is more likely to be lost from a rock than potassium, strontium or rubidium, the ^{87}Rb half-life inferred from such a comparison can be considered as a lower limit to the true half-life. Adopting 4.9×10^{10} yr as the ^{87}Rb half-life, would be sufficient to bring the ^{87}Rb-^{87}Sr and U-Pb model ages for the age of the moon into agreement.

Because the ^{40}K-^{40}Ca system does not involve gases and because ^{40}K-^{40}Ca and ^{87}Rb-^{87}Sr ages can be determined on the same sample, one would expect ^{40}K-^{40}Ca to more accurately define the time interval measured by ^{87}Rb-^{87}Sr than the ^{40}Ar-^{39}Ar technique. Russ (1970, unpublished) attempted to measure the ^{87}Rb-^{87}Sr and ^{40}K-^{40}Ca ages of potassium feldspar crystals isolated from the iron meteorite Colomera by Wasserburg, Sanz, and Bence [16]. (The measurements of Russ are summarized at the end of this proposition.) In the 1970 work, which was preliminary in nature, no determination was made of the terrestrial Ca isotopic composition or of the Ca composition in non-radiogenic meteoritic material. Assuming the Nier values [17] for the Ca isotopic composition, one can calculate two ^{40}K-^{40}Ca ages - one for the spiked analysis, which was normalized to the $^{48}Ca/^{42}Ca$ ratio of the spike solution, and one for the unspiked Ca analysis,

which was normalized to the Nier $^{42}Ca/^{44}Ca$ ratio [17]. From these data one calculates ^{40}K-^{40}Ca ages of $(4.20 \pm 0.04) \times 10^9$ yr and $(4.37 \pm 0.07) \times 10^9$ yr for the spiked and unspiked analyses respectively. The difference in these determinations appears to be due to the uncertainties in the ratios used for normalization. These uncertainties were not included in the quoted uncertainties of the ages. Although there is a possibility that the Ca in the meteorite differs from that in terrestrial material and although normalizing the data to the $^{48}Ca/^{42}Ca$ rates in the spike would not take this natural fractionation into account, the age determined for the spiked analysis should be more reliable because the choice of the normalization value does not affect the result as seriously as is the case when the data are normalized to a constant $^{42}Ca/^{44}Ca$ ratio. Using the spiked analysis for Ca and the measured radiogenic ^{87}Sr concentration, one calculates a half-life of $(4.47 \pm 0.07) \times 10^{10}$ yr for ^{87}Rb. The unspiked analysis implies $t_{1/2} = (4.66 \pm 0.09) \times 10^{10}$ yr.

While unlike the ^{40}Ar-^{39}Ar data, these data appear to support the measured ^{87}Rb half-life values rather than that of Aldrich *et al.* [2], they are critically dependent on the Nier [17] values for the isotopic composition of non-radiogenic Ca. For instance if the values of Backus, Pinson, Herzog, and Hurley [18] were used, both analyses would yield ^{40}K-^{40}Ca ages of 4.96×10^9 yr. In order to better determine the ^{40}K-^{40}Ca age of Colomera and other samples, to check the ^{40}K branching ratio, and to indirectly determine the ^{87}Rb half-life a series of experiments is proposed. The first measurement required is a more precise determination of the isotopic composition of

non-radiogenic terrestrial and extra-terrestrial calcium. By using a double spike of ^{42}Ca and ^{48}Ca which has been prepared gravimetrically from the separate spikes in such a way that the $^{42}Ca/^{48}Ca$ ratio is well known, one can mass spectrometrically determine the ratio of ^{40}Ca to ^{44}Ca in non-radiogenic samples. The Colomera concentration analysis shows that the uncertainty in the determination of $^{40}Ca/^{44}Ca$ due to ion statistics could be kept below 1‰ ($2\sigma_{mean}$) for a single analysis. Assuming the spike composition is well known, the only other sources of uncertainty should be in the normal $^{42}Ca/^{44}Ca$ and $^{48}Ca/^{44}Ca$ values and the tracer $^{42}Ca/^{44}Ca$ ratio. However, these uncertainties should not be significant. By multiple analyses the uncertainty in $^{40}Ca/^{44}Ca$ should be reduced significantly below 1 ‰. It should then be possible to analyse unspiked samples and by normalizing the data to the already measured $^{40}Ca/^{44}Ca$ ratio, to determine the $^{40}Ca/^{42}Ca$ to a similar precision. For an uncertainty of 1‰ each in the $^{40}Ca/^{44}Ca$ ratios of the non-radiogenic component and the sample, the ^{40}K-^{40}Ca age calculated for a ~4.5 x 10^9 yr old sample with the K/Ca ratio of the Colomera potassium feldspar grains would have an uncertainty of only 60 my or 1.3%. The product of the decay constant for ^{87}Rb and the sample age should also be measurable to an uncertainty of <1%; therefore, the half-life of ^{87}Rb can be determined to ~ $\pm$ 1% assuming the ^{40}K decay constants are well known. By measuring ^{40}K-^{40}Ca and ^{40}Ar-^{39}Ar ages for the same samples the branching ratio of the ^{40}K decay can be checked. The ratios of both radiogenic ^{40}Ar and ^{40}Ca to ^{40}K should be

measurable to $\pm$ 2%; so the branching ratio should be obtainable to ~ $\pm$ 3% for samples with good ^{40}Ar-^{39}Ar "plateaus". This resolution should be sufficient to favor either the Wetherill [13] or Beckinsale and Gale [12] branching ratios which differ by 6% ($\lambda_{Ar}/\lambda_{Ca}$).

The measurements on the Colomera feldspar grains would need to be supplemented by additional data before reaching firm conclusions about the half-life of ^{87}Rb or the branching ratio of ^{40}K. Kohman [9] has reviewed the samples which are likely to be suitable for ^{40}K-^{40}Ca dating. He lists several meteorites with high K/Ca ratios. Selected lunar samples, *e.g.*. 12013, also have high K/Ca ratios and should be studied by ^{40}K-^{40}Ca. In terrestrial rocks a variety of micas and evaporites have high K/Ca ratios. Coleman [11] concluded that because high K/Ca micas were usually pegmatitic they were likely to yield incorrect ages as a result inherited radiogenic components and/or open system behavior. This conclusion deserves further study.

Summary of Colomera Feldspar Measurements

A potassium feldspar sample of several milligrams was hand-picked under a microscope to eliminate those grains with other phases attached. This sample (6 mg) was dissolved and divided into two aliquots. One was spiked for potassium, rubidium, and calcium concentration measurements. The other was spiked for strontium. These samples were then put through cation exchange columns. The sample spiked only for strontium was put through a column which had never seen calcium or potassium spikes. From this column the calcium

and strontium aliquots were collected. The three spiked elements were collected from the other column. This procedure gave two calcium samples. One was analysed on the mass spectrometer for isotopic composition. The other was analysed for isotopic composition and concentration. This procedure was followed because in the spiked sample it was necessary to normalize the data to a constant ratio of 42/48 in the spike. This removes the isotopic fractionation introduced during the mass spectrometer run but does not correct for any natural fractionation which might be present. The composition analysis was normalized to Nier's value of $^{42}Ca/^{44}Ca$ [17]. The concentration and composition determined were corrected for mass fractionation, cross contamination from the spikes, and blanks. Errors were calculated as $2\sigma_{mean}$ for the mass spectrometer runs and reasonable errors were added quadratically for other uncertainties. The results are tabulated below:

$[^{40}K] = 0.3650 \pm 0.0006$ μm/g

$[^{44}Ca] = 1.332 \pm 0.018$ μm/g

$^{40}Ca/^{44}Ca = 49.27 \pm 0.05$ concentration analysis

$^{40}Ca/^{44}Ca = 49.51 \pm 0.10$ composition analysis

$[^{87}Rb] = 10.92 \pm 0.13$ μm/g

$[^{88}Sr] = 1.103 \pm 0.001$ μm/g

$^{87}Sr/^{86}Sr = 6.2660 \pm 0.0014$

$^{87}Sr/^{86}Sr$ (assumed initial) = 0.6990 [1]

$\lambda T_{Sr} = 0.06494 \pm 0.00076$

The difference in the $^{40}Ca/^{44}Ca$ almost certainly results from the uncertainty in the terrestrial $^{42}Ca/^{44}Ca$ ratio. The unspiked calcium analysis should be repeated to reduce the error in the measured $^{40}Ca/^{44}Ca$. The ^{87}Rb concentration should be remeasured using the silica gel method [1] which should reduce the uncertainty in the rubidium concentration by about a factor of 2.

References

[1] D. A. Papanastassiou and G. J. Wasserburg, Rb-Sr ages of igneous rocks from the Apollo 14 mission and the age of the Fra Mauro formation, Earth Planet. Sci. Letters 12 (1971) 36.

[2] L. T. Aldrich, G. W. Wetherill, G. R. Tilton and G. L. Davis, Half-life of Rb^{87}, Phys. Rev. 103 (1956) 1045.

[3] K. F. Flynn and L. E. Glendenin, Half-life and beta spectrum of Rb^{87}, Phys. Rev. 116 (1959) 744.

[4] C. C. McMullen, K. Fritze, and R. H. Tomlinson, The half-life of rubidium-87, Can. Jour. Phys. 44 (1966) 3033.

[5] A. H. Jaffey, K. F. Flynn, L. E. Glendenin, W. C. Bentley, and A. M. Essling, Precision measurement of half-lives and specific activities of ^{235}U and ^{238}U, Phys. Rev. C. 4 (1971) 1889.

[6] Fouad Tera and G. J. Wasserburg, U-Th-Pb systematics in three Apollo 14 basalts and the problem of initial Pb in lunar rocks, Earth Planet. Sci. Letters 14 (1972) 281.

[7] G. Turner, J. C. Huneke, F. A. Podosek, and G. J. Wasserburg, ^{40}Ar-^{39}Ar ages and cosmic ray exposure ages of Apollo 14 samples, Earth Planet. Sci. Letters 12 (1971) 19.

[8] M. G. Inghram, H. Brown, C. C. Patterson, and D. C. Hess, The branching ratio of K^{40} radioactive decay, Phys. Rev. 80 (1950) 916.

[9] Truman P. Kohman, Geochronological potential of the K^{40}-Ca^{40} system, Nuclear Chemistry and Geochemistry Research Carnegie-Mellon University, 1968-1969 (U.S.A.E.C. Report NYO-844-76, 1969) 34.

[10] Leonard F. Herzog, Rb-Sr and K-Ca analyses and ages, N.R.C. Nucl. Sci. Series Rept. 19 (1956) 114.

[11] M. L. Coleman, Potassium-calcium dates from pegmatitic micas, Earth Planet. Sci. Letters 12 (1971) 399.

[12] R. D. Beckinsale and N. H. Gale, A reappraisal of the decay constants and branching ratio of ^{40}K, Earth Planet. Sci. Letters 6 (1969) 289.

[13] George W. Wetherill, Radioactive decay constants and energies, Handbook of Physical Constants (Geol. Soc. Amer., Memoir 97, 1966) 514.

[14] G. J. Wasserburg and D. A. Papanastassiou, Age of an Apollo 15 mare basalt; lunar crust and mantle evolution, Earth Planet. Sci. Letters 13 (1971) 97.

[15] G. J. Wasserburg, G. Turner, F. Tera, F. A. Podosek, D. A. Papanastassiou, and J. C. Huneke, Comparison of Rb-Sr, K-Ar, and U-Th-Pb ages; lunar chronology and evolution, Lunar Science III (Lunar Sci. Inst. Cont. 88, 1972) 788.

[16] G. J. Wasserburg, H. M. Sanz, and A. E. Bence, Potassium-feldspar phenocrysts in the surface of Colomera an iron meteorite, Science 161 (1968) 684.

[17] A. O. Nier, The isotopic constitution of calcium, titanium, sulfur and argon, Phys. Rev. 53 (1938) 282.

[18] Milo M. Backus, W. H. Pinson, L. F. Herzog, and P. M. Hurley, Calcium isotope ratios in the Homestead and Pasamonte meteorites and a Devonian limestone, Geochim. Cosmochim. Acta 28 (1964) 735.

Proposition 5

The Oklo uranium deposit has apparently operated as a natural self-sustained nuclear reactor. Measurements of the isotopic composition of samarium in pitchblende samples from the Oklo deposit could be used to determine the neutron flux, fluence, and energy spectrum to which the samples have been exposed.

It has recently been reported by workers at the French atomic energy agency that uranium samples from the Oklo mine in the Gabon have depleted ^{235}U abundances and pronounced concentrations of fission products [1-4]. These results have been interpreted as indicating that ~1.7×10^9 yr ago this deposit acted as a naturally occurring nuclear reactor which burned ^{235}U in a self-sustaining chain reaction. The possibility of such phenomena occurring in nature was recognized by Kuroda [5], but no other evidence has been reported for such an occurrence.

The best available evidence for extensive fission in the Oklo material is the isotopic composition of the Nd in these samples [3,4] which closely resembles that produced by ^{235}U fission. Because ^{143}Nd has an appreciable neutron capture cross section for the formation of ^{144}Nd, the isotopic composition of Nd can be used to estimate the neutron fluences (~10^{21} n/cm^2) to which the samples have been exposed.

The extent of the depletions in ^{235}U can also be used to calculate neutron fluences; however, these depletions are only about half as large as would be expected from the Nd data. The French workers have attributed the lower ^{235}U depletions to conversion of ^{238}U to ^{235}U by the reaction $^{238}U(n,\gamma)^{239}U(\beta^-)^{239}Np(\beta^-)^{239}Pu(\alpha)^{235}U$ and have used the fact that the Nd isotopic data do not indicate a large ^{239}Pu fission component to argue that the average flux in the deposit during the neutron irradiation was low ($< 10^{9}$ n·cm^{-2}·sec^{-1}) and long-lived ($> 10^{4}$ yr).

Assuming that the neutron flux was reasonably well thermalized as one would expect if water was the moderator, the ratios of the ^{235}U and ^{238}U abundances and cross sections are such that the ^{239}Pu conversion path could have replaced only ~3% of the ^{235}U consumed by fission. It therefore seems unreasonable that the observed U isotopic composition could be explained by the conversion reaction given above. It seems equally unfounded to conclude on the basis of the Nd data that the flux was low because in a thermal flux the Pu concentration would have been too low to have contributed more than ~2% of the total fission produced Nd. (It should however be pointed out that for a poorly thermalized neutron spectrum the ^{239}Pu production rate relative to the ^{235}U fission rate would be increased.)

A more reasonable explanation of the relatively small ^{235}U depletions would be that additional "normal" uranium was added to the deposit after the fission products were produced. This interpretation is supported by several lines of evidence. 1) Certain

Oklo samples are reported to contain up to 85 weight percent U which would correspond to pure pitchblende. If these samples had in fact not had U added to them since they were deposited 1.7×10^9 yr ago, one would calculate from the rate of uranium decay that they were >100% U at the time of their formation which is obviously impossible. 2) Because ^{142}Nd is not produced in fission reactions, the abundance of ^{142}Nd can be used to estimate the Nd/U ratio at the time of the neutron irradiation assuming of course that the ^{142}Nd was present at that time. The observed Nd/U ratios are smaller than calculated from the Nd isotopic data. Such a disparity could be introduced by either Nd loss or U addition but only U addition can also explain the U isotopic ratios and the fluence indicated by the Nd isotopic data. Using the fluence and Nd/U ratio calculated from the Nd data, one can estimate the fractional amount of normal U which would have to be added to the depleted U to match the observed $^{235}U/^{238}U$ ratio. From the measured concentration of Nd one can also estimate the U concentration and compare this estimate to the measured concentration. For the sample for which such a comparison was made (No. 310), the predicted U concentration was 16 weight percent with ~25% of the U being added after the neutron exposure. The measured U concentration for this sample (15%) is in good agreement with this estimate. (However there may be some problem with the concentration data because the $^{148}Nd/^{238}U$ ratio reported for this sample (No. 310) [3] is not compatible with the reported U and Nd concentrations. If the $^{148}Nd/^{238}U$ ratio is correct

and applies to the time of irradiation additional fission perhaps from ^{239}Pu or ^{239}Pu produced ^{235}U would be required to explain the observed Nd isotopic composition.) 3) Samples with 15 weight percent U contain only 1% Pb whereas 1.7×10^9 yr old samples with such a U concentration should contain ~4% Pb produced by the decay of U. This third point does not necessarily require U addition but is compatible with it.

Measurements of the isotopic composition of Sm in the Oklo sample could provide information on the neutron flux and fluence to which the samples have been exposed and an estimate of the shape of the neutron energy spectrum. The latter two points have already been noted by the French workers and will therefore only be briefly considered here.

The stable isotopes of Sm produced in fission are 147, 149, 152, and 154. Of these isotopes 147, 149 and 152 have appreciable neutron capture cross sections; therefore, the observed abundances of the stable isotopes 147, 148, 149, 150, 152 and 154 can be used to calculate the neutron fluence to which the samples have been exposed. The amount of normal Sm present in addition to the fission component can be determined from the abundance of ^{144}Sm which is shielded from fission and has a small neutron capture cross section. The cross sections for ^{147}Sm and ^{149}Sm have different energy dependences therefore measurements of the relative amounts of ^{148}Sm and ^{150}Sm produced by neutron capture can be used to constrain the possible energy spectra for the neutron flux.

In addition to the stable isotopes, $^{151}Sm(t_{1/2} = 93$ yr), is produced by fission. Because this isotope has a large neutron capture cross section ($\sigma_{thermal} = 1.5 \times 10^4$ barns), in a high flux essentially all the ^{151}Sm will be transformed into ^{152}Sm, while in a low flux the ^{151}Sm will beta decay to ^{151}Eu. The amount of ^{152}Sm present is therefore a measure of the average neutron flux to which the samples were exposed. ^{151}Sm is unique in that it is the only fission product which is sensitive to average fluxes of less than about 10^{10} $n \cdot cm^{-2} \cdot sec^{-1}$ where the average is carried over the mean life of the nuclide. Considering the cross section to decay constant ratio and the precision obtainable in the determination of Sm isotopic abundances, one calculates that 100 yr average fluxes in the range 3×10^8 - 3×10^{12} $n \cdot cm^{-2} \cdot sec^{-1}$ should be measurable by this technique. Outside this range one could only set limits for the magnitude of the flux. The decay of ^{239}Pu is also sensitive to fluxes in approximately the same range; however, it is more difficult to determine whether ^{239}Pu decayed by fission or α emission and the abundance of ^{239}Pu is uncertain. ^{151}Sm averages the neutron flux over a period of ~100 years while ^{239}Pu averages over ~25,000 years. For this reason, ^{151}Sm is more sensitive to short periods of neutron exposure than ^{239}Pu. For instance if the deposit became critical and remained critical for one year then shut off and if during that year the fluence was 10^{19} n/cm^2, about 15% of the ^{151}Sm's produced would capture neutrons to form ^{152}Sm while only ~1% of the ^{239}Pu atoms would capture neutrons. The ratio of the capture products could therefore be used to estimate the constancy of the flux as well

as its magnitude.

References

[1] Robert Bodu, Henri Bouzigues, Noël Morin and Jean-Paul Pfiffelmann, Sur l'existence d'anomalies isotopiques recontrées dans l'uranium du Gabon, Comptes Rendus D 275 (1972) 1731.

[2] Michele Neuilly, Jean Bussac, Claude Frèjacques, Guy Nief, Georges Vendryes, and Jacques Yvon, Sur l'existence dans un passé reculé d'une réaction en chaîne naturelle de fissions, dans le gisement d'uranium d'Oklo (Gabon). Comptes Rendus D 275 (1972) 1847.

[3] Guy Baudin, Claude Blain, Robert Hagemann, Marcelle Kremer, Monique Lucas, Liliane Merlivat, Roger Molina, Guy Nief, Francois Prost-Marechal, Francois Regnaud, and Etienne Roth, Quelques données nouvelles sur les réactions nucléaires en chaîne qui se sont produites dans le gisement d'Oklo, Comptes Rendus D 275 (1972) 2291.

[4] Georges A. Vendryes, Recent discovery of a prehistoric nuclear reactor in Gabun, address presented at the American Nuclear Society Winter Meeting, Washington 1972.

[5] P. K. Kuroda, On the nuclear physical stability of the uranium minerals, J. Chem. Phys. 25 (1956) 781.